NATIONAL COOPERATIVE
HIGHWAY RESEARCH PROGRAM REPORT

298

PERFORMANCE OF ELASTOMERIC BEARINGS

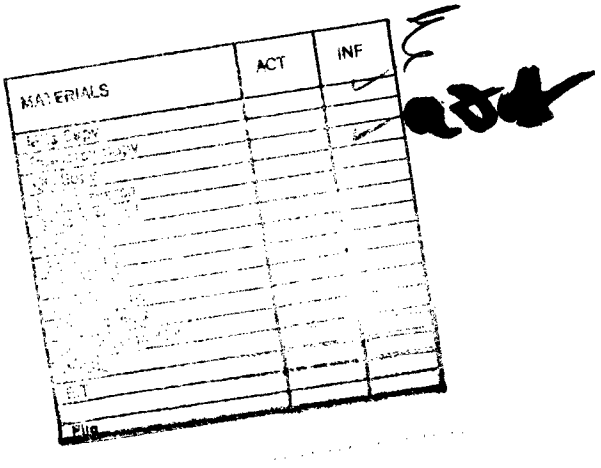

TRANSPORTATION RESEARCH BOARD
NATIONAL RESEARCH COUNCIL

NATIONAL COOPERATIVE HIGHWAY RESEARCH PROGRAM
REPORT 298

PERFORMANCE OF ELASTOMERIC BEARINGS

C. W. ROEDER, J. F. STANTON
and A. W. TAYLOR
Department of Civil Engineering
University of Washington
Seattle, Washington

RESEARCH SPONSORED BY THE AMERICAN ASSOCIATION OF STATE HIGHWAY AND TRANSPORTATION OFFICIALS IN COOPERATION WITH THE FEDERAL HIGHWAY ADMINISTRATION

AREAS OF INTEREST:

Structures Design and Performance
Construction
General Materials
(Highway Transportation, Public Transit, Rail Transportation)

TRANSPORTATION RESEARCH BOARD
NATIONAL RESEARCH COUNCIL
WASHINGTON, D.C.

OCTOBER 1987

NATIONAL COOPERATIVE HIGHWAY RESEARCH PROGRAM

Systematic, well-designed research provides the most effective approach to the solution of many problems facing highway administrators and engineers. Often, highway problems are of local interest and can best be studied by highway departments individually or in cooperation with their state universities and others. However, the accelerating growth of highway transportation develops increasingly complex problems of wide interest to highway authorities. These problems are best studied through a coordinated program of cooperative research.

In recognition of these needs, the highway administrators of the American Association of State Highway and Transportation Officials initiated in 1962 an objective national highway research program employing modern scientific techniques. This program is supported on a continuing basis by funds from participating member states of the Association and it receives the full cooperation and support of the Federal Highway Administration, United States Department of Transportation.

The Transportation Research Board of the National Research Council was requested by the Association to administer the research program because of the Board's recognized objectivity and understanding of modern research practices. The Board is uniquely suited for this purpose as: it maintains an extensive committee structure from which authorities on any highway transportation subject may be drawn; it possesses avenues of communications and cooperation with federal, state, and local governmental agencies, universities, and industry; its relationship to the National Research Council is an insurance of objectivity; it maintains a full-time research correlation staff of specialists in highway transportation matters to bring the findings of research directly to those who are in a position to use them.

The program is developed on the basis of research needs identified by chief administrators of the highway and transportation departments and by committees of AASHTO. Each year, specific areas of research needs to be included in the program are proposed to the National Research Council and the Board by the American Association of State Highway and Transportation Officials. Research projects to fulfill these needs are defined by the Board, and qualified research agencies are selected from those that have submitted proposals. Administration and surveillance of research contracts are the responsibilities of the National Research Council and the Transportation Research Board.

The needs for highway research are many, and the National Cooperative Highway Research Program can make significant contributions to the solution of highway transportation problems of mutual concern to many responsible groups. The program, however, is intended to complement rather than to substitute for or duplicate other highway research programs.

NCHRP REPORT 298

Project 10-20 FY '83

ISSN 0077-5614

ISBN 0-309-04567-3

L. C. Catalog Card No. 87-51180

Price $12.00

NOTICE

The project that is the subject of this report was a part of the National Cooperative Highway Research Program conducted by the Transportation Research Board with the approval of the Governing Board of the National Research Council. Such approval reflects the Governing Board's judgment that the program concerned is of national importance and appropriate with respect to both the purposes and resources of the National Research Council.

The members of the technical committee selected to monitor this project and to review this report were chosen for recognized scholarly competence and with due consideration for the balance of disciplines appropriate to the project. The opinions and conclusions expressed or implied are those of the research agency that performed the research, and, while they have been accepted as appropriate by the technical committee, they are not necessarily those of the Transportation Research Board, the National Research Council, the American Association of State Highway and Transportation officials, or the Federal Highway Administration, U.S. Department of Transportation.

Each report is reviewed and accepted for publication by the technical committee according to procedures established and monitored by the Transportation Research Board Executive Committee and the Governing Board of the National Research Council.

Special Notice

The Transportation Research Board, the National Research Council, the Federal Highway Administration, the American Association of State Highway and Transportation Officials, and the individual states participating in the National Cooperative Highway Research Program do not endorse products or manufacturers. Trade or manufacturers' names appear herein solely because they are considered essential to the object of this report.

Published reports of the

NATIONAL COOPERATIVE HIGHWAY RESEARCH PROGRAM

are available from:

Transportation Research Board
National Research Council
2101 Constitution Avenue, N.W.
Washington, D.C. 20418

Printed in the United States of America

FOREWORD

By Staff
Transportation
Research Board

This report contains the findings of a study that was undertaken to provide more refined design methods which will allow greater use of elastomeric bearings in highway bridges. The report includes recommended specifications for the design of bearings that are more highly stressed and more slender, providing bearings that are smaller or that impart lower horizontal forces on bridge piers and abutments. The contents of this report will be of immediate interest and use to bridge engineers, construction engineers, materials engineers, researchers, specification writing bodies, and others concerned with elastomeric bridge bearings.

The use of elastomeric bearings in highway bridge construction in the United States has increased greatly during the last 20 to 30 years. This is, in part, because of their desirable performance characteristics, maintenance-free durability, and relative economy of use. Initially, small, unreinforced elastomeric bearing pads were used to support short-span prestressed concrete beams. More recently, steel- and fiberglass-laminated elastomeric bearing pads have been used in situations requiring higher bearing stresses and stiffness.

NCHRP Project 10-20, "Elastomeric Bearings Design, Construction, and Materials," was initiated in 1981 to address the absence of detailed design procedures for the use of elastomeric bearings in the AASHTO *Standard Specifications for Highway Bridges*. Recommendations for improved specifications for unconfined, plain and reinforced elastomeric bridge bearings (Method A) were made at the conclusion of the first phase of research on the project. These recommendations were included in *NCHRP Report 248,* "Elastomeric Bearings Design, Construction, and Materials." One of the most significant aspects of the recommended specifications was the increase in the allowable bearing stress on elastomeric pads from 800 psi to 1100 psi. The recommended specifications were adopted in whole into the AASHTO *Standard Specifications for Highway Bridges* in 1985.

A second phase of NCHRP Project 10-20 was initiated in 1983 to develop improved specifications for elastomeric bridge bearings, and specifications for special applications. The Method A specification developed in the first phase of the research was based upon data and theories found in the recent literature. The second phase research included laboratory testing on actual bridge bearings in order to provide correlation of bearing performance and test data with the theories upon which the Method A specifications were based. Additionally, with a better understanding of elastomeric bearing behavior, a more rational design specification could be developed. Tests were performed to assess bearing compression, rotation, shear, stability, fatigue, and low temperature behavior.

This report documents the work performed under the second phase of NCHRP Project 10-20. It provides recommendations for a more rational bearing specification (Method B) that would allow bearing pressures as high as 1600 psi under some design conditions. The use of Method B will require a greater design effort and quality control during bearing fabrication. The use of Method B, however, should provide elastomeric bearings that are more efficient and provide better performance than bearings presently in use. It is expected that the AASHTO Subcommittee on Bridges and Structures will consider adoption of the recommended Method B specifications into the AASHTO *Standard Specifications for Highway Bridges* shortly.

CONTENTS

ACKNOWLEDGMENTS

This research was carried out under NCHRP Project 10-20. The principal investigators for the project were Charles W. Roeder and John F. Stanton. The other author of this report is Andrew W. Taylor. The authors would like to acknowledge the help of former graduate students Glen Scroggins, Kathleen Curry, Scott Branlund, and Gary Graff, continuing graduate student Ranga Kandadai, and former undergraduates Carmen Alma Jose and Derek Case, all of whom worked on the project. The design of the rotation test rig was based on the original idea of former graduate student Ken Olson.

PERFORMANCE OF ELASTOMERIC BEARINGS

SUMMARY

Elastomeric bridge bearings have been used in the United States for nearly 30 years. They are now more widely used than any other type of bearing, because they are economical, efficient, and maintenance-free. The AASHTO *Standard Specifications for Highway Bridges* (hereinafter referred to as AASHTO *Specifications* or *Specification*) contain rules for their design and for materials performance standards to be met in specific ASTM tests. These design and materials requirements have changed little since they were first included in 1961, and have fallen behind many foreign specifications in their versatility. NCHRP Project 10-20 was initiated in 1981 with the objective of evaluating the existing worldwide knowledge on the subject and preparing a proposal for revising the AASHTO *Specifications.* The report on that project (*NCHRP Report 248*) contained an improved but still simple design method (Method A), which pointed out a number of areas where the state of the art showed inadequacies or inconsistencies. Phase II of the project was initiated to resolve those shortcomings. This report describes the Phase II research and contains the resulting proposals for a more sophisticated design method (Method B) which allows the design of bearings that are more highly stressed and more slender, at the expense of greater design effort and tighter quality control. The potential benefits lie in smaller bearings and lower horizontal forces on the bridge piers.

The research consisted mostly of testing and correlation of results with existing theories. Compression, rotation, shear, stability, fatigue, and material modulus results are described in some detail in Appendixes B through G, respectively, of the report. A purely theoretical study was conducted on low-temperature bearing behavior, and that is reported in Appendix A. In the main body of the report the *a priori* state of the art is outlined, followed by condensed descriptions of the behavior studies and their findings; these, then, are used to develop the design provisions for Method B.

The low temperature study showed that typical steel-reinforced bearings will reach thermal equilibrium with their surroundings in approximately 6 hours or less, depending on size and shape. Thus, elastomers which crystallize rapidly at temperatures to be found in the field will stiffen significantly even during a short cold spell, and suitable measures for preventing high horizontal forces appear necessary. These could include provision of a sliding surface or choice of an elastomer with appropriate resistance to crystallization and low temperature thermal stiffening. To this end, proposals are made for dividing the country into three regions. In each region either a specific grade of elastomer or a slip apparatus should be used, or the piers should be designed to resist the higher forces arising from the stiffening. A number of questions remain open, and they can only be resolved by appropriate testing.

The compression studies showed that yielding and fracture of the reinforcement could be predicted by existing theories with reasonable accuracy. Theories were also developed for some cases of bearings with holes, and these showed that holes raise the steel stresses and reduce the fracture strength by a factor of about 2. Experimental verification was difficult (because the high stresses exist only locally), but it supported

the theoretical findings. Some poorly made bearings had very uneven elastomer layer thicknesses, and they failed at loads significantly below the predicted ones, demonstrating the need for good quality control during manufacture. In all cases debonding of the elastomer at the edge of the bearing occurred before fracture of the reinforcement, but the average compressive stress at which it took place showed very wide scatter, which prevented any reasonable correlation with the shear stresses at the bearing edge predicted by existing theories. Fiberglass-reinforced bearings were found to be more flexible in compression than similar bearings reinforced with steel and to have significantly lower fracture strengths.

Two types of rotation tests were conducted. In the first, increasing load was applied at constant eccentricity, and in the second a special rig was designed and built in which rotations could be imposed while a primary, concentric load was maintained constant. Both test series showed that moment-rotation curves at a given compressive load are very close to linear prior to lift-off, as predicted by theory. However, the rotational stiffness was found to increase significantly with greater compressive stress. The variation in rotational stiffness with plan dimensions correlated reasonably well with predictions. At high loads debonding started on the most highly compressed edge at average compressive stresses below those which had caused debonding in concentrically loaded specimens. This provides qualitative validation of theoretical predictions of the severity of the edge stresses under eccentric load, but there was too much scatter in the results to draw quantitative conclusions.

Shear tests were conducted both as an end in themselves and as a check on the material properties or condition of the specimens being used in other tests. The monotonic force-displacement relationship was found to be nearly linear, but some hysteresis was present in all the cyclic tests. This hysteresis increased at higher compressive loads. The loops degenerated for the first few cycles but became repeatable after about five or six. For displacements less than about half the total thickness of the elastomer, behavior appeared to be well represented by a simple shear model, but higher displacements caused roll-over at the bearing edges. In the elastomer this gave rise to stress concentrations and a probable component of vertical tension in addition to the imposed shear, and it caused local bending of the steel reinforcement, all of which are clearly undesirable. Direct stresses in the reinforcement caused by shear were found to be insignificant. The shear stiffness of a bearing is sensitive to temperature and to stability effects, as discussed in Appendixes A and E, but even in squat specimens at room temperature where these effects were negligible the shear stiffness was found to vary with the compressive stress which was applied at the same time.

Stability was investigated by finding the buckling strengths of columns made of different numbers of reinforced bearing units placed on top of one another. The measured buckling strength compared well with theoretical predictions (which include the effects of shear flexibility) for slender columns, but at lower slendernesses the theory was found to under-predict the true buckling load. To improve the correlation the theory was modified to incorporate the stiffness changes that occur as a result of changing geometry and material properties, but the improvements did not warrant the extra analytical effort. Transverse stiffness tests under varying levels of axial load were also conducted, and, while correlation was reasonable, the measured stiffnesses were somewhat smaller than predicted. In all the correlations the fact that the shear and rotational stiffnesses appeared to be sensitive to compressive stress made prediction of a unique buckling load impossible with existing theories, leading to the same problem in predicting a unique transverse stiffness.

Fatigue experiments were carried out separately in shear and compression. They had to be done quite slowly in order to avoid overheating the specimens, so lack of

time prevented generation of complete S-N curves. In shear, it was found that the most important variable was the range of the applied cyclic shear displacement, even though the simultaneous static compressive stress caused calculated (constant) shear strains, at the edge of the elastomer, which were considerably higher. Cyclic shear strains greater than ± 0.50 were particularly damaging. The natural rubber specimens (which were generally softer) showed better shear fatigue performance, but the harder specimens of both natural rubber and polychloroprene did best in the compression fatigue tests. Furthermore, fatigue life was not found to correlate well with any particular material property, such as elongation at break. Fatigue damage was manifested in both types of test by cracking and debonding at the edge of the elastomer-steel interface, although the nature of the cracking was slightly different in the two cases. The damage caused more difference to the compression than to the shear stiffness. Most specimens were tested without edge cover, so it is believed that the results are conservative. However, two specimens with cover were tested in shear fatigue, and the cover served effectively to hide the considerable damage that took place underneath. Thus the degree of conservatism inherent in the tests may not be as great as intuition would suggest.

The results of these test programs were evaluated and used as the basis for design provisions. The scatter in the data and the difficulty of selecting acceptable levels of fatigue damage from what is essentially a continuous spectrum mean that highly sophisticated design rules are not justified. The most significant design recommendations are that the absolute maximum compressive stress be raised to 1,600 psi, based on debonding observations, with lower values under many circumstances. The compressive stresses under total load and under live load alone are each limited to separate functions of the shape factor, the material modulus, and the rotation which is applied at the same time. The shear displacement between the conditions at setting of the girder and the extreme conditions is limited to 0.5 times the total elastomer thickness. The slenderness of the bearing is controlled only through the buckling load, permitting the use of bearings that are considerably taller than those allowed by the present *Specifications.* It is hoped that these proposed design rules will open up possibilities for improving the efficiency of elastomeric bearings, broadening their range of application, and designing bearings that will lead to smaller forces on the adjoining parts of the bridge.

CHAPTER ONE

INTRODUCTION AND RESEARCH APPROACH

BACKGROUND

Elastomeric bridge bearings are being used with increasing frequency. They support large gravity loads while accommodating movements due to thermal effects, shrinkage or creep, and generally they require minimal maintenance. These desirable attributes have resulted in present usage that has gone far beyond that originally envisioned in the American Association of State Highway and Transportation Officials (AASHTO) *Standard Specifications for Highway Bridges* (hereinafter referred to as the AASHTO *Specifications*) (*1*). Provisions for elastomeric bearings were first included in the 1961 editions of the AASHTO *Specifications.* They were based on the developmental work (*2*) performed by the DuPont Company, and were intended for plain (unreinforced) polychloroprene pads. These provisions remained in force with only minor changes for more than 20 years, but the needs of the bridge engineer changed dramatically during that period. As a result of these changes, the NCHRP Project 10-20 research program was started in 1981. The first phase consisted of a comprehensive state-of-the-art review (*3*) that resulted in a series of initial modifications to the AASHTO *Specifications* (*4*).

The final report (*3*) of the first phase showed that there were some severe deficiencies in the existing understanding of elas-

tomeric bearing behavior. Different design specifications contain wide discrepancies and contradictions, and offer no sound scientific reasons for selecting one design approach over another. As a result, a Phase II research program was initiated to resolve many of these inconsistencies, and to develop a new, more rational design specification. This report is the Final Report of this second phase of the NCHRP Project 10-20 research program. It includes detailed descriptions of the research performed, analysis of the research results, development of conclusions and recommendations, and a proposed modification to the AASHTO *Specifications.* The fundamental behavior of elastomeric bridge bearings is discussed at length in the earlier report (*3*), and is not repeated in this report.

PHASE II RESEARCH

The Phase II research was directed toward resolving serious unanswered questions found in the Phase I research and developing recommendations for an improved AASHTO *Specification.* Those questions fell into the following four major categories, which defined the first four tasks of the research.

1. *Task A—Low Temperature Effects.* Elastomers stiffen as they cool, and the degree of stiffening varies with time, temperature, and the elastomeric compound. Because the bridge also deforms with temperature, this low temperature stiffening may significantly increase the shear forces on the bearing and the bridge structure. These larger forces may cause damage to the structure or may cause the bearing to slip out from its proper position. This task was an analytical study, whose goal was to obtain the best available data on low temperature behavior and to estimate if and when low temperature stiffening is a problem. It did not include any experimental work because the necessary funds were not available.

2. *Task B—Confirmation of Theories of Behavior.* Most design specifications for elastomeric bearings limit the loads and deformations so that specified stress and strain limits are not exceeded. The theories used to predict these stresses and strains are usually based on simplified linear elastic models. However, it is well known (*3*) that elastomers are not perfectly elastic, and nonlinearities are introduced both by large strains and nonlinear materials effects. This task examined the validity of theories used to predict stress, strain, force, and deflection in bearings. The task was to focus on behavior under compression, shear, rotation, and combinations of these loadings. Theoretical predictions of the buckling loads and the effect of stability on the bearing stiffness were also to be considered. These theories were to be evaluated, compared to experimental results, improved where possible, and then used to provide a basis for better design provisions.

3. *Task C—Determination and Assessment of the Modes of Failure.* Design specifications limit the stress and strains in bearings to values that are believed to represent some fraction of the values that would cause failure of the bearing. It is well known (*3*) that bearings may fail by yield or rupture of the reinforcement, cracking or tearing of the elastomer, fatigue, delamination or separation of the elastomer from the reinforcement, buckling, slip of the bearing from under the load, creep, deterioration or excessive deflections. The limiting values for these modes of failure are not well understood or well documented. They often are functions of the quality of manufacture and the elastomeric compound. Therefore, experiments were performed to understand these modes of failure better and to develop more reliable limits for design. Task C is closely related to Task B, inasmuch as many experiments were used for both purposes.

4. *Task D—Evaluation of Material Behavior.* The elastomeric compound and its material properties have considerable impact on the bearing behavior. Further, many of the previous experimental and theoretical research programs (*3*) did not document these properties well. As a result, Task D was added to support the results of the earlier tasks. It had two major objectives. One objective was to document the properties of bearings used in the experiments so that reasonable comparisons could be made between theoretical and experimental results. The second objective was to test a wide range of elastomeric compounds, which are commonly used in bridge bearings, to determine how different compounds affect the modes of failure. Task D was closely associated with Tasks B and C.

Structure of the Report

Many of the experiments and analyses are relevant to more than one of the Tasks A through D. The work is thus reported by type of behavior rather than by Task. The main report contains a summary and analysis of the most important findings, and the details and the proposed *Specification* are contained in the appendixes.

Chapter One of this report provides an introduction to the research and a brief summary of the different theoretical and experimental portions of the work described in full in the appendixes. Also included in this chapter is a glossary of the notation used throughout this report. Chapter Two briefly summarizes the major research results found in the appendixes, and Chapter Three discusses the rationale for the major recommendations in the proposed design provisions and correlates these with the research results summarized in Chapter Two. Chapter Four summarizes the major conclusions, design recommendations, and recommendations for further research.

Appendix A contains the analysis of bearing behavior at low temperature. Appendix B describes the behavior of bearings subjected to compression. Appendix C describes the research related to bearings subjected to relative rotation of the top and bottom surfaces, and Appendix D contains a discussion of response to shear and combined loading. Appendix E describes the work on buckling and stability, and fatigue research is contained in Appendix F. Appendix G outlines some special observations on material behavior. The proposed modifications for the AASHTO *Specifications* and commentary constitute Appendix H.

RESEARCH APPROACH

Low Temperature Research

The existing literature (*3,5,6*) on low temperature material properties of elastomeric compounds typical of those used in bridge bearings was reviewed. Inconsistencies and contradictions between different data were noted, and upperbound and lowerbound limits were developed both for low temperature crystallization and instantaneous thermal stiffening. These bounding values were inserted into a simple mathematical model, which approximately simulates both instantaneous and time-dependent

stiffening. Historic low temperature records were then gathered for five different cities in the United States (Lubbock, Texas; Colorado Springs, Colorado; Duluth, Minnesota; Albany, New York; Fairbanks, Alaska), and these were used to estimate the time-dependent temperature of the elastomeric bearing and the thermal deformation of the bridge. The temperature records include daily high and low temperatures for one month with a daily sinusoidal variation, because stiffening of the elastomer depends on the time and duration of the temperature in addition to the lowest temperature. Heat flow calculations were performed on the bearing to estimate its temperature as a function of time for the monthly periods. The simple mathematical model was then applied to these time-dependent temperature profiles, and the time-dependent expansion (or contraction) of the bridge was used to estimate forces in the bridge bearing. The calculations are imprecise because of the many assumptions and simplifications made in the analysis. However, upperbound and lowerbound limits on stiffening behavior were used in the analysis, and so their results should provide a "worst case" and "best case" indication of low temperature behavior.

Compression Loading

The theoretical and experimental research related to bearings loaded under compression is described in detail in Appendix B. The theoretical work started with the work of Conversy, Gent, and others (*3,15,16,17,18*). Formulas for predicting the stress and strain in the steel and the elastomer were reviewed, and limitations of the theories were described. Approximate theories were examined and compared to the more refined solutions. Several extensions, which simulate large strain conditions, were then evaluated, and modified theories for circular bearings and bearings with holes were derived. In addition, several finite element analyses were performed on rectangular bearings with and without holes. The results of these different analyses and analytical methods were compared with one another and with the analytical results of other research. They also were compared to experimental results.

Experiments were performed to investigate both working-stress behavior and modes of failure, and to provide a basis for appraising the theories. In these experiments, the loads were applied in small increments, and the bearings were closely examined for cracking of the elastomer, delamination or separation of the elastomer and reinforcement, excessive bulging of the elastomer, and yield or rupture of the reinforcement.

Figure 1 illustrates a typical test set-up for the compression tests. The loads were applied with a 2.4 million pound Baldwin Hydraulic Test machine, and they were measured electronically with a calibrated load cell. Four linear variable differential transformers (LVDT's) were used to measure the vertical deflection of the bearings, and for some tests additional LVDT's were used to measure the bulging of the elastomer. A wide range of bearings were tested to cover a wide range of practical field conditions. Shape factors typically varied between 5 and 12, and circular bearings, square bearings, two-to-one and four-to-one rectangular bearings were tested. Comparison of these test results shows how size, shape, and shape factor affected the mode of failure, bearing behavior, and the comparison between theory and experimental results. Most bearings had steel reinforcement, but some used layers of fiberglass. Nearly all of these specimens were loaded to failure or until the test machine capacity was

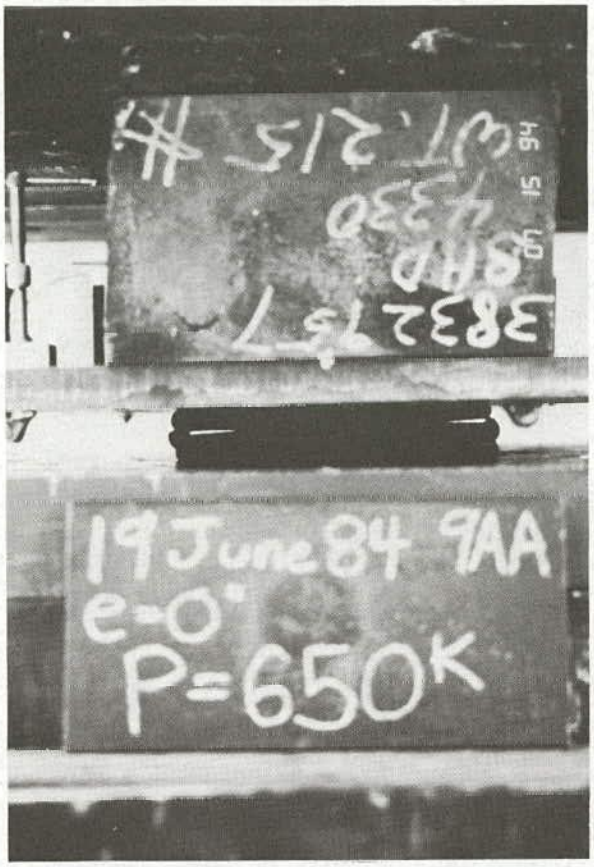

Figure 1. Test setup for the compression tests.

reached. In practice, holes are frequently placed in elastomeric bearings (*3*) to pin the bearing in place in the field, and some fabricators also make holes in the reinforcement to hold it in place during manufacture. These may be subsequently plugged with elastomer. As a result, some specimens with holes were tested to evaluate the effect of this practice.

All bearings were carefully examined before and after testing. Layer size and spacing and overall geometry were measured. Some bearings had strain gages attached to the reinforcement in an attempt to measure the distribution of stress and strain in the laminate at working stress levels and to compare them to those predicted by theory. These bearings were not tested to destruction.

Many compression stiffness tests were also performed. They are not considered to be a part of the compression loading research program described in Appendix B, because they were performed to measure the initial properties of the bearing or to estimate the extent of deterioration or damage produced by other testing such as fatigue. Therefore, they are discussed in the appropriate appendixes. The procedure for these stiffness tests was nearly identical to that described in this section, and, thus, the results are usually provided with minimal discussion.

Rotation

Bending of a bridge girder causes end rotation about a hor-

izontal axis perpendicular to the longitudinal bridge axis. The top surface of the bearing is then forced to rotate relative to the bottom surface. Such relative rotation may also be caused by the dead loads if the underside of the girder is not perfectly parallel to the pierhead. The action is called rotation in this report, but it is also referred to elsewhere as bending, edge loading, or nonuniform loading.

Previous research (*3*) has suggested that rotational deformation of the bearing is one of the most severe loadings which can be applied. Theoretical models for rotation are typically extensions (*3,36*) of compression theories. These theories were examined in detail, and the results are summarized in Appendix C. Stress, strain, moments and rotations, and forces and deflections were computed and were compared to experimental results.

Two types of rotation experiments were performed. The first type was an extension of the compression test procedure and is shown in Figure 2. The loads were applied with a hydraulic test machine, but they were applied at an eccentricity with respect to the centroid of the bearing. As in the compression tests LVDT's measured the vertical deformations at four locations, and both the rotation and average vertical deflection were determined from these measurements. The moment was determined by the axial force and the eccentricity of the applied load, which consisted of both an initial eccentricity plus an additional component due to rotation of the load assembly. This rotation also imposed a shear deformation in addition to the rotation and compression. Most bearings were tested with several eccentricities; however, each bearing in this series was ultimately tested to failure or to the maximum load capacity of the test machine. Bearings of different size, shape, and shape factor were tested. Each bearing was carefully examined at intervals throughout each test for delamination, cracking of the elastomer, uplift of the load from the bearing, and failure of the reinforcement.

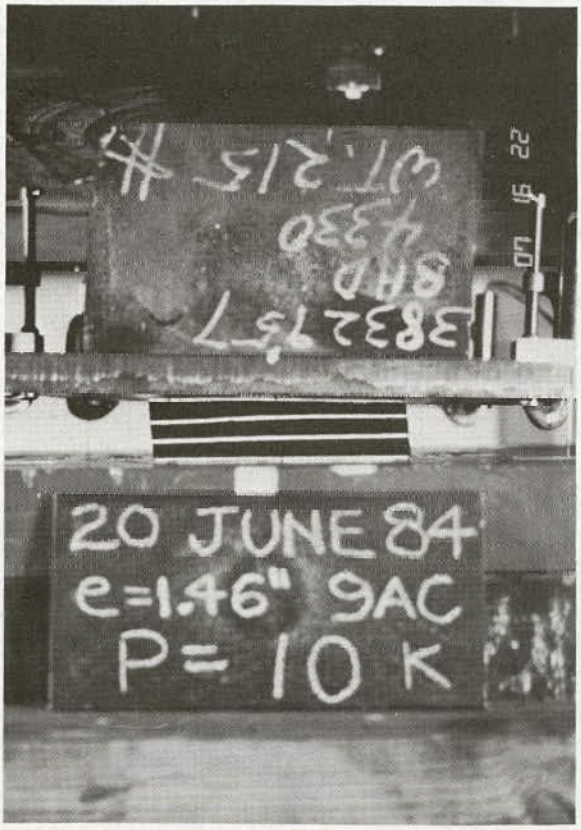

Figure 2. Test setup for the eccentrically loaded bearing rotation tests.

The first rotational test procedure was closely related to the compression loading. It provided valuable evidence of failure modes and general rotation behavior, but moment-rotation stiffness data could be determined only by indirect methods. As a result, a second rotation test method was devised, and is shown in Figure 3. This test procedure permitted independent application of the compression load and the applied moment or rotation, and the moment-rotation stiffness could be measured directly. However, the test apparatus was usable only for relatively small bearings (i.e., shape factor of approximately 5 or less) and small loads (i.e., less than 300 kip in compression). The bearing was placed at the center of rotation of a split cylinder as shown in Figure 3. The compressive load was applied through the split cylinders by a hydraulic test machine, and the moment was applied by a small ram acting through the lever arms. The split cylinders rolled with minimal resistance and introduced a true rotational deformation on the bearing to coincide with the applied moment. Rotations and vertical deflections were measured with LVDT's. Several bearings of different shapes had strain gages attached, and these gages were used to estimate the effect of rotation on the strains in the steel reinforcement.

Shear and Combined Loading

Theoretical models for shear deformation of elastomeric bearings invariably assume that the bearing deforms in simple shear and that the average shear stress is linearly related to average strain even at very large strain levels. Shear tests are always performed with an axial load applied, since the compression load is needed to prevent slip of the bearing. The stress and strain under combined loading are computed by superposition of the individual solutions. However, it is very questionable whether superposition should be applied, since the computed strains greatly exceed the limits of infinitesimal strain theory (*3*). Series of tests were performed to evaluate the limits and validity of these theories, and they are described in detail in Appendix D.

The shear tests were conducted in a self-equilibrating test frame as shown in Figure 4. A number of bearings of different size, shape, and shape factor were tested. Some bearings had strain gages attached to the steel reinforcement as in the compression and rotation test. LVDT's were used to measure vertical deflections and horizontal displacements. The compression load was applied with a hydraulic test machine and was maintained nearly constant during the cyclic shear deformation. Each bearing was tested for a range of different compression loads. The shear deformation was applied by a second hydraulic ram as shown in Figure 4. These specimens were typically not tested to failure. Instead the shear strains were subjected to a small number of cycles of strain within or somewhat above service limits. The bearings were closely examined at intervals

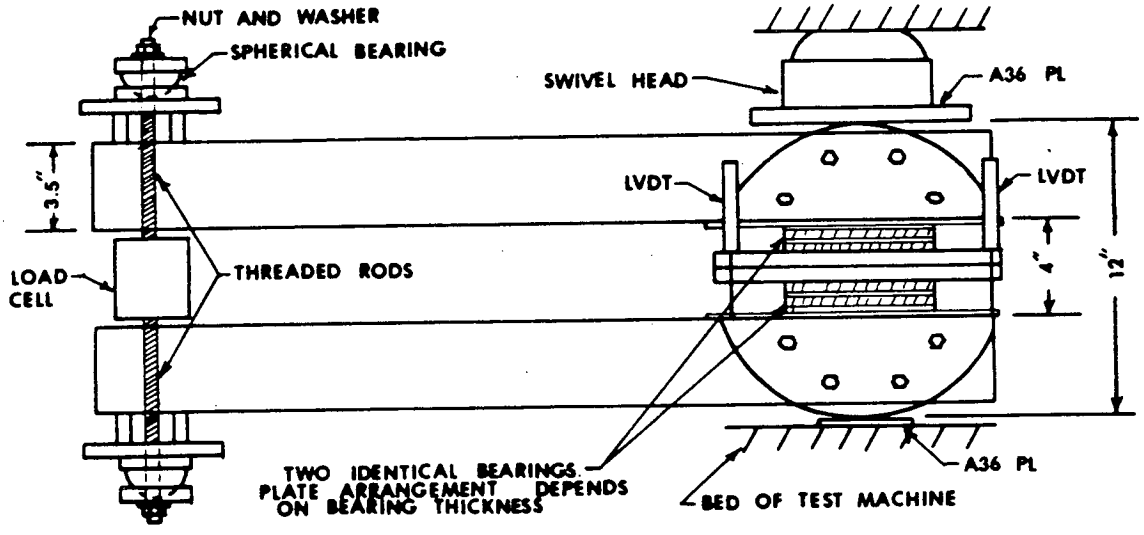

Figure 3. Test setup for the true rotation tests.

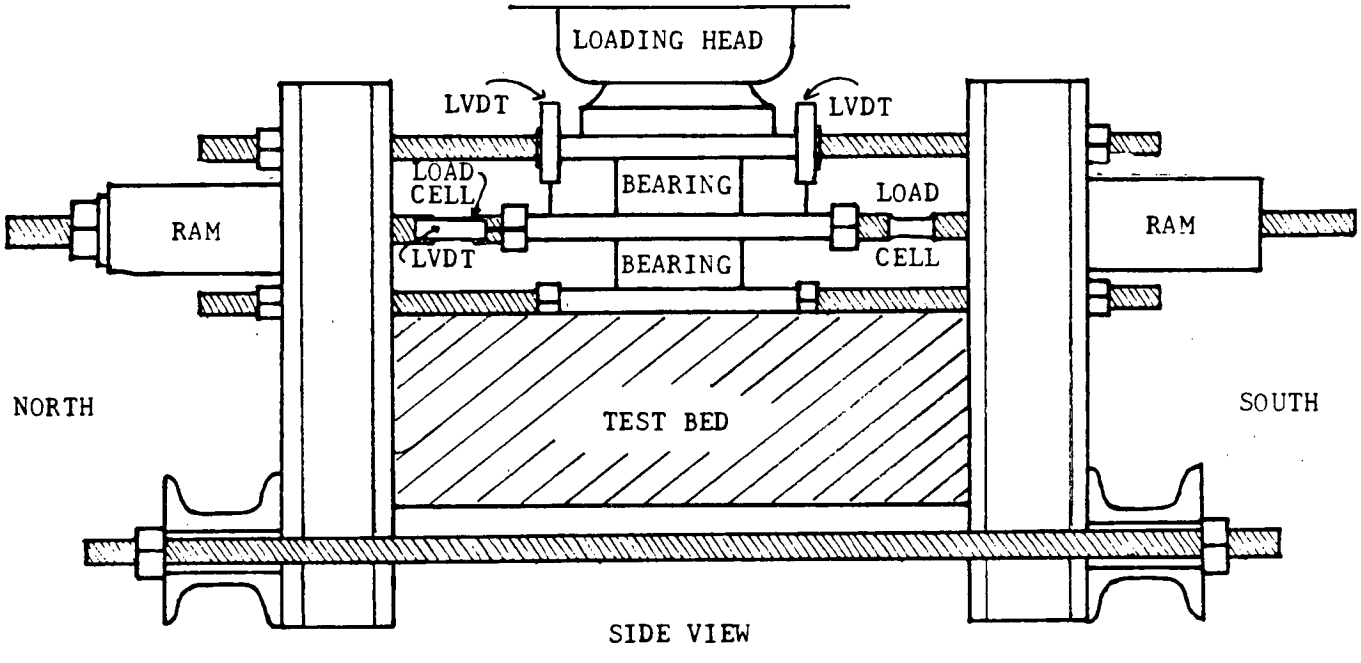

Figure 4. Self-equilibrating test frame for the shear tests.

during the test, but failures of the types noted in the compression or rotation tests were not expected.

Many shear tests were also performed to measure bearing stiffness, to estimate material properties, and to evaluate the deterioration caused by other modes of testing. These tests were performed in the test rig shown in Figure 4 or other similar test frames. These tests supported other test programs (such as stability and fatigue), and so they are not discussed in Appendix D. The test procedures were nearly identical to the shear tests described in this discussion, and so their results are usually summarized without additional discussion.

Stability

The experimental research related to buckling of bearings and the reduction in shear stiffness caused by the stability effect are described in Appendix E. Elastomeric bridge bearings are usually stiff in compression and rotation but flexible in respect to shear deformation. Haringx (*47*) derived the first buckling theory for shear flexible systems, and this work was extended by Gent, Schapery, Skala, and others (*41,48,49*). This basic theoretical work was reviewed, and the limitations were examined. Extensions for these theories were then derived. These extensions partially accounted for the large strains and the shortening effects that accompany large compression loads on elastomeric bearings. Previous experiments (*41*) concerned with the stability of bearings have been performed on small bearings with very

small shape factors (shape factors of 1 or less). These tests compared well to the existing theories, but they were well outside the range of practical bridge bearings. Therefore, tests were performed on two bearing sizes of more practical geometry. Sixteen bearings of nominally identical size, shape, shape factor, and material were made in each of two different sizes and shape factors. Each bearing had two elastomer layers and three steel laminates. The bearings were 2 to 1 rectangles, and they could be stacked to simulate a wide range of heights and slenderness ratios as shown in Figure 5.

The axial shortening of the stack was measured with LVDT's, and the lateral deflection was measured with LVDT's at the midheight of the stack and at the quarter points as shown in the figure. The compressive load was slowly increased, and the lateral and vertical deflections were measured at various load intervals. The lateral deflections and compressive load were plotted in the Southwell plot format, and the buckling load was determined for each height and bearing type. The more slender stacks were loaded to incipient collapse, but this was not practical for the shorter stacks, because material failure would have preceded buckling. These measured buckling loads were compared to theoretical predictions, and the validity of the existing and newly derived mathematical models was assessed.

A steel plate was then inserted at midheight of the stack, and shear tests were conducted at different compressive loads to investigate the influence of compressive load on shear stiffness. These tests were done for a number of stack heights. The results were also compared with theoretical predictions and were used to assess the accuracy of the analytical models.

In order to establish the material properties as accurately as possible, several pairs of bearing were subjected to shear tests under various compressive loads. These two-bearing stacks were too short to be influenced significantly by stability effects and were used to isolate material effects from the geometric ones involved in buckling. These tests are described in Appendix G.

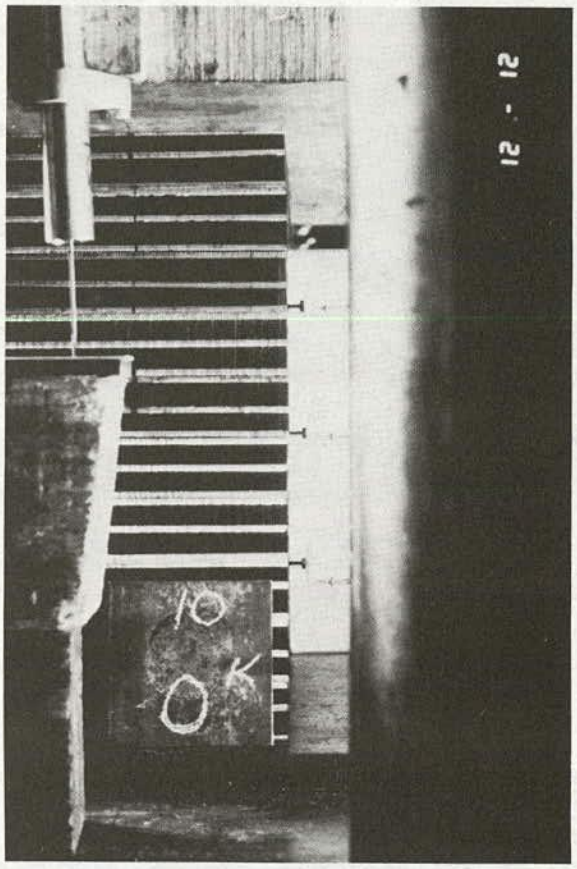

Figure 5. Stacked bearing configuration for the stability tests.

Fatigue

Fatigue was the last major mode of failure considered in this Phase II research program. Fatigue tests have been previously performed by other investigators (*38,62,63*), but the results were often poorly documented or of limited applicability to present elastomeric bearing design practice. This existing research was carefully reviewed, and the major research conclusions were noted. An experimental fatigue research program was then instituted to fill in the gaps of the existing knowledge and to develop approximate, conservative design guidelines which minimize potential fatigue problems. These fatigue tests were performed on bearings of practical size and geometry. Their primary objectives were the determination of the effect on fatigue life and behavior of load type, load rate, mean stress or strain, stress or strain range and elastomeric compound.

Two types of tests were performed. Some bearings were tested under approximately constant compression with severe cyclic shear deformation. Figure 6 illustrates this test apparatus. Twenty thousand cycles were chosen, representing one cycle for each day of a 55-year life expectancy. The compression load was kept as nearly constant as possible during these fatigue tests, and it represented the mean stress due to gravity loads. The compression load was applied with four tension rods and was held constant with elastomeric springs placed in series with the

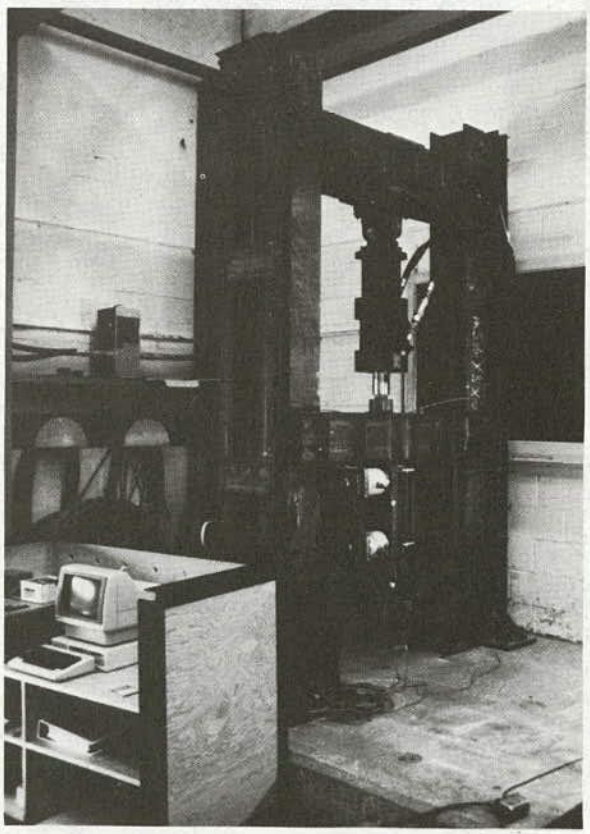

Figure 6. Test setup for the cyclic shear fatigue tests.

test specimens. The cyclic shear deformation was applied with an MTS actuator under displacement control. Compressive deflection and shear deformation were measured with LVDT's, and the temperature of the bearing was measured with a thermocouple.

Thirteen pairs of bearings were tested. The first test was a pilot one covering a range of load rates, and was intended to determine the fastest loading that could be imposed without seriously influencing the fatigue behavior. Rapid loading causes higher temperatures that are detrimental to fatigue resistance, and, even at constant temperature, higher loading rates appear more damaging. However, time constraints dictated that the tests be done as fast as reasonably possible. Other shear tests evaluated the effect of different compressive stress or strain levels and different shear strain ranges. In addition, five tests used comparable strain levels but employed bearings made from a wide range of elastomeric compounds. The compounds were selected from the possible range that could meet AASHTO (*1*) property requirements, but would develop the maximum variation in hardness, tensile strength and elongation at break. These later tests were intended to measure the effect of these elastomer properties on fatigue behavior.

A second series of fatigue tests were performed with bearings under compression with the test frame as shown in Figure 7. The compressive load was applied with an MTS actuator under load control. The bearings were tested with a constant minimum (or mean) stress to simulate dead load and a stress range to simulate the live load. The primary objective of these tests was to evaluate the effect of mean stress, stress range, and material properties on the fatigue life and behavior. Thus, these parameters were varied for different tests as in the shear fatigue tests. Two million cycles of severe compression loading were used. It was believed that the number of cycles was small, but the stress range was large compared to field conditions. This loading history was required by time constraints, because elastomeric bearings cannot be tested at the rapid rates used for steel or other materials. Further, other research (*64*) has suggested that 2 million cycles of a severe truck load such as HS-20 may approximate a 46-year life expectancy of typical bridge fatigue loading. As a result, it was felt that this test procedure should provide approximate design limits for fatigue control.

The bearings were carefully measured and examined before and after the fatigue tests and at intervals during the test. Cracks and tears in the elastomer were observed and measured, and their growth was monitored during the test. The shear and compression stiffnesses were also measured at intervals to determine if any deterioration had occurred.

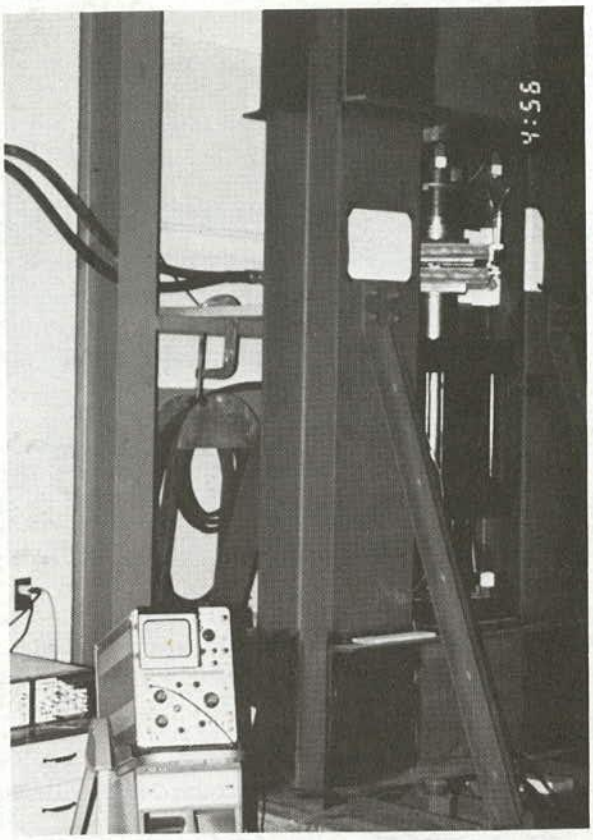

Figure 7. Test setup for the compression fatigue tests.

NOTATION

A ..... Plan area of bearing
A_c ..... Dimensionless compressive stiffness coefficient
A_r ..... Dimensionless rotational stiffness coefficient
A_s ..... Shear area of the bearing
A_{s0} ..... Shear area of the bearing in the unloaded state
A_0 ..... Plan area of the bearing in the unloaded state
B_c ..... Dimensionless compressive stiffness coefficient
B_r ..... Dimensionless rotational stiffness coefficient
C_c ..... Dimensionless coefficient relating the maximum shear strain in the bearing to the compressive strain
C_1, C_2 ..... Limits on allowable total shear strain, under total load and live load
C_3 ..... Dimensionless constant in Eq. E-37a relating limiting slenderness to shape factor
C_4, C_5 ..... Constants in Eq. E-55 relating experimentally observed buckling stress to slenderness
C_6 ..... Constant in Eq. A-5 relating crystallization rate to temperature
c_{kc} ..... Dimensionless coefficient of K, the bulk modulus, in Eq. B-2b for compressive stiffness including compressibility
c_{kr} ..... Dimensionless coefficient of K, the bulk modulus, in Eq. C-4 for rotational stiffness including compressibility
c_s ..... Strength coefficient, relating reinforcement failure strength to average compressive stress on the bearing (see Eq. B-16)
c_{th} ..... Specific heat
D_{th} ..... Thermal diffusivity $= k_{th}/\rho\, c_{th}$
D_1 ..... Dimensionless constant $= (4\pi \phi/B_c)\sqrt{(B_r G/E)}$, used in buckling load calculation and defined in Eq. E-54b
E ..... Young's modulus
E_c ..... Effective Young's modulus in compression of the bearing, neglecting bulk compressibility
E'_c ..... Effective Young's modulus in compression of the bearing, accounting for bulk compressibility
E_r ..... Effective Young's modulus in rotation of the bearing, neglecting bulk compressibility

E'_r ..... Effective Young's modulus in rotation of the bearing, accounting for bulk compressibility

$E(T)$ ..... Temperature-dependent Young's modulus of the elastomer

E_0 ..... Young's modulus at reference (room) temperature of the elastomer

EB ..... Elongation at break of the elastomer

F_y ..... Yield strength of the reinforcement in uniaxial tension

f_c ..... Dimensionless compressive stiffness coefficient $= A_c + B_c S^2$

f_r ..... Dimensionless rotational stiffness coefficient $= A_r + B_r S^2$

G ..... Shear modulus of the elastomer

G_a ..... Apparent shear modulus of the elastomer, including the contribution of bending to the total transverse displacement

g_r ..... Dimensionless coefficient relating rotation angle to maximum shear strain in the elastomer (see Eq. C-5b)

H ..... Transverse force on one bearing

H_c ..... Time in hours for the elastomer to harden by 10 durometer points at its optimum crystallization temperature, T_A

h_c ..... Combined thickness of elastomer and steel in one layer of a reinforced bearing

h_{ct} ..... Total combined thickness of elastomer and steel in all layers of a reinforced bearing

h_{ct0} ..... Total combined thickness of elastomer and steel in all layers of a reinforced bearing in the unloaded state

h_p ..... Thickness of shear panel

h_r ..... Thickness of elastomer in one layer of a reinforced bearing

h_{r0} ..... Thickness of elastomer in one layer of a reinforced bearing in unloaded state

h_{r1}, h_{r2} ..... Thickness of elastomer layers either side of a layer of reinforcement

h_{rt} ..... Total thickness of all elastomer layers in a reinforced bearing

h_{rt0} ..... Total thickness of all elastomer layers in a reinforced bearing in the unloaded state

h_s ..... Thickness of steel reinforcement in one layer of a reinforced bearing

h_{st} ..... Total thickness of all steel layers in a reinforced bearing

I ..... Moment of inertia of the bearing

I_0 ..... Moment of inertia of the bearing in the unloaded state

K ..... Bulk modulus of the elastomer

K_c, K_r, K_s ..... Strain-dependent stiffnesses in compression, rotation, and shear of a bearing

K_t ..... Transverse stiffness of a bearing, including stability effects

K_{t0} ..... Transverse stiffness of a bearing, including stability effects, at zero compressive load

k ..... Effective length factor used in prediction of the buckling load

$\bar{K}$ ..... Dimensionless coefficient in the equation $E_c = E(1 + 2\bar{k}S^2)$ for the compressive stiffness derived from experimental data

k_{th} ..... Thermal conductivity

L ..... Plan dimension, parallel to the bridge span, of a rectangular bearing

L_c ..... Instantaneous column length

L_{c0} ..... Instantaneous column length under zero axial load

l ..... Bridge span

M ..... Bending moment

M_o ..... Bending moment at the end of shear-flexible beam-column

m ..... Exponent in the approximate expression for K_t, Eq. E-66

N ..... Axial force

n ..... Exponent or index

P ..... Vertical load on the bearing

P_{cr} ..... Buckling load

$P_{cr,\lim}$ ..... Buckling load of a bearing with limiting slenderness, below which buckling is impossible

P_E ..... Euler buckling load in fundamental mode

P_n ..... n^{th} Euler buckling load

P_s ..... Buckling load of a column with shear flexibility alone, $= GA_s$

Q_n ..... Dimensionless constant, $= \sqrt{1 + (E/K)(L/n\pi H_r)^2}$, used in the series solution for rotational stiffness

q ..... Dimensionless constant used to calculate the buckling load of a shear-flexible column, $= \sqrt{P/\xi EI}$

R ..... Radius of a circular bearing

R_n ..... Dimensionless constant, $= \sqrt{1 + 4(E/K)(L/n\pi h_r)^2}$, used in the series solution for compressive stiffness

$R_1(T), R_2(T)$. Dimensionless functions of temperature used in prediction of low-temperature bearing stiffness

r ..... Radial coordinate, or radius of gyration

r_0 ..... Radius of gyration in the unloaded state

S ..... Shape factor

S_0 ..... Shape factor in unloaded state

SF ..... Safety factor

T ..... Temperature

T_A ..... Temperature for maximum rate of crystallization

T_C ..... Temperature at which Young's modulus for the elastomer reaches 10,000 psi

T_O ..... Temperature of the outside of the bearing

t ..... Time

u ..... Longitudinal displacement of a point within a shear-flexible beam-column

$\bar{u}$ ..... Longitudinal displacement of a point within a shear-flexible beam-column that lies on the member axis

V ..... Shear force

v ..... Transverse displacement of a point within a shear-flexible beam-column

$\bar{v}$ ..... Transverse displacement of a point within a shear-flexible beam-column that lies on the member axis

W ..... Plan dimension perpendicular to the bridge span of a rectangular bearing

x, y ..... Cartesian coordinates in the plane of the reinforcement

z ..... Through-thickness coordinate of the bearing

α ..... Coefficient of thermal expansion of bridge deck

β ..... Dimensionless coefficient in specification equation for allowable compressive stress
$\gamma_c, \gamma_r, \gamma_s$.... Shearing strains caused by compression, rotation and shear
Δ_c..... Compressive deflection
Δ_s..... Shear deflection
Δ_t..... Transverse deflection, accounting for instability effects
Δ_T ..... Change in temperature
ΔU..... Change in strain energy
ΔV..... Change in potential energy
ϵ..... Direct strain
ϵ_c ..... Average compressive strain in bearing
ϵ_{xx} ..... Direct strain in x direction
ϵ_{lim}..... Compressive strain at incipient buckling in a column of limiting slenderness, below which buckling is impossible
ζ..... Diameter of the hole/Diameter of the bearing in a circular bearing with a central hole
η..... Coefficient of EB in the formula for maximum allowable shear strain in the former British specification BE1/76
θ..... Rotation angle
θ_{max}..... Maximum allowable rotation angle
λ..... Extension ratio (in kinetic theory of elastomers), $= 1 - \epsilon_c$, or slenderness ratio (in buckling theory), $= kh_{rt}/r$
$\bar{\lambda}$..... Modified slenderness ratio, $= \lambda/f_r$
λ_0..... Slenderness ratio in the unloaded state
$\lambda_{0,lim}$ ..... Limiting slenderness ratio in unloaded state, below which the column will not buckle
ν..... Poisson's ratio
ν_r..... Poisson's ratio for the elastomer
ν_s..... Poisson's ratio for steel
ρ..... Mass density
σ_c..... Average compressive stress on the bearing
σ_{cr}..... Buckling stress
$\sigma_{s,max}$ ..... Maximum steel stress
τ..... Shear stress
τ_c, τ_r, τ_s .... Maximum shearing stresses in bearing caused by compression, rotation, and shear
$\tau_{rr}, \tau_{\theta\theta}, \tau_{zz}$ .. Radial, hoop, and vertical stresses respectively
τ_{rz}..... Shear stress in the elastomer at its interface with the reinforcement
ξ..... Dimensionless constant used in calculating K_t
$\frac{1}{(1 + P/GA_s)}$ for Haringx's theory
$(1 - P/GA_s)$ for Engesser's theory
ϕ ..... Ratio of total combined thickness to total elastomer thickness in a reinforced bearing
ψ ..... Total rotation of the cross-section in a shear-flexible column
ω ..... Dimensionless constant used to calculate K_t (see Eq. E-24)

CHAPTER TWO

FINDINGS

LOW TEMPERATURE BEHAVIOR

The analytical study of the low temperature behavior of elastomers indicated that the stiffness of the elastomeric compounds used in bridge bearings may vary widely at low temperatures. Two types of low temperature stiffening occur. Crystallization is a time-dependent phenomenon, and it occurs over a wide range of low temperatures (almost any temperature lower than 32°F). However, the rate of crystallization appears to be greatest at temperatures on the order of +15°F. Polychloroprenes generally crystallize faster than natural rubber, but there is considerable variation among the different types. Compounds made from the commonly used type W neoprene base polymer crystallize more rapidly than those made from type WRT, which has slightly different chemistry, is more expensive, but has been found to perform better at low temperatures (*5*). However, the rate of crystallization is very sensitive to the complete compound (*6*), and a good polychloroprene compound has much better resistance to crystallization than a poor natural rubber compound. Generally, compounds which crystallize rapidly also stiffen more over time (*6*), and the elastomer stiffness may increase to as much as 10–20 times the normal room temperature value (*6*).

Thermal stiffening or glass transition occurs instantaneously after the material cools to the transition temperature. This transition occurs at temperatures on the order of −35°F to −55°F (−37°C to −49°C), with polychloroprene compounds generally stiffening at the higher end of this range, and natural rubber, at the lower end of the range. Stiffness increases of several orders of magnitude may occur at these low temperatures. Small specimens may become brittle and may shatter under impact at these temperatures, but the likelihood of practical bridge bearings experiencing this extreme form of behavior appears very remote.

The experimental data for crystallization and instantaneous thermal stiffening were analyzed, and upperbound and lowerbound limits were postulated. These limits were used in an approximate time and temperature-dependent model to estimate the temperature-dependent forces experienced by the bearing, the bridge pier, and the superstructure. The temperatures of the bridge and the bearing were estimated for five different record-low monthly temperature records from different cities in the United States, and the time delay caused by heat flow through the bridge and the bearing was considered. Time is required for bearings to reach a given temperature; therefore, low temperatures of very short duration should not adversely affect the bearing behavior. The calculations suggest that a duration of 1

to 2 hours is required for cooling of most practical-sized bearings, and durations of 8 to 12 hours may be required for large bridge bearings. These time delays are particularly sensitive to the quality and thickness of the cover layers, and should be used with caution in design.

The calculations further suggest that record-low temperatures in most of the continental United States could introduce significant stiffening due to crystallization. If elastomers with good crystallization properties (i.e., very resistant to low-temperature crystallization) are used in these regions, little increase in force can be expected. However, bridge bearings with less than ideal crystallization characteristics for the region may develop forces in the bearing that are three to four times the forces that would have been found if the bearing had retained its room temperature stiffnesses. Figure 8 is a typical plot of the bearing force for a given low temperature record with an elastomer that is not well suited to the climate. The bearing force is normalized by dividing it by the "design force," defined as the shear force that would be induced in the bearing at room temperature if it was subjected to a shear strain of 50 percent. This additional force will not break the bearing, but it may damage the pier or the superstructure or cause the bearing to slip out of position. The elastic deflection of the piers and support structure was not considered in these calculations, and a flexible supporting structure would help to alleviate the induced forces.

The calculations indicate that instantaneous thermal stiffening is important only for a few northern tier or mountainous areas of the continental United States, Canada, and Alaska. However, bearings that have inadequate thermal stiffening properties (i.e., the second order transition temperature is too low) may develop forces that are many times greater than the design bearing force.

COMPRESSION LOADING

The linear elastic theories for compression of bearings can be expressed as

$$\sigma_c = \frac{P}{A} = E_c\epsilon_c = Ef_c\epsilon_c \tag{1}$$

where $f_c = A_c + B_cS^2$.

The A_c term depends only on the uniaxial deformation, and its effect is small for practical-sized bridge bearings. The term B_c has been derived theoretically differently by different researchers, but similar results are usually obtained. This second term takes into account the bulging shown in Figure 9, and for design purposes the approximate equation

$$f_c = 1 + 2\bar{k}S^2 \tag{2}$$

is frequently employed. The constant k simulates the volumetric deformation effect and is a function of the hardness of the elastomer. It varies between 0.55 and 0.75 for practical bridge bearing compounds. This approximate theory is not precise because it does not account for the effect of shape on the bearing behavior or for nonlinear behavior. However, it is simple to use, and it is difficult to justify a more refined calculation for most practical conditions.

Important features of behavior under compression are revealed by these theoretical analyses, and were confirmed by finite element analyses. Harder elastomers and larger shape factors lead to stiffer bearings. Strains in the elastomer increase with applied stress, and are reduced by higher shape factors and material moduli. The stress in the steel reinforcement increases with increasing compressive load, increasing elastomer thickness, and decreasing laminate thickness. Holes in the reinforcement introduce a stress increase due to the stress concentration effect and the loss of net section, and this increase influences the ultimate load capacity and yield behavior.

Experiments were performed on different size, shape, and shape factor bearings, and the results were compared to the theories. The experiments agreed well with the general trends indicated by the theories, but specific comparisons were often

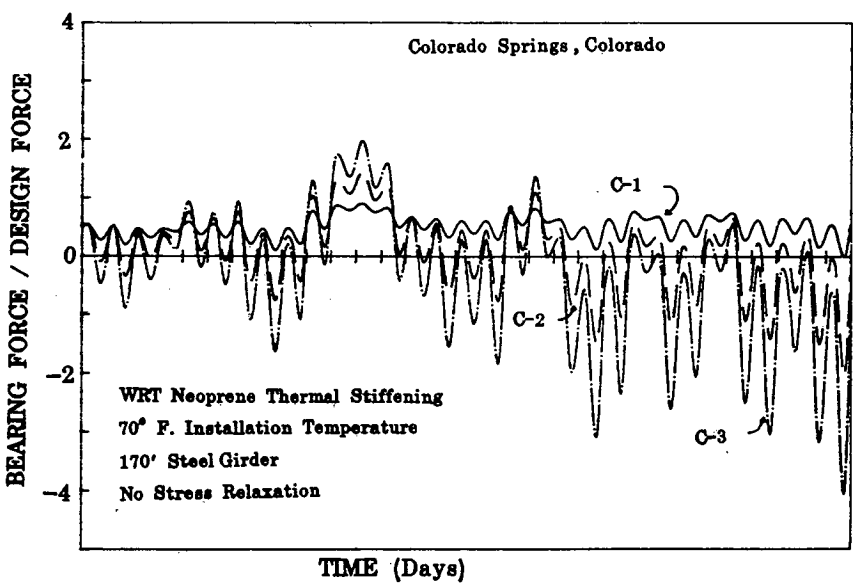

Figure 8. Typical plot of the normalized bearing shear force due to low temperature effects.

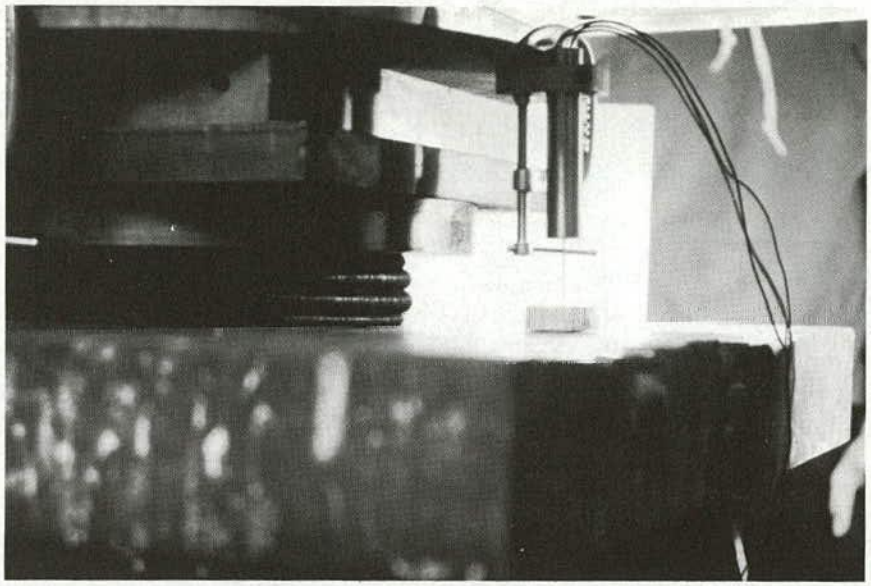

Figure 9. Typical bulge pattern of an elastomeric bearing loaded in compression (8-in. diameter bearing shown).

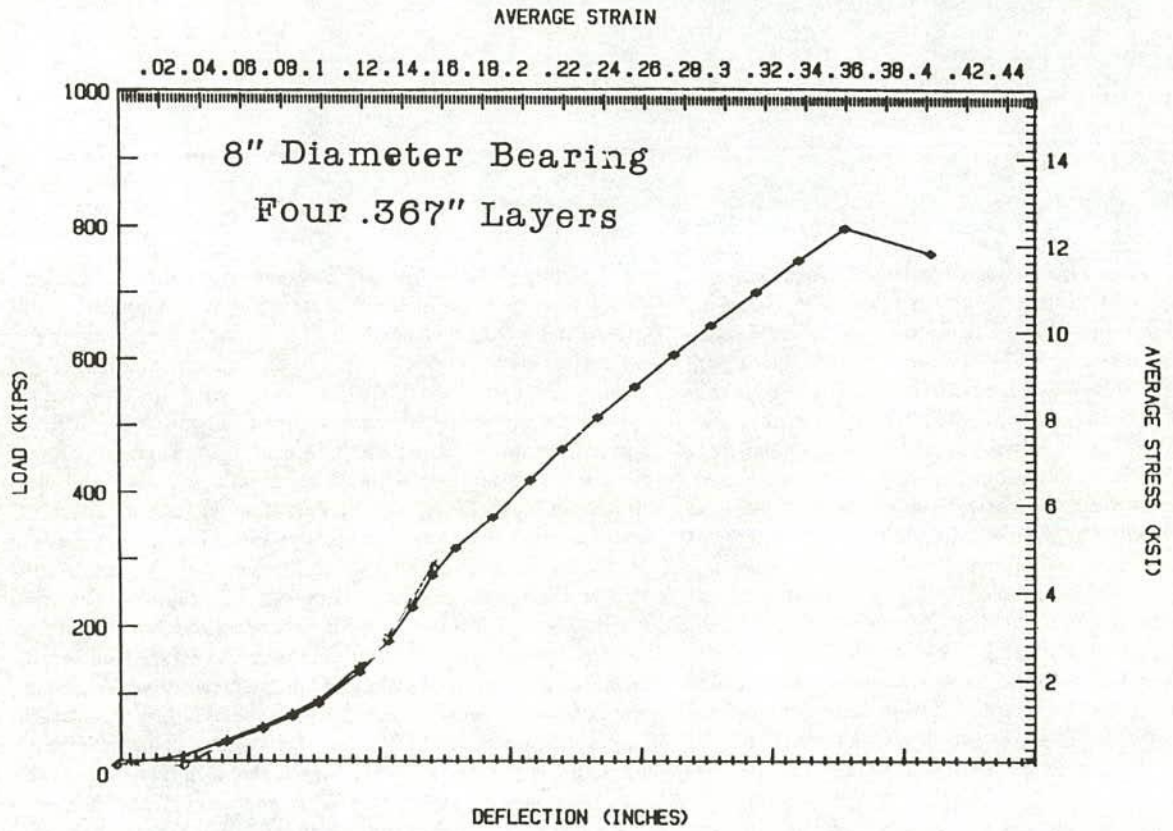

Figure 10. Typical average compressive stress-strain curve for an elastomeric bearing.

fair to poor. A typical experimental average stress-strain curve is shown in Figure 10. The deflections and strains were generally larger for smaller shape factors, thicker elastomer layers, or softer elastomers as predicted by the theories. However, comparison of specific deflections to computed values was less favorable. Other research (*35*) has indicated that this less favorable comparison may be due to the seating-in required to overcome initial imperfections in the bearing. The flat zone of the curve at low stress levels is influenced strongly by the initial out of flatness of the platens and the bearings. A much better comparison between theoretical and experimental force-deflection results if the comparison is made for incremental stress at higher stress levels (i.e., tangent stiffness comparison).

The sudden loss of stiffness, which can be seen in the load-deflection curve, is caused by yielding of the reinforcement, and the load at which it occurred correlated well with the theoret-

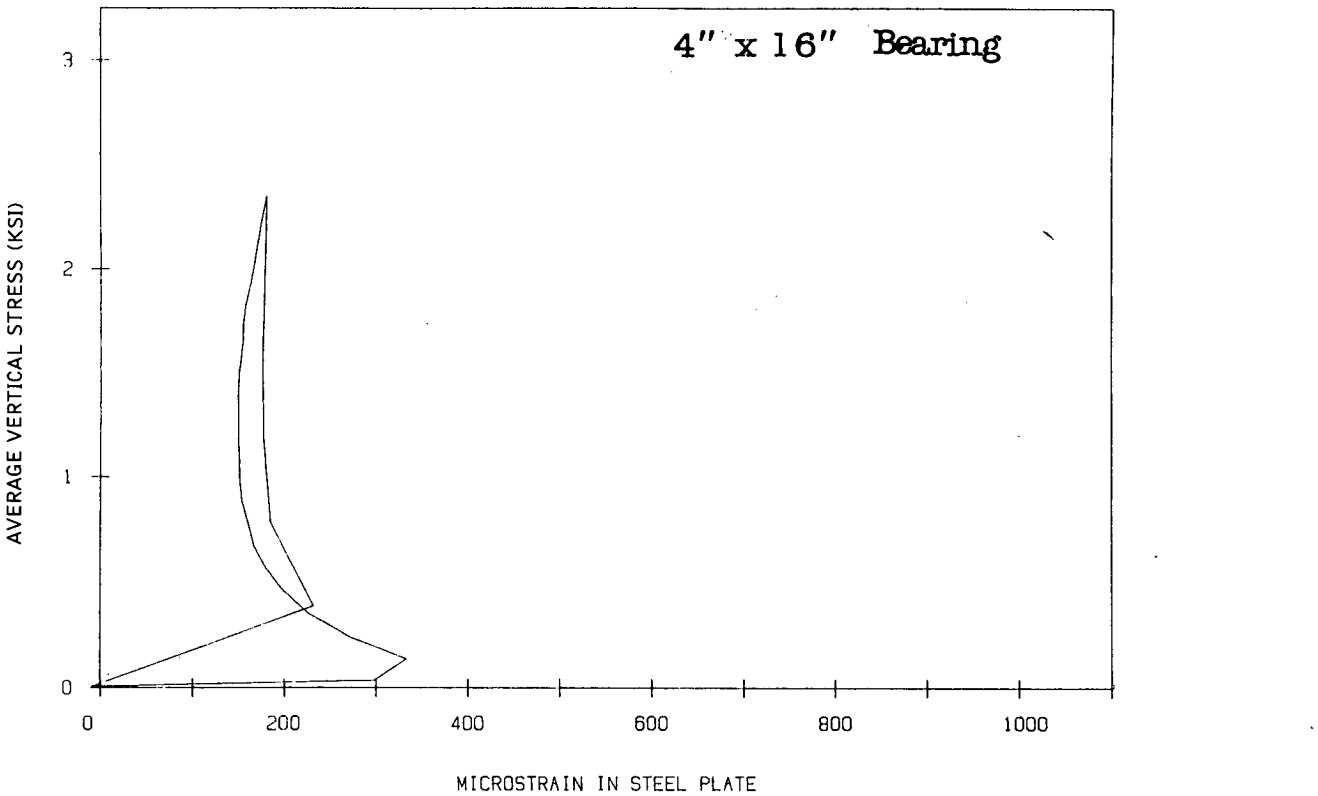

Figure 11. Typical strain in the steel laminate as a function of the compressive load.

ically predicted value. This provided evidence that the theoretical models for predicting steel stress were reasonable. However, the strains in the reinforcement measured during the experiments at working stress levels were extremely erratic and bore no relation to the theoretical predictions as can be seen from the typical values shown in Figure 11. It is believed that they were influenced greatly by initial imperfections in the bearings (*35, 43*), and they were so erratic that they could not be used. Holes in the reinforcement clearly reduced the ultimate load capacity of the bearing as suggested by the theory, but they did not appear to have as large an impact on the load to cause first yield. This may reflect more the difficulties in detecting a local effect (first yielding) from a global measure (force-deflection curves) than a real phenomenon. This gross yielding of the section is relatively insensitive to stress concentrations and thus is less affected by holes in the reinforcement. Initiation of yielding is affected by the stress concentrations, but would not be observable from the overall bearing behavior and the load deflection results.

The experiments also showed that long narrow bearings are less influenced by holes than those of compact shape (circular or square). This finding is in agreement with simple post-yield analyses. Fiberglass-reinforced bearings exhibited a sequential failure mode in which individual fibers began to break well before total failure occurred. The presence of holes in the reinforcement did not significantly affect the failure load. The compressive stresses at failure were typically 1,800–2,200 psi, well below those observed for steel-reinforced bearings, because the fiber reinforcement was much weaker than the steel. For this reason, the proposed compressive stress limits are lower for fiber-reinforced than for steel-reinforced bearings.

The compressive stiffness of elastomeric bearings is high compared to their shear stiffness, because of the bulging restraint provided by the reinforcement. The elastomer is flexible and bulges as shown in Figure 9, and the bulging induces larger shear stress and strain in the elastomer, which, in turn, induce the tensile stress in the reinforcement. Theories predict that these shear strains increase with increasing load and layer thickness and also increase with decreasing shape factor and elastomer hardness. This general observation was supported by the compression test results. The bearings bulged under compressive load, and the size of the bulge increased with increasing load and decreasing shape factor. However, all attempts to measure accurately the shear strains or the size of the bulge were fruitless.

The second mode of failure commonly observed during the compression tests was delamination or separation of the elastomer from the reinforcement. This mode of failure was a cracking or tearing of the elastomer in a plane very near the steel-elastomer interface rather than a true bond failure. As a result, it is reasonable to expect that delamination is closely related to the shear strain in the elastomer, and therefore to the compressive stress and shape factor of the bearing. Figure 12 shows the average compressive stress for which delamination was first observed. The data exhibit tremendous scatter. The data are somewhat obscured by the fact that some specimens were tested in rotation or had been previously tested to a larger compressive load, but it appears that the scatter in the data is greater than the shape factor effect. This may indicate that the shear strain is not a good indicator of delamination behavior, or it may suggest that other factors, such as quality control, dominate the phenomenon.

The compression tests also illustrate the influence of quality

control during the manufacture on the strength and stiffness of the bearing. Several specimens had extremely poor layer thickness control. They were much more flexible than comparable bearings with uniform layer thickness, and they tended to fail (both in delamination and yield and rupture of the reinforcement) at much lower stress levels.

ROTATION

Theories for predicting the behavior of bearings under rotation are extensions of the theories for bearings under compression (*36*). The equations for rotational stiffness are

$$M = E_r I \frac{\theta}{h_r} = f_r E I \frac{\theta}{h_r} \tag{3}$$

where $f_r = A_r + B_r S^2$.

There are several different theories for predicting the constants A_r and B_r, and a range of A_r values result. However, A_r has minimal impact on the rotational stiffness of practical bridge bearings because the second term is much larger, and there is fairly general agreement on the values of B_r.

Two types of rotation experiments were performed. One was an eccentrically loaded test as depicted in Figure 2, and, in the other, rotations were applied at constant compressive load (Fig. 3). Both experiments indicated that the moment-rotation curves are essentially linear (see Fig. 13), but the stiffness increases with increasing compressive stress. This increase in stiffness with compressive load is caused partly by the dimensional changes (reduced layer thickness and increased plain area) which result from the compression. At large rotations the moment-rotation curves soften and become nonlinear. This nonlinearity apparently is caused by lift-off of the loading device from the edge of the bearing, and it causes severe deformation of the laminate and an increase of the strains in the elastomer. Lift-off should therefore be avoided because it introduces the possibility of damage or fatigue of the reinforcement and delamination or tearing of the elastomer.

SHEAR AND COMBINED LOADING

Theories of shear behavior are generally based on the assumption that the average shear stress and strain are linearly related. That is

$$\tau = \frac{H}{A} = G_{a\gamma s} = G_a \frac{\Delta_s}{h_{rt}} \tag{4}$$

The apparent shear modulus, G_a, depends on the material shear modulus, but for thick bearings it is also related to the magnitude of the compressive load through the stability effect. The theoretical aspects of this phenomenon are discussed in Appendix E. Experiments were performed with the test apparatus shown in Figure 4. The experiments generally support this linear theoretical model. The shear stress and strain invariably were nearly linearly related with a hysteresis as shown in Figure 14. The stiffness of the linear curve varied with compressive load, and generally decreased with the first few cycles of shear loading. The shear test appears to be the most repeatable and reliable measure for evaluating the material properties of the elastomer,

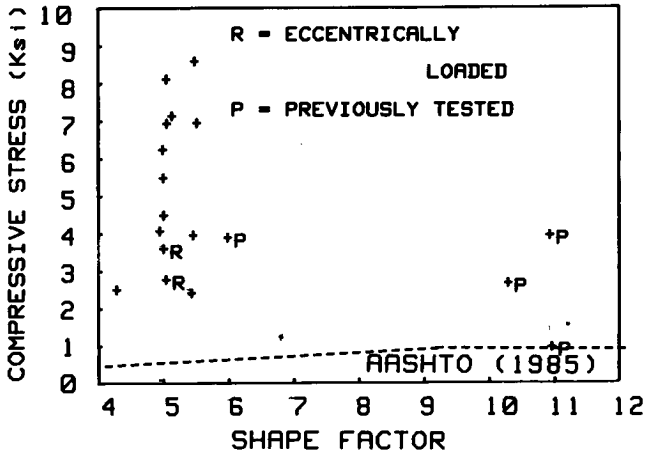

Figure 12. Average compressive stress vs. shape factor at which delamination was first observed.

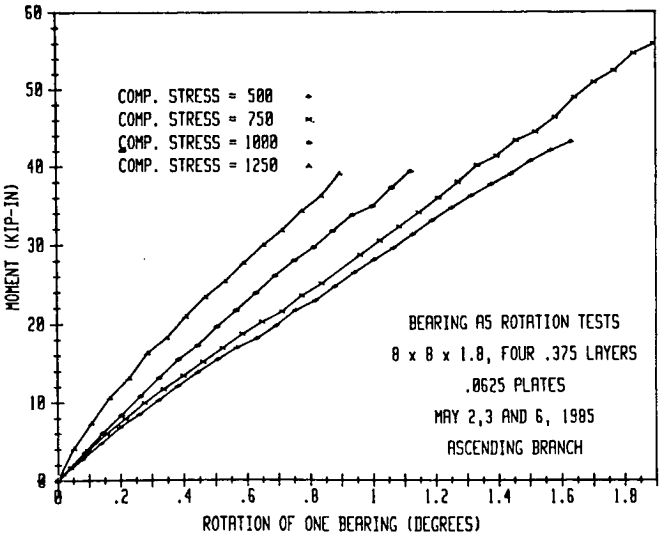

Figure 13. Typical moment vs. rotation curve of an elastomeric bearing.

but any such test must account for the stiffness changes associated with multiple load cycles and compression load.

Bearings typically displayed the simple shear deformation illustrated in Figure 15a. However, the corners of the bearing typically rolled over as illustrated in Figure 15b if the shear strain exceeded 50 percent. The roll-over effect became quite severe at large shear strains, and it may potentially damage the reinforcement or tear the elastomer. This indicates that shear deformation should be limited in bridge bearings to prevent damage.

STABILITY

Stability theory indicates that buckling of structural members depends on their bending and shear stiffness. Elastomeric bridge

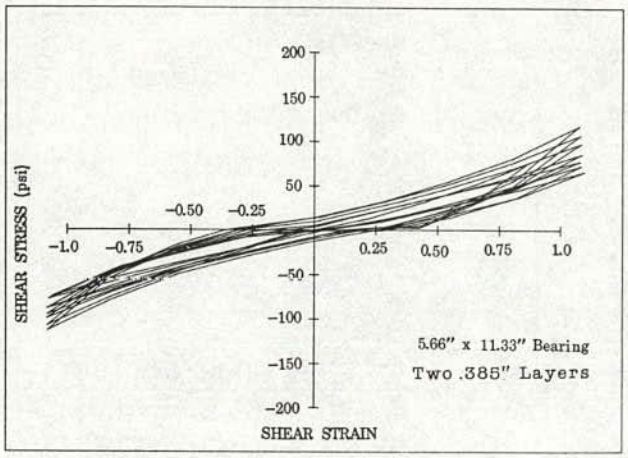

Figure 14. Typical hysteretic shear stress vs. strain curve for an elastomeric bearing.

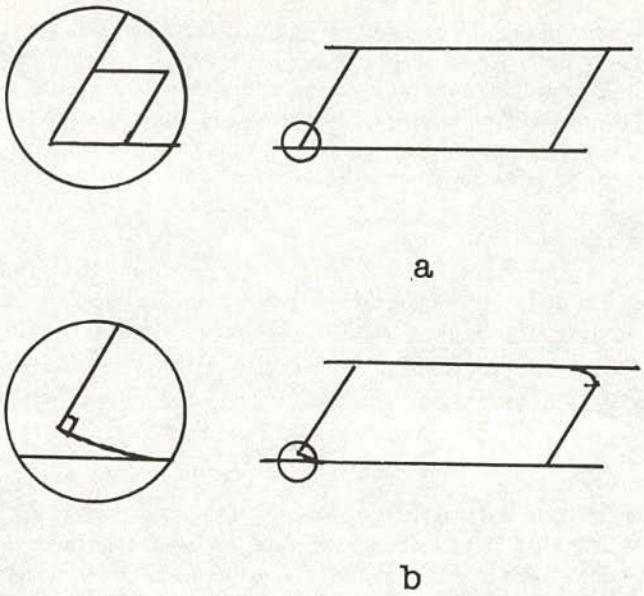

Figure 15. Typical shear deformation of an elastomeric bearing: (a) at strains less than 50 percent, and (b) at large strains with rollover.

bearings are relatively quite flexible in shear, and this stiffness is the dominant term in the buckling equation. Under these conditions the simplest theory (*41*) suggests that

$$P_{cr} = \frac{\phi G A_s}{2}\left\{\sqrt{1 + \frac{4\pi^2 f_r EI}{GA_s (kh_{rt}\,\phi)^2}} - 1\right\} \qquad (5)$$

where $\phi = (h_{st} + h_{rt})/(h_{rt})$.

This theory was examined in detail and extensions were considered which include geometric and material nonlinearity. These extensions changed the buckling load somewhat. They generally increased the buckling load for short bearings and had minimal impact on the buckling load of tall bearings. They also implied that sufficiently squat bearings cannot buckle at any stress.

Experiments were performed on a wide range of bearing heights for two different bearing geometries. The range of bearing heights tested was chosen for the purpose of verifying the theory, not just to simulate bearings in current use. Therefore, some bearings were considerably taller than would be expected in practice. The tall bearings buckled as shown in Figure 16, and the buckling loads were typically close to the theoretical prediction. Bearings of moderate height also buckled, but the buckling loads were larger than the theoretical predictions both for the basic and the extended theories. For very short bearings, incipient buckling could not be reached without damage to the bearing, and the Southwell plot technique was unable to provide a buckling load. This may simply indicate that the buckling load was greater than the test limits, but it may also lend support to the theoretical prediction, discussed in Appendix E, that very short bearings cannot buckle. In either case, the buckling load of very short bearings is well above practical service loads and is of no practical importance to bridge design.

The buckling theory also provides an estimate of the apparent shear modulus, G_a, of a bearing when it is subjected to compression loading. The experimental shear stiffness was significantly smaller than the predicted value. This could be important for shear tests run for quality assurance purposes, in which some compression is also applied.

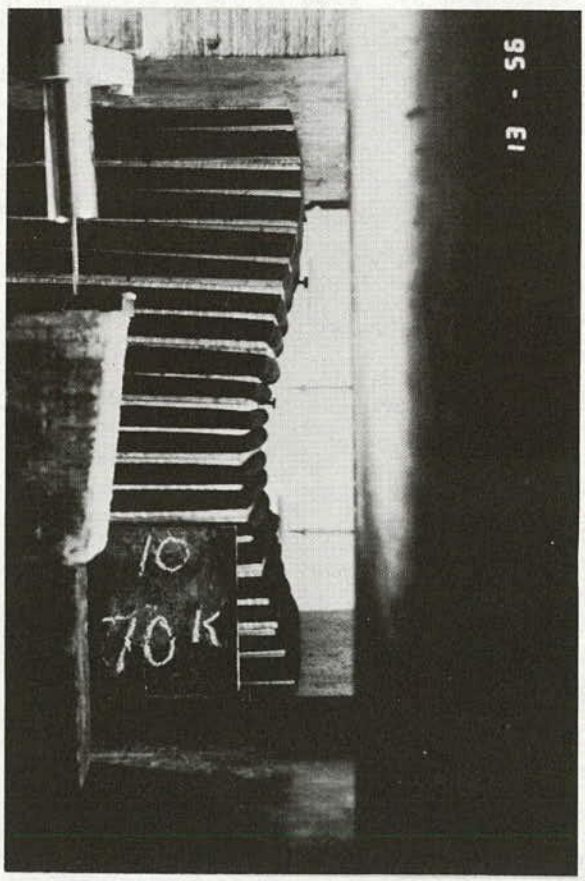

Figure 16. Buckling of a tall bearing.

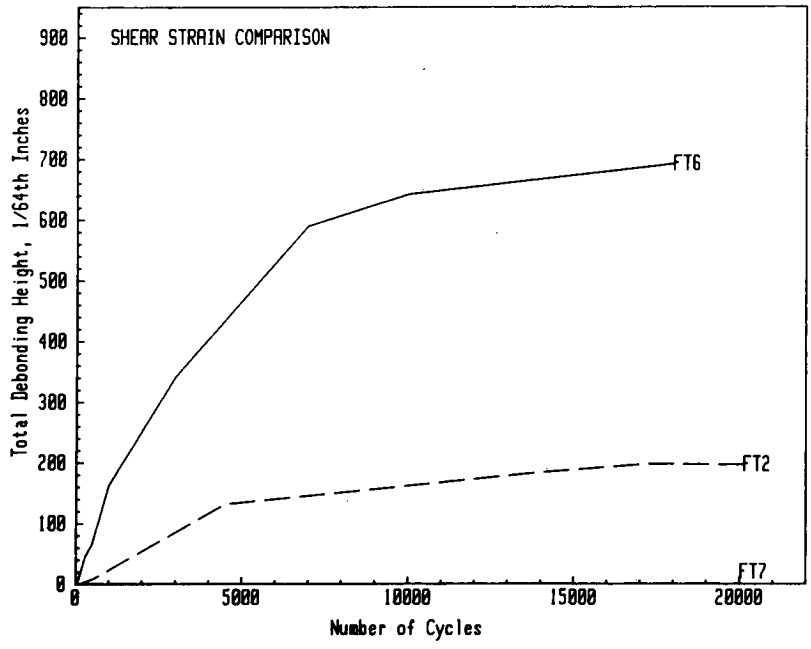

Figure 17. Typical growth rate of the measure of relative crack size in the shear fatigue tests.

FATIGUE

Shear and compression fatigue tests were performed as described in Appendix F. The shear tests were based on 20,000 cycles of full shear cycles. Fatigue cracks developed in the elastomer near the steel interface, and the cracks grew with time, as illustrated in Figure 17. Pilot tests at different loading rates showed that rapid loading caused the cracks to grow more quickly and to a larger size. Since the shear tests were conducted at an accelerated rate, this suggests that the test results represent a conservative basis for estimating fatigue life of a bearing in a bridge subjected to a daily temperature cycle. These observations may be unconservative for bridges subjected to cyclic shear deformation due to other phenomena, such as braking forces or vibrations, since many more, and more rapid, cycles may result. The cracks grew deeper and more rapidly when the cyclic shear strain was larger. Increased compressive strain also increased cracking. The material properties of the elastomer had considerable impact on the fatigue cracking, but there was no evidence that greater elongation at break improved the fatigue behavior, as suggested by some design specifications (*3, 27, 28*).

The compression fatigue tests were based on 2 million cycles of severe compression load cycles combined with a minimum stress level to simulate dead load. The crack growth for these fatigue tests was different, as shown in Figure 18. The crack growth did not stabilize in the compression tests as it frequently did in the shear tests. A large strain range greatly increased cracking. The mean strain affected the fatigue life, but it was a much weaker effect than the strain range. The material properties of the elastomer also had considerable impact on fatigue cracking, but there was again no evidence that increased elongation of break increased the fatigue life.

The bearings were usually tested without cover because this facilitated the observation of cracking. Edge cover may delay cracking somewhat, but it also tends to obscure crack development. Therefore, it is believed that the fatigue tests were conservative, but not overly so. However, it is very difficult to define an acceptable crack level. It is clear that some of the severely cracked specimens were well beyond acceptable serviceability limits. It is equally clear that the most lightly damaged specimens were well within acceptable limits, but the actual demarcation is difficult to define. Shear and compression stiffness tests show that some of the severely damaged specimens experienced dramatic stiffness change. These stiffness results may be useful in defining an appropriate design limit.

In assessing the results of these fatigue tests it is important to realize that the applied loading did not replicate actual bridge loading. Time constraints made that impossible. The loading was chosen to produce enough damage in the available time to

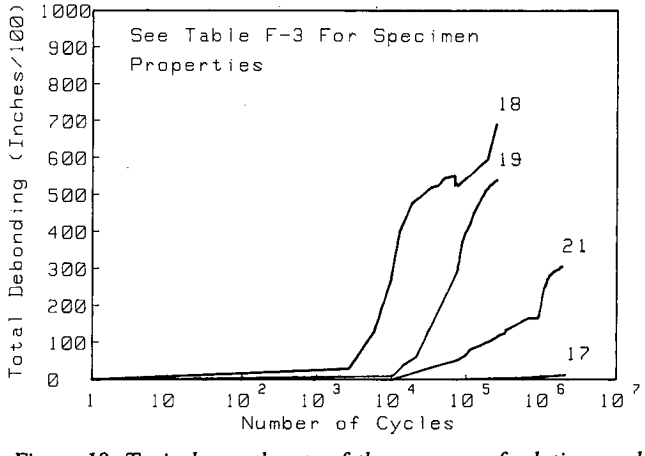

Figure 18. Typical growth rate of the measure of relative crack size in the compression fatigue tests.

permit comparison between the effects of different parameters such as material properties and load amplitude. The most severe load histories were therefore more punishing than those to be expected in practice, especially in view of the unavoidable heat build-up which they caused.

CHAPTER THREE

ANALYSIS OF RESULTS

PROPOSED DESIGN SPECIFICATION

The research results described in Chapters One and Two and Appendixes A through G were translated into a series of proposed design recommendations. The recommendations are included as a proposed design specification and commentary in Appendix H. This chapter provides a more detailed analysis of the research results and a rationale for some of the more critical design recommendations.

SHEAR DEFORMATION AND LOW TEMPERATURE STIFFENING

Expansion and contraction of bridge girders cause shear deformations in bridge bearings as shown in Figure 15a. The maximum shear deformation, Δ_s, depends on ΔT, the difference between either the maximum or minimum temperature for the region and the installation temperature, whichever difference is larger. The shear strain is then

$$\gamma_s = \frac{\Delta_s}{h_{rt}} = \frac{\alpha 1 \Delta T}{h_{rt}} \tag{6}$$

It should be kept below 0.5 because the corners of bearings tend to roll over if γ_s exceeds this value. Many design specifications (*8, 30*) have gone to a 0.7 strain limitation, but this higher limit may sometimes result in damage to the reinforcement or tensile cracking of the elastomer.

The shear deformation induces a shear force in the bearing, which at room temperature can be estimated by the equation

$$H = G_a A_s \gamma_s \tag{7}$$

The apparent shear modulus, G_a, depends on the true material modulus, the bearing geometry, and the compressive load, and may be obtained from tests such as those described in Appendixes D and E. It is fairly constant at loads well below the buckling load. Most field bearings would be compressed to a load significantly below the buckling load, and so the material shear modulus usually may be substituted for G_a under many practical conditions. The bridge piers and other structural components must be designed for this force, or slip must be permitted. Elastomeric compounds stiffen at low temperatures, and the shear modulus of the material may increase by one or more orders of magnitude under low temperature conditions. Therefore, the bridge designer must either design the piers and structural components for forces much larger than H, or specify an elastomer that controls the stiffening effect, or provide a slip mechanism that limits these forces in the structure.

The calculations provided in Appendix A are very approximate, but they provide reasonable bounds on stiffening based on the best available experimental data on low temperature crystallization and thermal stiffening. These calculations indicate that bearings in most parts of the United States would be subject to low temperature crystallization, and bearing forces of three to four times the force computed using the room temperature stiffness may occur when the bearing has an inappropriate grade of elastomer. As a result, it is recommended that the continent be divided into three major regions for purposes of low temperature design. Region I consists of areas such as the Gulf Coast, Pacific Coast, and Hawaii where low temperatures are not a problem. Possible guidelines for this region are extreme low temperatures higher than 0°F (−18°C) and temperatures not below 25°F (−5°C) for more than 6 hours duration on 3 consecutive days. Region II would include most of the United States—those regions where the temperature does not fall below −30°F (−35°C). Region III would contain those areas where the extreme low temperature is below −30°F (−35°C).

The grade of elastomer needed in each region is related to the design force for the bearing. This is defined as the force that would be induced in the bearing when it is subjected to the maximum shearing deformation required by changes in bridge length, assuming that the shear modulus of the elastomer remains at its room temperature value. In Regions I and II, elastomer of ASTM grades 1 and 2, respectively, will be permitted provided that either a positive slip apparatus is installed or the structural components of the bridge can resist the forces arising from a bearing force of at least four times the design force. Otherwise, grades 2 and 3, respectively, will be used. In Region III grade 5 must be used under all circumstances and will always require separate tests to evaluate low temperature stiffening. It must be emphasized that the primary concerns here are damage to the structure or walking of the bearing from its required position. The latter may limit the forces, but the bearing

may cease to be functional when needed for future deformations. Breaking of the bearing is not believed to be a valid concern.

COMPRESSIVE STRESS LIMITS

The experimental research has clearly shown that well-designed and manufactured reinforced elastomeric bridge bearings may support compression loads that are much larger than those presently permitted by the AASHTO *Specification*. Larger allowable compressive stresses will result in smaller bearings and will produce numerous benefits to the bridge engineer. First, smaller bearings will result in smaller design shear forces and may sometimes result in more slender and economical piers and support structures. Second, larger stress levels may permit the use of reinforced elastomeric bearings in many structures that would ordinarily require other more expensive bearing systems, such as pot bearings or mechanical bearings. Finally, smaller bearings require less material and may be more economical. However, it is essential that the bearings be manufactured with good quality control, and they must be designed to avoid several modes of failure including delamination, rupture or yield of the reinforcement, buckling or stability failure and fatigue.

Yield and rupture of the reinforcement is important, because the large compressive load capacity of the bearing can only be developed if the bulging of the elastomer is restrained by the steel. The reinforcement applies restraining shear stresses on the elastomer, which introduce tensile stress in the reinforcement. In steel-reinforced bearings, these tensile stresses will first cause the steel to yield. As more load is added, the yielding spreads and some strain hardening occurs, and eventually the steel ruptures. Depending on the shape of the bearing, considerable inelastic stress redistribution may take place. Fiberglass reinforcement does not develop the desirable redistribution of stress, and it is generally much weaker than steel. Therefore, high compressive stresses cannot be permitted in these bearings. Similarly, unreinforced pads lack the necessary bulging restraint, and so they too cannot support high stresses.

Theoretical predictions of the maximum reinforcement stress have been made for strip and circular bearings. For steel-reinforced bearings, these theories have been confirmed by experiments, and the equation

$$h_s \geq \frac{1.5(h_{r1} + h_{r2})\,\sigma_c}{2\,F_y/SF} = \frac{1.5(h_{r1} + h_{r2})\,\sigma_c}{F_y} \qquad (8)$$

gives a reasonably conservative value for the plate thickness, if the allowable steel stress is ½ of F_y.

Both theory and experiments have shown that holes in the reinforcement cause stress concentrations and rupture of the reinforcement at reduced loads. Holes are frequently placed in bearings for anchor pins, and some fabricators use holes to align the plates during manufacture and fill the holes after completion. In either case, the steel thickness must be at least double that required by Eq. 8.

Delamination of the elastomer from the reinforcement is also a potential failure mode that could limit the compressive load. Normal theoretical considerations would suggest that delamination is related to the maximum shear strain in the elastomer and, therefore, related to the applied compressive stress and the shape factor. An approximation for the maximum shear strain due to compression loading, γ_c, is

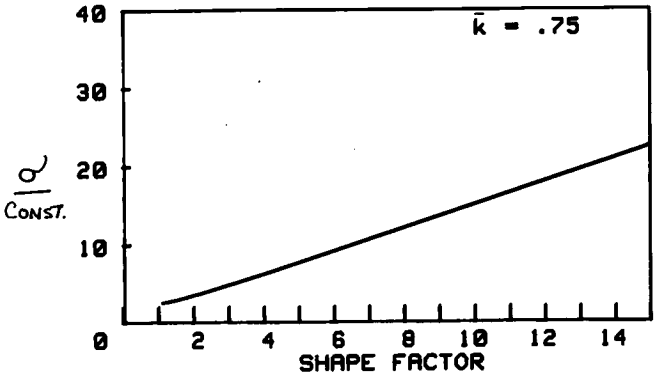

Figure 19. Theoretical variation in the stress at delamination.

$$\gamma_c = 6\,S\epsilon_c \qquad (9)$$

where

$$\epsilon_c = \frac{\sigma_c}{3G(1 + 2\bar{k}S^2)} \qquad (10)$$

Delamination is clearly a tearing or cracking of the elastomer near the steel interface. If it is postulated that the cracking occurs when γ_c attains a given strain level, the maximum compressive stress should be as shown in Figure 19. The delamination was physically observed in the compression tests, and the stress at which delamination cracking was first observed is shown in Figure 12. It is obvious that there is great scatter in these data. It is probable that the data are related to shear strain, but other factors, such as quality of manufacture, must play a dominant role. In view of these factors it is believed that the wisest course of action is to place a fixed upper limit on the average compressive stress to control delamination. All specimens except one delaminated under monotonic load at a stress greater than 2,500 psi, and the one specimen that delaminated at a lower stress had been tested earlier. An upper limit of 1,600 psi on the service load appears to be appropriate for present practice, because it employs a factor of safety that is on the order of that commonly used for bridges. However, this limit may be increased somewhat in the future as the quality of manufacture improves or the mode of failure is better understood.

STABILITY

The theoretical work of Gent (*41*) can be simplified to provide

$$P_{cr} = \frac{\phi GA_s}{2}\left\{\sqrt{1 + \frac{4\pi^2 EIf_r}{GA_s(kh_{rt}\phi)^2}} - 1\right\} \qquad (11)$$

for a rectangular bearing with boundary conditions on the top and bottom surfaces which are characterized by effective length factor k. The ratio ϕ is $\phi = (h_{st} + h_{rt})/(h_{rt})$. This ratio is invariably greater than 1 but seldom greater than 1.2 in practical bridge bearings. The rotational stiffness term, f_r, is discussed in

Appendix C and is a function of bearing geometry. However, it can be approximated as

$$f_r = \frac{4}{3} + 0.267S^2 \tag{12}$$

for a long strip, and

$$f_r = 1 + 0.742S^2 \tag{13}$$

for a square bearing. The empirical equation

$$f_r = 1 + \left(1 + \frac{2L}{W}\right)\frac{S^2}{4} \tag{14}$$

approximates both of these expressions and is compared with the exact theoretical solution in Figure 20. With this empirical approximation

$$\sigma_{cr} = \frac{GL}{kh_{rt}}\frac{\pi}{2}\sqrt{1 + \left(1 + \frac{2L}{W}\right)\frac{S^2}{4}} \tag{15}$$

where L is less than W and h_{rt} is the total thickness of the elastomer in the bearing. The buckling stress predicted by this equation is shown in Figure 21. This figure illustrates the normalized buckling capacity for a bearing subject to lateral movement (sideways) but not end rotation ($k = 1$). The curves are normalized with respect to the shear modulus, G, but they contain no factor of safety. The shear modulus, G, is approximately 110 psi for 55 hardness elastomer. If a safety factor of 1.7 is maintained against buckling, the buckling stress must be at least 2,720 psi in order to use the maximum working stress of 1,600 psi. This buckling stress can be developed for most practical bridge bearings. For example, for a 2 to 1 rectangle with a shape factor of 6 and an effective length factor of 0.5, it requires only that the $h \leq L/1.8$. Very tall bearings or square bearings of intermediate height may be controlled by stability design.

Gent's theory compares well with experimental results for very tall, slender bearings and is very conservative for shorter bearings. Modified theories are available, but they do not offer sufficient improvements in correlation to warrant their extra complexity. Therefore, it is believed that this equation will result in safe and satisfactory stability designs. However, the conservatism will not be excessive because stability will seldom control the design in squat bearings, where the equation is most conservative.

The empirical Eq. 14 for f_r is compared with the series solution for it in Figure 20. Comparisons are made both for an incompressible material and for a material with a bulk modulus 1,000 times greater than the elastic modulus. These values bound the normal stiffness of bridge bearing elastomers. Comparisons are made for a square bearing, a 2 to 1 rectangle and a 4 to 1 rectangle. The empirical model underestimates f_r for the rectangular bearing. It overestimates f_r for the square bearings with the compressible material, but is quite close for the compressible value. The buckling stress is proportional to the square root of f_r. The error in f_r never appears to be greater than 20 percent, and so the maximum error in the buckling stress should be less than 10 percent. In view of this, it would appear that the factor

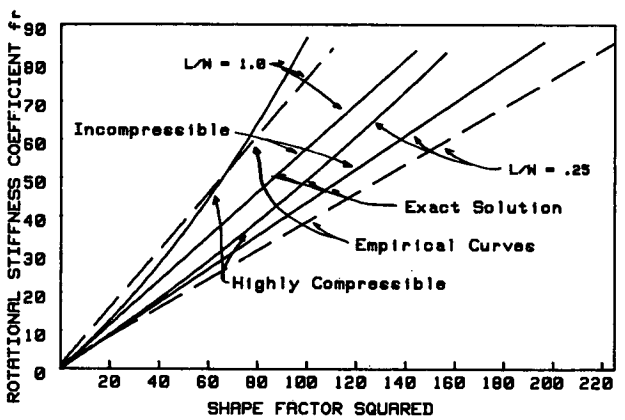

Figure 20. Comparison of the empirical rotational stiffness to the exact solutions for square and rectangular bearings.

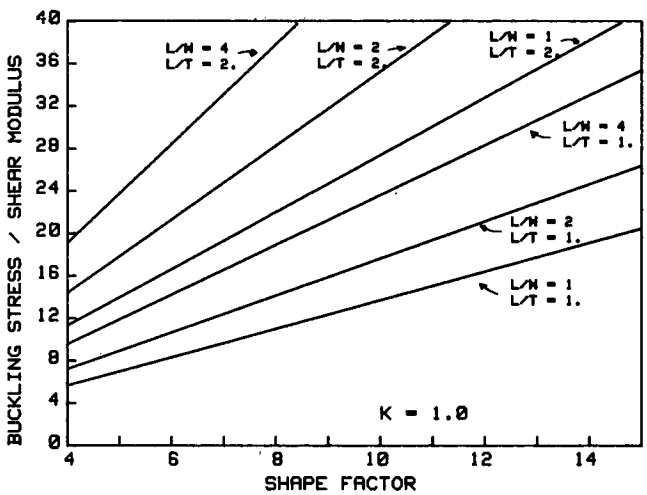

Figure 21. Theoretically predicted buckling stress for different elastomeric bearings ($k = 1$).

of safety could be increased from 1.7 to 1.8 to account for any inconsistencies in the simplified equation.

FATIGUE

The fatigue tests showed significant fatigue cracking for many specimens, but they provided no clear guidelines for defining the tolerable upper limit for cracking. The tests further showed that the strain range and mean strain were important parameters, but the strain range appeared to be the more important. The material properties of the elastomer also appeared to influence the results, but there was no evidence to support the hypothesis that greater elongation at break (or any other specific property) improved the fatigue performance.

Fatigue damage in the experiments was associated with shear failure in the elastomer next to the steel laminates, whether the load on the bearing was compressive or shear. The European approach of limiting the total shear strain thus appears the most logical. Two separate limits are proposed

$$\gamma_s + \gamma_c + \gamma_r \leq C_1 \tag{16}$$

for dead and live loads combined, and

$$\gamma_s + \gamma_c + \gamma_r \leq C_2 \tag{17}$$

for live loads alone. The two limits are needed because the live load strain varies cyclically over a range, and is clearly more important than the constant dead load strain. The constant limits, independent of the elastomer properties, are proposed because there is no rational justification for using a more sophisticated limit.

The experimental results must be used to define these limits. Tables 1 and 2 define the maximum shear strains for the shear fatigue and compression fatigue tests. In the shear fatigue tests (Table 1) the mean shear strain is the shear strain caused by compression, calculated from Eq. 9, and the cyclic strain range quoted is from maximum positive to maximum negative shear displacement. Thus, the absolute maximum shear strain is the mean plus half the range. Because in all cases half the range was less than the mean, the shear strain throughout the bearing never changed sign. Examination of these strains indicates that relatively little damage occurred in specimens with both a total shear strain less than 3 and a live load shear strain less than 1.5. This suggests that upper limits of C_1 and C_2 should be 3.0 and 1.5 respectively. The shear strain due to imposed shear deformations is limited to 0.5 for other reasons. It is conservative, therefore, to take

$$\gamma_c + \gamma_r \leq 2.5 \tag{18}$$

for total load, and

$$\gamma_c + \gamma_r \leq 1.0 \tag{19}$$

for live load only. These limits may be raised by 0.5 in bearings fixed against translation. The compressive shear strain may be estimated by

$$\gamma_c \doteq 6S\epsilon_c \tag{20}$$

where

$$\epsilon_c = \frac{\sigma_c}{3G(1+2\bar{k}S^2)} \tag{21}$$

and $\bar{k}$ is a constant depending on elastomer hardness. It has been suggested that $\bar{k}$ varies between 0.75 and 0.55 for 50 to 65 hardness elastomers. Practical bridge bearings have large shape factors, so the term $(1+2\bar{k}S^2)$ may be approximated by $2\bar{k}S^2$, giving

$$\gamma_c = \frac{\sigma_c}{G\bar{k}S} \tag{22}$$

Using an average value of $\bar{k}$ ($\bar{k} = 0.65$) and the limits on combined shear strains derived above, the maximum compressive stress on a bearing with maximum shear and no rotation is

$$\sigma_c \leq 1.625\ GS \tag{23}$$

Table 1. Shear fatigue test shear strains.

Test No.	Compressive Strain	Number of Cycles	Mean Shear Strain	Cyclic Strain Range	Total Shear Strain	Relative Damage
1	.04	21000	1.27	1.20	1.87	182
2	.11	20100	3.50	1.00	4.00	300
3	.11	20000	3.50	1.00	4.00	697
4	.12	20000	3.82	1.00	4.32	83
5	.14	20000	4.45	1.00	4.95	356
6	.12	20000	3.82	1.70	4.67	1081
7	.11	20000	3.50	.30	3.65	0
9	.11	20000	3.50	1.70	4.35	1186
10	.13	20000	4.13	1.70	4.98	1350
11	.12	20000	3.82	1.70	4.67	961
12	.13	20000	4.13	1.70	4.98	1188
13	.13	20000	4.13	1.70	4.98	919

Table 2. Compression fatigue test shear strains.

Test No.	Compressive Strain		Number of Cycles	D.L. Shear Strain	L.L. Strain Range	Total Shear Strain	Relative Damage
	Mean	LL					
17	.066	.041	2121	1.37	1.23	2.60	12
18	.053	.075	245	.47	2.25	2.72	690
19	.075	.056	254	1.41	1.68	3.09	539
20	.045	.063	338	.41	1.89	2.30	495
21	.075	.046	2003	1.56	1.38	2.94	308
22	.092	.091	2053	.84	1.64	2.48	545
23	.078	.053	662	1.54	1.59	3.14	273
24	.071	.057	1205	1.28	1.71	2.99	520
25	.084	.050	554	1.77	1.50	3.27	224
26	.058	.047	499	1.32	1.80	3.13	438
27	.086	.051	484	1.81	1.53	3.35	131
28	.084	.052	490	1.74	1.56	3.30	130
29	.071	.051	663	1.37	1.53	2.90	98

for combined dead and live load, and

$$\sigma_c \leq 0.65\ GS \tag{24}$$

for live load only. The limits in Eqs. 23 and 24 are rounded to $\frac{5}{3}$ and $\frac{2}{3}$, and, for bearings fixed against translation, they are raised to 2.0 and 1.0. Approximate allowable stresses for elastomers with different shear moduli are shown in Figure 22.

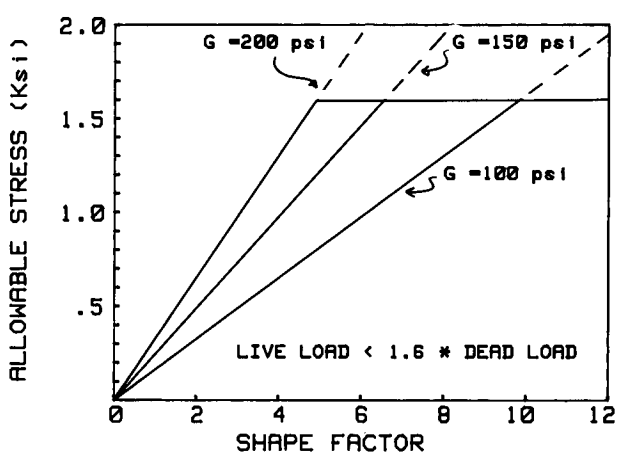

Figure 22. Approximate allowable stress permitted by the fatigue provisions for different hardness and shape factor.

No increase in the loads to allow for impact is required. This is because the demarcation between acceptable and unacceptable fatigue damage is arbitrary, because the live load generally represents only a small proportion of the total load, and because the impact fraction defined in the AASHTO *Specifications* bears little relation to the true impact load on a bearing.

Many bearings are subjected to rotation in conjunction with an applied compression and shear strain. Rotation increases the shear strain in the bearing. In many cases, the rotation is due to initial camber or imperfections during construction, and so it contributes only to the total strain, and not to the cyclic strain range.

The conditions that

$$\gamma_c + \gamma_r < C_1 \tag{25}$$

and

$$\Delta_c = \frac{\sigma_c h_{ri}}{6G\bar{k}S^2} \tag{26}$$

lead to

$$\sigma_c \leq \frac{(6\bar{k}C_1/C_c)GS}{1 + \dfrac{C_r}{2C_c}\dfrac{\theta L}{\Delta_c}} \tag{27}$$

where C_r and C_c are coefficients relating maximum shear strain to imposed compression and rotation. The ratio C_r/C_c is plotted against bearing aspect ratio W/L in Figure 23. Two curves are shown for different assumptions about the material properties, and they bracket the range for practical bridge bearing elastomers. Taking C_r/C_c as a constant value of 0.5 for all circumstances can be seen to be a reasonable approximation. Using the same values for C_1, C_c and k as before

$$\sigma_c \leq \frac{1.66\ GS}{1 + \dfrac{\theta L}{4\Delta_c}} \tag{28}$$

for total load and

$$\sigma_c < \frac{0.66\ GS}{1 + \dfrac{\theta L}{4\Delta_c}} \tag{29}$$

for live load alone. θ and Δ_c in Eq. 29 are the rotation and vertical deflection caused by live load alone. It is shown in the next section that θ should be restricted to $2\Delta_c/L$, so when the rotation takes on its larger permissible value, the effect is to reduce the allowable compressive stress by a factor of 1.5 over the value for no rotation.

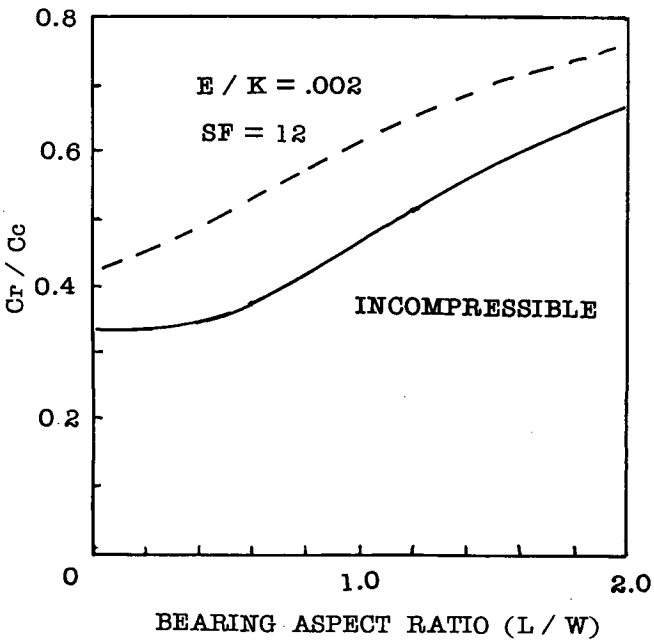

Figure 23. Shear strain due to rotation (γ_r) divided by the maximum shear strain due to compression (γ_c) for rectangular bearings with different shape factors (theoretical values).

ROTATION

The maximum rotation permitted on elastomeric bridge bearings may be based on one of several limits. Some specifications base it on the prevention of lift-off and others employ maximum rotations that may be three times as large as the lift-off value. This higher rotation limit is based on the prevention of strain reversal at the lightly loaded edge. The experimental results suggested that lift-off may severely damage the bearing, and so rotation is limited to $\theta_{max} \leq (2\Delta_c/L)$ where L is the plan dimension perpendicular to the axis of rotation. This limit is only applicable to total loads. The rotation caused by live load alone need not be limited.

Both initial lack of parallelism and the dead and live load rotations contribute to the total rotation. The magnitude of each component depends on the continuity and method of construction in the bridge. Continuous bridges will have relatively small live load rotations. There is no initial lack of parallelism in a poured-in-place concrete bridge, and that in prefabricated bridges (steel or precast concrete) will depend on the girder tolerances and the accuracy with which the bearings are set on the piers.

CHAPTER FOUR

CONCLUSIONS AND SUGGESTED RESEARCH

CONCLUSIONS

This report has described the research results from Phase II of the NCHRP Project 10-20 research program. During the research the behavior of bearings under different types of loading was considered, and the important modes of failure were investigated theoretically and experimentally. These modes of failure include delamination, yield or rupture of the reinforcement, fatigue cracking of the elastomer, excess deformation and buckling of the bearing. Theories were investigated and compared to experimental results, and where possible improvements were made. This information was then combined into a draft specification which is provided in Appendix H.

This draft specification will permit bearings that are more slender and more highly stressed than those in use today. The combined effect of these two factors is a potential reduction in the shear force transmitted by the bearing. However, the use of these provisions requires more design effort and tighter quality control in the manufacture of the bearing.

While this study has improved the understanding of the behavior of elastomeric bridge bearings, there is still considerable room for improvement. A better understanding of these existing deficiencies may further enhance elastomeric bearing design.

RESEARCH NEEDS

The major topics which are not fully resolved include the following:

1. *Low Temperature Behavior.* The Phase II research included an analytical study of thermal stiffening of bridge bearings. This study provided mathematical bounds on the low temperature problem, but experimental research is needed to translate these theoretical limits into practical design rules. In particular, the existing low temperature elastomer grades are defined by the hardness change caused by a given temperature condition. Hardness is a very poor indicator of elastomer stiffness, and research is needed to develop a low temperature grading system that is based on the stiffness of the elastomer after a given time and temperature. In addition, the low temperature test must be correlated to local climatic conditions. Research is needed to develop certification tests which can be correlated to the local climate where the bearing will be used.

2. *Fatigue.* A number of fatigue tests were performed during the Phase II research. These tests helped to develop a better understanding of fatigue in practical bridge bearings, and they also served as a basis for the design guidelines which were proposed for the AASHTO *Specification*. However, the understanding of fatigue is by no means complete. The fatigue tests showed that material properties definitely affect fatigue cracking and fatigue life, but no one parameter which controls this behavior could be found. Further, the fatigue tests were based on an arbitrary constant amplitude test procedure. Research is needed to translate these effects into realistic variable load histories. Fatigue studies on steel structures have shown that this true load behavior may result in very different fatigue life expectancy. A better understanding of these phenomena may result in increased refinements in elastomeric bearing design.

3. *Field Studies.* Research into the actual field performance of elastomeric bearings is needed. Phase I of the NCHRP Project 10-20 research program made design recommendations that were adopted by AASHTO, which increased the allowable stresses by 25 to 37 percent on some reinforced bearings. This report recommends allowable stresses that are as much as 100 percent larger than those permitted prior to the start of this project. This is a significant increase, and field observations are needed to determine the actual consequences of the changes. Bridge engineers are frequently enthusiastic about elastomeric bearings. They believe that they never fail. However, discussion also suggests that they seldom, if ever, examine the bearings. Poor elastomeric bearing performance is unlikely to result in the collapse of a bridge, but it may result in a dramatic reduction in its service life. Examination of bearings is needed to assure that they are performing well at the increased stress levels. Field measurements of actual bridge movements and stress and strain levels in rotation, translation and compression would provide valuable information for the future improvements in the design of bearings.

4. *Combination of Large Strains.* The design recommendations employ the concept of superposition of stress and strain. Elastomeric bearings sustain very large strains. Local shear strains of several hundred percent may occur at service load conditions. These strains are several orders of magnitude larger than the strains encountered in steel and concrete, and infinitesimal strain theory clearly does not apply. The effect of combined loading was studied both in the fatigue tests and monotonic loading, but very large gaps in the understanding of this behavior still exist.

5. *Friction and Slip.* The friction developed between the bearing and its contact surface is not well defined. Slipping of the bearing from its required position is an important mode of failure which must be controlled. Research is needed to understand this frictional behavior better.

6. *Material Properties.* The material property tests presently in the AASHTO *Specifications* are misleading. They appear to set out precisely the necessary and sufficient conditions for assuring good bearing performance, but this is not the case. In fact they have evolved because bearings that satisfy them have generally worked well at present loading levels, although the reasons for such satisfactory performance are not clear. Tests which are related more directly to performance requirements and which are independent of material type would be desirable,

and could lead to better performance and more economical bearings.

Elastomers are at present specified almost exclusively by their nominal hardness, and the selection of ingredients is left to the fabricator. This leads to significant differences in real properties when two manufacturers produce bearings that are meant to be the same. A better understanding of the relationship between the physical properties of the finished elastomer and the methods and materials used in its manufacture would help to reduce these differences. It is also necessary if more appropriate tests are to be developed.

Improvements in fiber-reinforced bearings require both stronger fiber reinforcement and better bond to the elastomer. The ability to make large sheets of material from which individual bearings can subsequently be cut is appealing from a commercial point of view, and measures to increase the strength of fiber-reinforced bearings could provide the impetus for significant developments.

7. *Manufacturing Tolerances.* Quality control during manufacture has a significant influence on bearing behavior. The most obvious areas with potential for improvement are the control of elastomer layer thickness and edge cover. The former affects both static and fatigue strength, and the latter influences temperature changes and so makes a difference to low temperature behavior.

8. *Secondary Factors.* Many other factors relating to elastomeric bearing behavior require study. PTFE slide surfaces are frequently used with elastomeric bearings, but their behavior is not well understood or precisely defined.

9. *Theoretical Models.* Finally, this research has again illustrated the serious limitations in the existing theoretical models. Improvements in this area could result in significant improvements in the design and behavior of bridge bearings. Perhaps the most pressing need in this category is a means of establishing reliably the stresses in the elastomer at the edge of the reinforcing plates, and the ability of the elastomer to withstand them.

APPENDIX A

EVALUATION OF LOW TEMPERATURE BEHAVIOR

INTRODUCTION

It is well known that elastomeric bearings stiffen at low temperatures. Structural bearings are designed to support the structure while accommodating bridge movements from causes such as thermal expansion. Excessive stiffening of the elastomer may prevent fulfillment of this function. However, the low temperature behavior of elastomers is not fully understood, even from a laboratory standpoint, and furthermore, precise data on actual low temperature field conditions are often not available. As a result, a study of low temperature behavior was performed. The objectives were to determine if and when low temperatures might cause structural problems and to develop practical guidelines for minimizing those problems. It neither included experimental research nor considered the use of new elastomers or elastomeric compounds. It utilized the best available data for evaluating compounds that are typical of those encountered in present-day use.

This appendix describes the results of the study. The existing knowledge of the low temperature material properties of elastomers is reviewed in detail. Simple mathematical models are generated to characterize their behavior, and responses to the models are compared to existing experimental data. Typical extreme low temperature records are obtained for various parts of the United States, and these are used to estimate how temperature varies with time in the bridge and bearing. Bearing response calculations are then performed for different elastomer types, bridge types, and temperature records. These calculations are evaluated and conclusions and design recommendations are developed.

Before describing this research, it is essential to note that the work described in this chapter is approximate. The authors believe that the results indicate trends that can be readily used in design, but individual calculations are necessarily imprecise. There are two main reasons for this imprecision. First, the calculations are complex and require several implicit and explicit assumptions, which are discussed in detail in this appendix. Second, the analyses make use of material properties that vary widely with elastomeric compound and are substantiated by only limited experimental data. However, the assumptions made and properties used were selected to be consistent with the best available information.

MATERIAL PROPERTIES

Only limited research (*5, 6*) has been conducted on the low temperature behavior of elastomeric compounds typically used in bearings. Murray and Detenber (*5*) performed an experimental study of low temperature properties with emphasis on polychloroprene. They showed that two types of low temperature stiffening occur, referred to as crystallization (or first order transition) and thermal stiffening. In addition a third phenomenon occurs, called glass transition, when the material becomes brittle and small specimens may shatter under impact.

Crystallization is time-dependent. The material becomes harder and stiffer with time because of a temperature-dependent reorientation of the molecular structure. The rate of crystallization was measured by the time in hours at constant temper-

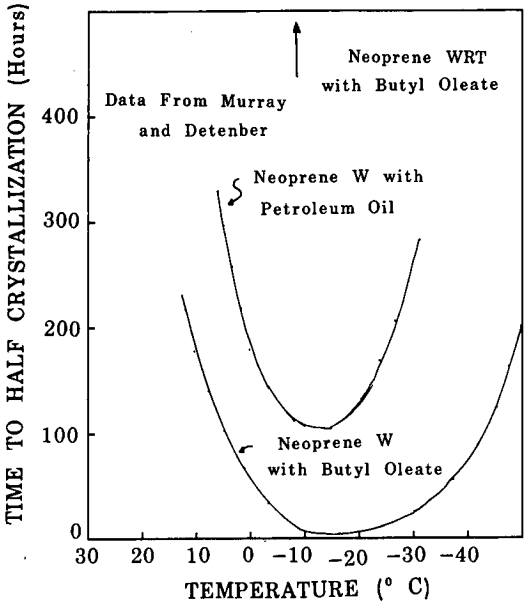

Figure A-1. Experimental data for crystallization of neoprene.

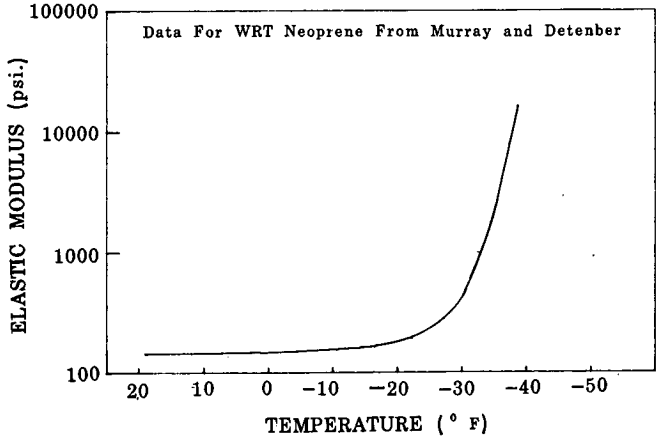

Figure A-2. Experimental data for thermal stiffening of neoprene.

ature to half crystallization, which was defined by a 10 durometer point increase in Shore A hardness. It was found to depend on temperature and elastomeric compound. For Neoprene compounds, the time to half crystallization varied approximately parabolically with temperature, and its minimum occurred at about −12°C (+10°F) as shown in Figure A-1.

Three neoprene compounds were studied based on neoprene base polymers types GN, W, and WRT, and the compound based on type W was found to crystallize much more rapidly than the other two. All three base polymers are polychloroprenes, but they have slightly different molecular structures which give rise to different physical properties in the finished compound. In general, neoprene compounds based on type W have the least resistance to crystallization and are used in moderate environments because they are the most economical choice. Type WRT has the highest resistance to stiffening at low temperatures but is more expensive and, therefore, is used primarily in cold regions. Type GN has low temperature properties that lie between those of types W and WRT. However, precise isolation of the effects of the base polymer is difficult because the physical properties are also influenced by the other constituents of the compound and by the curing procedure, and these vary from one compound to another. One such constituent is plasticizer, which is required to facilitate manufacture and to control the hardness. Increasing the plasticizer content was found to shorten the crystallization time. Crystallization is completely reversible, and neoprene vulcanizates were found to decrystallize quite quickly when held at a temperature more than 15°C (27°F) above the crystallization temperature.

The second order transition is not a phase change in the molecular structure of the elastomer, and is not time-dependent, but consists of instantaneous stiffening and brittleness. Murray and Detenber defined as the thermal stiffening temperature the temperature at which the material modulus reached 10,000 psi. This represents a stiffness which is 25–40 times the room temperature value. For natural rubber, Type W neoprene, and Type WRT neoprene they found thermal stiffening temperatures of −52°C, −38°C, and −39°C (−62°F, −36°F, −38°F) respectively. While Type WRT neoprene displayed the slowest crystallization rate of all the polychloroprenes, its thermal stiffening temperature was slightly higher than that of Type W. Its thermal stiffening characteristics are shown in Figure A-2.

All elastomers except butyl reached a glass transition at a temperature approximately 5°C (9°F) below the thermal stiffening temperature. At this temperature, a thin specimen will shatter on bending or sudden impact. This fracture depends on the rate of loading and specimen size and is not likely to be a serious problem with practical bridge bearings. Butyl has been proposed as a polymer that is suitable for bridge bearings subjected to low temperatures. Murray and Detenber's work suggests that thermal stiffening in butyl occurs at higher temperature than in polychloroprenes and a lower temperature than in natural rubber; however, the glass transition temperature of butyl is higher than its thermal stiffening temperature. This is an undesirable situation and raises concerns about the use of this material. However, other data (*7*) may dispute this contention.

Another comprehensive set of experimental data was reported by Stevenson (*6*). Seven compounds of natural rubber and two of polychloroprene were extensively tested for low temperature behavior as well as undergoing normal certification tests. The carbon black and sulfur contents of the individual compounds were recorded, and the normal certification tests for tensile strength, elongation at break, and aging resistance were preformed. Hardness, compression set, and elastic modulus tests were then conducted at low temperature. These tests were performed in accordance with common standards (*8*), but more detailed tests were also performed. Elastomer stiffness, hardness and compression set were reported for −10°C and −25°C (14°F and −13°F) for exposure times varying from 1 min to 5,000 hours. Figure A-3 shows a typical plot of stiffness and hardness at constant temperature as a function of time for a typical specimen normalized by dividing by the values at 70°F. The curves for all the specimens exhibited similar characteristics. That is, they had similar shapes and the hardness, modulus, and compression set appeared to have consistent relationships with one another.

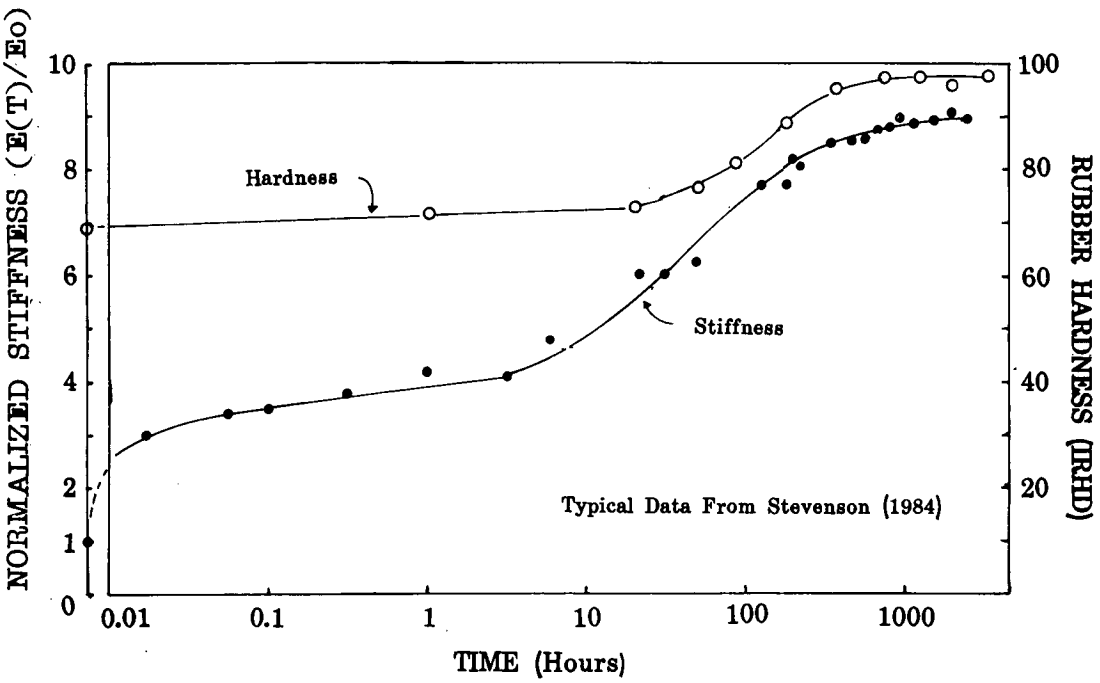

Figure A-3. Typical time-dependent low-temperature behavior of elastomer.

Stevenson's report does not distinguish between crystallization and thermal stiffening, but correlation with these separate phenomena can easily be made, because the time is plotted on a logarithmic scale. Figure A-2 shows that thermal stiffening increases rapidly as the second order transition temperature is approached, and it is known that this is an instantaneous effect. In all of Stevenson's data the stiffness increased rapidly within the first minute and then remained constant for approximately one hour. The initial stiffness increase was not time-dependent inasmuch as it occurred instantly after the specimen achieved thermal equilibrium, and therefore it may be accounted for by the thermal stiffening noted by Murray and Detenber. After one or more hours, the stiffness started to increase with time, which is attributable to crystallization. The hardness also increased with time and temperature as shown in Figure A-3. In all cases, specimens which had a large increase in hardness (more than 10 or 20 IRHD hardness points) also had a large increase in stiffness, but the hardness increase was usually delayed until the stiffness had increased substantially. The stiffness had usually increased by 800 percent to 1,000 percent when a 10 point hardness increase was noted.

The slopes of the curves in Figure A-3 determine the rate of crystallization, and specimens which had a larger crystallization rate also stiffened much more. A few specimens stiffened by only very small amounts, and their hardness increased by less than 10 IRHD points even after 5,000 hours exposure. Some natural rubber specimens exhibited considerable low temperature crystallization and thermal stiffening, but the best natural rubber compound had considerably better low temperature characteristics than the two polychloroprene compounds. This suggests that natural rubber is better for low temperature applications than polychloroprene. However, it must be emphasized that low temperature behavior is highly dependent on many aspects of the elastomeric compound, and it is much better to use a well-formulated polychloroprene compound than a poor natural rubber one. This is particularly true in the light of the trade-off that appears to exist between obtaining good low temperature characteristics and maintaining acceptable values for other physical properties. Compounds that were relatively resistant to low temperature crystallization and thermal stiffening often had difficulty meeting other requirements such as tensile strength, elongation at break, or ageing resistance. This is an important observation, inasmuch as it clearly indicates that elastomers designed for low temperature operation in tires, gaskets, or seals will not necessarily work in bridge bearings because they are unlikely to satisfy normal acceptance criteria.

Figure A-3 shows that the observations of Murray and Detenber (*5*) and the data reported by Stevenson (*6*) are consistent, but the time to half crystallization chosen by Murray and Detenber is not the ideal definition for evaluating structural behavior, because structural engineers are more concerned with bearing stiffness than elastomer hardness. Further evidence of the correlation between the two sets of data is shown in the next section.

NUMERICAL APPROXIMATION OF EXPERIMENTALLY OBSERVED LOW TEMPERATURE BEHAVIOR

The results of the experiments on low temperature behavior must be expressed in numerical form before they can be readily used as a predictive tool. A mathematical model for thermal stiffening was derived by fitting a curve to the experimental data developed by Murray and Detenber, and it can be expressed as

$$E(T) = E_0 + \frac{E_0}{(T-T_c-1)^2} \qquad \text{(A-1)}$$

where E_0 is elastic modulus at room temperature, T is temperature, and T_c is the temperature at which the modulus reaches 10,000 psi. This curve is empirical and it was selected as the best, most rational fit of the family of exponential and hyperbolic forms examined. It can also be used for other elastomers such as natural rubber with published (*5*) data for T_c and Figure A-4 shows the comparison of these empirical curves for neoprene WRT and natural rubber with test data provided by Stevenson (*6*). The comparison is adequate for both materials. Figure A-5 shows a comparison of Eq. A-1 with the experimental data of Murray and Detenber (*5*).

The time-dependent low temperature data (*6*) can be approximated by the family of curves represented by Figure A-6. The figure shows that this simple model is consistent with the experimental observations illustrated in Figure A-3. It has an instantaneous thermal stiffness component that occurs immediately after attaining thermal equilibrium. Crystallization is time-dependent and can be approximated by

$$\frac{E(T)}{E_0} = 1 + \frac{1}{(T-T_c-1)^2} \qquad \text{if } t \leq 1 \qquad \text{(A-2)}$$

or

$$\frac{E(T)}{E_0} = 1 + \frac{1}{(T-T_c-1)^2} + R_2(T) \log t \qquad \text{if } t > 1 \qquad \text{(A-3)}$$

where t is the exposure time in hours and $R_2(T)$ is the slope of the semilog curve and is a measure of the rate of crystallization. The function $R_2(T)$ must be larger for rapidly crystallizing elastomers. A mathematical expression for $R_1(T)$, the rate of crystallization, was first derived from existing experimental data such as that shown in Figure A-1, and then $R_2(T)$, the rate of stiffness increase due to crystallization, was derived from it. Previous research (*5*) has shown clearly that low temperature crystallization is most rapid at certain optimum temperatures (approximately +10°F or −12°C for neoprene) and the rate varies approximately as a parabola for other temperatures. Therefore, the rate of crystallization can be approximated with an empirical equation for $R_1(T)$

$$R_1(T) = \frac{(T-T_A)^2 \sqrt{H_c}}{15} + H_c \qquad \text{(A-4)}$$

where T_A and H_c are the optimum crystallization temperature and the hours needed to increase durometer hardness by 10 durometer points at this optimum rate for the given compound, as shown in Figure A-7. T is the temperature in degrees Celsius. The predictions of Eq. A-4 are compared with experimental data in Figure A-8.

It is generally accepted that the elastic modulus is directly related to hardness, but the relationship is not precise. Gent (*9*) proposed a model which would suggest that a 10 durometer point hardness increase would produce a 60 percent increase in stiffness for the hardness range commonly encountered in bearings, and as the hardness increases his data suggest that a 220 percent increase is plausible. Low temperture tests by Stevenson

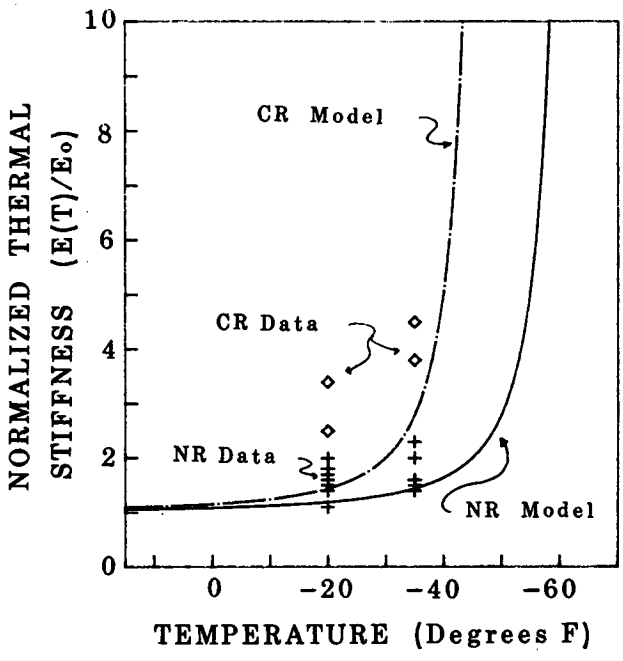

Figure A-4. Comparison of experimental data of thermal stiffening to empirical model (NR = natural rubber, CR = chloroprene).

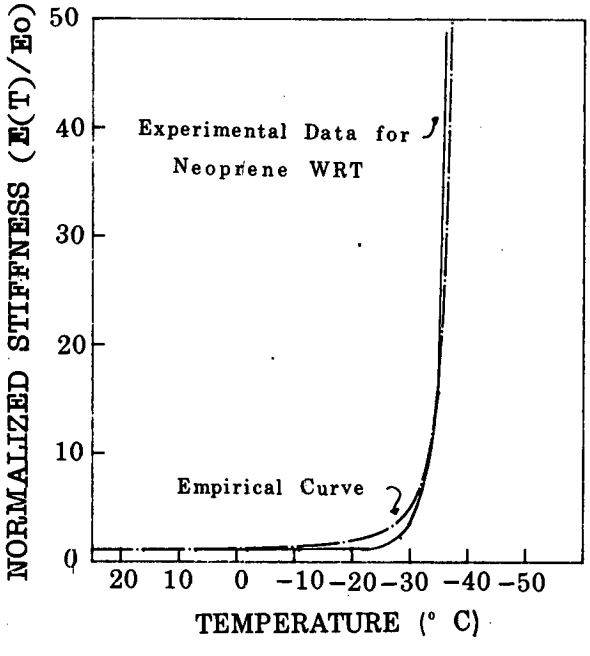

Figure A-5. Comparison of empirical model of thermal stiffening to experimental data for WRT neoprene.

indicate that stiffness increases in the order of 600 percent to 1,000 percent may occur if the elastomer hardens by 10 durometer points. With this knowledge $R_2(T)$ can be approximated as

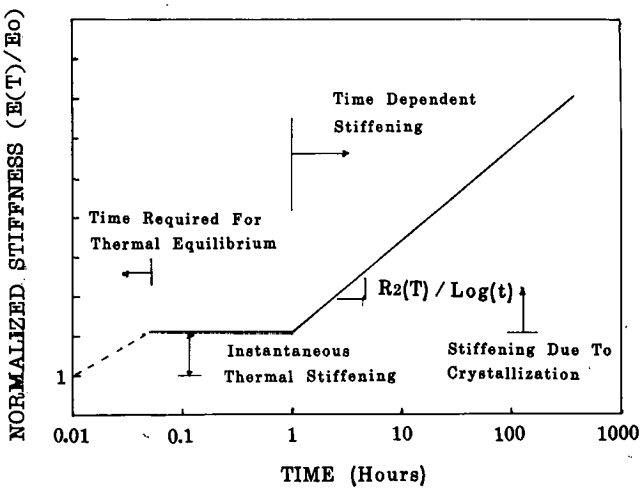

Figure A-6. Mathematical model for time- and temperature-dependent stiffening.

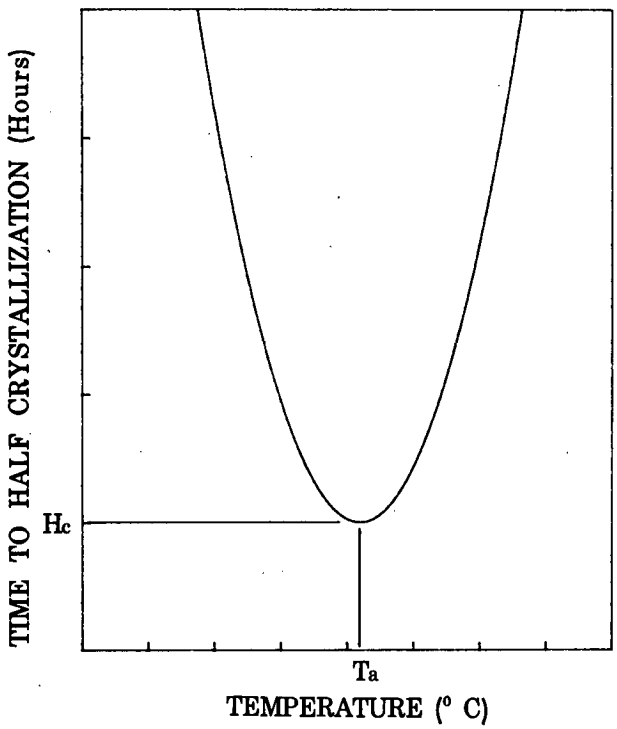

Figure A-7. Definition of parameters used in crystallization model.

$$R_2(T) = \frac{C_6}{\log_{10}\left\{\left(\frac{(T-T_A)^2\sqrt{H_c}}{15}\right) + H_c\right\}} \qquad \text{(A-5)}$$

The constant C_6 cannot be precisely defined, but Gent and Stevenson's data lead to approximate bounds of 0.6 and 7.5. Elastomers which do not crystallize easily will have large values of H_c and small values of C_6. For purposes of illustration, six hypothetical compounds were chosen, and constants for use in Eq. A-5 were selected for them. Three were polychloroprenes (C-1 through C-3) and three were natural rubber (N-1 through N-3). They were all based on realistic values selected from the experimental data in Refs. *5* and *6*, with the index 1 signifying the slowest and 3, the fastest, crystallization. In Figure A-9 they

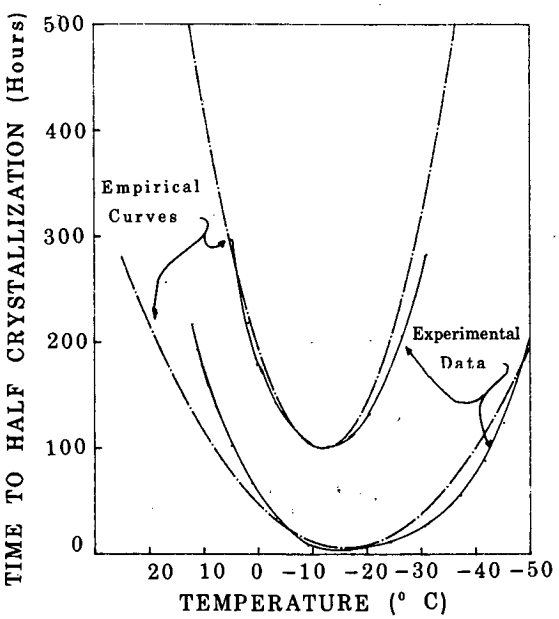

Figure A-8. Comparison of temperature-dependent experimental data for crystallization with approximate model.

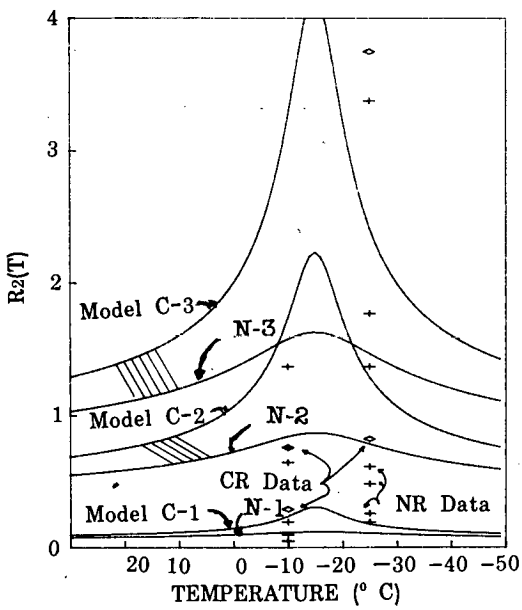

Figure A-9. Three crystallization models and comparison with experimental data.

are compared with Stevenson's test data (*6*). The three crystallization stiffening models provide reasonable bounds for the experimental data. However, the data near the lower curve were taken from compounds that hardened less than 10 IRHD degrees at 5,000 hours. This again suggests that hardness is not a sensitive model for crystallization stiffening, because a 5,000-hour test is likely to be extreme for most practical applications.

TEMPERATURE OF THE ELASTOMER

In the previous discussion, formulas were defined to model approximately the experimentally observed low temperature behavior of elastomers. From them, stiffness can be obtained as a function of time and temperature. However, the temperature of the bearing must be known, and, although it is clearly related to the ambient air temperature, the two may be quite different because elastomers are such poor conductors of heat.

Heat flow in a 3-dimensional solid is a complex phenomenon (*10, 11*), and for linear isotropic behavior it is typically modeled by a form of the Laplace equation

$$\frac{\partial^2 T}{\partial_x^2} + \frac{\partial^2 T}{\partial_y^2} + \frac{\partial^2 T}{\partial_z^2} = \frac{1}{D_{th}} \frac{\partial T}{\partial t} \qquad \text{(A-6)}$$

where D_{th} is the diffusivity, which is defined by

$$D_{th} = \frac{k_{th}}{c_{th}\,\rho} \qquad \text{(A-7)}$$

where k_{th} is the thermal conductivity, ρ is the mass density, and c_{th} is the specific heat. These values are frequently published for materials such as steel and concrete, for which diffusivity values of about 0.0186 and 0.000651 in.^{2}/sec (12.0 and 0.42 mm^2/sec) are commonly used. However, the properties for elastomers are less well known. It has been suggested that the conductivity, k_{th}, of rubber increases with increasing filler content, and the specific heat is believed to vary somewhat with temperature. Further, vulcanization also appears to modify these thermal properties. In view of the many uncertainties involved with the elastomeric compound, a diffusivity of 0.000124 to 0.000264 in.^{2}/sec (0.08 to 0.17 mm^2/sec) would appear to be appropriate over the range of interest (*12, 13*). Neoprene and the harder natural rubbers may lie in the lower portion of this range, and softer natural rubbers may reach the higher portion of this range. This suggests that polychloroprene is a slightly poorer conductor of heat than natural rubber and thus will cool somewhat more slowly when exposed to low temperatures.

The solution to the differential equation is quite difficult for most practical boundary conditions, and it is seriously complicated by the composite nature of elastomeric bearings. Equation A-6 must be satisfied separately for the elastomer and steel laminates, and the temperature and heat flow boundary conditions must be satisfied at the interface. This makes the exact solution of the thermal problem impractical for elastomeric bearings, but a very close approximation can be developed by taking into account the geometry of a typical bearing. Bearing height is usually limited by stability requirements to less than ⅓ the minimum base dimension, and so the top and bottom surface area is usually considerably larger than the area on the edge. Heat transfer between a solid and the environment is dependent on the surface area, and the through-thickness heat flow may be expected to dominate the solution. If through-thickness heat flow alone is considered, Eq. A-6 simplifies to

$$\frac{\partial^2 T}{\partial_z^2} = \frac{1}{D_{th}} \frac{\partial T}{\partial t} \qquad \text{(A-8)}$$

and the diffusivity can be simplified by selecting a composite value that is dominated by the diffusivity of the elastomer since the diffusivities are acting in series. Standard solutions (*11*) to heat flow problems may be adapted for this particular case, and Figures A-10 and A-11 show time-temperature profiles for two

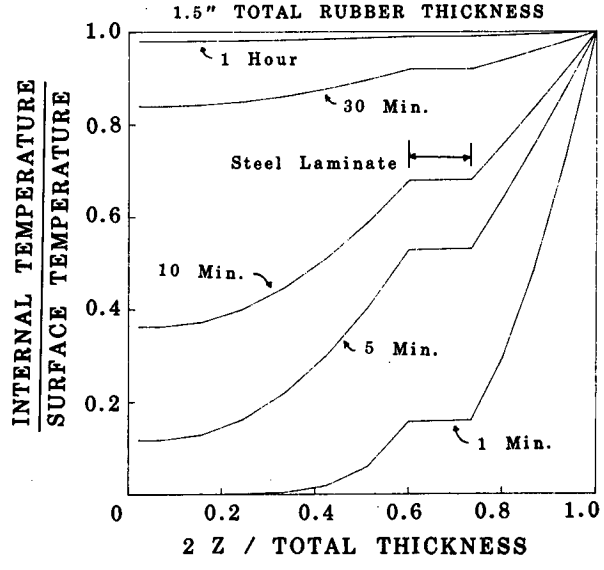

Figure A-10. Temperature profiles at different times for a 1.5 in. elastomeric bearing exposed to a constant temperature on its top and bottom surfaces (through-thickness heat flow only; internal temperature starts at 0°).

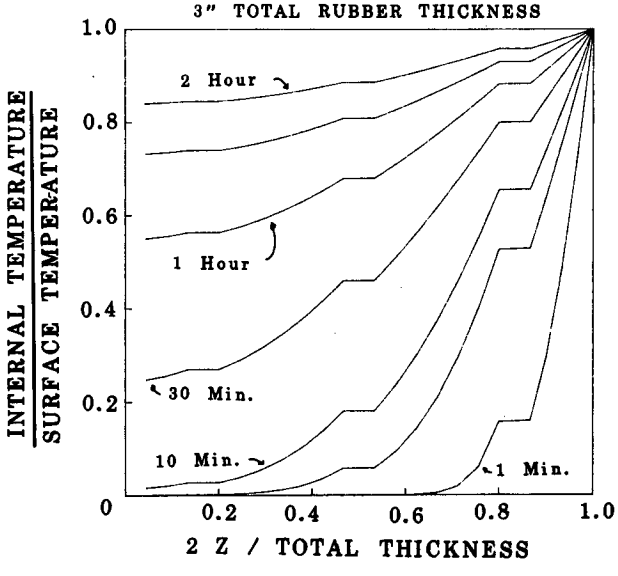

Figure A-11. Through-thickness temperature profiles at different times for a 3-in. elastomeric bearing exposed to a constant temperature on its top and bottom surfaces (through-thickness heat flow only; internal temperature starts at 0°).

bearings that are exposed to a constant exterior temperature T_0 on their top and bottom surfaces. The bearings had ¼-in. cover, ½-in. elastomer layers and ⅛-in. steel plates. One had two elastomer layers and the other, five. The diffusivity of the elastomer was taken as 0.000264 in.^{2}/sec, so the times shown should be increased by 110 percent if the lowest value of diffusivity is used. The origin of coordinates is at the center of the bearing, and z is measured through the thickness.

This analysis is based on the assumption that the transverse heat flow is negligible compared to the through-thickness flow. The validity of this assumption can be checked by analyzing the transverse flow in a circular bearing. A circular bearing is radially symmetric, and so a one-dimensional solution (*11*) and a composite diffusivity can be used. The composite diffusivity for flow through the layers is dominated by the insulating qualities of the elastomer; however, the heat flow parallel to layers is more strongly influenced by the steel. Figures A-12 and A-13 show the radial temperature distribution for the bearing of Figure A-10 when the shape factor is 5 and 10 respectively. These figures are based on constant steel and elastomer layer thicknesses, and so the larger shape factor implies a larger radius. The internal temperature is assumed to start at 0° relative to the T_0° at the outside. Radial flow is strongly influenced by edge cover, and Figure A-14 shows the temperature distribution when the edge cover is decreased from 0.25 in. to 0.125 in. Examination of Figures A-10 to A-14 reveals several facts. First, through-thickness flow controls the bearing temperature in nearly all practical cases. Radial flow becomes more important only when the bearing is very thick, the shape factor and radius are very small, or the edge cover is thin or defective.

For bearings of common dimensions (i.e., 2 in. thick or less) the time required to essentially reach thermal equilibrium is typically less than one hour. This is short enough for the bearing to reach a low temperature close to that of the air. However, it may increase to 8 or 12 hours for very large thick bearings (i.e., those bearings with more than 6 in. elastomer thickness). The time to reach thermal equilibrium may double from the above with hard natural rubber or neoprene. This delay may provide a beneficial effect in that bearings that are subjected to rapid changes in air temperature may not have time to stiffen. However, it may also have a negative effect in that the bearing will remain stiff during a sudden warming period. Thus, both the local, time-dependent air temperatures and the bearing's thermal properties must be accounted for when estimating the extent of thermal stiffening and crystallization.

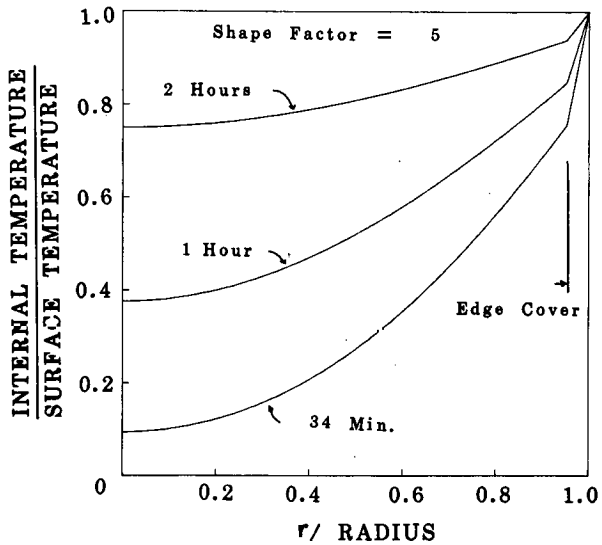

Figure A-12. Radial temperature profile for the circular bearing of Figure A-10 and a shape factor of 5, exposed to a constant temperature around its free edge (radial heat flow only; internal temperature starts at 0°).

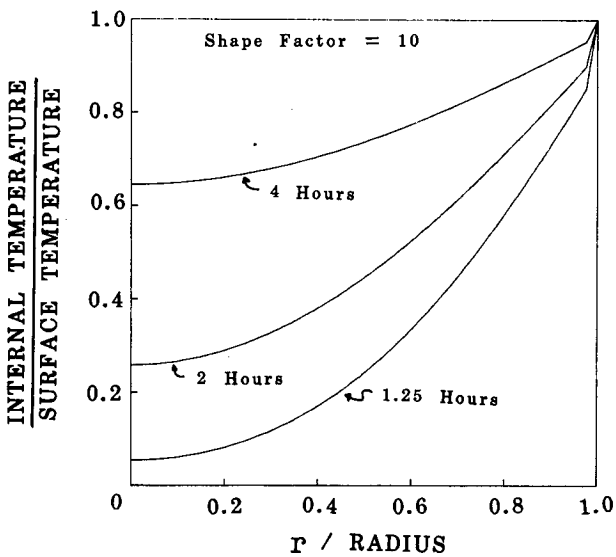

Figure A-13. Radial temperature profile for the bearing of Figure A-10 and a shape factor of 10, exposed to a constant temperature around its free edge (radial heat flow only).

LOW TEMPERATURE RECORDS

A wide range of climatic conditions exists within the United States. Daily high and low temperatures are tabulated at many locations within each state. These daily data are recorded in standard publications (*67, 68*) and extremes are summarized on a periodic basis. These data were examined to estimate the range of low temperatures to be expected. Five historic lows (prior to 1974) were chosen to reflect extreme low conditions for different parts of the United States. These are:

1. −16°F, Lubbock W.B. Airport, Texas, January 13, 1963.
2. −21°F, Colorado Springs, Colorado, January 13, 1963.
3. −28°F, Albany, New York, January 19, 1971.
4. −38°F, Duluth W.B. Airport, Minnesota, January 14, 1965.
5. −56°F, Fairbanks W.B. Airport, Alaska, December 14, 1964.

These low temperatures were historic lows (as of 1974) for the specified locations, and so the low temperature values have a very small probability of being achieved in a given year. A statistical analysis of the data was not performed, but an intuitive examination of the data suggests that these lows have recurrence intervals in the range of 10 to 50 years.

The performance of elastomeric bearings depends not only on the low temperature, but also on the duration of the exposure

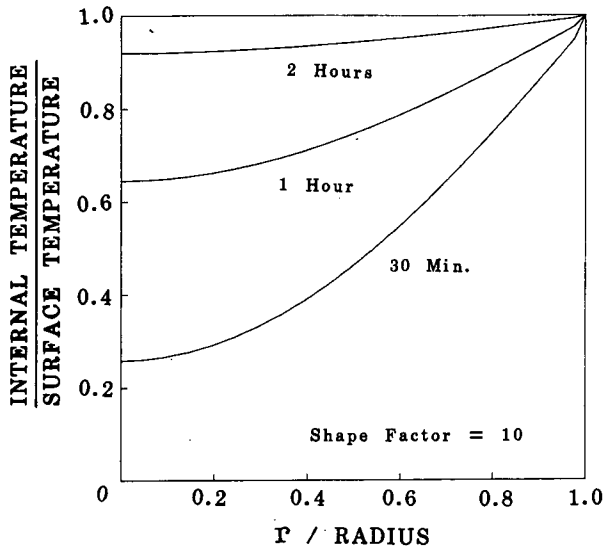

Figure A-14. Radial temperature profile for the bearing of Figure A-13 but with 0.125-in. edge cover.

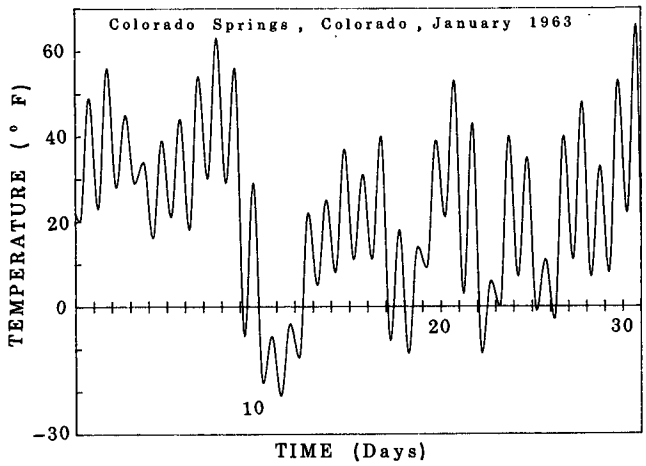

Figure A-16. Time-temperature record for January 1963 in Colorado Springs, Colorado.

to it. Therefore, daily high and low temperatures were noted for the month in question, and intermediate temperatures were postulated with a sinusoidal variation. This resulted in the five time-temperature records shown in Figures A-15 through A-19. Examination of these figures suggests that time-history characteristics may also vary widely with location. The Lubbock, Texas, record may be reasonably representative of extreme temperatures to be expected in some of the milder inland climates, but it may be somewhat extreme for many Gulf Coast or Pacific Coast regions. A very low overnight temperature may occur, but it is of short duration. The Colorado Springs and Albany records may be more representative of the more central regions. Extreme overnight lows may occur for several nights in succession, but some warming will usually occur during the day. The Duluth record may be representative of the northern

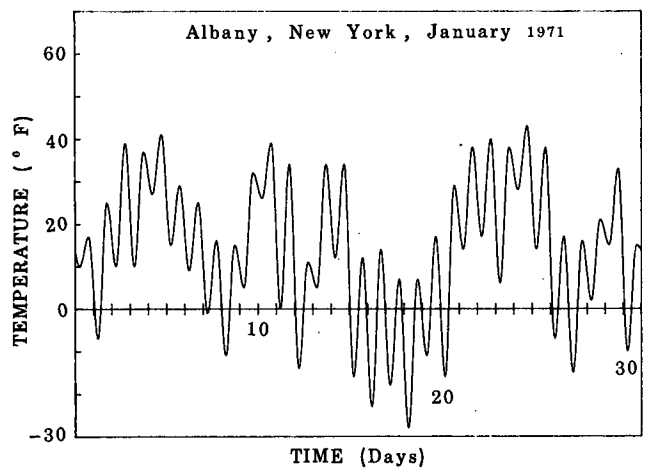

Figure A-17. Time-temperature record for January 1971 in Albany, New York.

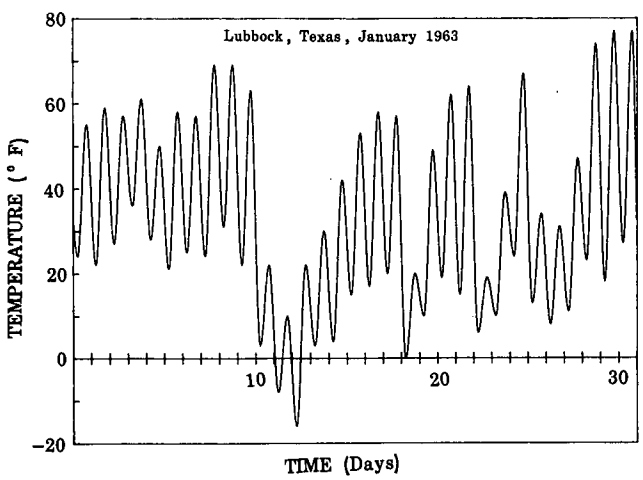

Figure A-15. Time-temperature record for January 1963 in Lubbock, Texas.

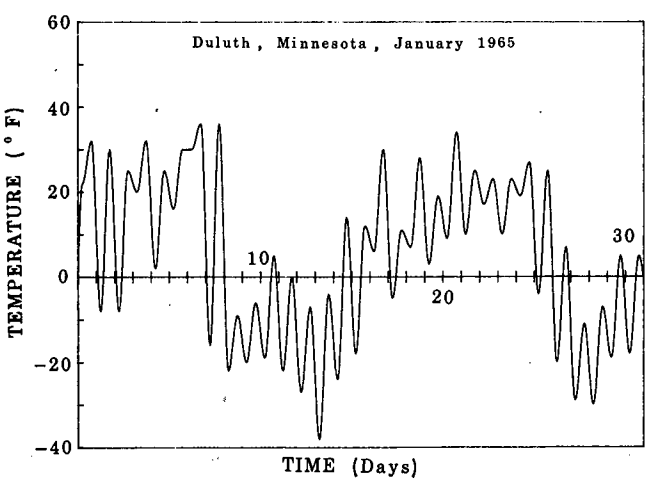

Figure A-18. Time-temperature record for January 1965 in Duluth, Minnesota.

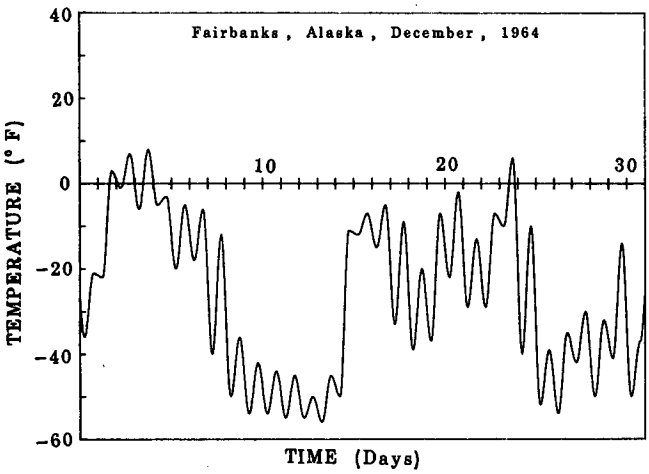

Figure A-19. Time-temperature record for December 1964 in Fairbanks, Alaska.

tier states and some mountainous regions. Here the overnight lows and daily highs are lower and may continue for 1 or 2 weeks. The Fairbanks record is extreme in that it is extremely low with little warming during the day, and it continues for several weeks.

ANALYSIS OF THE BEARING

Typical bridge bearings were analyzed for the five low-temperature records to obtain the through-thickness time-dependent temperature of the bearing. These calculations were performed for the given temperature records using one-dimensional through-thickness heat flow modeled by Eq. A-8 and previously illustrated in Figures A-10 and A-11. The calculations were quite complex because of the time-dependent air temperature, but they were of a well-documented (*11*) form. They employed a step-by-step time-dependent solution, where the temperature at time $t + \Delta t$ can be computed as a function of the temperature at time t by the equation

$$T(z, t + \Delta t) = T_0(t + \Delta t) + \frac{z}{h_{ct}} \sum_{n=0}^{\infty} \exp\left(\frac{-D_{th}(2n+1)^2\pi^2\,\Delta t)}{4h_{ct}}\right) \left\{\frac{\cos(2n+1)\pi z}{2h_{ct}} \times \left[\frac{2h_{ct}(-1)^n T_0(t+\Delta t)}{(2n+1)\pi} + \int_0^{h_{ct}} \frac{T(z', t)\cos(2n+1)\,z'}{2h_{ct}}\,dz'\right]\right\} \quad \text{(A-9)}$$

where T_0 is the air temperature and z is the through-thickness coordinate and h_{ct} is the total thickness of the bearing. The solution is an infinite series, but even under the most extreme conditions only the first few terms contribute to the solution. The integral had to be evaluated for each time step by approximate integration methods. This solution was programmed into a Hewlett Packard HP9816 computer and the time-dependent temperature profile was computed.

The computed temperatures were then used to estimate the temperature-dependent stiffness of the bearing and the force on its supporting bridge pier. In all, six different material behavior models (i.e., C-1, C-2, C-3, N-1, N-2, N-3) were used, based on different thermal stiffening models (see Fig. A-4) and three different crystallization models (see Fig. A-9). These combinations covered a wide range of low temperature behavior expected for neoprene and natural rubber bearings. The force transferred by the bridge bearing was then estimated and compared to the design force that was based on the estimated installation temperature of the bearing, predicted extreme low temperature, the expansion length, and the design shear modulus with 0.5 shear strain. When estimating the bridge expansion, both steel and concrete girders were examined.

Figure A-20 shows the typical time-dependent and temperature-dependent bearing force for a bearing subjected to the 1963 Lubbock record. This analysis was based on a steel girder with a 180-ft expansion length resting on a bearing with 2.5 in. total elastomer thickness, installed at 80°F. The response to the Lubbock record was not affected by thermal stiffening, but was influenced by crystallization resistance. Elastomers with high resistance to low temperature crystallization (model C-1 or N-1) showed no significant increase in bearing force over the design value, but those with low resistance (model C-3 or N-3) experienced stress levels as large as 8 times the design value. This is surprising because Texas is not regarded as a cold climate, but it illustrates two important observations. First, the behavior shown in Figure A-20 is a potential problem for climates that have relatively cool nights but warm days. Crystallization is time-dependent and temperature-dependent, because the bearing gets stiffer with time and its most rapid rate of stiffening occurs at a relatively high temperature (approximately 10°F or −12°C). The bearing thaws from these temperatures, but thawing requires time and does not start until the bearing is heated more than 27°F (15°C) above the crystallization temperature. Therefore, the bearing is consistently stiffer when the bridge is elongating due to rising temperature than when it is shortening due to falling temperatures, and the growth in bearing forces shown in Figure A-20 will occur.

However, while the growth phenomenon is realistic, the degree of it shown in Figure A-20 is probably excessive. The mathematical model included the thawing action of the rubber,

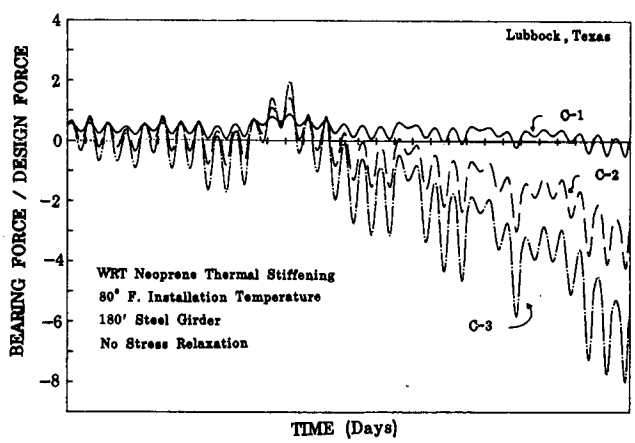

Figure A-20. Normalized bearing force for a 2.5-in. elastomeric bearing subjected to the Lubbock temperature record.

but after the bearing has thawed, the excess stress will begin to relax through a stress relaxation process. Stress relaxation is a complex phenomenon that is not included in Figure A-20. Only limited experimental data are available for estimating the rate of stress relaxation, but Meinecke (*14*) has proposed a mathematical model for creep and stress relaxation. This model combines a Voigt solid with a Maxwell viscous fluid. Four parameters are required by the model, and they were estimated from the results of compression creep tests and other typical test results. There is clearly considerable scatter in these parameters, but Figure A-21 shows a modified version of Figure A-20 with stress relaxation included. Stress relaxation clearly reduces the extreme forces noted in Figure A-20, but forces on the order of 2 to 3 times the design force must still be expected if an elastomer with poor crystallization properties (i.e., C-3 or N-3) is used. Note that all the anlayses show that several days are required for the crystallization effects to become apparent. This time is required because crystallization prior to the first day is not considered.

The material used in the bridge girder also affects the force response. Steel conducts heat quickly, and there is usually only a slight difference between air temperature and the temperature of the girder. Reinforced or prestressed concrete usually has a large thermal mass, and there may be considerable lag between air temperature and girder temperature. Figure A-22 illustrates this temperature lag. It shows the average temperature of the concrete girder with an 8-in. average concrete thickness as compared to air temperature. The concrete girder reduces the extreme temperatures by approximately 8°F and also introduces a time lag of several hours. This changes the bearing load history somewhat, but it does not have a great impact on the maximum forces and deformations experienced by the bearing, and so no separate time history calculations are shown for the concrete girders. Figures A-23, A-24, and A-25 show the time history records for the Colorado Springs, Albany, and Duluth temperature records, respectively. These time history curves show that low temperature crystallization is important for all cases since elastomers with low crystallization resistance (Model C-3) experienced bearing forces that are approximately three times the design values. Elastomers with intermediate crystallization re-

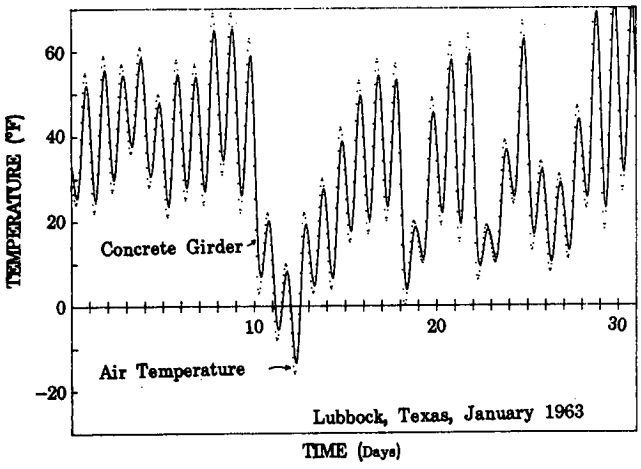

Figure A-22. Comparison of the air temperature with the average temperature of a concrete girder with the Lubbock record.

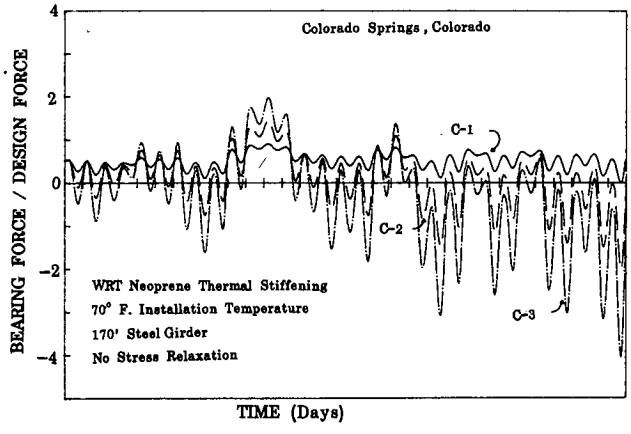

Figure A-23. Normalized bearing force for a 2.5-in. elastomeric bearing subjected to the Colorado Springs temperature record.

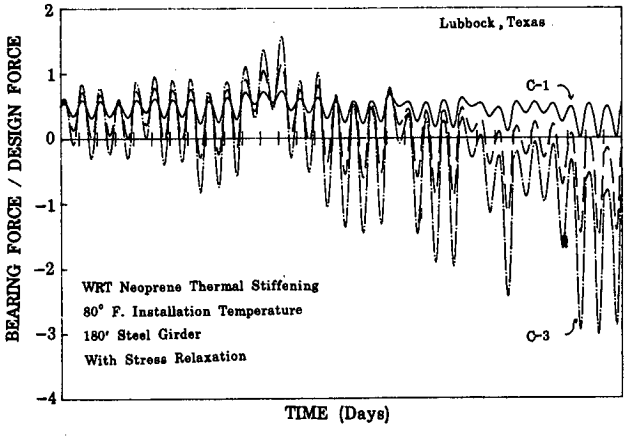

Figure A-21. Normalized bearing force for a 2.5-in. elastomeric bearing subjected to the Lubbock temperature record with stress relaxation included.

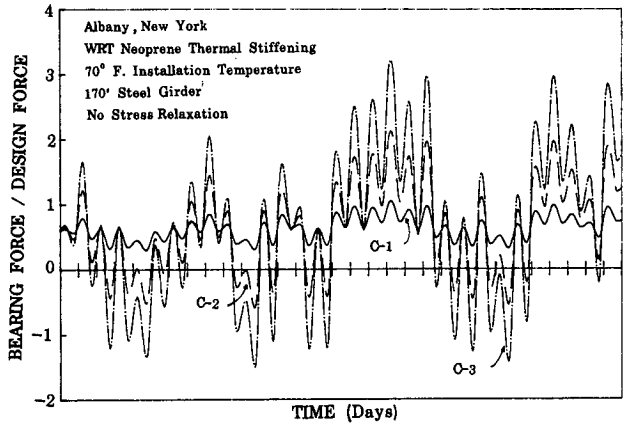

Figure A-24. Normalized bearing force for a 2.5-in. elastomeric bearing subjected to the Albany temperature record.

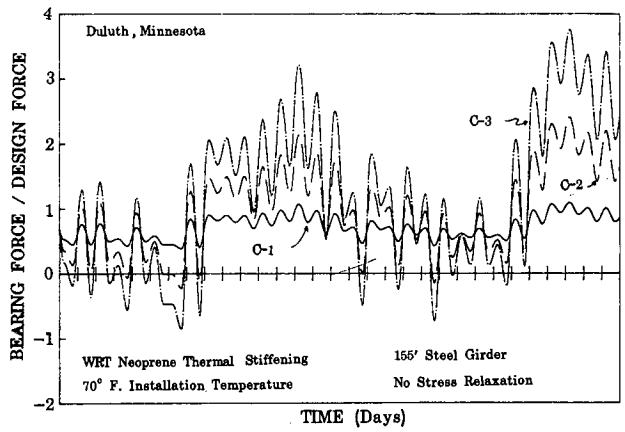

Figure A-25. Normalized bearing force for a 2.5-in. elastomeric bearing subjected to the Duluth temperature record.

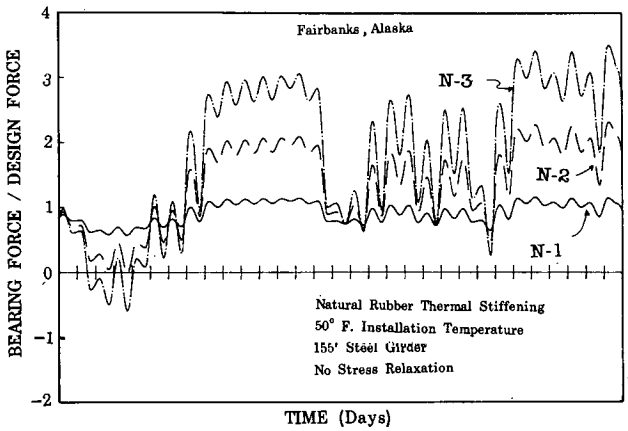

Figure A-26. Normalized bearing force for a 2.5-in. elastomeric bearing subjected to the Fairbanks temperature record.

sistance experience force levels one to two times the design value. Stress relaxation is not included in these figures, and it would have very little impact on the results for the Duluth and Albany records because they experience few thawing cycles. It does have some impact on the Colorado Springs results, but it is much smaller than that noted for Lubbock since daily warming cycles were smaller. Thermal stiffening has virtually no impact on the Albany and Colorado Springs results. It is of increasing importance for the Duluth record, because −35°F (−37°C) is near the glass transition of polychloroprene; however, it is still less significant than crystallization.

Figure A-26 shows the force history for a typical bearing subjected to the Fairbanks temperature record. Response is dominated by thermal stiffening, and the figure shows only the response with the natural rubber thermal stiffening model (see Fig. A-4). It is not greatly affected by low temperature crystallization. For bearings based on WRT neoprene (Model C-1) forces several hundred times the design value were predicted and are not shown. Crystallization is still important, in that it influenced the response of even the highly resistant natural rubber (Model N-3), but −56°F (−49°C) represents a temperature range that is clearly approaching the lower limits of suitability for all elastomeric bearings.

The foregoing figures all showed the predicted response for modest-sized bearings. Thick bearings have somewhat different responses. Large thick bearings with sound edge cover change temperature more slowly than smaller bearings, and they may not feel the extreme short time variations in temperature which may occur. This may reduce the force levels somewhat, but it also introduces potential problems. For example, a sudden warming trend may cause very large forces with a very thick bearing and may negate any benefits noted on the cooling cycle. Therefore, it appears to be of questionable wisdom to try to use this delay in practice.

SUMMARY AND CONCLUSIONS

In this appendix, the best available data on low temperature behavior were presented and discussed. A mathematical model of crystallization and thermal stiffening was developed and used to analyze bearing response. The results are necessarily approximate, because very limited experimental data are available. However, within these limitations several important conclusions and recommendations can be made.

1. Crystallization appears to be a problem for any temperature lower than approximately 32°F or 0°C. The rate at which it happens depends on temperature, and it occurs fastest at temperatures around 10°F (−12°C). It has been suggested that low temperature crystallization is primarily a problem of polychloroprene (*3*), but the available data (*6*) indicate that some natural rubber compounds also crystallize quite rapidly while others are highly resistant to it. WRT neoprene appears to have much higher crystallization resistance than type W neoprene. In most parts of the United States, elastomers with low resistance (similar to model C-3) may experience bearing forces that are three to four times the design force, and those with high crystallization resistance should experience forces quite close to the design values.

2. Thermal stiffening may be a serious problem for Alaska, much of Canada, and limited parts of the continental United States. Neoprene becomes extremely stiff and approaches a glass transition at approximately −40°F (−40°C) and the best available data suggest that natural rubber approaches a glass transition at approximately −67°F (−55°C). At these temperatures bearing forces that are many times the design value may be attained, and an elastomer should only be used if its second order transition behavior is proven by test to be acceptable.

3. Tests required by codes and specifications do not appear to be particularly relevant to crystallization or thermal stiffening behavior of bearings in service. The ASTM standard D4014 (*69*) appears to be the most useful, because it separates elastomers into several low temperature grades according to their performance in compression set and hardness tests at different temperatures. Bearing stiffness at low temperature is the most important measure of serviceability of the bearing, but unfortunately the only standard tests (compression set, hardness, and brittleness) are not good indicators of it. Thus, modification of the ASTM standard to include a stiffness test is desirable.

4. Several important observations were made based on the crystallization models and thermal stiffening models used in the

analyses of this chapter. Figures A-4 and A-9 show that these models cover the range of observed experimental behavior but that there is considerable scatter. However, correlating these results with the standard ASTM grades (*69*) is useful. The correlation is not precise, but the chloroprenes which approximated crystallization model C-3 generally failed to satisfy grade 2 or 3 criteria or satisfied them only with difficulty. Those which approximated model C-1 easily satisfied grade 3 requirements, and probably would satisfy grade 5.

5. Finally, it should be noted that low temperature behavior is both an important and overstated concern. It is important because with poor low temperature crystallization resistance, bearings can easily develop loads that are several times the design values. This could cause considerable damage to the structure. Further, thermal stiffening may cause a much larger effect in extreme climates. However, the problem may be overstated since a properly designed and tested elastomer can avoid both of these problems, and there is evidence that both neoprene and natural rubber can be used. It is logical to ask why, if there is a potential problem, there have not been a large number of failures observed. There are several reasons. First, it is only in recent years that any effort has been made in the United States to compute the bearing stiffness and the resulting design forces on the piers and superstructure. Thus, in the vast majority of existing bridges, these components are much stronger than necessary to carry the bearing forces. Second, many (perhaps most) of the existing bearings may have good low temperature properties. However, continual economic changes in the industry mean that it is necessary to assure that bearings provided today and in the future are of adequate quality for the more sophisticated designs. Finally, bearings that are overloaded will frequently slip or experience relaxation before damage occurs. These phenomena were not included in the analysis because insufficient data are available to consider them reliably. Clearly more test data are needed.

TENTATIVE DESIGN RECOMMENDATIONS

Based on the above conclusions and the analyses that preceded them, a series of tentative design recommendations are presented. They are tentative because the analyses were approximate and based on limited data. It is first recommended that the North American continent be divided into 3 regions. Region I would be the areas where the temperature never falls low enough to cause serious problems for elastomeric bearings. Such areas as the southern Pacific Coast, Gulf Coast, and Hawaii would fall in Region I. Possible criteria for inclusion in this region would be that the temperature never falls below 0°F (−18°C) and that it does not drop below 25°F for more than 6 hours duration at any one time or for shorter periods on more than 3 consecutive days. Region II would include most of the remaining United States. It could be defined as all areas that do not qualify for Region I and have extreme low temperatures not lower than −30°F (−35°C). Response of bearings in Region II would be influenced by low temperature crystallization but not thermal stiffening. Region III would consist of most of Alaska and Canada, and the portions of the United States that do not qualify for Regions I and II.

A basic design force must be derived for each region. The design force for an individual bearing is:

$$H = AG\,\gamma_s \tag{A-10}$$

where A is the gross plan area of the bearing and G is the shear modulus at 70°F (21°C) as defined by AASHTO Method A or by test results. The shear strain γ_s should be limited to less than 0.5 and be defined by

$$\gamma_s = \frac{\Delta T \alpha l}{h_{rt}} \tag{A-11}$$

where α is the coefficient of thermal expansion of the bridge, l is the expansion length, and h_{rt} is the total elastomer thickness. The temperature increment, ΔT, shall be defined as the difference between the extreme air temperature of the region and the extreme installation temperature of the girders. For example, if the bridge girders are to be installed in October, ΔT could be the larger of the difference between the historic low temperature for October and the historic high for the area, or the difference between the historic high temperature for October and the historic low for the area.

For Eq. A-10 to provide the necessary safety and serviceability in the field, either G for the chosen elastomer must not increase excessively, or the structure must be able to resist forces several times larger than those predicted by Eq. A-10. Thus, in Region I, grade 2 elastomers would always be acceptable, and grade 1 elastomers could only be used if the structure could resist bearing forces at least three times the design value multiplied by an appropriate load factor. In Region II, the use of grades 2, 3, and 5 would require that the structure could withstand forces 4, 3, and 2 times the design value multiplied by an appropriate load factor. Region III should always require the use of grade 5 elastomers and, in addition, tests should be required to assure that the glass transistion is at least 5°F below the historic low temperature for the region. The structure should be able to resist total bearing forces of two times the design force with an appropriate load factor.

The above structural design forces may be reduced if a reliable mechanism which allows slip, such as a stainless steel-PTFE slider, is provided, and a lower grade elastomer may be used for Regions I and II under these conditions.

Low temperature stiffening is an important characteristic and needs to be addressed more directly than it is now. First, the certification requirements for the various elastomer grades should include a test to measure low temperature stiffness itself, rather than relying on indirect indicators such as compression set. Second, the measures needed to achieve satisfactory stiffness should be examined. While it is possible to design a compound that has either excellent low temperature performance or excellent physical properties (such as tensile strength) at normal temperatures, test data show that achieving both together is very difficult. In view of the importance of low temperature stiffening, a slight reduction in the physical property requirements could be considered. This should only be done in cases where it is impossible to produce a compound that will meet both objectives, and even then care should be taken not to open up the possibility of new problems such as excessive creep.

APPENDIX B

COMPRESSION

INTRODUCTION

The behavior of bearings subjected to compression was investigated using analysis and testing. This appendix describes response to pure compression, while rotation and eccentric compression are described separately in Appendix C, even though in many tests one bearing was subjected to concentric and eccentric compression in turn. Analysis is treated first so that when the test results are presented, a theoretical basis with which to compare them already exists. Previous analyses are reviewed in more detail in Ref. *3*.

LINEAR ANALYSIS

GENERAL

In classical elasticity theory, deformations are assumed to be small, so that negligible errors are introduced by assuming that strains are linearly related to displacements and that the equilibrium equations can be written in the undeformed geometry. An elastomeric bearing in service undergoes significant deformations and so neither of these assumptions is strictly true, but because of the extreme difficulties of performing any analysis which models the true behavior more closely, analyses (*15, 16, 17, 18*) based on classical theories have been widely used. Efforts have been made (*19, 20*) to incorporate the effects of large deflections by modifying the end results and, while they appear to provide improvement, these analyses are not rigorous.

Studies based on complete nonlinear finite element formulations are presently under way (*22*). Discrete analysis, in which each elastomer or steel layer is broken down into a number of separate elements, proves prohibitively expensive. Replacing the true layered medium with a homogeneous one that has equivalent properties shows promise in predicting overall behavior, but is necessarily unable to provide detailed information about conditions at the critical steel-elastomer interface.

The following discussion describes typical closed-form solutions, their shortcomings, solutions for a bearing with a central hole, and results of a linear finite element analysis.

Elastic Solutions

A number of investigators (*3, 15, 16, 17*) have developed closed-form load-deflection relationships for reinforced bearing layers. They have all assumed that the reinforcement is inextensible and that the elastomer bulges parabolically, and they have all considered the case of completely incompressible elastomer. Only Conversy (*16*) provided solutions that incorporate finite compressibility. The solutions can be expressed in the form

$$\sigma_c = E_c \epsilon_c = E f_c \epsilon_c \qquad \text{(B-1a)}$$

where

$$f_c = A_c + B_c S^2$$
$$S = \text{shape factor} \qquad \text{(B-1b)}$$
$$A_c \text{ and } B_c = \text{dimensionless constants}$$

and

$$\sigma_c = P/A \qquad \text{(B-1c)}$$

Conversy (*16*) and Rejcha (*18*) treated the problem in a single step and obtained $A_c = 0$, which is clearly incorrect when S tends to zero. Gent (*15*) treated it in two steps. In the first, the bearing is compressed while the elastomer is free to expand laterally, and in the second, shearing stresses are imposed at the elastomer-steel interface to restore the lateral displacements, while the vertical displacements remain fixed. The resulting B_c coefficients are identical to Conversy's, and for rectangular bearings with sides L and W, are plotted against L/W in Figure B-1 as a solid line. Gent gives $B_c = 2.0$ for a circle. Gent's (*15*) value for A_c varies from 1.0 to 1.33, depending on plan shape, so, for practical shape factors of 5 or more, Eq. B-1b shows that the coefficient B_c is much more important.

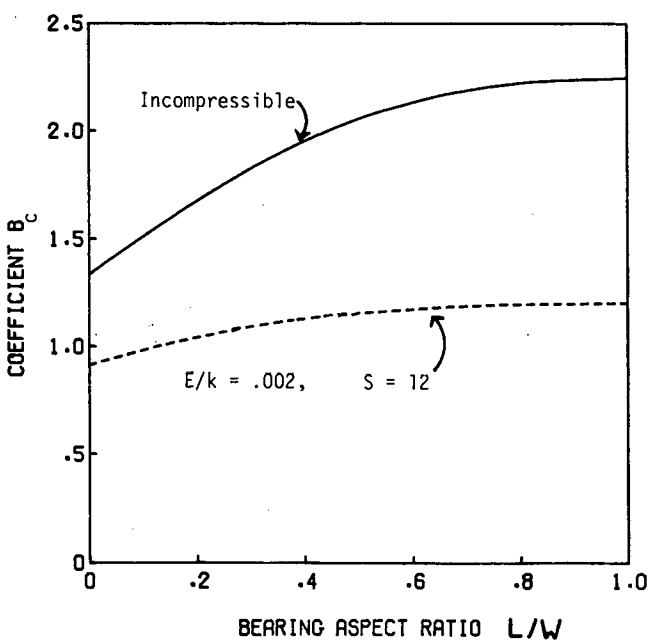

Figure B-1. Variation of compressive stiffness coefficient B_c *with bearing aspect ratio.*

It should be noted that arbitrarily choosing the bulged shape of the elastomer to be a parabola means that some equations of equilibrium cannot be satisfied, and that the foregoing equations cannot be exact. The fact that they provide reasonable solutions shows that the chosen bulged shape is close enough to the true one to cause only minor, local violations of equilibrium.

The bulk modulus of the elastomer has a significant influence on compression stiffness for bearings with large shape factors. The coefficient B_c becomes smaller, by an amount which depends both on S and on E/K. (E and K are the Young's modulus and bulk modulus.) Values of B_c derived from (*16*) for the most extreme case considered ($S = 12$ and $E/K = 0.002$) are shown in Figure B-1 as a dashed line. Gent (*10*) suggested accounting for bulk modulus by the approximate formula

$$\frac{1}{E'_c} = \frac{1}{E_c} + \frac{1}{K} \tag{B-2a}$$

where E'_c and E_c are the effective compression moduli including and excluding the influence of bulk compressibility. Conversy's more rigorous analysis can be simplified to give

$$\frac{1}{E'_c} = \frac{1}{E_c} + \frac{1}{c_{kc}K} = \frac{1}{E}\frac{1}{f_c} + \frac{1}{c_{kc}}\frac{E}{K} \tag{B-2b}$$

where c_{kc} is a constant. For the range investigated ($3 \leq S \leq 12$, $0 \leq E/K \leq 0.002$ and $0.001 \leq L/W \leq 2.0$), c_{kc} varied only from 0.728 to 0.838. A value of 0.75 represents practical shaped bearings very well and, if used in Eq. B-2b, provides a slight improvement on Eq. B-2A. The bulk modulus of an elastomer is not easy to measure (*24*), but E/K is commonly taken as 0.001 for bridge bearing materials.

The strain in the elastomer consists of a shear component plus a small bulk compression. The shear strain is largest at the elastomer-steel interface, and it increases linearly towards the outer edge of the bearing (*15*). There it falls sharply to zero in order to satisfy the condition that there be no shear stress on the vertical free elastomer surface. The maximum shear strain is given by

$$\gamma_c = C_c S \epsilon_c \tag{B-3a}$$

where for rectangular bearings

$$C_c = \frac{48}{\pi^2}\left(1 + \frac{L}{W}\right)\sum \frac{1}{n^2 R^2_n}\left(1 - \operatorname{sech}\frac{n\pi W}{2L}R_n\right) \tag{B-3b}$$

and

$$R^2_n = 1 + \frac{4E}{K}\frac{L}{(n\pi h_r)^2} \tag{B-3c}$$

Figure B-2 shows, for the incompressible case, the variation of C_c with aspect ratio in rectangular bearings. For a circular bearing, $C_c = 6.0$.

Gent's (*15*) analysis was modified to include the effects of a hole, giving

$$f_c = 1 + 2S^2 f(\zeta) \tag{B-4a}$$

where

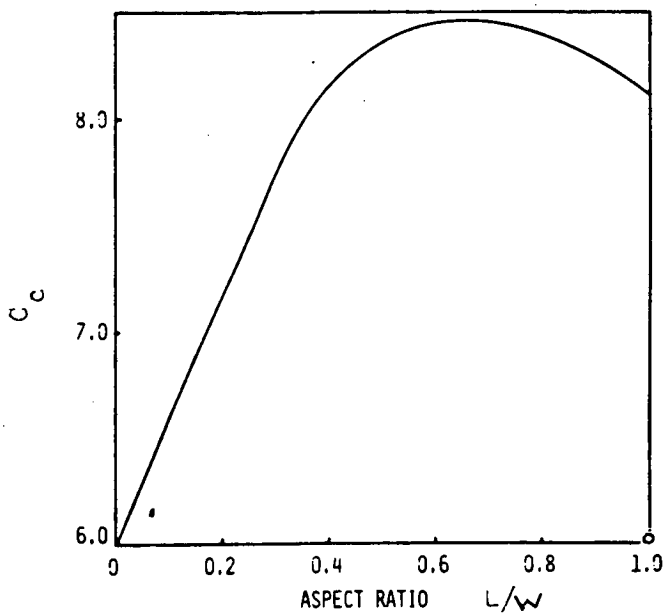

Figure B-2. Shear strain coefficient C_c as a function of aspect ratio.

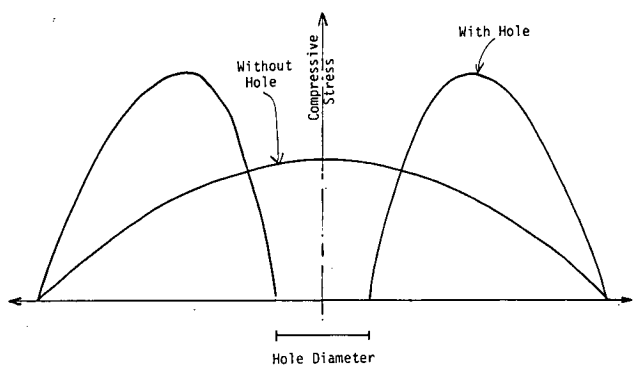

Figure B-3. Distribution of compressive stress in a circular bearing with and without a hole.

$$f(\zeta) = \frac{1 - \zeta^4 + 4\zeta \ln \zeta}{(1 - \zeta^2)(1 - \zeta)^2} \tag{B-4b}$$

and

$$\zeta = \frac{\text{hole diameter}}{\text{bearing diameter}} \tag{B-4c}$$

Where ζ approaches zero, $f(\zeta)$ approaches 1.0, so Eq. B-4a gives the same value as Gent had derived for the bearing with no hole, as it should. The theory suggests that the presence of a hole may significantly change the stress distribution within the bearing as shown in Figure B-3. In Eq. B-4a the free surface around the hole should be included in the definition of S. Equation B-4b is plotted in Figure B-4 and shows that treating $f(\zeta)$

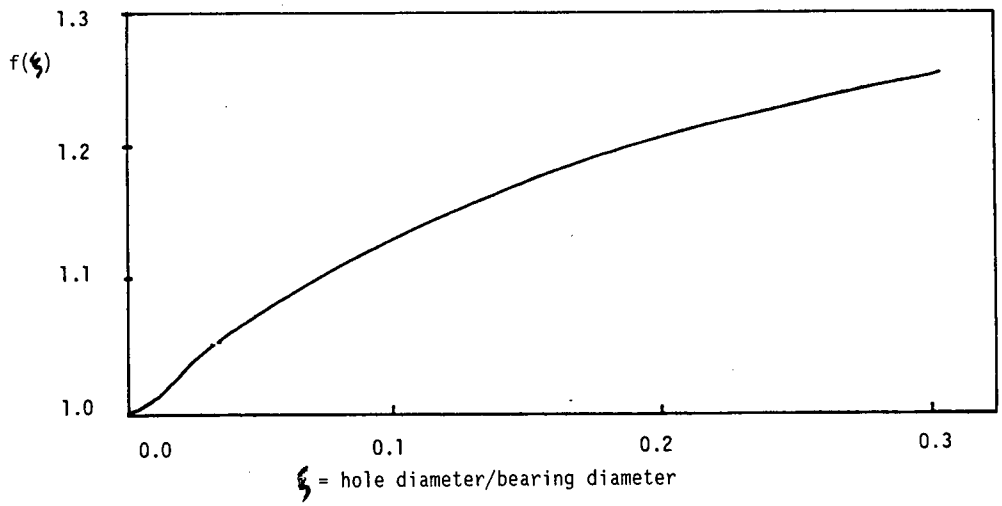

Figure B-4. Compressive stiffness coefficient for a circular bearing with a hole.

as 1.0 in the interests of simplicity is a slightly conservative procedure. The error for practical bearing sizes is likely to be less than 10 percent.

Gent (*23*) conducted experiments on circular bearings with holes, for values of ⅛, ¼, and ½. He found that Eq. B-4a with $f(\zeta) = 1.0$ gave reasonable correlation with the measured stiffness, provided again that the free surface around the hole was included in the definition of S.

Finite Element Analyses

As a check on the accuracy and validity of the foregoing closed-form elasticity calculations, finite element analyses were performed on a sample circular bearing layer both with and without a hole. The program, AXISOL, (*25*) is based on conventional elasticity and small deformations. Symmetry was used to reduce the size of the problem, so the analysis was performed on only one-half of the thickness of the real elastomer layer. Axisymmetric elements were used in a mesh of 6 × 24 elements, and their aspect ratio was restricted to 2:1 for accuracy. A shape factor of 2.0 was used, because a larger one would have required more elements or more elongated element shapes. The steel reinforcement was replaced by a rigid boundary.

With no hole and a Poisson's ratio of 0.49975 (i.e., $E/K = 0.0015$), the compressive stiffness was found to be 0.95 $(1 + 2S^2)$, whereas Eq. B-2b gives 0.98 $(1 + 2S^2)$ for the same conditions. This close agreement lends support to Eq. B-2b, provided the materials behave in the linear elastic manner assumed.

For the case with a hole, two runs were done with different values of E/K which bracketed the values for the real material. The results are given in Table B-1. Also shown for comparison are values derived using Eq. B-2b, using $c_{kc} = 0.75$ and $c_{kc} = 1.0$. It should be recalled that Gent suggested the formula with $c_{kc} = 1.0$ but provided no rigorous proof, and that the $c_{kc} = 0.75$ value was derived from more rigorous theoretical data on rectangular bearings rather than the circular bearing analyzed here. Furthermore, neither bearing had holes. In both runs, the finite element value for f_c was about 10 percent lower than that given by Eq. B-2b.

Table B-1. Compression stiffness: comparison of predicted values of f_c using finite element analysis and Eq. B-2b (8-in. diameter × 0.4-in. thick elastomer layer, 1-in. dia. hole).

Run Number	1	2
Poisson's Ratio	0.49995	0.490
E/K	0.0003	0.06
f_c, Finite Element	0.89 $(1+2S^2)$	0.26$(1+2S^2)$
f_c, Eqn. B-2b (c_{kc} = 1.0)	0.9884 $(1+2S^2)$	0.2979 $(1+2S^2)$
f_c, Eqn. B-2b (c_{kc} = 0.75)	0.9845 $(1+2S^2)$	0.2414 $(1+2S^2)$

Similar analyses were done using the general purpose Finite Element Program STRUDL (*26*) on a 2:1 rectangular bearing with a central hole. For E/K values of 0.006, 0.0015, and 0.0006, the ratios of the computer-predicted stiffnesses to those of Eq. B-2b (with $c_{kc} = 0.75$) were 0.9473, 1.0269, and 2.3433. The first two values show the same pattern as did the AXISOL analyses, namely that the finite element value for f_c was smaller than the one given by Eq. B-2b for high E/K, but was larger for lower E/K. In both cases the agreement was good. The last figure is seriously in error, and is believed to be caused by numerical problems associated with the size of the model (2,500 nodes) and the fact that Poisson's ratio was so close to 0.50.

Thus the finite element analyses provided verification that Eq. B-2b, with $c_{kc} = 0.75$, simulates reasonably well the influence of bulk modulus on the compression stiffness. The differences are on the order of 5 percent when $E/K = 0.0015$, both with and without holes in the bearing.

APPROXIMATE THEORIES

Gent (*10*) presented an alternative, approximate expression for compression stiffness, namely

$$f_c = 1 + 2k\,S^2 \qquad \text{(B-5)}$$

It was derived from experimental data on natural rubber, and k was found to vary with hardness, falling from 0.80 to 0.55 for rubbers of 45 and 65 degrees IRHD. (The International Rubber Hardness Degree scale is simply an alternative to the Shore hardness scale for elastomers. It is more widely used in Europe, and for practical purposes the two scales are identical over the range of bridge bearing elastomers.) The reasons underlying the need for the correction factor k were not clear at the time, but were thought to involve at least the effects of bulk compressibility. This expression has been used in specifications (*27*) for a number of years.

NONLINEAR BEHAVIOR

The above theories do not account for nonlinearities, which are clearly shown by test results to be present. Previous researchers' efforts to include geometric nonlinearity are reviewed in Ref. *3*.

An alternative, and reasonably simple, approach would be to assume that incremental stress and strain, based on the instantaneous geometry, are related by elastic constants E and G which are independent of strain. If nominal stress and strain are defined by

$$\sigma_c = \frac{P}{A_0} \tag{B-6a}$$

$$\epsilon_c = \frac{\Delta_c}{h_{r0}} \quad \text{(positive in compression)} \tag{B-6b}$$

where h_{r0} = original elastomer layer thickness, and Δ_c = compressive deflection. Then the assumption of incompressibility leads to

$$h_r = \text{instantaneous elastomer thickness} = h_{r0}\,(1 - \epsilon_c) \tag{B-6c}$$

$$A = \text{instantaneous average plan area} = \frac{A_0}{(1 - \epsilon_c)} \tag{B-6d}$$

$$S = \text{instantaneous shape factor} = \frac{S_0}{(1 - \epsilon_c)^{1.5}} \tag{B-6e}$$

Finite increments of stress and strain are then related by

$$\Delta\sigma_c = E\,(A_c + B_c S^2)\,\frac{\Delta\epsilon_c}{(1 - \epsilon_c)^2} \tag{B-7}$$

If A_c is taken as zero for simplicity, infinitesimal load increments give a tangent modulus, in terms of nominal stress and strain, of

$$E_c = \frac{d\sigma_c}{d\epsilon_c} = E\,B_c\,S^2{}_0\,(1 - \epsilon_c)^5 \tag{B-8a}$$

leading to

$$\sigma_c = \frac{EB_c\,S^2{}_0}{4}\,\{\,(1 - \epsilon_c)^{-4} - 1)\,\} \tag{B-8b}$$

Attempts were made to correlate this equation with experimental data, but the fit was not very good. Matching a nonlinear equation to an experimental stress-strain curve is made difficult by problems of establishing a zero for strain and by the initial "bedding in" of the bearing. Attempts were made to fit an equation of the form

$$\sigma_c = \frac{\text{constant}}{n}\,[\,(1 - \epsilon_c)^{-n} - 1] \tag{B-9}$$

to experimental curves using three points, the lowest of which was chosen arbitrarily to be 200 psi. It was found that the best fit for most test results occurred with n values greater than 4. For example, $n = 10$ was found to agree very closely with the data from tests on the 11.33 in. × 5.66 in. bearings used in the buckling experiments described in Appendix E. For this bearing shape, like many others, Eq. B-8b was therefore insufficiently nonlinear. No obvious rationale exists for the choice $n = 10$, but it indicates that even the incremental (instantaneous) stress and strain must be linked by a stiffening relationship.

DEFORMATIONS AND STRESSES IN THE ELASTOMER

The linear closed-form analyses are based on simplifying assumptions, so they will not produce exact values for stresses in the elastomer any more than they do for load-deformation relationships. Comparison with the finite element analysis of the circular bearing is illuminating. Figure B-5 shows the outer part of the mesh in its deformed state, and significant vertical deformations can be seen. Figure B-6 shows the radial displacement profile across the diameter, while Figures B-7 and B-8 show the distribution of shear and direct stresses. In each figure it is clear that conditions at the outer edge are not a simple extrapolation of the parabolic bulging found in the interior of the bearing. The vertical stress is tensile, and the shearing stress and radial displacement depart significantly from the otherwise linear distributions, none of which are predicted by the closed-form analyses. The effects appear to be sufficiently localized that by about half-way into the center of the bearing, conditions are very close to those predicted by the closed-form analyses. Unfortunately, the response at the outer edge of the bearing is

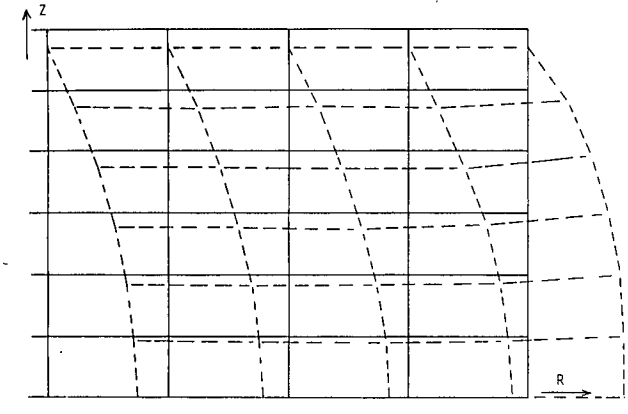

Figure B-5. Undeformed and deformed grid-section through outer part of circular bearing.

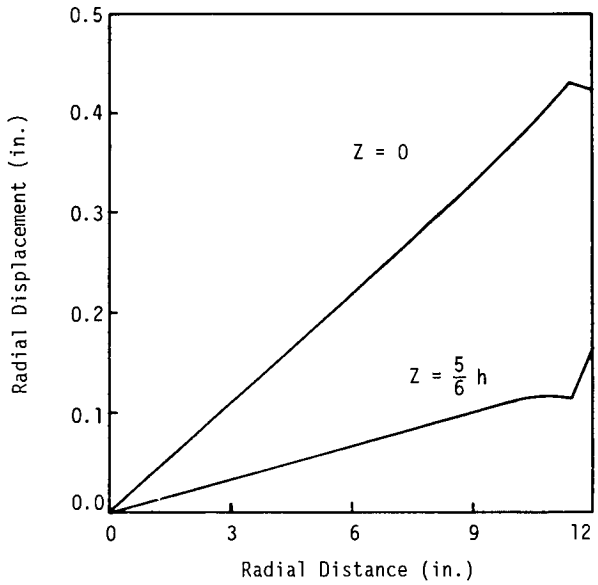

Figure B-6. Computed radial displacements vs. radial distance for a 24-in. diameter bearing.

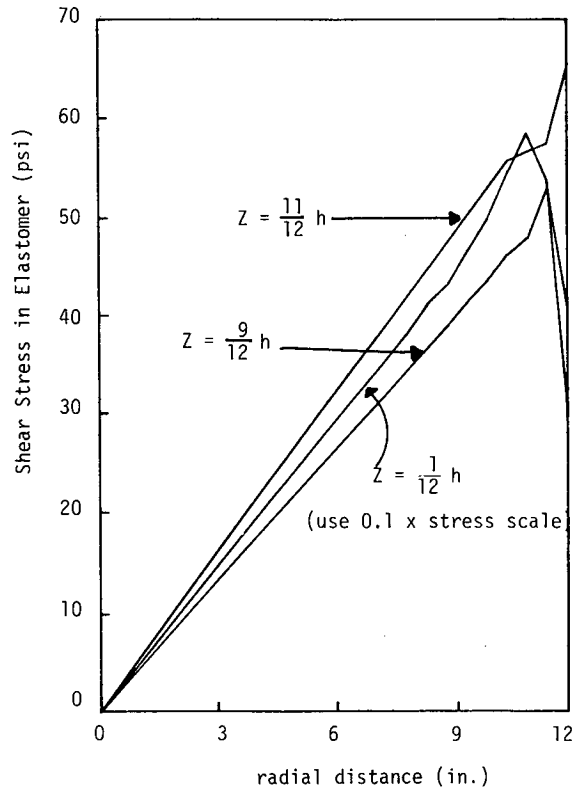

Figure B-7. Computed elastomer shear stress vs. radial distance for a 24-in. diameter bearing.

the largest and so is the most important, but it is also subject to the greatest uncertainty. The finite element procedure is itself far from perfect (it is numerically sensitive because Poisson's ratio is so close to 0.5 and because the finite mesh size is incapable of detecting with any accuracy the shear stress singularity at the corner), but it demonstrates that conditions near the edge are not simple. The vertical tension is noteworthy. It can be shown using simple arguments and incompressible elastomer that bulging will lead to vertical tension strain at the edge when the average compressive strain, ϵ_c, exceeds $\frac{1}{6}S^2$, where S is the shape factor. For a typical bearing in practice S might be 5 and ϵ_c 5 percent, so the outer surface will be in tension both vertically and in the hoop direction. This finding is in qualitative agreement with the finite element results and with the horizontal splits at the crest of the bulge observed in both the laboratory and the field. It is not predicted by the closed-form methods because they do not include geometric nonlinearity.

Perhaps the most serious concern is that none of the approaches is able to predict the true stress or deformation field where it matters most—at the corner of the elastomer. The implication for design is that one of two approaches must be adopted. The first would require a detailed stress analysis, capable of accounting for the stress singularity at the corner, coupled to a three-dimensional failure theory for elastomer (analogous to, say, von Mises' theory for metals), which incorporates large deflections. This could be thought of as a "microscopic" approach. The second, "macroscopic," approach would be to identify on a more general level those conditions that give rise to failure in the elastomer and to construct a failure criterion from them without regard to detailed stresses or strains. Although the requirements in most codes (*27, 28, 29, 30*) today give the appearance of falling into the first category, they in fact do not, because they depend on inadequate analysis and an unproven failure theory. By contrast the German regulations (*31*) have opted for the macroscopic approach.

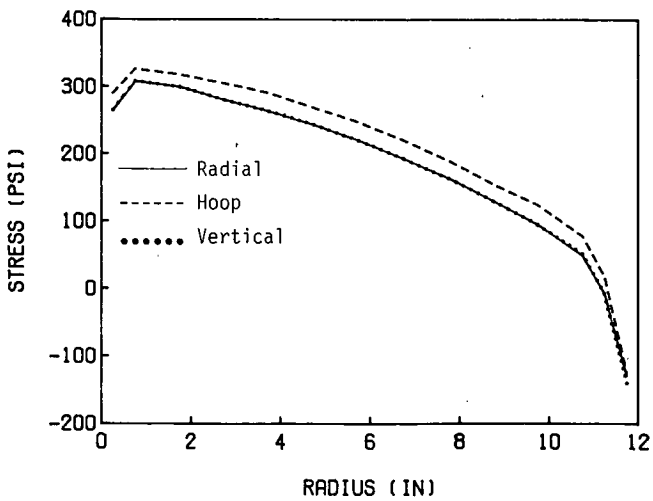

Figure B-8. Computed elastomer stresses in a 12-in. diameter circular bearing.

STRESSES IN THE REINFORCEMENT

In steel-reinforced bearings under service loads the steel behaves elastically, so its deformations are much smaller than those of the elastomer. Thus it is acceptable to analyze the

stresses in the elastomer assuming that the bonded boundary is perfectly rigid, and then to analyze the steel stresses by applying to the plate the shears in the elastomer at the interface. This procedure has the advantages of simplicity and numerical stability.

It appears that the closed-form approaches could be used to give acceptable predictions for the stress in the steel. The theories are not exact. They tend to break down at the outside edges of the bearing, but this location is far from the center of the bearing where the maximum steel stress occur. Furthermore, the steel stress is an integration of the shear stress imposed by the elastomer and the integral is inherently less sensitive to local inaccuracies.

Closed-form expressions for maximum steel stress can be found for circular and long thin rectangular bearings. For practical shape factors of 5 and greater, the latter is given (*3*) by

$$\sigma_{s,\max} \doteq 1.5 \left(\frac{h_{r1} + h_{r2}}{2h_s}\right) \sigma_c \qquad \text{(B-10)}$$

where $\sigma_{s,\max}$ = maximum steel stress, $\sigma_c = (P/A_0)$, and h_{r1}, h_{r2} = elastomer layer thickness on each side of the reinforcement.

Steel stresses in a circular bearing have not previously been established. However, the assumptions of the closed-form theories lead to a shear stress imposed by the elastomer on the steel of

$$\tau_{rz} \doteq \frac{\sigma_c}{S} \frac{r}{R} \qquad \text{(B-11)}$$

for an incompressible elastomer and a shape factor greater than about 5. Then it can be shown (*32, 33*) that the vertical, hoop, and radial stresses in the steel plate are

$$\tau_{zz} = 2\,\sigma_c \left(1 - \frac{r^2}{R^2}\right) \qquad \text{(B-12a)}$$

$$\tau_{\theta\theta} = \sigma_c \left(\frac{h_{r1} + h_{r2}}{2h_s}\right)\left(\frac{3 + \nu_s}{2}\right) \left\{1 - \left(\frac{1 + 3\,\nu_s}{3 + \nu_s}\right)\frac{r^2}{R^2}\right\} \qquad \text{(B-12b)}$$

$$\tau_{rr} = \sigma_c \left(\frac{h_{r1} + h_{r2}}{2h_s}\right)\left(\frac{3 + \nu_s}{2}\right)\left(1 - \frac{r^2}{R^2}\right) \qquad \text{(B-12c)}$$

These are plotted in dimensionless form in Figure B-9 using a Poisson's ratio for steel of 0.3, and $h_{r1} = h_{r2} = 6h_s$. Yielding of the steel may be predicted by either the Tresca or von Mises criterion, which in this case both give the result

$$F_y = \sigma_c \left\{1.65\,\frac{(h_{r1} + h_{r2})}{2h_s} + 2\right\} \qquad \text{(B-13a)}$$

where F_y is the uniaxial yield strength of the steel required to prevent yield in the circular plates. This too is plotted in Figure B-9 as the "Equivalent Yield" stress. Its value is very similar to that for the infinite strip that is

$$F_y = \sigma_c \left\{1.50\,\frac{(h_{r1} + h_{r2})}{2h_s} + 1.5\right\} \qquad \text{(B-13b)}$$

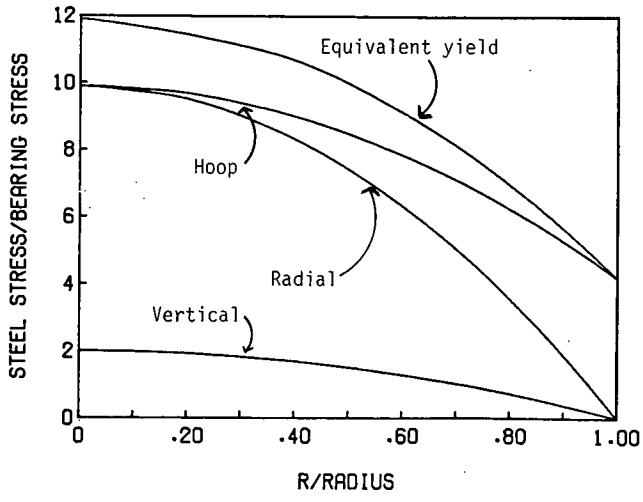

Figure B-9. Computed steel stresses in a circular bearing without a hole (absolute values shown).

The effects on the steel stress of a hole in the bearing were investigated in (*33*). Only circular bearings were considered, and closed-form expressions were checked against finite element analyses using Program AXISOL (*25*). The stresses in the steel were found to be dependent on the value of E/K (or ν_r) used for the elastomer, reflecting the fact that the elastomer stresses are themselves influenced by E/K. Without holes the finite element analyses gave stresses that had the same distribution but were smaller than those predicted by Eqs. B-12a–B-12c. They approached the closed-form predictions as Poisson's ratio approached 0.5.

Two conditions with holes were studied. In the first, only the steel had a hole in it. This is the condition that would arise when a manufacturer uses dowels to locate the reinforcing plates during molding, and later plugs the dowel hole with elastomer. In the second case the hole penetrated the whole bearing. The incompressible analysis for the first case leads to

$$\tau_{zz} = -2\,\sigma_c \left(1 - \frac{r^2}{R^2}\right) \qquad \text{(B-14a)}$$

$$\tau_{\theta\theta} = \left(\frac{3 + \nu_s}{2}\right)\left(\frac{h_{r1} + h_{r2}}{2h_s}\right) \sigma_c \left\{1 - \frac{r^2}{R^2}\frac{(1 - 3\,\nu_s)}{(3 + \nu_s)} + \zeta^2\left(1 + \frac{R^2}{r^2}\right)\right\} \qquad \text{(B-14b)}$$

$$\tau_{rr} = -\left(\frac{3 + \nu_s}{2}\right)\left(\frac{h_{r1} + h_{r2}}{2h_s}\right) \sigma_c \left\{\frac{r^2}{R^2} - \zeta^2\left(\frac{R^2}{r^2} - 1\right)\right\} \qquad \text{(B-14c)}$$

and

$$F_y = \tau_{\theta\theta} - \tau_{zz} \qquad \text{(B-14d)}$$

where ζ = hole diameter/bearing diameter.

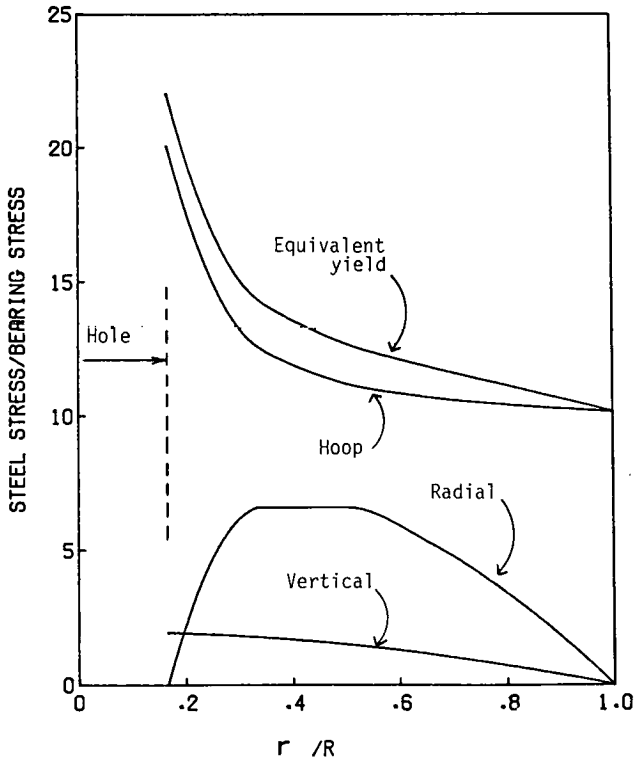

Figure B-10. Steel stesses in a circular bearing with a hole (absolute values shown).

These are shown in Figure B-10 for $\zeta = 1/6$, $h_{r1} = h_{r2} = 6h_s$, and $\nu_s = 0.3$. The finite element analyses again gave stresses which depended on E/K and approached the closed form ones as ν_r approached 0.5. The hoop stress, $\tau_{\theta\theta}$ appeared to be the most sensitive. The equivalent yield stress, F_y, was largest at the inner edge, at which point the agreement between the two solutions was close. There

$$\tau_{zz} = -2\,\sigma_c\,(1 - \zeta^2) \qquad \text{(B-15a)}$$

$$\tau_{\theta\theta} = \left(\frac{3 + \nu_s}{2}\right)\left(\frac{h_{r1} + h_{r2}}{2h_s}\right) \sigma_c \left\{2 + \zeta^2 \frac{(4 - 2\,\nu_s)}{(3 + \nu_s)}\right\} \qquad \text{(B-15b)}$$

For ζ values corresponding to typical dowel holes, $\zeta^2 << 1$ and can be neglected. So, for $\nu_s = 0.3$

$$F_y = \tau_{\theta\theta} - \tau_{zz} \doteq \sigma_c \left\{2 + 3.3 \frac{(h_{r1} + h_{r2})}{2h_s}\right\} \qquad \text{(B-15c)}$$

This is roughly double the value without a hole, and for small holes, it is nearly independent of hole size.

In the case of a hole through the whole bearing, satisfactory closed-form solutions could not be obtained, so finite element analyses were undertaken. They were found to be rather sensitive to E/K, or ν_r. As ν_r was increased up to 0.49995, they appeared to be converging to one solution, and the maximum steel stress was found about half way out from the inside edge. However, for $\nu_r \geq 0.49999$, numerical problems appeared to influence the solution, because the location of the maximum steel stress moved to the inside edge. For practical bridge bearing elastomers, $E/K = 0.001$ (so $\nu_r = 0.49983$), in which range the results are believed to be reliable. They showed that for all hole sizes, $\tau_{\theta\theta}$ and F_y were both smaller than their counterparts in the case of a hole in the steel alone.

Thus, for circular bearings, a conservative appraisal of the steel stresses under elastic conditions is given by using a stress concentration factor of 2, regardless of the hole size and whether it exists in the elastomer.

Finite element analysis was also carried out (*34*) on square and 2:1 rectangular bearings with and without holes, using STRUDL (*26*). In each case only one quadrant by half an elastomer layer thick of the bearing was analyzed with a basic mesh for the 2:1 rectangle of 12 × 24 elements in plan by 4 elements deep. Near holes, the mesh was refined, over a transition length of two-hole diameters, to elements of ¼ the linear dimensions of the standard ones. Poisson's ratio for the elastomer was taken as 0.49975 (i.e., $E/K = 0.0015$).

Despite the fine mesh, the stress distribution in the vicinity of the holes was not very smooth. The presence of the hole caused the largest increases in the tangential stress around the hole, and the largest of them occurred in the rectangular bearing with a central hole for the stress parallel to the short side, where the computed increase was 28 percent.

This value should be treated as approximate. This is partly because of the approximations inherent in the finite element method itself, which prevent it from giving exact response at a free edge (verified in this case by the fact that the normal stresses at the edge were in many cases not exactly zero). Further approximations are introduced because the stresses are only given at element centroids, and they must be extrapolated to give edge stresses. The 28 percent increase is well below the value found for the circular bearing, and so it is believed that the approximations led to an underestimate of the true steel stress.

For the square bearing the maximum computed stress increase over the case without holes was 21 percent. A square bearing might be expected to behave rather like a circular one, in which the increase in the circular bearing was on the order of a factor of 2.0.

In addition to direct tension, some bending was computed in the plates around the holes and, to a much smaller extent, at the bearing edge. It was extremely localized, disappearing by approximately half a hole diameter from the free surface of the hole, and it is not clear whether it was real or just an idiosyncrasy of the model. In the extreme case, the bending stress in the steel was about half as big as the maximum direct stress. Mesh refinement for increased accuracy was not possible because of program limits on the number of elements. Thus, while these finite element results are believed to be qualitatively correct, the local extreme values almost certainly underestimate the true ones.

The stress concentration factor must be less than 3.0, because that is the factor for a plate with a small hole subjected to uniaxial tension. Thus, the local hoop stress is increased by a factor between 1.21 and 3.0, but most likely close to 2.0.

TEST RESULTS—GENERAL

Tests were carried out to study the behavior of bearings in concentric compression. In some of the tests the load was applied

concentrically at first, then at different eccentricities. Eccentric compression and rotation are discussed in Appendix C.

Three main test series were run: (1) concentric compression to failure, (2) concentric compression to service loads with strain gages attached to steel, and (3) concentric compression on glass fiber-reinforced bearings.

A further test series was concerned with combined compression and rotation, and some results from it at zero rotation are included here.

Specific effects studied included steel strength, shape factor, aspect ratio, size, and presence and location of holes.

CONCENTRIC COMPRESSION TO FAILURE

General Behavior

Fifteen tests were conducted and are summarized in Tables B-2, B-3, and B-4. All testing was performed in a 2.4 million pound Baldwin Universal testing machine. Values of load, deflection, and where appropriate rotations were recorded, but steel strains were not. Most bearings behaved in a similar manner. At low loads the elastomer bulged around its free surface in a roughly parabolic shape. As the load increased the bulging did also, obscuring the steel reinforcing plates as shown in Figure B-11. The elastomer has to deform considerably to obscure the plates in this way, but no permanent damage was visible. The compressive stress at which the plates were obscured for concentrically loaded bearings with 0.066-in. thick plates was between 1,000 and 1,500 psi for the shape factor 5 bearings and about 2,500 psi for shape factor 10. When a bearing was loaded eccentrically, this happened much sooner. For example, in the 12 in. $\times$ 24 in. bearing the steel was hidden at stresses of 2,500, 1,400, 700, and 500 psi when the eccentricity was 0 in., 1 in., 2 in., and 3 in. In bearings used in the field the same conditions would not arise because the presence of the cover would change the deformations at the edge of the plates and reduce the local strains in the bearing. However, it is still a useful indication of the severity of the deformation in the elastomer.

Table B-2. Effect of shape on bearing strength (A = area (in.^{2}), S = shape factor (dimensionless), h_r = elastomer layer thickness (in.), h_s = steel layer thicknes (in.), c_s = strength coefficient for steel, L.B. = lowerbound, U.B. = upperbound).

Brg No.	Shape	Unloaded A / h_r	Unloaded S / h_s	L.B. Yield h_r / σ_c / c_s	U.B. Yield h_r / σ_c / c_s	Fracture h_r / σ_c / c_s
3 A	Circle	51 .377	5.34 .066	.318 5.098 .625	.313 6.078 .733	.225 16.627 1.048
4 B	Square	64 .378	5.29 .066	.318 4.688 .575	.313 5.313 .641	.233 14.453 .943
9 AA	2:1 Rectangle	69.8 .392	5.01 .066	.338 5.014 .653	.334 5.731 .738	.294 10.745 .885
10 A	4:1 Rectangle	96.3 .370	5.28 .066	.300 4.673 .540	.296 5.192 .593	.250 9.865 .691

Table B-3. Effect of holes on bearing strength (terms as in Table B-2).

Brg No.	Shape	Unloaded A / h_r	Unloaded S / h_s	L.B. Yield h_r / σ_c / c_s	U.B. Yield h_r / σ_c / c_s	Fracture h_r / σ_c / c_s
3 A		51.0 .377	5.34 .066	.318 5.098 .625	.313 6.078 .733	.225 16.627 1.048
3 C		50.9 .372	5.41 .066	.306 4.912 .579	.300 5.894 .682	.256 9.823 .704
3 D		51.0 .384	5.24 .066	.312 4.902 .590	.305 5.882 .692	.269 9.549 0.615
4 B		64.0 .378	5.29 .066	.318 4.688 .575	.313 5.313 .641	.233 14.453 .943
4 C		64.0 .347	5.76 .066	.283 4.688 .511	.276 5.469 .582	.230 10.938 .705
7 B		64.0 .368	5.44 .118	.283 6.250 .328	.279 7.031 .364	.239 14.391 .493
4 D		64.0 .370	5.41 .066	.299 4.688 .540	.295 5.469 .622	.254 9.875 .702
4 A		64.6 .365	5.51 .066	.294 4.644 .526	.289 5.418 .604	.256 9.093 .652
9 AA		69.8 .392	5.01 .066	.338 5.014 .653	.334 5.731 .738	.294 10.745 .885
9 AB		69.8 .397	4.95 .066	.340 5.014 .657	.335 5.731 .740	.317 8.095 .719
10 A		96.3 .370	5.28 .066	.300 4.673 .540	.296 5.192 .593	.250 9.865 .691
10 B		93.8 .346	5.53 .066	.274 4.797 .507	.267 5.864 .604	.239 9.051 .606
10 C		93.8 .389	4.92 .066	.312 4.797 .577	.308 5.330 .633	.281 8.294 .653

Table B-4. Effect of size on bearing strength (terms as in Table B-2).

Brg No.	Shape	Unloaded A / h_r	Unloaded S / h_s	L.B. Yield h_r / σ_c / c_s	U.B. Yield h_r / σ_c / c_s	Fracture h_r / σ_c / c_s
3 A	Circle	51.0 .377	5.34 .066	.318 5.098 .625	.313 6.078 .733	.225 16.627 1.048
5 A	Circle	203.4 .368	10.93 .066	.311 4.916 .589	.306 5.900 .696	.253* 11.554 .819
4 A	Square	64.0 .378	5.29 .066	.318 4.688 .575	.313 5.313 .641	.233 14.453 .943
6 A	Square	256.0 .368	10.89 .066	.311 4.688 .562	.306 5.469 .645	.274* 9.180 .704

* Note: Fracture not reached. Test stopped at capacity of loading system.

Debonding of the elastomer from the reinforcement occurred in all bearings tested to either failure or machine capacity. The compressive stress at which this was first noticed varied considerably, from about 3,900 psi in bearing 8 A (16 in. $\times$ 16 in.) to 8,000 psi in bearing 7 A (8-in. dia with a 1-in. hole). This probably indicates a variation in the local bond strength between the two materials. The data are shown in Figure 12 of the main report. The eccentrically loaded bearings started to debond at

lower stresses than their concentric counterparts (e.g., 6,250, 3,600, and 2,850 psi for eccentricities of 0 in., 0.97 in., and 1.46 in. in bearings 9 AB, 9 AD, and 9 AC, respectively). The way that the bearings are manufactured also influences debonding. One of the early trial bearings was a 5:1 rectangle which debonded badly along one short side at a low stress, although the maximum shear stress occurs at midlength of the long sides. After failure this bearing was taken apart, and it was found that during fabrication the steel plates had been kept spaced apart by disc-shaped spacers of partially cured elastomer. These had not adhered properly to the reinforcing and, because they were placed near the ends of the bearing, they had initiated the debonding failure there.

Tests on the biggest bearings (5 A, 6 A) were stopped when the machine capacity of 2.4 million pounds was reached, but plate fracture had not occurred. Bearings 9 AC and 9 AB were tested in eccentric compression and had to be stopped before the plates ruptured because the rotations were large enough that parts of the loading rig came into hard contact. In all these cases debonding was extensive when the test was stopped.

All the bearings had four layers of elastomer and five of steel. In most tests some shearing deformation occurred early in the test, and it increased with load. In some cases the top plate moved laterally with respect to the bottom one, in others the center plates moved laterally with respect to the top and bottom ones, and in yet others the center plates rotated about a vertical axis. These motions appeared to be related to instability, in the same way that an initially bent steel column will show increased deflection when axial load is applied. However, they occurred at loads well below the buckling load. They were probably exacerbated by the unavoidable slack (about $\frac{1}{8}$ in.) known to exist in the head of the test machine, which corresponds well with the approximate magnitude of the lateral movement observed in the top plate. It is believed that this movement made little difference to the rupture load, although it could have influenced the debonding load.

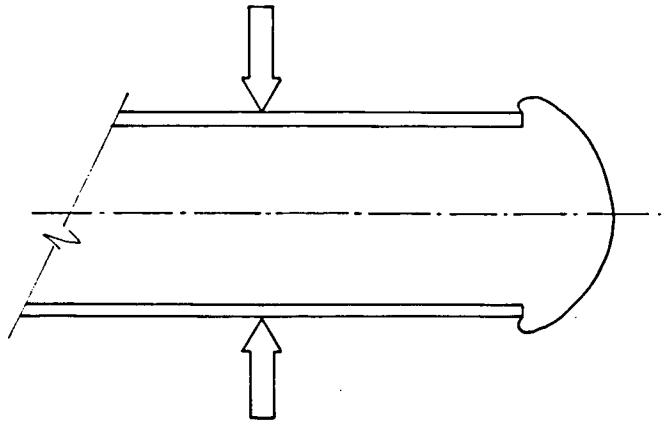

Figure B-11. Bulging pattern at large loads.

Yielding of Reinforcement

Figure B-12 shows the load-deflection curve for bearing 3 A, which was 8 in. in diameter. The curves for other bearings were similar. The upper line represents values read directly after reaching the new loads; and the lower one, reading taken 60 sec later. Between readings the test machine was locked, so the displacement remained constant and the difference between readings represents relaxation in the materials. Three phases of behavior can be seen. In the first, behavior is elastic but, as expected, nonlinear and stiffening, and little relaxation takes place. That which does is attributed to the elastomer. At 250 kip (5,000 psi) the stiffness dropped to about 70 percent of its last elastic value and the relaxation increased significantly. Both signs indicate the onset of yielding in the steel. At 350 kip (7,000 psi) the stiffness dropped again to about 40 percent of the last elastic value, and then stayed constant until one of the inner plates fractured at 848 kip (16,900 psi). (No reading could be taken on the data recorder at the peak load, so this point is not shown on the plot.) The second loss of stiffness is believed to represent the spread of yielding through the plate. After fracture the bearing could still carry some load, but was functionally useless.

The bearing showed considerable strength after first yielding. Application of the Tresca yield criterion to Eqs. B-12a–B-12c shows that the hoop stress at the edge is only 34 percent of the yield stress when yielding starts at the center. Thus, considerable gains in strength through inelastic redistribution are possible, provided adequate ductility exists. The large inelastic steel strains observed in the tests suggest that it does. The steel used in the bearing was ASTM A569, which has no specified yield point. It was used because structural steels are not available in the desired $\frac{1}{16}$ in. thickness. Coupon tests gave average yield and ultimate strengths of 39.3 and 54.1 ksi, which values were used for the calculations here. The elongation at break was 32 percent in an 8-in. gage length, or 50 percent in the 2-in. gage in which fracture occurred. Such ductile steel behavior means that, in this and other bearings, both redistribution and strain-hardening probably contributed to post yield strength.

After failure the bearing had the approximate dimensions shown in Figure B-13, which also shows how the center plate (No. 3) fractured. The outer plates (1 and 5) had hardly stretched at all, and plates 2 and 4 had stretched considerably but had not fractured.

The effect of bearing shape on first yield can be seen from Table B-2. Equations B-13a and B-13b relate the average compresisve stress at first yield to the steel yield strength. If the second term in parentheses is neglected because it is small compared to the first, they can be rearranged in the form

$$\sigma_c \doteq c_s F_y \frac{2h_s}{(h_{r1} + h_{r2})} \qquad \text{(B-16)}$$

where the constant c_s is $\frac{1}{1.5}$ or 0.667 for the strip, and 0.606 for the circular bearing. It was expected that the analogous equation for bearings of other shapes would have a similar form but a different c_s value.

Values for c_s can be obtained from the experimental data if σ_c is taken as the average compressive stress at the kink in the load deflection curve, which corresponds to first yield, and F_y is the steel yield strength. Table B-2 and Figure B-14 show such a comparison, in which h_r is the average thickness of the two central elastomer layers at the load in question. Upperbound and lowerbound yield values are given because a reading was not necessarily taken at the exact point at which the steel yielded. The data for bearings without holes are fairly consistent. The coefficient c_s varies from 0.540 (lowerbound yield for 4:1 rec-

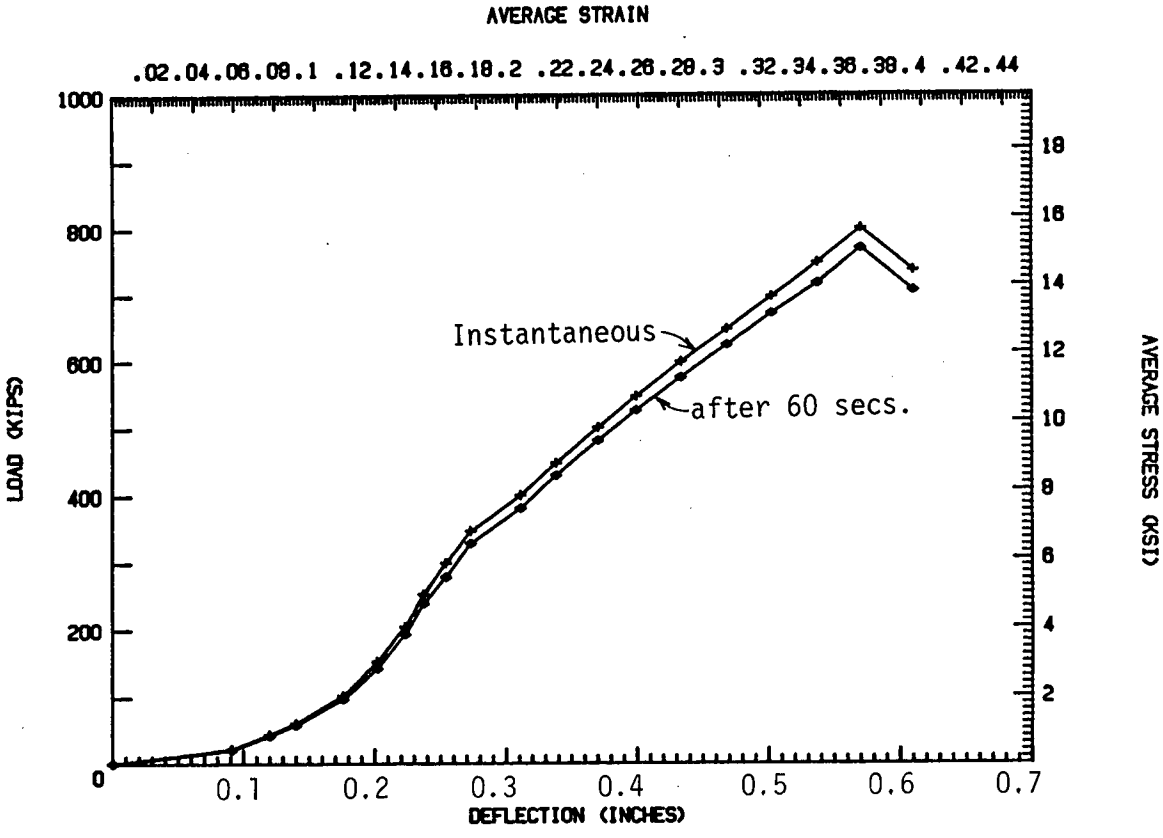

Figure B-12. Load-deflection curve for bearing Type 3 A (8-in. diameter).

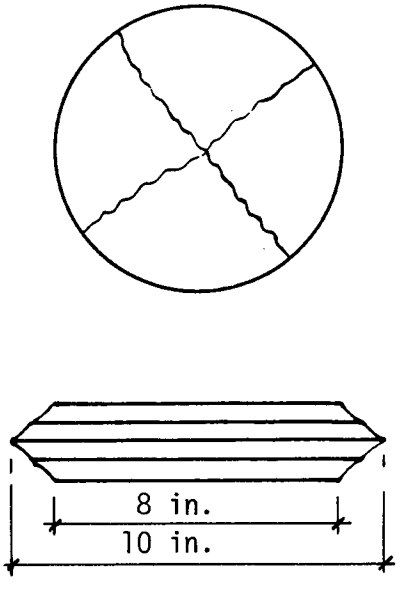

Figure B-13. Bearing Type 3 A after rupture of the steel reinforcement.

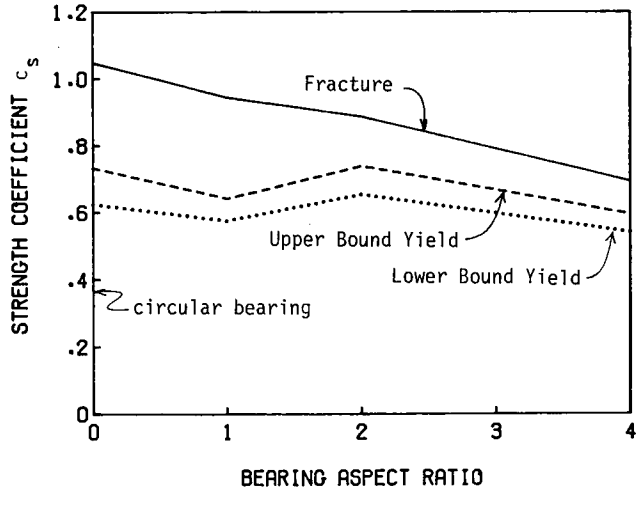

Figure B-14. Effect of aspect ratio on strength coefficient.

tangle) to 0.851 (upperbound yield for circle), suggesting that Eq. B-16 is applicable for a wide range of shapes.

There appears to be one inconsistency in the data, because the circular bearing should theoretically have a slightly lower coefficient than the 4:1 rectangle, whereas the values based on first yield in the experiments are higher. However, yielding in the circular bearing initially takes place only at a single point (the center), whereas in a true strip it takes place along the whole length of the bearing. The former is much harder to detect on a load deflection plot, and it is therefore likely that

the quoted coefficient values for the compact shapes (square and circle) really correspond to a state somewhat beyond initial yield, whereas those for the strip correspond more closely to first yielding.

Values of the strength coefficient c_s were also calculated for the fracture load, although they are less meaningful because the nature and the extent of the inelastic redistribution are not known precisely. However, the data show that the ratio of (c_s at fracture)/(c_s at first yield) becomes smaller for more elongated shapes, all the more so if the measured coefficients at first yield for the compact shapes are reduced a little for the reasons stated above. This suggests that the compact shapes have a greater potential for inelastic redistribution of stress than do more elongated shapes. This experimental evidence is in keeping with theoretical steel stresses, since, in the absence of strain hardening, a truly infinite strip would fracture immediately after first yield (because the yielding would occur along its whole length), whereas a circular bearing would not fail until additional load had raised the hoop stress at the edge from its initial yield value of 0.34 F_y to 1.0 F_y.

Information on the fracture strength of the bearing has limited usefulness for specifications such as AASHTO (*22*), which are based on working stress design. However, information on bearing stresses needed to cause yield is directly applicable. Together, they serve to confirm the general understanding of the nature of the steel stresses.

The foregoing arguments suggest that Eq. B-16, with a coefficient of $\frac{2}{3}$ for all shapes, is adequate to predict the load to cause first yield. That the value $\frac{2}{3}$ slightly exceeds the theoretical 0.606 for a circular bearing is offset by the circular bearing's greater potential for inelastic redistribution. The safety factors normally used in design would mask the slight discrepancy.

Effect of Holes on Bearing Strength

Table B-3 shows the relevant data for studying the effects of holes on the compressive stress needed to cause yield or fracture of the reinforcement. Measured shape factor, S, plan area, A, and steel and elastomer layer thicknesses h_s and h_r are given for all bearings in the unloaded state. Then the instantaneous elastomer thickness, average compressive stress and strength coefficient c_s are given for lowerbound yield, upperbound yield, and fracture. All bearings but 7B were made with 0.066-in. thick ASTM A569 steel, for which the measured F_y and F_u were 39.3 and 54.1 ksi, and the elongation at fracture was 32 percent on 8 in., or 50 percent on 2 in. Bearing 7B was made from 0.118-in. thick ASTM 572 gr 33, for which F_y and F_u were measured to be 45.6 and 59.0 ksi, and the elongation at fracture was 28 percent on 8 in., or 48 percent on 2 in. In all cases the holes were 1-in. diameter and were cut clear through the bearing.

For any bearing shape it is possible to compare values of the strength coefficient for a bearing with no holes and those for the same bearing with different arrangements of holes. Because the experimental compression stress to cause yield is bounded rather than known precisely, only general trends rather than precise relationships can be discerned. The most important are the following:

1. Holes have more influence on bearings of compact shape than on long narrow ones.
2. For compact shapes, holes appear to have a significant influence on fracture strength but almost none on the load to cause initial yielding. This latter is in direct contradiction to the theoretical findings but may be partly explained by the difficulties in detecting first yield from a load deflection plot, especially if it occurs in a highly localized region.
3. Within the limits of experimental error, two symmetrically placed holes appear to be no more damaging than one central one. This is in agreement with the results of the finite element analyses on the 2:1 rectangular bearing.
4. In the square bearing, placing the holes on the diagonal appears to reduce the strength slightly more than does placing them on a perpendicular axis. This observation is based on the facts that the bearing with one hole (4 C) fractured along the diagonals and the fracture load for 4 A (2 holes on the diagonal) was lower than 4D (2 holes on the perpendicular axis). However, 4 A did not fracture cleanly along the diagonals but had a rather random crack pattern, so the effect is minor.

Effect of Nonuniform Elastomer Thickness

Two bearings (7A and 7B) had very uneven layer thicknesses. At one location in each bearing, the steel plates, which should have been separated by a $\frac{3}{8}$-in. elastomer layer, were actually touching. They were both cut from the same stock made with 0.118-in. ASTM 572 steel reinforcement. A central hole had been cut in each on the assumption that the test machine capacity would be too small to cause plate fracture in a bearing without a hole.

Their strength coefficients are about one-half of those of the other bearings. (Only 7B is shown in Table B-3.) In both cases the middle plate fractured along a single line, one end of which coincided with the point where the two plates were in contact. The strength coefficients for all of the other bearings are sufficiently close, despite the variety of geometries tested, to confirm that Eq. B-16 is fundamentally sound, so it is necessary to look elsewhere for reasons for the low strength of specimens 7 A and 7B. Possible causes are uneven layer thickness or inability to redistribute the stresses concentrated around the hole. The latter could have been caused by a lack of ductility in the A572 steel, but that is unlikely because the steel coupon test showed considerable ductility. Also, the strength coefficients are low at both yield and fracture. Thus, it is believed that the uneven layers caused the problem, although the exact mechanism for doing so is not clear.

Effect of Size

Table B-4 gives the test results for four bearings of different sizes cut from the same stock. If a size effect exists, it should be visible when the results from bearings of the same shape but different size are compared. In the two large bearings the steel yielded, but the test machine was not strong enough to cause fracture.

The strength coefficients for the two bearing sizes were close for both shapes and for the upper and lower bounds on the yield point. It is thus concluded that no size effect exists, or that if it does, it is small enough to neglect.

Compressive Strength of Glass Fiber-Reinforced Bearings

Eight bearings were cut from a single sheet of 1-in. thick

material. The arrangement of layers is one commonly used in highway bridges in California and is shown in Figure B-15. The layer thicknesses were very consistent. Shore A durometer readings taken on the top layer averaged 64, but the true elastomer hardness must have been smaller because the top layer of reinforcement must have influenced the readings. Pad data and test results are given in Table B-5.

All specimens displayed similar behavior. At low loads the elastomer bulged, with virtually all of the vertical deflection occurring in the two $\frac{3}{8}$ in. layers. The compressive stiffness of the bearings appeared to be essentially independent of shape factor or plan shape, which was surprising in view of the strong influence of shape factor in steel-reinforced bearings. At a vertical stress between 0.8 ksi and 1.5 ksi horizontal splits started to occur around the edges of the bearing at the peak of the bulge. They followed the line of the joint between the individual $\frac{1}{8}$ in. layers of which the bearing was made up. Then at a stress between 2.1 and 2.8 ksi the reinforcement ruptured with a clearly audible popping sound, and the load dropped suddenly. Loading continued and the fiberglass continued to rupture, and in addition other, different, tearing sounds were heard which were attributed to delamination. After the tests, the bearings were inspected and found to have a maze of orthogonal cracks where the reinforcement had ruptured. In some instances, a fiberglass layer had also separated from the adjacent elastomer.

Separation of the individual $\frac{1}{8}$ in. layers was the first sign of distress in all the bearings, and it occurred at a compressive stress and strain which were not clearly related to any bearing property such as shape factor, aspect ratio, etc. Bulging of the elastomer at the free edge causes an elongation in the vertical direction. Simple calculations suggest that it is a function of ϵ_c / S^2, which would mean that bearing F 8, whose shape factor of 13.3 was twice that of the others, should not have started splitting until well after the others. Bearing F8 split at an average compressive stress and strain of 1.0 ksi and 7.8 percent, compared to an average for the shape factor 6.67 bearings of 1.17 ksi and 6.6 percent strain. The differences between these values are of the same order as the scatter in the data and, therefore, cannot be considered significant. Calculation of the elongation around the bulge, though rational, therefore fails to provide an estimate of load at splitting. Little choice remains but to take the minimum, or average, value from the tests. The minimum compressive stress at splitting was 0.8 ksi, the mean was 1.143 ksi, and the mean minus two standard deviations was 0.691 ksi.

The strength coefficients, c_s, at rupture varied from 0.64 to 0.79. They were based on the code-required minimum rupture strength of 800 lb/in. for the fiberglass, because no test results were available. These c_s values are close to the value of $\frac{2}{3}$ which is proposed for use with steel-reinforced bearings of all shapes.

The effect of aspect ratio can be studied using bearings F1, F7, and F9. The square and 2:1 rectangle had essentially the same c_s value, while that of the 4:1 rectangle (F-9) was 23 percent higher. These results are in agreement with the theory, but are the opposite of what was found for steel-reinforced bearings at fracture. They probably also reflect the fact that woven fiber reinforcement has little ductility and, therefore, unlike the steel bearings, the compact shapes gained little from inelastic redistribution. However, the use of Eq. B-16 with c_s equal to $\frac{2}{3}$ still gives acceptable results for fiber-reinforced bearings of all aspect ratios.

The effect of holes on strength was surprising. Fiberglass yarn, like all cloth, has virtually no shearing stiffness or strength, so it cannot redistribute the stresses around a hole in the same way that a steel plate can. Yet, bearing F2 with one central hole failed at a load 10 percent higher than F1 which had no hole. Scatter in the results is larger than any trend, and it appears that holes representing a small percentage of the bearing plan area have only an insignificant effect on rupture strength. The test results do, however, show that holes make the bearing more flexible by an amount which is about twice that implied by using a shape factor modified to account for the extra free surface around the holes.

Most of the bearings had saw-cut edges on all 4 sides. Bearing F9 had one untrimmed factory edge with about 0.1 in. of elastomer cover over the ends of the fiberglass. Even after being loaded to 33 percent compressive strain and sustaining a lot of damage internally and to the other edges, the edge with cover appeared undamaged. This suggests that the cover is effective in preventing horizontal edge splits but also that undamaged cover should not be taken as an indicator that the interior of the bearing is functioning properly. However, most bearings will have no cover because they are manufactured in large sheets and cut to size with a band saw.

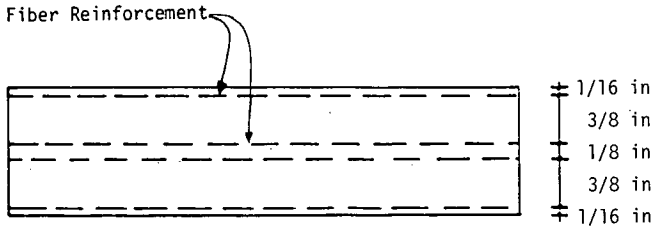

Figure B-15. Cross-section through fiberglass-reinforced pad.

Table B-5. Fiberglass-reinforced specimens.

Brg No.	Plan Dimensions (in)	Stress at First Split (ksi)	Stress at Rupture (ksi)
F 1	10 x 10	1.4	2.3
F 2	10 x 10	1.2	2.5
F 3	10 x 10	0.8	2.1
F 5	10 in dia	1.5	2.2
F 6	7.5 x 15	-	2.1
F 7	7.5 x 15	1.1	2.3
F 8	20 x 20	1.0	2.8
F 9	6.25 x 25	1.0	2.8

DIRECT COMPRESSION AT SERVICE LOADS

General

Seven pairs of bearings were tested at service load levels in

order to investigate steel stresses and overall load-deflection behavior. A variety of configurations were chosen to permit study of the effects of plan geometry and size. All bearings were designed to have the same shape factor (5.0), and all but two, to have the same area (64 in.^{2}) in order to eliminate any variations due to these two effects. The last two bearings had areas of 32 in.^{2} and 128 in.^{2} in order to investigate the effects of size.

Most of the bearings were fabricated with no top or bottom cover and had strain gages attached directly to the plates. To avoid crushing the gages, a spacer plate was placed between the instrumented plate of the bearing and the loading head. The spacer plate had slots milled in it which bridged the gages and allowed the lead wires to be brought out to the data acquisition system. Vertical deflection was measured by averaging the readings from four LVDT's, one at each corner of the bearing. The bearings were generally tested in pairs in order to provide a greater total elastomer thickness (giving larger total deflections that were easier to read accurately) and to average out any effects of irregular layer thickness. The layer thicknesses were rather uneven and varied both over any given layer and among different layers of the same bearings. The load deflection relationships had the expected form, but great difficulties were experienced with the strain gages, as described below, and the data from them were ultimately of little use.

Load Deflection Behavior

Average stress-strain plots for four bearings are shown together in Figure B-16. They were superimposed by aligning the point on each curve at which the compressive stress is 250 psi, in order to eliminate spurious discrepancies caused by differences in the strain zeros. The curves are clearly nonlinear, and they can be approximated by any of the three proposed (*3, 20, 21*) nonlinear expressions, or by Eq. B-8c, to give

$$\sigma_c = f_c \frac{E_c}{(1 - \epsilon_c)^3} \tag{B-17a}$$

$$\sigma_c = f_c \frac{E}{3} (\lambda^{-2} - \lambda) \tag{B-17b}$$

$$\sigma_c = f_c E (\lambda^{-1} - 1) \tag{B-17c}$$

$$\sigma_o = f_c \frac{E}{4} [(1 - \epsilon_c)^{-4} - 1] \tag{B-17d}$$

where $\lambda = 1 - \epsilon_c$.

These can be expanded to give, respectively,

$$\sigma_c \doteq f_c E (\epsilon_c + 3\,\epsilon_c^2 + 6\,\epsilon_c^3 + 10\,\epsilon_c^4 + \ldots.) \tag{B-18a}$$

$$\sigma_c \doteq f_c E \left(\epsilon_c + \epsilon_c^2 + \frac{4}{3}\epsilon_c^3 + \frac{5}{3}\epsilon_c^4 + \ldots.\right) \tag{B-18b}$$

$$\sigma_c \doteq f_c E (\epsilon_c + \epsilon_c^2 + \epsilon_c^3 + \epsilon_c^4 + \ldots.) \tag{B-18c}$$

$$\sigma_c \doteq f_c E (\epsilon_c + 2.5\,\epsilon_c^2 + 5\,\epsilon_c^3 + 8.75\,\epsilon_c^4 + \ldots.) \tag{B-18d}$$

Equations B-17b and B-17c, the kinetic theory and the incremental approach, will clearly give very similar results, particularly for small ϵ_c values. All four equations were fitted to the results from the square bearing (A 5) by shifting them along the strain axis and choosing a value for Ef_c so that they coincided with the test curve at 250 psi and 3,100 psi. They are shown in Figure B-17. None of the equations is sufficiently nonlinear, and it was found that Eq. B-9 fitted well with $n = 10$ if the

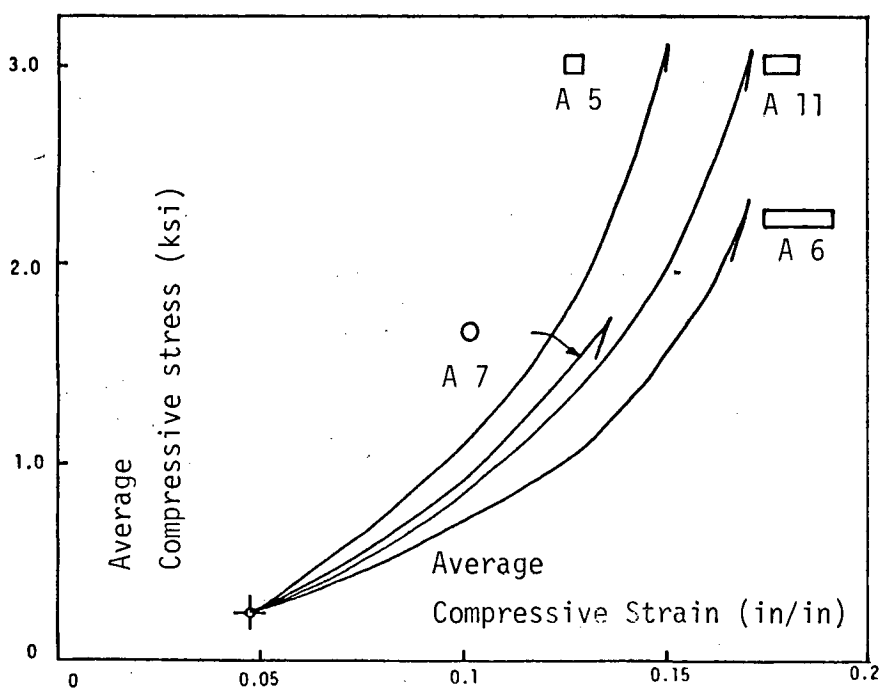

Figure B-16. Influence of plan shape on measured compressive stress-strain curves (each bearing has area = 64 in., shape factor = 5).

strains were shifted so that the theoretical and experimental curves matched at 250 psi. This is shown on Figure B-16, but it should be recalled that Eq. B-9 has no rational basis.

Figure B-16 shows that, of the rectangular bearings with the same shape factor, a larger aspect ratio leads to a less stiff bearing, which is in agreement with the predictions of linear theory (see Ref *1* Fig. 17).

Steel Stresses

Data from the strain gages attached to the steel plates proved disappointingly erratic. Strains bore little or no relation to theoretically predicted patterns or magnitudes, and in some cases even changed direction during monotonic loading of the bearing.

Several potential causes of error were investigated. Lateral restraint of the reinforcement due to friction against the test platens was ruled out by greasing the interface between them. Effects of transverse bending of the reinforcement as it bridged the slot milled in the spacer plate were investigated theoretically and found to cause less than 1 percent error in the strain readings. It is believed that flattening out of slight initial curvatures in the bearings may have been responsible for the difficulties. This has been shown theoretically (*35*) to cause errors in the strains that can be much larger than the tensile strain to be measured.

SUMMARY AND CONCLUSIONS

1. *Reinforcement Stresses.* Equations are available which predict reliably the load to cause first yield in the reinforcement of a steel-reinforced bearing without dowel holes. The equations' validity was demonstrated for a wide variety of shapes by the good agreement between the kink in the experimental load-deflection curve and the theoretically predicted load to cause yield. Reliable, direct measurements of the steel strains could not be obtained.

The average compressive stress to cause yielding of the reinforcement depends on the ratio of elastomer to steel layer thicknesses, but not on the plan area of the bearing.

Elastomer layers of nonuniform thickness can reduce the loads to cause yield and fracture in the reinforcement by a factor of 2.

Considerable reserve strength beyond first yield exists in steel-reinforced bearings of compact shape and without holes. This is attributed to strain hardening and to inelastic stress redistribution. Less inelastic redistribution is possible as the plan shape becomes more elongated.

A central hole in the steel but not the elastomer was shown theoretically to cause the stress to increase by up to 100 percent. Problems were encountered in predicting steel stress increases when the hole penetrated both steel and elastomer. The best estimate, based on linear finite element analysis, is that the increase is approximately 100 percent.

Experimental confirmation of first yield was difficult because of the problems in detecting from a load deflection plot a highly localized first yield. The hole was also found to cause a significant reduction in the post yield strength, but the effect was most prevalent in square and circular bearings and virtually nonexistent in the 4:1 rectangle. Two holes placed away from the center were slightly less damaging than one at the center. Holes generally caused a smaller reduction in experimental fracture load than the factor of 2.0 theoretically predicted for the load to cause first yield.

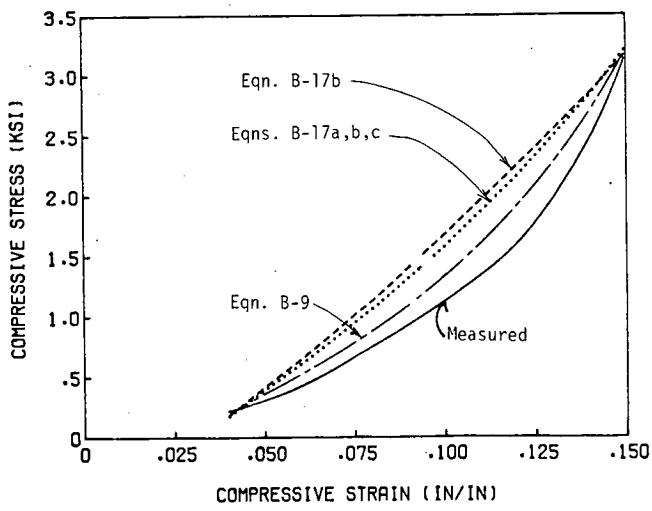

Figure B-17. Comparison of nonlinear compression theories with measured data.

Reinforcement failure in fiberglass-reinforced bearings can be predicted using the same equations as are used for steel-reinforced bearings, provided the actual, and not the nominal, layer thicknesses are used.

Holes in fiberglass-reinforced bearings have a negligible effect on the rupture strength.

2. *Debonding.* Debonding at the steel-elastomer interface initiated at a wide range of stresses from 3,900 to 8,000 psi in the various bearings tested. It did not correlate well with any particular property of the bearing or applied stress.

Conventional linear theories are inadequate to describe properly the true conditions of stress in the elastomer at the crucial corner of the steel-elastomer interface, at which a stress concentration exists.

In the fiberglass-reinforced test bearings, the $\frac{1}{8}$ in. layers from which they were built up started to separate at their outer edges when the compressive stress reached about 1,000 psi. This stress appeared to hold true regardless of shape factor. In some specimens the reinforcing layer completely separated from the adjacent elastomer at about the load required to rupture the reinforcement.

3. *Load-Deflection Relationships.* The load-deflection relationship of all bearings was found to be nonlinear before the reinforcement yielded. The various rationally derived theoretical expressions are not sufficiently nonlinear to describe the relationship well.

Stiffness of steel-reinforced bearings is a function of both shape factor and plan shape. For a given shape factor linear theory shows compact shapes to be stiffer, and this was confirmed in the nonlinear test results.

The stiffnesses of the fiberglass-reinforced bearings appeared to be essentially independent of shape factor and plan shape. This may have been due to elastic stretching of the reinforcement and, in the higher shape factors tested, to bulk compression of the elastomer.

Holes made both types of reinforced bearing more flexible. In the steel-reinforced bearings the difference could be adequately described by using a modified shape factor which accounts for the perimeter added and plan area lost as a result of the hole. This procedure underestimated the change in stiffness in the fiber-reinforced bearings.

APPENDIX C

ROTATIONAL DEFORMATIONS

INTRODUCTION

Almost all bearings have to accommodate some relative rotation between the top and bottom surfaces. It may be caused by a lack of parallelism between girder and seat, or by rotations of the end of the girder due to dead and live loads. The resulting deformations of the bearing are referred to in this study as rotational deformations.

Two aspects are of interest to the designer: damage to the bearing and adverse effects on the adjoining structural components. The bearing could suffer damage if the combination of compression plus rotational deformations causes excessive bulging and shear strains in the elastomer, leading to debonding. In extreme cases lift-off may occur and the nonuniform compressive stress distribution could lead to bending of the steel plates. Rotational deformation also causes the location of the compressive force on the substructure to shift. In many cases the moment induced will be negligible compared with the member capacities. However, if the members are quite slender, a reliable estimate of the bearing's moment-rotation characteristics is needed to predict the eccentricity of the load.

Theoretical analyses of rotational deformations are first reviewed. Two types of test were performed, and these are discussed next. Some were eccentric load tests, in which the eccentricity was held constant while the load was increased, and others were true rotation tests in which a variable rotation was applied to the top surface at a constant compressive load and the moment was measured. A number of true rotation tests were conducted at different average compressive stresses.

THEORY

Theoretical analyses based on small deflections have been presented (*3, 16, 18, 36*) which follow closely the lines of similar analyses for compression, except that the compressive strain is assumed to vary linearly across the bearing. The analyses all depend on the same assumptions as do the closed-form compression theories (i.e., small deflections, parabolic bulging, and plane sections remaining plane) so they are subject to the same shortcomings.

The equations for rotational stiffness are all of the form

$$M = E_r I \frac{\theta}{h_r} = f_r EI \frac{\theta}{h_r} \qquad \text{(C-1a)}$$

where

$$f_r = A_r + B_r S^2 \qquad \text{(C-1b)}$$

A_r and B_r are constants depending on the plan geometry and the value of E/K (Young's modulus divided by bulk modulus) for the elastomer. Conversy (*16*) treated the problem in one step and covered both compressible and incompressible cases. His analysis gives $A_r = 0$ for all rectangular shapes. This clearly becomes incorrect as h_r tends to infinity and S tends to zero, under which conditions A_r should approach 1.0. Rejcha (*18*) performed a similar analysis, but for the incompressible case only.

Gent and Meinecke (*36*) split the problem into two parts, but treated only the incompressible case. In the first part, the rotation is applied to the top surface, and the elastomer undergoes free lateral expansion. In the second, vertical displacements are held fixed while shear stresses are applied at the elastomer-steel interface to restore the conditions of zero lateral displacement. The first step gives the coefficient A_r, for which the empirical expression

$$A_r = \frac{4}{3} - \frac{2}{3}\left(\frac{WL + 4h_r^2}{W^2 + L^2 + 8h_r^2}\right) \qquad \text{(C-2)}$$

was presented, where L and W represent the sides of a rectangular bearing or the axes of an elliptical bearing, and h_r is the elastomer layer thickness. A_r thus varies from 1.33 for an infinite strip to 1.00 for a compact shape.

The analysis for the second step was not presented, but the final equation is identical to the special case of $E/K = 0$ (i.e., complete incompressibility) in Conversy's analysis. The more general form, adapted from (*3*), is

$$B_r = \frac{24}{\pi^2}\left(1 + \frac{L}{W}\right)\sum_{n=1}^{\infty}\frac{1}{n^4 Q_n^2}\left(1 - \frac{L}{n\pi WQ_n}\tanh\frac{n\pi WQ_n}{L}\right) \qquad \text{(C-3a)}$$

where

$$Q_n^2 = 1 + \frac{E}{K}\left(\frac{L}{n\pi h_r}\right)^2 \qquad \text{(C-3b)}$$

This expression is for the case when the top surface rotates about an axis parallel to the side which is W long. This axis is referred to as the transverse axis, because bearings are usually placed so that they are perpendicular to the longitudinal axis of the bridge girders. B_r is plotted against aspect ratio L/W as a solid line in Figure C-1 for $E/K = 0$. In this case B_r is the same for all shape factors. When bulk compressibility is taken into account, B_r decreases and depends slightly on E/K, S, and L/W. However, analysis of these results showed that the compressible case could be approximated well by the empirical equation

$$\frac{1}{E'_r} = \frac{1}{E_r} + \frac{1}{c_{kr}K} \qquad \text{(C-4)}$$

where E'_r, E_r = effective moduli for rotational deformations, respectively, including and excluding compressibility; K = bulk modulus of elastomer; and c_{kr} = stiffness constant for rotational deformations.

Correlating Eq. C-4 against the more rigorously derived theoretical results from Ref. *16* showed that the constant c_{kr} lay between 0.64 and 0.70 in all cases for $3 \leq S \leq 12$ and $0 \leq E/K \leq 0.002$; therefore, a single value of 0.66 appears to be a reasonable compromise. Bulk modulus is difficult to measure precisely, but a value of $E/K = 0.001$ is often taken as representative of common bridge bearing materials. The most extreme case ($S = 12$, $E/K = 0.002$) is shown in Figure C-1 as a dashed line. B_r lies in the range 0.5–1.0 for most practical bearing shapes, therefore, for practical shape factors of 5 and above the rotational stiffness depends primarily on B_r, and the precise value of A_r is relatively unimportant.

No analysis of rotation of circular bearings is known.

Tests show that the compressive load-deflection curve for a bearing is nonlinear, and the same might be expected for rotation. On this basis Tamhankar and Chhauda (*37*) proposed that a stress-dependent value of rotational modulus be used, in which E_r is taken to be the same as the stress-dependent compression modulus, E_c, which can be determined experimentally. Gent and Meinecke (*36*) point out that this could lead to substantial errors even in the linear range, where E_c is 3 to 5 times as large as E_r. It is also reasonable to suppose that moment-rotation curves will be less nonlinear than compressive force-deflection curves because rotation requires no change in volume of the elastomer between the steel plates, whereas compression does. However, Eq. C-16 suggests that the rotational stiffness will increase when the bearing is compressed because h_r becomes smaller and S, larger. Both aspects of behavior were confirmed in the tests performed in this study.

Shear strains in the elastomer (*16*) may be expressed in the form

$$\gamma_r = g_r \theta \frac{L}{2h_{ri}} \tag{C-5a}$$

where

$$g_r = C_r S \tag{C-5b}$$

θ = relative rotation between top and bottom surfaces of the bearing

and

$$C_r = \frac{12}{\pi^2}\left(1 + \frac{L}{W}\right)\sum_{n=1}^{\infty}\frac{1}{n^2 Q_n^2}\left(1 - \operatorname{sech}\frac{n\pi W}{L}Q_n\right) \tag{C-5c}$$

C_r is plotted against L/W in Figure C-2. As with B_r, C_r is the same for all shape factors when $E/K = 0$, and C_r decreases somewhat for the compressible case, in a manner depending on E/K, S, and L/W.

It is useful to compare γ_r with γ_c (the shear strain caused by compression) when both cause the same compressive strain at the edge of the bearing. If this strain is ϵ, then

$$\gamma_c = C_c S \epsilon \tag{C-6a}$$

$$\gamma_r = C_r S \epsilon \tag{C-6b}$$

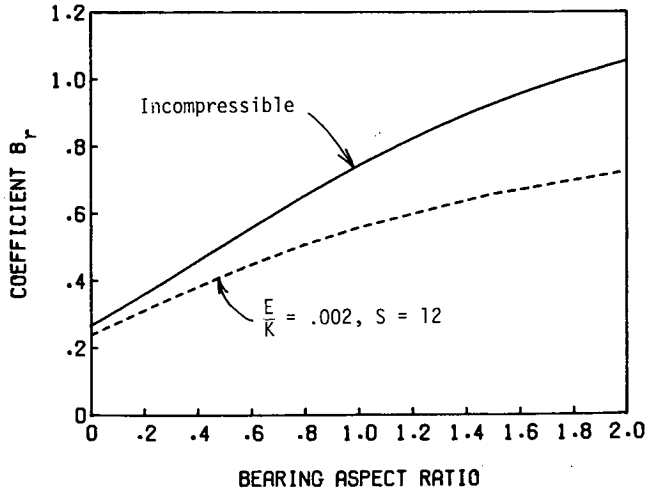

Figure C-1. Rotational stiffness coefficient B_r *vs. aspect ratio.*

where C_c is defined in Appendix B.

Thus

$$\frac{\gamma_r}{\gamma_c} = \frac{C_r}{C_c} \tag{C-7}$$

and this ratio is plotted against L/W in Figure C-3.

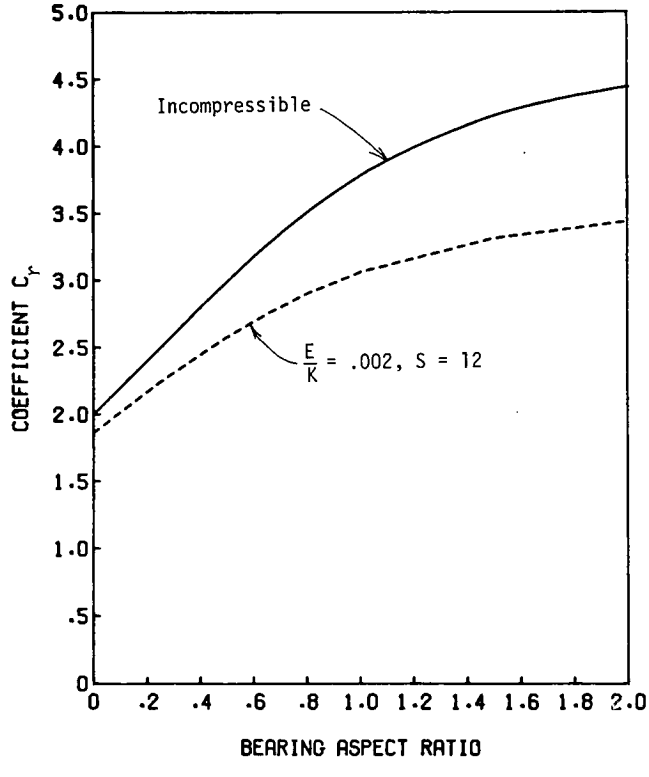

Figure C-2. Dimensionless shear strain due to rotation vs. aspect ratio.

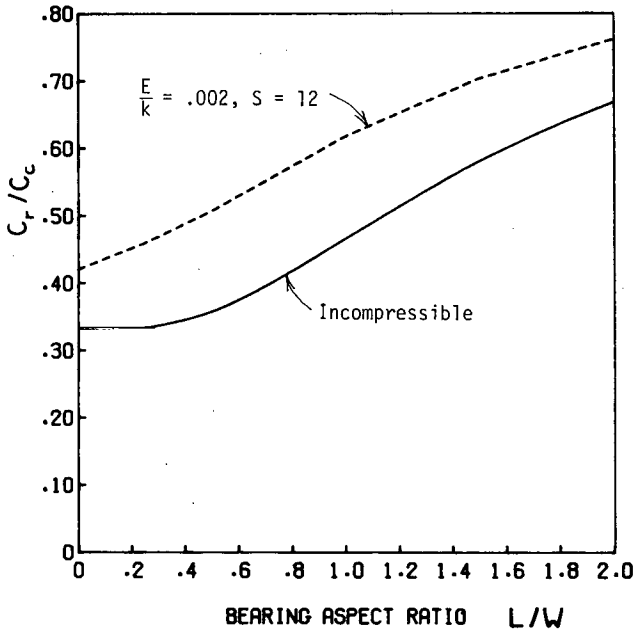

Figure C-3. Ratio of shear strains due to rotation and compression vs. aspect ratio.

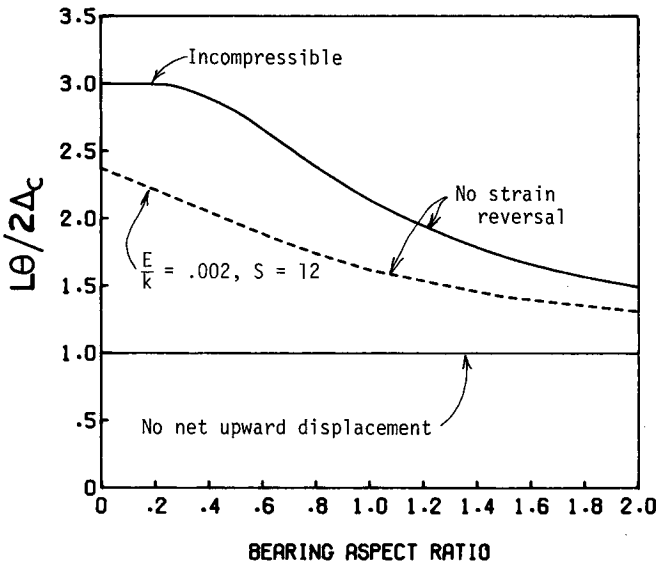

Figure C-4. Nondimensionalized allowable rotation vs. aspect ratio.

The solid line represents the incompressible case for all shape factors, and the dashed line represents the extreme case of compressibility considered. The shearing strain for rotation is seen to be ⅓ to ⅔ of that caused by compression for common bearing shapes with $L/W \leq 1.0$.

Three significant stages of rotation may be defined which could be used as criteria for design. They are:

1. Net upwards movement of the rising edge of the bearing (i.e., the upward movement due to rotation exceeds the downward movement due to compression).
2. Reversal of shear strain at the rising edge (i.e., the shear strain due to rotation becomes greater than and opposite to that due to compression).
3. Edge loading (i.e., lift-off has occurred and the rotation of the girder is greater than the rotation of the top surface of the bearing, so the girder lifts off everywhere except at one edge).

The rotations needed to cause the first two are plotted in Figure C-4.

The first criterion must result in vertical tensile stress in the elastomer at the outer edge. However, such tensile stress may, in fact, occur at smaller rotations. Simple calculations, taking into account bulging, show that overall compression on the bearing causes the outer face of the elastomeric layer to stretch vertically if the shape factor is low. If, for medium shape factors, this effect is combined with rotation, net tension could occur earlier than it would if it was predicted on the basis of rotation alone.

The second criterion could be important in light of the fact that resistance to fatigue damage has been found to be significantly better (*38*) when the material does not undergo strain reversals. However, it should be noted that Eq. C-5a predicts only the maximum shear strain, which occurs in the middle of the sides parallel to the rotation axis.

The third criterion represents a highly undesirable limit state but requires rotations about 5 times as large as those for the second criterion. The calculations used to predict it are based on the assumption that the top surface of the bearing rotates as a rigid body. In practice, such edge loading would probably cause the reinforcement to bend; therefore, the calculated value represents an upperbound to the rotation required to cause edge loading.

EXPERIMENTS

Two sets of tests were performed to evaluate rotation: true rotation tests in which moment was applied at a constant compression load, and eccentric load tests in which increasing load was applied at constant eccentricity. Previous tests conducted by others have used eccentric loads or a fixed rotation applied through a tapered load plate (*36, 37*), largely because no special equipment is required. However, the applied moment is difficult to control and measure accurately; therefore, any moment-rotation curves at constant load derived from the data are subject to larger potential for error.

True Rotation Tests

The test rig shown in Figure C-5 was designed and built for rotation tests at constant compression. The test bearings are placed between two partial cylinders of hardened steel, interleaved with enough steel packer plates to ensure that the two cylindrical surfaces lie on a circle. Two lever arms are attached to each partial cylinder, and moment is applied by means of a threaded rod between them acting through a load cell. Compressive load is applied by a universal test machine through the partial cylinders. When the nut on the threaded rod is advanced, the lever arms are pulled together, the two partial cylinders roll,

and the upper and lower surfaces of the test bearings rotate with respect to each other. The only resistance to rotation inherent in the rig is that due to rolling friction, which is small.

The vertical displacement of the bearings changes by only a second-order amount, given in this case by $2(1 - \cos \theta)$ in., where θ is the total rotation of one lever arm with respect to the other. If the compressive load applied on the universal test machine is kept constant, the total compressive load on the bearings increases slightly with moment, due to the load in the threaded rod. However, the effect is small. Vertical deflections are measured using four LVDT's at the corners of the partial cylinders, and rotations are calculated from them.

Several pilot tests were run, and details of the rig were modified to improve performance. Then, in the main test sequence, three pairs of bearings were tested in four configurations, shown in Table C-1. Each set of bearings was first subjected to a concentric compression test in the rig up to 2,000 psi, to establish a load deflection relationship. That load was released, and then rotation tests were conducted at constant compressive stresses of 500, 750, 1,000, and 1,250 psi.

The test procedure was as follows. The arms of the rig were first blocked up in a horizontal position, with no vertical load on the specimen. Zero readings were taken. A 1-kip compressive load was applied, which was enough to hold the rig in place, and the arms were released. Their weight caused them both to drop slightly, thereby imposing a small amount of shear displacement on the bearings. The compressive load was raised to the desired value, and relative rotation was then imposed using the nut and threaded rod.

The bearings eventually lifted off the center plate placed between them. Lift-off was detected by means of trying to insert a piece of paper in the gap or by placing a cotton thread between bearing and plate before the test, hanging a small weight on it and watching for its release. Neither method was perfect, but they indicated roughly when lift-off occurred. Lift-off always started at the corners of the bearings and then progressed to the middle of the tension edge, which is the location for which it is reported.

Table C-1. Bearings for true rotation tests.

Bearing	Shape	Elastomer Layers Number/Thickness	Steel Layers Number/Thickness
A 5	8" x 8"	4 / 0.375	5 / 0.066
A 7	9" dia	2 / 0.375	3 / 0.118
A 11	11.33"x5.66"	2 / 0.375	3 / 0.118

Note: Type A 11 bearings were tested about strong and weak axes separately.

The maximum relative rotation was limited so as not to inflict damage on the compression edge of the bearings. In the case of the Type A 11 bearings tested about their strong axis, it was limited by the test rig capacity.

Results are plotted in Figures C-6 through C-9. Each figure shows moment-rotation curves for one bearing at the four different compressive stresses. Lift-off is also indicated. The four curves have been slightly shifted along the rotation axis so they all pass through a common origin.

Several aspects of the behavior are worth noting. First, the curves are close to linear after an initial slightly stiffer segment. This linearity is in marked contrast to the distinctly nonlinear shape of measured compressive load-deflection curves. Second, some hysteresis is present, as is almost always the case in tests on elastomer products. Third, the rotational stiffness consistently increases with applied compressive stress for all bearings.

An attempt was made to correlate the measured and predicted rotational stiffnesses, but the accuracy of the results is limited by the fact that no experiments could be done at zero compressive stress, whereas that is the only condition for which a formal theory exists. The apparent variability of material prop-

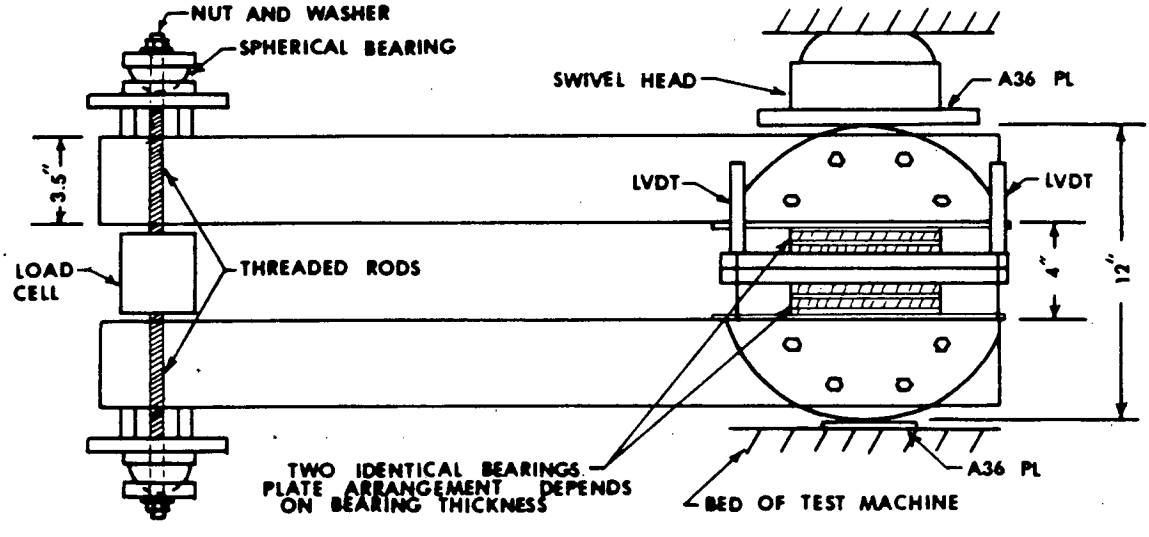

Figure C-5. Test rig for true rotation tests.

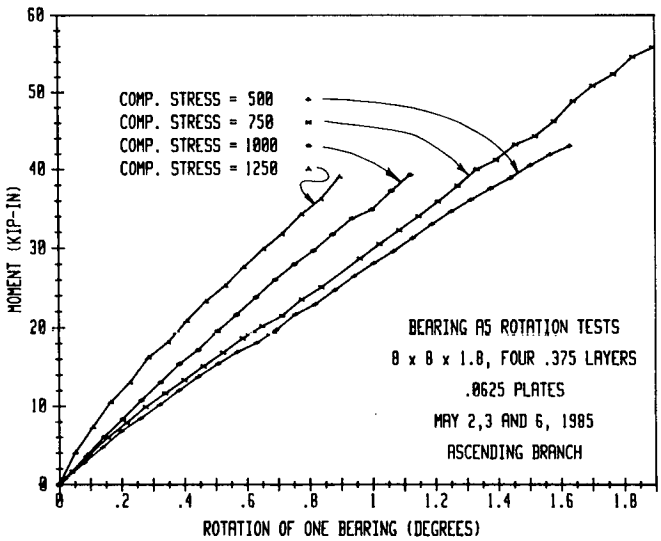

Figure C-6. Moment-rotation curves for a square bearing from the true rotation tests.

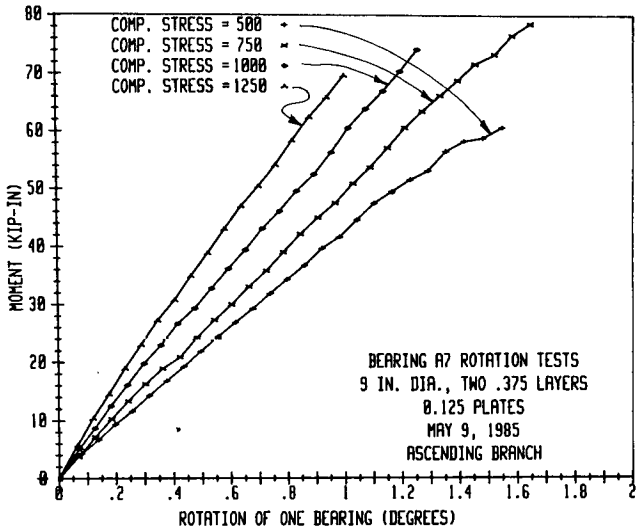

Figure C-7. Moment-rotation curves for a circular bearing from the true rotation tests.

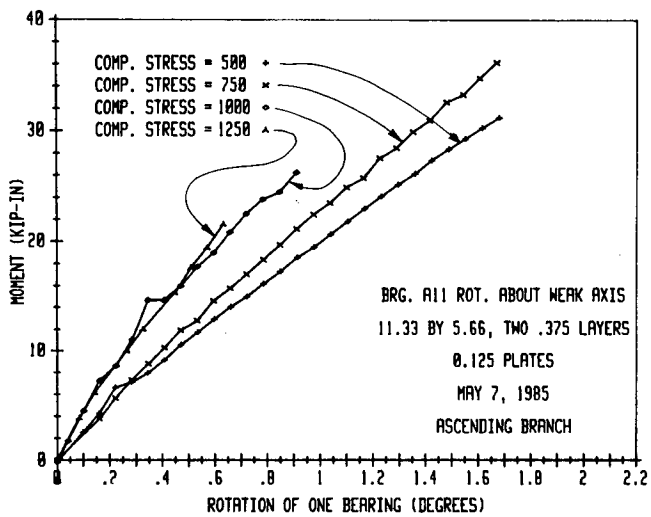

Figure C-8. Moment-rotation curves for a 2 to 1 rectangular bearing about the weak axis from the true rotation tests.

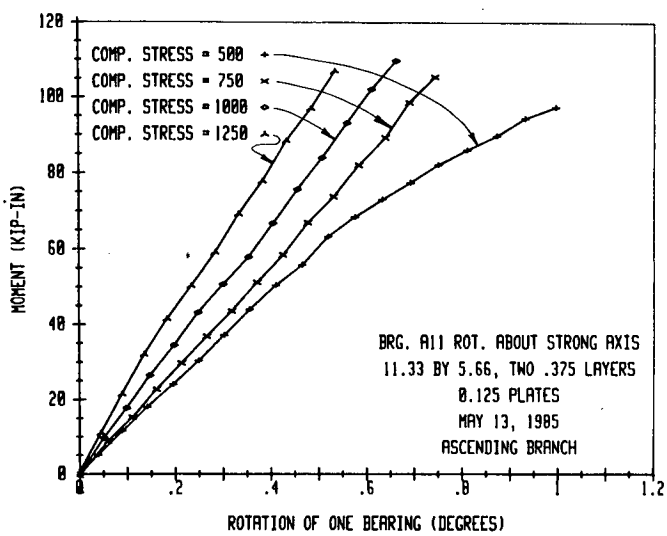

Figure C-9. Moment-rotation curves for a 2 to 1 rectangular bearing about the strong axis from the true rotation tests.

erties with strain (discussed in Appen. G) and the (slight) non-linearity of the moment-rotation curves both created difficulties as well.

The stiffness selected for comparisons was the secant value at the largest practical rotation for each bearing (1.0° for A 9 and A 11 (weak), 0.9° for A 5 and 0.5° for A 11 (strong)). These are given in Table C-2, and in Figure C-10 as multiples of the stiffness at 500 psi. The increase in stiffness with compressive stress is different for each bearing, and was largest for the A 11 (strong) bearing. The fact that the A 11 (weak) bearing showed the next greatest stiffening suggests that stiffening is more closely related to material properties than plan shape, but this hypothesis is tentative because of the difficulties noted previously. Back-projecting the curves to a compressive stress of 0 psi suggests that the stiffness at 0 psi lies between 0.8 and 1.0 times the stiffness at 500 psi. Assuming the 0.8 figures, E = 351 psi (from the shear tests described in Appen. G), and A_r = 1.0, the "measured" B_r values given in Table C-2 are obtained. No basis for comparison exists for the circular bearing, but the three rectangular bearings are compared with theoretical B_r values from Figure C-1. E/K was taken as 0.001 . The measured values are smaller than the theoretical values, with the difference steadily increasing with L/W. In all cases the correlation would be slightly closer if A_r was taken as 0.0, as implied by Conversy (*16*). The ratio of measured/theoretical stiffness would then reach 0.90 for the narrowest bearing (A 11), which is reasonable in view of the uncertainties involved.

No reliable way of measuring the shear stress or strain in the elastomer was found, so the predicted values could not be verified. The theoretical strains are based on assumptions such as plane sections remaining plane and parabolic bulging of elastomer. Observations during the experiments suggest that these assumptions are approximately correct, but it is likely that local strains would be very sensitive to minor variations from the assumed displacement field. This is particularly true at the critical location, at the edge of the steel-elastomer interface. As a result, only theoretical predictions are available for the strains in the elastomer, and these results should be viewed with caution. Strain gages were attached to the steel reinforcement during some of these tests. Readings from them were often erratic under increasing compressive load, which was attributed to initial imperfections. However, the measured strains were insensitive to increased rotation, indicating that the stress (and strain) in the reinforcement are not greatly influenced by moment or rotation. This finding is in agreement with theoretical predictions.

Table C-2. Stiffnesses from true rotation tests.

Bearing	Shape	Meas. Stiffness (in-kip/deg)	$EI(\sigma_c=0)$ (in-kip)	B_r (meas)	B_r (theo)	B_r meas/ theo
A 5	8" x 8"	25.0 26.7 32.5 38.9	1719	0.470	0.713	0.659
A 7	9" dia	42.2 48.5 58.2 69.0	1455	0.330	-	-
A 11 (Weak)	5.66"x11.33"	19.6 22.6 28.4 33.4	674	0.404	0.495	0.817
A 11 (Strong)	11.33"x5.66"	108.0 137.0 163.0 198.0	3713	0.570	0.995	0.573

Eccentric Load Tests

A number of bearings of different size, shape, and shape factor were tested under rotation induced by eccentric loading. The load was applied through a 1 in. × 1 in. steel bar, which was chamfered so that the loaded area was ¼ in. wide, causing the bar to act much like a knife edge. The use of a knife edge required heavy plates to distribute the load evenly to the bearing, as shown in Figure C-11. The knife edge loading was applied at different eccentricities, and the compressive deflection and rotation were measured with 4 LVDT's as shown in the photograph. The thick loading plates rotated with the bearing, introducing a shear deformation in addition to compression and rotation, and increasing the eccentricity of the load on the bearing. This added eccentricity must be added to the knife edge eccentricity in computing the true moment on the bearing.

Square, circular, and rectangular bearings were tested with shape factors varying between 5 and 10. The material was nominally the same 55 hardness elastomer for all tests. The loads were applied with a 2.4 million pound Baldwin Hydraulic Test machine, and the loads and deflections were recorded with a Hewlett Packard computerized data acquisition system. The tests are summarized in Table C-3. A typical load vs. rotation curve for a 16-in. square bearing with different eccentricities is

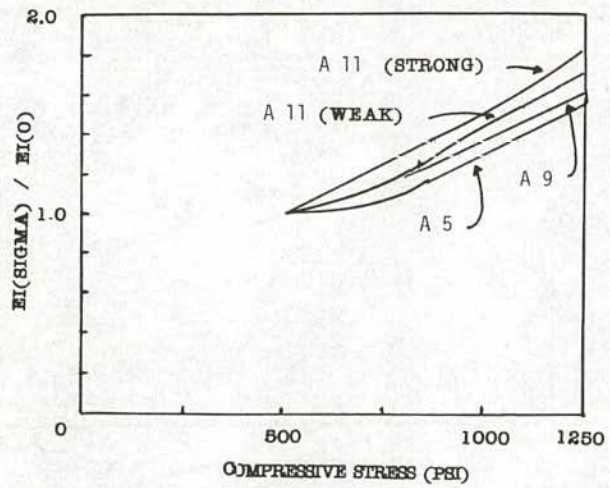

Figure C-10. Comparison of the normalized experimental rotational stiffness for different bearing shapes.

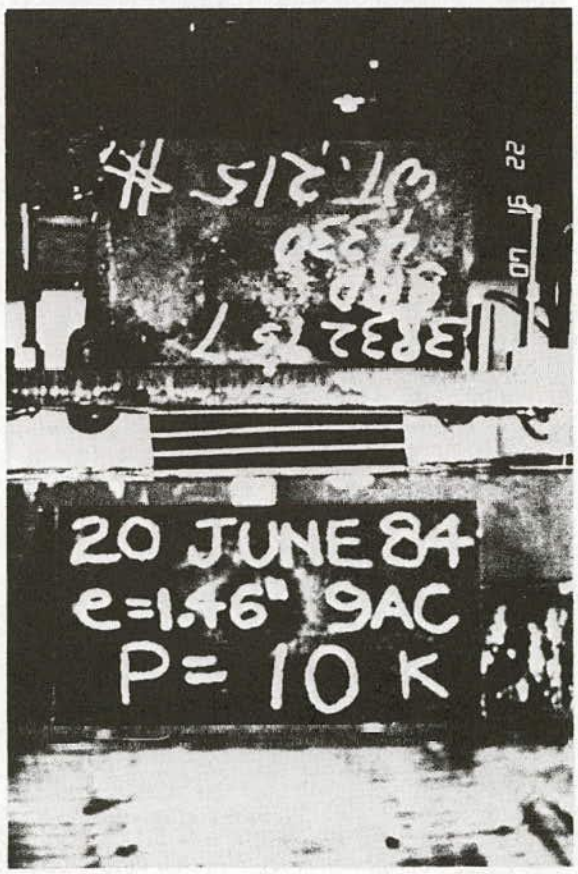

Figure C-11. Test setup for the eccentric load rotation tests.

Table C-3. Eccentric load test specimens.

Bearing	Shape	Elastomer Layers	Shape Factor	Ecc. (in)	Max. Load (kip)
5 A	16" dia	4 @ 0.368"	10.93	0 1 2 4	600 600 600 600
6 A	16" x 16"	4 @ 0.368"	10.89	0 1 2.67 4	300 750 750 750
8 A	16" x 6"	4 @ 0.369"	5.95	0 1 1.5	300 225 150
9 A	11.75"x 23.75"	4 @ 0.392"	10.26	0 1 2 3	775 700 700 775
9 AA 9 AB 9 AC 9 AD	5.88"x 11.88" 5.88"x 11.88" 5.88"x 11.88" 5.88"x 11.88"	4 @ 0.392" 4 @ 0.392" 4 @ 0.392" 4 @ 0.392"	5.0 5.0 5.0 5.0	0 0 1.46 0.97	750* 565* 240 420

(Note: * denotes test to reinforcement failure)

shown in Figure C-12. The figure shows that there was a small amount of rotation when the eccentricity was nominally zero. This is attributed to the fact that the specimen could only be aligned to an accuracy of about ± 1/16 in. in the rig. The effect was observed in all tests with this rig. Moment-rotation curves at fixed compressive stress levels were then obtained by taking a single moment-rotation pair from each eccentric loading curve. Figure C-13 illustrates typical moment-rotation curves for the bearing in Figure C-12. All four curves are nearly linear for small eccentricities, but they become nonlinear for large eccentricities. This nonlinearity appeared to be caused by lift-off of the load plates from the bearing, which invariably occurred at the largest eccentricities. Lift-off did not appear to cause any distress within the elastomer, but it caused severe bending of the plates and increased bulging and strains in the elastomer. It is believed that these deformations greatly increase the potential for fatigue damage, rupture of the plates and delamination of the elastomer, and should be avoided. The slope of the moment-rotation curves generally increased as the compressive load increased, as observed in the true rotation tests.

Attempts were made to test two steel-reinforced bearings (9 AC and 9 AD) and one fiber-reinforced bearing to failure under eccentric compression. The two steel-reinforced bearings suffered extensive debonding, and the loading was stopped before the reinforcement fractured. Specimen 9 AC was tested at 1.5-in. eccentricity (one-fourth of the bearing width) up to 740 kip (3,300 psi), at which load the rotation was large enough to cause hard contact at one of the plates supporting the knife edge. At the tension edge, lift-off occurred and the elastomer displaced inwards to a concave shape. Debonding occurred on both sides of the bearing, but on the tension side it was aggravated by debonding damage from a previous test. Speciman 9 AD was loaded at 1-in. eccentricity (at the kern) to 420 kip (5,830 psi), at which load extensive debonding had taken place. The test was again stopped because of hard contact. Yielding and stretching of the plates was also evident because they buckled when the elastomer tried to return to its original shape on unloading.

An attempt was made to test a fiberglass-reinforced bearing (specimen F-6) to destruction at an eccentricity of 2.0 in. (well outside the kern) but the bearing squeezed out of the test rig sideways. It was repositioned in the rig, and then loaded to failure of the reinforcement (at 2.1 ksi average compressive stress) at an eccentricity of 0.75 in. This is about 25 percent below the strength of the concentrically loaded bearing with no holes, and about the same as the concentrically loaded bearing with 2 holes.

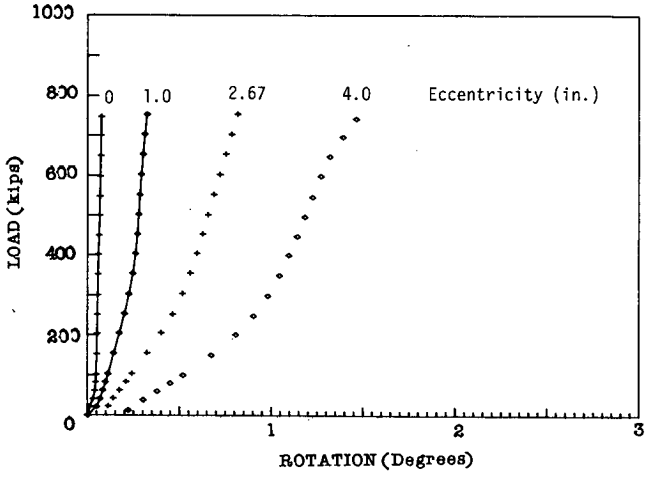

Figure C-12. Load-rotation test results at different eccentricities for a 16-in. square bearing.

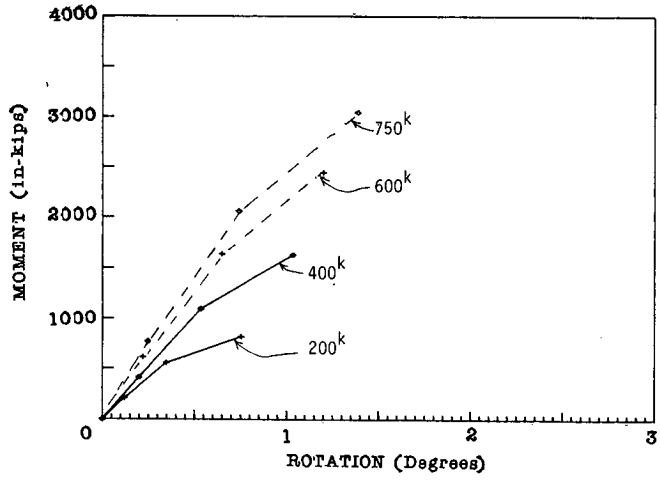

Figure C-13. Moment-rotation curves derived from the eccentric load tests for a 16-in. square bearing.

SUMMARY AND CONCLUSIONS

1. Tests were conducted to study eccentric compression and constant compression accompanied by variable moment.

2. Eccentric load tests on steel-reinforced bearings showed a moment rotation curve that was roughly linear (but softened slightly in most cases at higher moments) and had a slope which increased with increasing compressive load.

3. The true rotation test showed a moment-rotation curve that was closer to linear. The rotational stiffness increased with compressive load.

4. Eccentric load tests on a fiberglass-reinforced bearing showed an almost linear, but slightly softening, moment rotation-curve, whose slope was predicted by linear theory, counting only the thicker (3/8 in.) layers.

5. In tests to failure with eccentric load:

- The fiberglass-reinforced bearing slid out of place when the eccentricity was 2 in. (158 percent of the kern distance).
- The fiberglass reinforcement broke at a load about 25 percent lower than the concentric failure load when tested at 0.75-in. eccentricity (60 percent of the kern distance).
- In the steel-reinforced bearing loaded at the kern point, the reinforcement yielded and debonded, but limitations of the rig caused the test to be stopped before fracture of the reinforcement.
- In the steel-reinforced bearing loaded at 1.5 in. (150 percent of the kern distance) no yield occurred, but the test was stopped because the test rig reached its maximum rotation. Debonding was extensive.

6. The linear elastic analysis methods were evaluated. They appear to provide good general comparison with experimenal results for rotational stiffness. It was not possible to verify experimentally the strains in the elastomer predicted by theory.

APPENDIX D

SHEAR AND COMBINED LOADING

INTRODUCTION

Shear deformation is a very important aspect of elastomeric bridge bearing behavior. Shear deformation accommodates thermal expansion and contraction of the bridge superstructure and creep and shrinkage of concrete girders. In some elastically restrained structures, shear stresses in the bearing also resist vehicle acceleration and braking forces. Previous research (*3*) has suggested that a shear stiffness test on a completed bearing is the most reliable measure of quality control for the elastomer used. Therefore, a good understanding of shear behavior is essential to bearing design.

Many factors (*3*) affect the shear stiffness and general shear behavior of elastomeric bearings. The force deflection behavior generally appears to be nearly linear and can be approximated by the equation

$$H = G_a \frac{\Delta_s A_s}{h_{rt}} \qquad \text{(D-1)}$$

where G_a is the apparent shear modulus, A_s is the plan area of bearing effective in shear, Δ_s is the shear deformation as defined in Figure D-1, H is shear force, and h_{rt} is the total thickness of the elastomer. It is generally not practical to test bearings under pure shear or even simple shear, because a substantial compressive load is needed to develop the friction required to prevent slip under shear loading. This compression causes the bearing to bulge, which introduces uncertainty as to the loaded area that should be used in Eq. D-1 (*40*). Further, the addition of a compressive load introduces the potential for instability and buckling, which may greatly modify the apparent shear stiffness of the elastomer. Porter and Meinecke (*40*) suggest that there is a geometric effect associated with shear deformation. They included a horizontal component of the compression load when

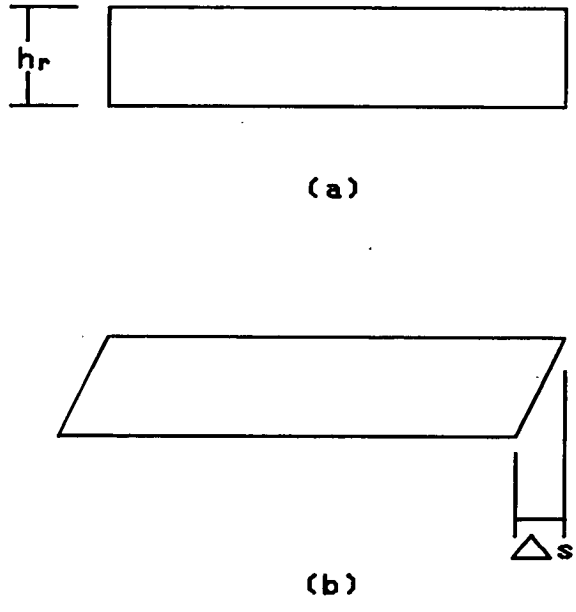

Figure D-1. Geometry and typical shear deformation of an elastomeric bearing.

analyzing the experimental results of bearings with a shape factor of 0.6. It has also been suggested that the shape and shape factor of the bearing may affect the shear behavior, but it is generally believed that this effect is smaller than that observed for stability and the bulging effect. An experimental program was performed to evaluate these effects and to determine which effects are important in elastomeric bearing design. Many shear tests were performed. Some were used to estimate the material properties of the bearings used in the stability tests, and these are described in Appendix G. Others were conducted at intervals throughout the fatigue tests to obtain a measure of the change in bearing stiffness due to cracking, and these tests are discussed in Appendix F. This appendix provides an overview of shear behavior. The general test configuration is described, and a few tests on bearings with different sizes, shapes, and shape factors are described in greater detail. General observations from the test results and the basic requirements for the performance and interpretation of shear test results are presented. The tests described in this appendix were conducted in an attempt to address several specific questions raised in earlier research (*3*). These include:

1. Is the simple shear model (Eq. D-1) reliable for designing bearings and predicting their behavior?
2. What, if any, failure modes are associated with shear deformation and what is a reasonable design limit for it?
3. What are the requirements for a repeatable shear test? How should the test be performed? How should the results be interpreted? What variation in the results must be expected?

TEST APPARATUS

Shear tests were performed on different bearings with different materials, sizes, shapes, shape factors, loads, and load rates. The bearings were always tested in pairs as shown in Figure D-2, in conjunction with an applied compression load. The two bearings were separated by a steel plate, to which a horizontal load $2H$ was applied. The steel plates were part of a self-equilibrating shear frame, which maintained a balance of horizontal shear loads but allowed the bearings to deform freely in compression.

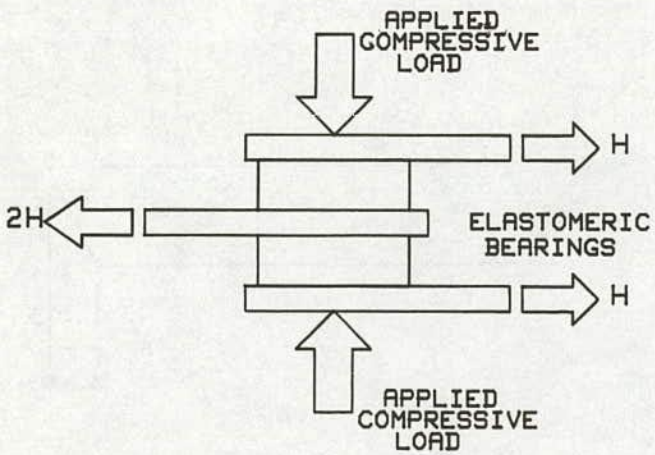

Figure D-2. General shear test configuration.

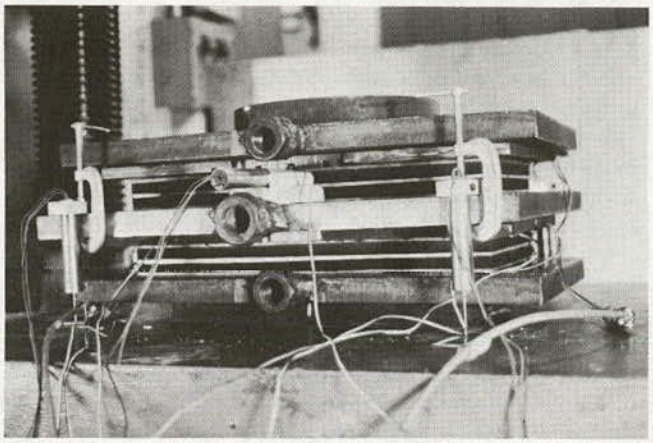

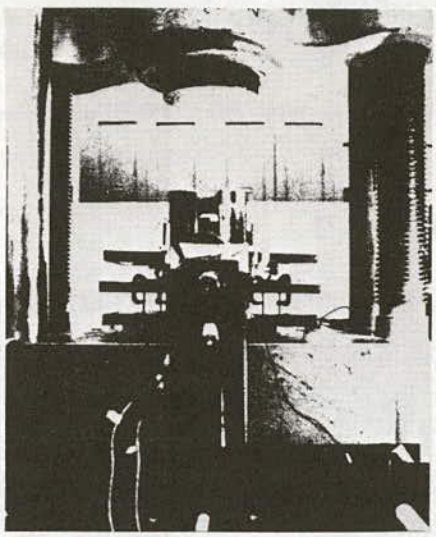

Figure D-3. Test rig for shear loading.

The shear and compressive deformations and the applied loads, P and $2H$, were measured with LVDT's (linear variable differential transformers) and load cells, respectively. The data were accumulated with a Hewlett Packard computerized data acquisition system.

Figure D-3 shows two photographs of the test rig, although a modified rig (*42, 43*) was required for the larger circular bearings. The compression was applied with a Baldwin hydraulic testing machine, and it was held as nearly constant as possible during the shear deformation. The applied shearing load, $2H$, was applied with a pair of hydraulic center-hole rams to which the hydraulic pressure was applied by a pump. Each ram acted only in compression, and the pair were oriented in opposing directions to permit cyclic loading. The vertical deflections were measured at the four corners of the test rig, and shear deflections were measured at two locations.

The shear load was cycled in all tests, including those described in Appendixes E, F, and G. In the tests described here, the shear strain varied between ± 100 percent strain, and the average compressive stress varied between 0 and 3,000 psi. The compressive stress was applied and held for a short period before the two complete cycles of shear deformation were slowly but continuously imposed. Data were taken at intervals during loading. For most tests (*43*), the two bearings were cut from a single sheet so that the material properties and geometry were theoretically the same. However, this was impractical for the two large circular bearings (*42*), Table D-1 summarizes the bearing sizes, geometry, and load ratios employed in these tests. Strain gages were attached to the steel laminates for several of these tests, and the steel strains were monitored with the load and deformation.

Table D-1. Properties of bearings used in shear tests.

Plan Dimensions	Layer Thickness	Total Elastomer Thickness	Compressive Stress Level (kips)	Shear Strain Range
8" x 8"	.375"	1.50"	25 50 75 100	-.60 to +.60 -.80 to +.80 -1.0 to +1.0 -1.0 to +1.0
4" x 16"	.30"	.60"	40 80 120 150	-.75 to +.75 -1.0 to +1.0 -1.0 to +1.0 -1.0 to +1.0
9" Dia	.425"	.85"	25 50 75 100	-.50 to +.50 -1.0 to +1.0 -1.0 to +1.0 -1.0 to +1.0
5.66" x 1.3"	.385"	.77"	50 100 150 200	-1.0 to +1.0 -1.0 to +1.0 -1.0 to +1.0 -1.0 to +1.0
24" Dia	.625"	2.62"	226 488 905 1357	-0.0 to +.60 -0.0 to +.60 -0.0 to +.60 -0.0 to +.60

TEST RESULTS

Figure D-4 shows a typical cyclic stress strain curve from a test conducted with constant compressive load. The nominal shear stress is

$$\tau_s = \frac{H}{A_s} \tag{D-2}$$

and the nominal strain is

$$\gamma_s = \frac{\Delta_s}{h_{rt}} \tag{D-3}$$

The curves invariably were approximately linear with a distinct observable hysteresis. The stiffness of slope of the curve generally decreased for the second and subsequent cycles, but the stiffness remained more stable for later cycles. This suggests that a shear test will produce more repeatable results if the stiffness of a later cycle is employed. Further, the stiffness generally was larger at small values of strain than at large values of strain.

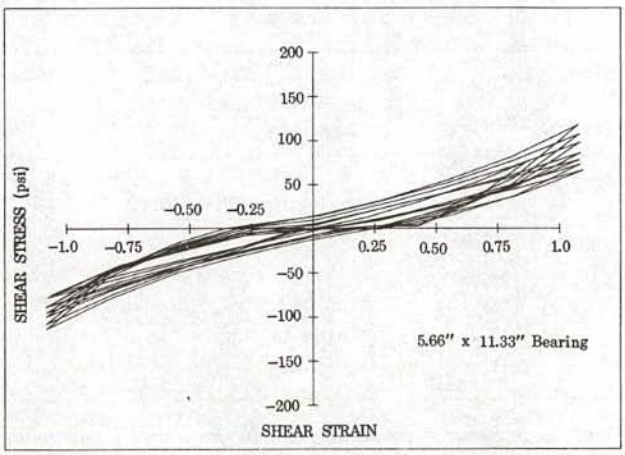

Figure D-4. Typical cyclic shear stress-strain curve.

All specimens were cycled to relatively large strains. Figure D-5 is a photograph of a typical fully deformed bearing. The bearing deformation approximates simple shear with roll-over at the corners as noted in previous research (*3*) and is probably due to the stress free boundary that must exist at the edge of the bearing. The roll-over is not clearly seen in the photograph. It is first visible at shear strains, Δ_s, greater than 50 percent and increases dramatically at higher values. Observations during the tests showed that extreme roll-over could aggravate debonding of the steel laminates and could potentially damage the laminate in bearings with thin reinforcement. Some debonding was observed at large shear strains in several of the tests. However, there was no clear evidence of failure of the reinforcement due to shear deformation in any of the bearings.

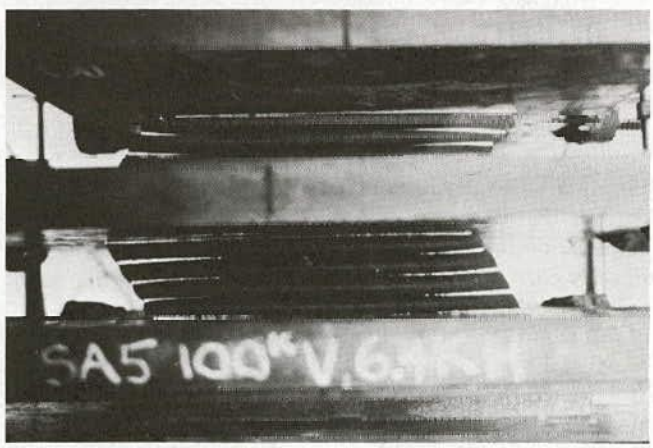

Figure D-5. A typical bearing fully strained in shear.

Figures D-6, D-7, D-8, and D-9 show the shear stress-strain curves for a circular, square, 2 to 1 rectangular, and 4 to 1 rectangular bearing, respectively. The material and shape factors were nominally the same for all bearings. The curves represent the first half cycle of shear loading of each specimen at different compressive loads and clearly illustrate that the shear stiffness is influenced by the compressive load. However, the form of this influence is not obvious from the plots. It is generally believed (*3, 41*) that the apparent shear modulus, G_a, is reduced with increasing compressive load due to stability effects, as

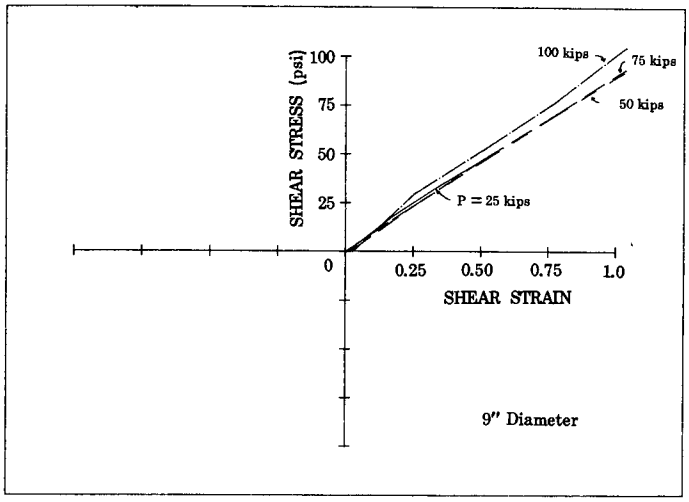

Figure D-6. Shear stress-strain behavior for a circular bearing.

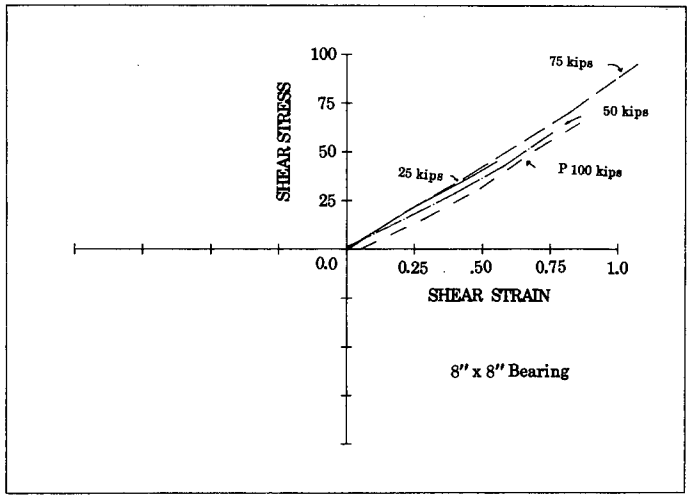

Figure D-7. Shear stress-strain behavior for a square bearing.

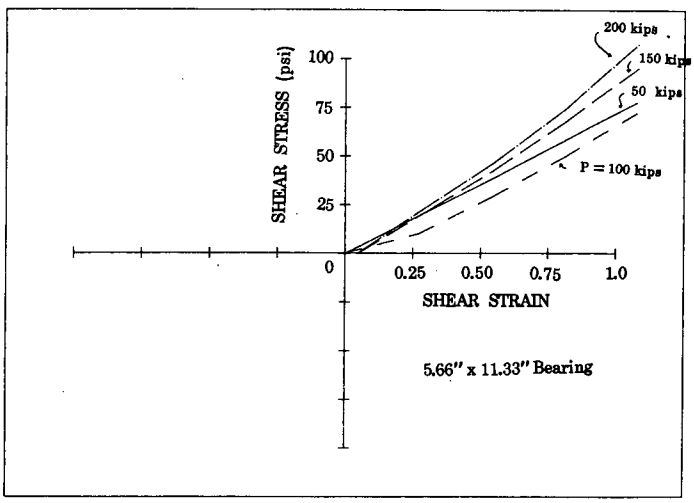

Figure D-8. Shear stress-strain behavior for a 2 to 1 rectangular bearing.

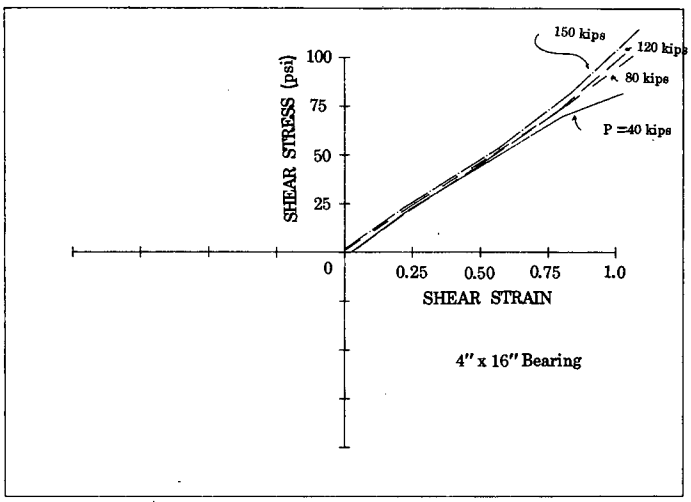

Figure D-9. Shear stress-strain behavior for a 4 to 1 rectangular bearing.

discussed in detail in Appendix E. However, an increase in G_a also occurs with increasing compressive load because of the reduced thickness, the increased bulging, and the correspondingly increased shear area of the bearing (*3, 40*). Figure D-10 combines all of the data of the preceding four figures. This suggests that the shape of the bearing does not have a great influence on the shear stiffness. Any influence of shape, presumably caused by differences in the bending and compression stiffness for different shaped bearings, is probably less significant than the influence of the applied load. This is particularly true if the strains are limited to less than 50 percent. The analysis of these effects is discussed in Appendix E, but it should be noted that these stability concepts were applied to the four test bearings with only partial success, because the stability and bulging corrections did not remove all scatter from the data.

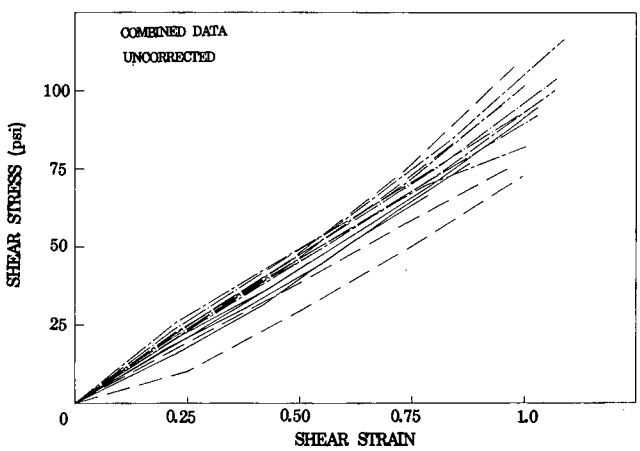

Figure D-10. Combined shear stress-strain data for all four bearings.

Strain gages were attached to the steel reinforcement for the four specimens described earlier. The strains were monitored during the application of the compressive load and during application of the cyclic shear deformation with the constant compression. The steel strains varied significantly with the application of the compression load, but they were relatively insensitive to the cyclic shear loads. This suggests that considerable stress is introduced into the reinforcing steel by compressive load but not by shear force.

The vertical deflection of the test specimens were monitored at the four corners of the bearings. Figures D-11 and D-12 show typical plots of the average compressive strains (i.e., the average vertical deflection divided by the total unloaded elastomer thickness) as a function of shear stress from different compressive loads. These figures indicate that the average compressive strain tends to increase during shear cycling when the compressive load is held constant. The strain increase is largest for the first cycle and generally tends to grow smaller for later cycles. This apparent softening of the material with cycling is somewhat analogous to the reduction in apparent shear stiffness that occurs with shear cycling. The average compressive strain also tends to be smaller at large shear strain levels. The reason for this phenomenon is not clear. Generally, an increase in compressive strain implies that bulging is increasing, and therefore the apparent shear stiffness should increase. Thus, the behavior illustrated in Figures D-11 and D-12 may be symptomatic of a nonlinear material behavior, or it may reflect the fact that the shear displacement reduces the area effective in resisting compression, leading to larger compressive strains. The cause cannot be determined with certainty because the effects were too small and were not sufficiently consistent from one test to another.

Several shear tests were also performed on a pair of large (24-in. diameter) bearings made of natural rubber of nominal 60 Shore A durometer hardness and a nominal shape factor of 9.3. The elastomeric compound used in these bearings was different from the others discussed in this appendix, and so the curves cannot be compared directly. However, the general stress-strain behavior was similar to that of the smaller specimens. That is, the stress-strain behavior was approximately linear with an observable hysteresis. Local debonding was observed at a few locations at the extreme loads and deformations.

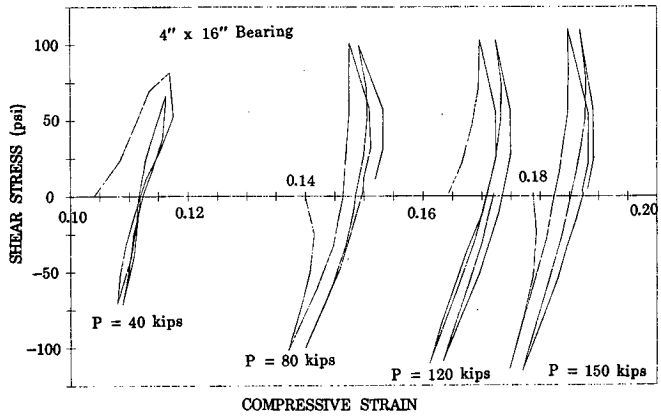

Figure D-11. Average shear stress vs. average compressive strain for a 4 to 1 rectangular bearing.

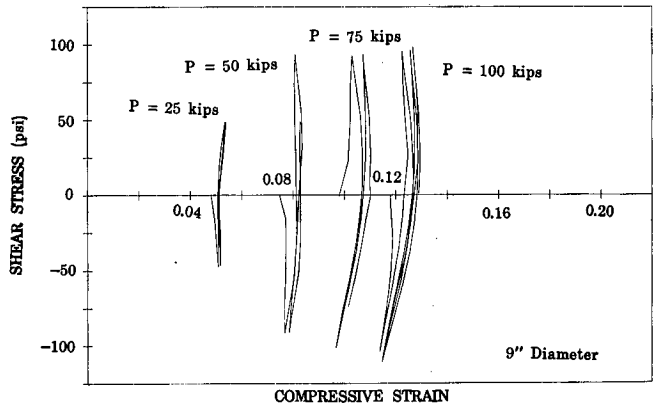

Figure D-12. Average shear stress vs. average compressive strain for a circular bearing.

SUMMARY AND CONCLUSIONS

1. Shear stiffness is an important property in elastomeric bridge bearing design, because it controls the magnitude of bearing shear forces that are transmitted to the bridge due to movements such as creep, shrinkage, and thermal expansion. Further, the shear stiffness is probably the most reliable measure of the elastic properties of the elastomer, and therefore is a reasonable acceptance criterion for elastomeric bearings.

2. In evaluating shear behavior, the simple linear model provided by Eq. D-1 is suitable for most practical applications. The experiments described in this appendix confirmed that the force-deflection relationship is approximately linear. There is some hysteresis and other evidence of nonlinear material behavior, but these effects appear to be acceptably small if the apparent shear modulus, G_a, is corrected for instability and for bulging due to compression. These corrections are discussed in greater detail in Appendixes E and G. However, these corrections are not precise, and some scatter in the shear stiffness data must be expected.

3. A shear test, which is used for the accceptance testing of bearings, is best performed with bearings in pairs, because this produces a symmetrical test configuration. Further, it tends to average out variations in material properties. A compressive force is needed to clamp the pair of bearings and to develop the friction needed to prevent slip. The shear stiffness decreases significantly with the first few cycles of loading, but remains fairly stable after that. This suggests that acceptance tests should be based on the stiffness of later cycles such as the 5th, inasmuch as these are likely to be more repeatable. However, it should be remembered that the bearing stiffness relevant to stability or deformation in the field is more likely to be related to the stiffness during the first cycle and will be slightly larger than the acceptance test value.

4. Bearings subjected to combined shear and compressive load exhibit a simple shear type of deformation. However, the corners of the bearing begin to roll over if the shear strain exceeds approximately 50 percent. The combined shear and

compression loading causes a concentration of shear strain at the edge of the bearing. This strain concentration causes local delamination in some cases. The roll-over effect exacerbates the strain problem. Further, roll-over increases the probability of damage to the edge of thin steel laminate. In view of these factors, it is believed that the shear strain, γ_s, should be limited to 50 percent rather than the 70 percent employed in some specifications (*3*).

5. Shear stiffness may be affected by the shape of the bearing, but the effect appears to be smaller than the compressive load effects and may well be caused by differences in the bending stiffness of the different shaped bearings.
6. Shear deformation does not appear to cause any significant stress in the reinforcing steel.

APPENDIX E

STABILITY

INTRODUCTION

Tall, slender structural components may fail by instability rather than material rupture. Elastomeric bearings are no exception. In addition, their unusual mechanical properties lead to complex buckling behavior not found in columns made of conventional structural materials, and buckling controls their failure at slenderness ratios that seem very low.

The present AASHTO *Specifications* (*1*) require the height of a rectangular bearing to be no greater than one-third of its least lateral dimension, effectively eliminating any possibility of buckling failure. The least restrictive specifications are the now outdated BE 1/76 (*27*), which contain no formal limits but advise the designer to investigate buckling when the bearing's height-to-width ratio exceeds 1.0. The Australian specifications (*28*) follow BE 1/76, and some bearings have been installed there with heights about equal to their widths. Seismic isolation bearings often have similar proportions.

Low bearings with large plan areas resist vertical loads well, but they must undergo large shear strains in order to accommodate the necessary bridge movements. These strains cause large horizontal forces, which can increase the costs of bridge piers and foundations. Taller bearings would be less stiff in shear and could lead to cost savings in the substructure which would more than offset the extra bearing cost. Buckling controls the maximum height, so an understanding of it is important if designers are to take advantage of the benefits of more slender bearings.

In practice, potential buckling problems are restricted to reinforced bearings. An unreinforced pad tall enough to buckle would be far too flexible in compression and would have no use in bridge engineering.

THEORETICAL BACKGROUND

General

Two features of tall bearing behavior are important: the critical compressive load to cause buckling and the effective shearing stiffness, or transverse stiffness, when a compressive load acts simultaneously. The basic Euler theory (*45*) proves inadequate for calculation of either quantity because it is necessary to account for shear deformations in the bearing (which are ignored in the Euler theory but may be large compared to the bending deflections in a bearing) and because the bearing geometry changes significantly under compressive load. Theories exist for modifying the linear Euler theory to include the effects of shear flexibility, and they are discussed in the following section. Accounting for the nonlinearities caused by changes in bearing geometry is more difficult, and is discussed later in this appendix.

Linear Theories Including Shear Flexibility

At least two different ways of including shear deformations in a linear buckling theory exist (*45*). When the shear flexibility of the column becomes negligibly small, both approaches return the traditional Euler solution, but they give very different critical loads for shear-flexible columns. Both are continuum theories appropriate for a homogeneous medium, whereas a reinforced bearing is a nonhomogeneous composite in which the steel and elastomer components have very different properties. If these theories are to be applied to reinforced bearings, the way in which the equivalent continuum properties are derived and the choice of theory are both important.

Figure E-1 shows free body diagrams for the two theories. In both, place sections are assumed to remain plane, but planes normal to the center line of the column before loading do not remain so after loading. The following relationships then hold.

The deflection at any point along the center line is defined as $(u(x), v(x))$, and the total rotation of any cross section is $\psi(x)$. Assuming deflections small enough that $(dv/dx) << 1$, the displacements of a general point (x, y) are

$$u(x,y) \doteq \bar{u}(x,y) - y\psi(x) \tag{E-1}$$

$$v(x,y) \doteq \bar{v}(x) \tag{E-2}$$

Strain-displacement relations:

$$\epsilon_{xx} = \frac{\partial u}{\partial x} = \frac{\partial \bar{u}}{\partial x} - y\frac{\partial \psi}{\partial x} \tag{E-3}$$

$$\gamma_{xy} = \frac{\partial u}{\partial y} + \frac{\partial v}{\partial x} = -\psi + \frac{\partial \bar{v}}{\partial x} \tag{E-4}$$

Constitutive relations:

$$\sigma_{xx} = E\,\epsilon_{xx} = E\frac{\partial \bar{u}}{\partial x} - y\frac{\partial \psi}{\partial x} \tag{E-5}$$

$$\bar{\tau}_{xy} = G\gamma_{xy} = G\left(\frac{\partial \bar{v}}{\partial x} - \psi\right) \tag{E-6}$$

where E is Young's modulus and G is the shear modulus of the material. Force-displacement relations:

$$M(x) = \int_A y\,\sigma_{xx}dA = -EI\frac{\partial \psi}{\partial x} \tag{E-7}$$

$$V(x) = \int_A \bar{\tau}_{xy}dA = GA_s\left(\frac{\partial \bar{v}}{\partial x} - \psi\right) \tag{E-8}$$

where A_s is the area effective in shear, and I is the rotational moment of inertia of the cross section.

The above equations hold for both theories. In Engesser's theory (*46*) (Fig. E-1a) the shear force defined by Eq. E-8 is assumed to act in a direction perpendicular to the deflected center line of the column, giving equilibrium equations

$$M = M_o + H(x + \bar{u}) = P\bar{v} \tag{E-9}$$

$$V = H\cos\left(\frac{\partial \bar{v}}{\partial x}\right) + P\sin\left(\frac{\partial \bar{v}}{\partial x}\right) \tag{E-10}$$

$$\doteq H + P\frac{\partial \bar{v}}{\partial x}$$

if second order terms are ignored.

Combining Eqs. E-7 through E-10, assuming that u is negligible compared to x, and eliminating u gives

$$EI\frac{\partial^2 \bar{v}}{\partial x^2}\left(1 - \frac{P}{GA_s}\right) + P\bar{v} = -M_o - Hx \tag{E-11}$$

In Haringx's theory (*47*) (Fig. E-1b), the shear force V is assumed to act parallel to the rotated plane section, so Eq. E-9 holds true but Eq. E-10 is replaced by

$$V \doteq H + P\psi \tag{E-12}$$

leading to

$$\frac{EI\dfrac{\partial^2 \bar{v}}{\partial x^2}}{\left(1 + \dfrac{P}{GA_s}\right)} + P\bar{v} = -M_o - Hx \tag{E-13}$$

For a column of length L_c which is fixed against rotation at both ends but is free to translate, the boundary conditions (for both theories) are

$$\psi(0) = \psi(L_c) = 0 \tag{E-14}$$

For Engesser's approach, setting

$$\xi = \left(1 - \frac{P}{GA_s}\right) \tag{E-15a}$$

$$q^2 = \frac{P}{\xi EI} \tag{E-15b}$$

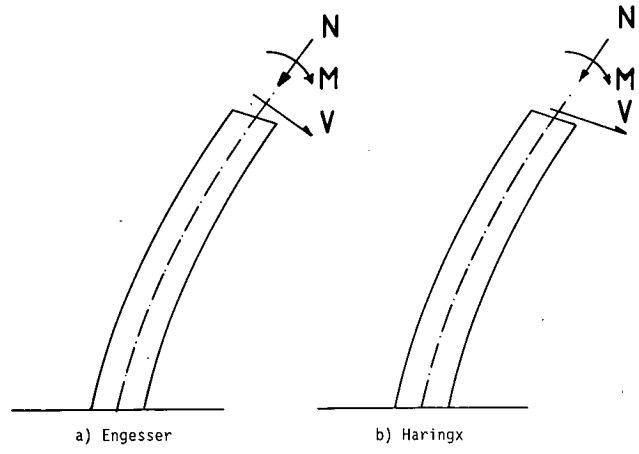

Figure E-1. Free body diagrams for shear-flexible buckling theories.

Then

$$\frac{\bar{v}(L_c)}{H} = \frac{2(1-\cos qL_c) - \xi qL_c \sin qL_c}{P\xi q \sin qL_c} = \frac{L_c}{P}\left(\frac{\tan qL_c/2}{\xi qL_c/2} - 1\right) \tag{E-16}$$

This is the transverse flexibility of the column. For small values of P (i.e., $qL_c << 1$), it reduces to

$$\frac{\bar{v}(L_c)}{H} = \left(\frac{1}{\xi}\right)\left(\frac{L_c}{GA_s} + \frac{L_c^3}{12EI}\right) \tag{E-17}$$

as it should. The flexibility becomes infinite (i.e., the stiffness falls to zero) when $qL_c = n\pi$, where $n = 1,2,3\ldots$, or

$$\frac{PL_c^2}{\xi EI} = n^2\pi^2 \tag{E-18a}$$

so

$$\frac{1}{P_{cr}} = \frac{1}{P_n} + \frac{1}{P_s} \tag{E-18b}$$

where

$$P_n = n^2\pi^2 EI/L_c^2 \tag{E-19a}$$

$$P_s = GA_s \tag{E-19b}$$

Solving the same problem using Haringx's approach, but setting

$$\xi = \frac{1}{1 + \dfrac{P}{GA_s}} \tag{E-20}$$

the solution is once again defined by the same equations (Eqs. E-16, E-17, and E-18a). Substituting for ξ gives

$$P_{cr} = \frac{P_s}{2}\left\{\sqrt{1 + \frac{4P_n}{P_s}} - 1\right\} \qquad \text{(E-21)}$$

The critical loads for the two theories are plotted in Figure E-2 in dimensionless form, for the first mode ($n = 1$). For the special case of $n = 1$, P_n is designated P_E. At low P_E/P_s (i.e., slender columns dominated by flexural effects) both approaches tend towards the Euler formula, as might be expected. At high P_E/P_s (i.e., short columns dominated by shearing effects) they give different solutions, converging to asymptotes

$$P_{cr} = P_s \qquad \text{(Engesser)} \qquad \text{(E-22a)}$$

and

$$P_{cr} = \sqrt{P_s P_n} \qquad \text{(Haringx)} \qquad \text{(E-22b)}$$

Since shear-flexible columns are the ones of interest, the selection of the right approach is important.

Gent (*41*) adapted Haringx's approach to reinforced bearings by substituting for EI and GA_s the average rotational stiffness, K_r, and shear stiffness, K_s of a multilayer bearing. They were derived from the properties for a single elastomer layer, then adjusted to allow in the averaging process for the steel thickness.

The transverse stiffness (the inverse of Eq. E-17) and the buckling load (Eq. E-21) then become

$$K_T = \frac{P}{\phi h_{rt}} \frac{1}{\frac{\xi \tan\omega}{\omega} - 1} \qquad \text{(E-23)}$$

and

$$P_{cr} = \frac{\phi GA_s}{2}\left\{\sqrt{1 + \frac{4EIf_r}{GA_s}\left(\frac{\pi}{\phi h_{rt}}\right)^2} - 1\right\} \qquad \text{(E-24)}$$

where

$$\xi = \frac{1}{1 + \frac{P}{GA_s}} \text{ and } \omega = \frac{\phi h_{rt}}{2}\sqrt{\frac{P}{\xi \phi EIf_r}}$$

in which h_{rt} = total elastomer thickness, ϕ = total bearing thickness (including steel)$/h_{rt}$, and f_r = bending stiffness coefficient.

Equation E-24 is referred to hereafter as the "Basic Theory."

Gent performed experiments which demonstrated generally good agreement with the theoretical predictions of both buckling load and transverse stiffness in the presence of axial load. However, the test bearings had thick, rigid steel reinforcing plates and were relatively slender. The stresses and strains were consequently low, and the conditions in his test resembled closely the assumptions underlying the Basic Theory. However, they did not reflect conditions to be expected in field bearings.

This experimental evidence lends strong support to the use of Haringx's rather than Engesser's approach for the conditions of the tests. Taking the shear force defined by Eq. E-8 as being parallel to the rotated plane section also seems reasonable, because the flexurally rigid reinforcement defines such a plane

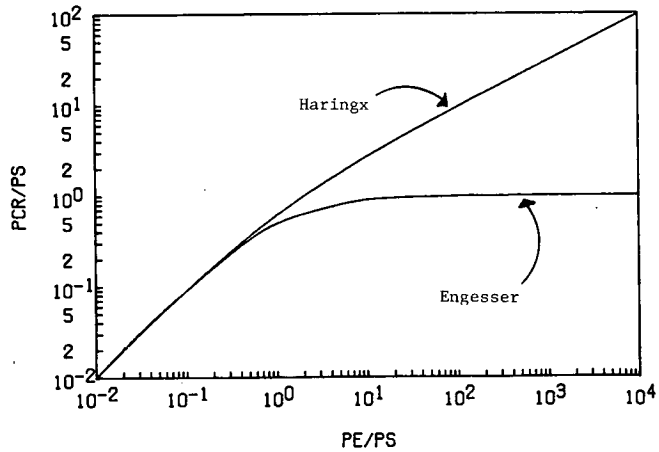

Figure E-2. Comparison of dimensionless buckling load: Engesser's and Haringx's theories.

and the shear stresses applied by the elastomer to it would appear to be well described by Eq. E-6. Thus, Haringx's approach appears to be the most suitable when the reinforcement is flexurally rigid and is initially perpendicular to the column center line.

By contrast, the sandwich panel shown in Figure E-3 is better characterized by Engesser's equations. If the face sheets are idealized as being inextensible and having no bending stiffness, and the core has a (low) shear modulus of G, on buckling, the change in strain energy of the system is close to

$$\Delta U = 1/2 Gh_p b \int_0^L \left(\frac{\partial v}{\partial x}\right)^2 dx \qquad \text{(E-25a)}$$

and the change in potential of the load is

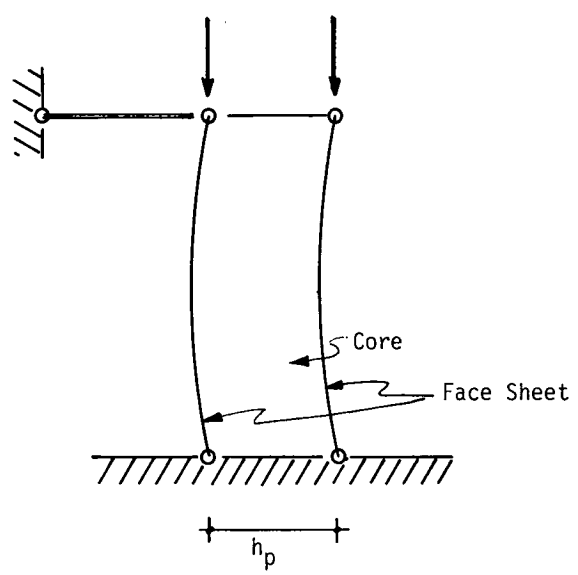

Figure E-3. Buckling of shear panel.

$$V = P \int_0^L 1/2 \left(\frac{\partial v}{\partial x}\right)^2 dx \qquad \text{(E-25b)}$$

so

$$P_{cr} = G\, bh_p = GA_s = P_s \qquad \text{(E-26)}$$

This is the Engesser solution for columns short enough to be controlled by shearing deformations, and is always lower than the Haringx solution. It appears to be the appropriate choice when the stiff reinforcement of the composite runs parallel to the column axis. If the bending stiffness is truly negligible the theory has the surprising property that any shape is a buckling mode shape, and all mode shapes give the same buckling load.

Questions must arise over the choice of theory when the column has plates that are either flexible (such as in a fiber-reinforced bearing) or nonexistent, or when the steel plates are poorly aligned. Schapery and Skala's work (*48*) on helicopter rotor bearings with initially curved plates provides a useful starting point, but is not conclusive. In the remainder of this study only well-made steel-reinforced bearings with flat, parallel plates stiff enough to satisfy the Haringx assumptions are considered.

The foregoing calculations were made for a column with ends that are free to translate but not rotate. An effective length factor can be introduced into Eq. E-21 to account for other boundary conditions, giving

$$P_{cr} = \frac{\phi GA_s}{2}\left\{\sqrt{1 + \frac{4\pi^2 EIf_r}{GA_s(\phi kh_{rt})^2}} - 1\right\} \qquad \text{(E-27a)}$$

This gives exact results for three cases (both ends fixed against rotation and either free to sway or not, and pinned ends with no sway possible) but not when one end is fixed, the other is pinned and sway is prevented. Then, the solution is given by the roots of the transcendental equation:

$$(1 - h_{rt} \cot qh_{rt}) = -P_{cr}/P_s \qquad \text{(E-27b)}$$

In that case Eq. E-27a errs on the unsafe side, but a bearing with such boundary conditions is unlikely to occur in practice. The error is a factor of 1.36 for a square bearing half as high as it is wide, with a shape factor of 6. For taller bearings (in which buckling is more likely) the error is smaller.

Buckling by tension is also predicted by the Basic (Haringx) Theory. If in Eq. E-23 the load P is negative, the transverse stiffness tends to zero, and so buckling occurs, when

$$|P_{cr}| = \phi GA_s \qquad \text{(E-28)}$$

No experiments are known of to confirm such behavior, but it would presumably involve rotation of the reinforcement to an orientation parallel to the column axis. Its only practical application would be in cases of extreme uplift when lift-off is prevented, in which case it could occur before the material suffers the internal rupture discussed by Gent and Lindley (*54*).

Extensions to Include Geometric Nonlinearity

In the linear theory of structures the geometry under load is assumed to be identical to the initial undeformed geometry. This vastly simplifies the calculations, and in most cases it produces accurate enough results. In any buckling analysis the transverse deformations must be included, but, in the case of elastomeric bearings, further complications arise because the axial deformations may also be important.

Elastomeric bearings are peculiar among structural elements in that, before material distress occurs, they may undergo a significant decrease in height and increase in effective plan area. Both changes will increase the buckling load over the value calculated using the original dimensions, so in practice Eq. E-27a may be expected to under-predict real buckling loads, especially for short bearings in which the effect is most prevalent. It is also possible that the material itself experiences changes in its moduli under stress, which could further increase the buckling load if they represent stiffening. (For example, in independent tests for moment-rotation curves at a constant axial stress, the moment was found to be linearly related to rotation angle over a wide range of deformation, but the constant of proportionality increased significantly with simultaneous axial stress.)

One consequence of this behavior is that buckling may be impossible for bearings with a slenderness ratio kh_{rt0}/r_0 less than a limiting value. When an increment of load is added, the geometric changes it causes may increase the buckling strength by an amount that is greater than the load increment. The applied load thus becomes an increasingly small percentage of the buckling strength for that instantaneous geometry, rendering buckling impossible. Timoshenko (*45*) discusses such behavior using a simple stiffness model for a helical spring.

Consider a shear-flexible homogeneous column and define

$$\epsilon_c = \frac{L_{c0} - L_c}{L_{c0}} \qquad \text{(E-29)}$$

Let the axial, shearing and rotation stiffness be load (or strain) dependent and be denoted by $K_c(\epsilon_c)$, $K_s(\epsilon_c)$ and $K_r(\epsilon_c)$, so that

$$N = K_c(\epsilon_c)\frac{\partial \bar{u}}{\partial x} \qquad \text{(E-30a)}$$

$$M = K_r(\epsilon_c)\frac{\partial \psi}{\partial x} \qquad \text{(E-30b)}$$

$$V = K_s(\epsilon_c)\left\{\frac{\partial \bar{v}}{\partial x} \psi\right\} \qquad \text{(E-30c)}$$

The equation for the buckling load written in terms of the instantaneous stiffnesses K_c, K_s, and K_r is

$$P_{cr} = \frac{K_s}{2}\left\{\sqrt{1 + \frac{4\pi^2 K_r}{K_s/(kL_c)^2}} - 1\right\} \qquad \text{(E-31a)}$$

where L_c = instantaneous length = L_{c0} $(1 - \epsilon_c)$.

If ϵ_c has the value ϵ_{cr} at buckling, Eq. E-31a can be rearranged to give

$$\epsilon_{cr}(1 - \epsilon_{cr})^2 \left\{\frac{K_c(\epsilon_{cr})}{K_s(\epsilon_{cr})}\epsilon_{cr} + 1\right\}\frac{K_c(\epsilon_{cr})}{K_r(\epsilon_{cr})} = \left(\frac{\pi}{kL_{c0}}\right)^2 \qquad \text{(E-31b)}$$

This equation can be used to solve for ϵ_{cr} if the stiffnesses are known as functions of strain, and Eq. E-30a then gives the critical axial load. In practice, however, efforts to establish stiffnesses at zero load, let alone a good description of their variation with load, met with difficulties.

As a simple example (referred to here as the Poisson model) assume that the increase in plan dimensions of the bearing due to bulging can be approximated by:

$$K_c(\epsilon_c) = f_c E A_0 (1 + \nu \epsilon_c)^2 \qquad \text{(E-32a)}$$

$$K_r(\epsilon_c) = f_r E I_0 (1 + \nu \epsilon_c)^4 \qquad \text{(E-32b)}$$

$$K_s(\epsilon_c) = G A_{s0} (1 + \nu \epsilon_c)^2 \qquad \text{(E-32c)}$$

where ν is chosen arbitrarily to represent the average increase in area of the elastomer-steel composite. It is not the same as the Poisson's ratio for the elastomer alone, which for most practical purposes may be taken as 0.5. Coefficients f_c and f_r account approximately for the stiffening caused by the steel's restraint of the elastomer's bulging. Theoretical values are given by Gent and Meinecke (*36*), and they are discussed in more detail in Appendixes B and C. They have the general form

$$f_c = A_c + B_c S^2 \qquad \text{(E-33a)}$$

$$f_r = A_r + B_r S^2 \qquad \text{(E-33b)}$$

For practical S values A_c and A_r may be neglected without serious error, and that is done here. Setting $E = 3G$, $I_0 = A_0 r_0^2$, and $A_{s0} = A_0$, Eq. E-31b then becomes

$$f(\epsilon_c) = \left(\frac{1 + \nu\epsilon_c}{1 - \epsilon_c}\right) \frac{\pi}{\sqrt{\frac{B_c}{B_r}(1 + 3B_c S^2 \epsilon_c)\,\epsilon_c}} = \frac{kL_{c0}}{r_0} \qquad \text{(E-34)}$$

A plot of $f(\epsilon_c)$ vs. ϵ_c is shown in Figure E-4 using $B_c = 1.3$, $B_r = 0.75$, and $\nu = 0.3$. Its intersection with the horizontal line $f(\epsilon_c) = \dfrac{kL_{c0}}{r_0}$ gives the ϵ_{cr} at which buckling happens for that particular slenderness. The minimum of $f(\epsilon_c)$ represents the limiting kL_{c0}/r_0 for which buckling is possible, because for lower values no real value exists for ϵ_{cr}. It occurs when the differential of Eq. E-34 vanishes, namely

$$\frac{(1 + \nu)\,\epsilon_c}{(1 + \nu\epsilon_c)(1 - \epsilon_c)} = 1 - \frac{1}{(6B_c S^2 \epsilon_c + 2)} \qquad \text{(E-35)}$$

For practical S values and short columns, $(6B_c S^2 \epsilon_c + 2)$ is much larger than 1.0, so Eq. E-35 is essentially independent of S. Then

$$\epsilon_{c,\text{lim}} = \frac{1}{\nu}(\sqrt{1 + \nu} - 1) \doteq \frac{1}{2} - \frac{\nu}{8} \qquad \text{(E-36)}$$

Substituting back into Eq. E-34 shows that

$$\left(\frac{kL_{c0}}{r_0}\right)_{\text{lim}} = \frac{1}{C_1 S} \qquad \text{(E-37a)}$$

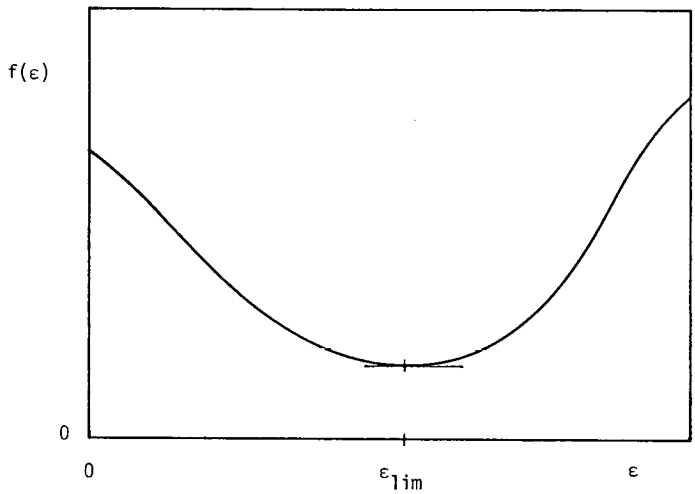

Figure E-4. Strain at limiting slenderness below which buckling is impossible.

where

$$C_1 = \frac{1}{(1 + 0.5\,\nu)} \sqrt{\frac{3}{16\pi^2} \frac{B_c^2}{B_r}} \qquad \text{(E-37b)}$$

The constant C_1 is relatively insensitive to the equivalent Poisson's ratio, ν, but depends quite strongly on the compressive stiffness coefficient B_c.

The load at this limiting slenderness is calculated from Eq. E-32a with the strain from Eq. E-36, giving

$$P_{cr,\text{lim}} \doteq B_c S^2 A_0 (1 + \sqrt{1 + \nu}) \qquad \text{(E-38)}$$

A different model (*66*) (referred to here as the Tangent Stiffness model) may be constructed which includes the effect of the steel plate thickness on the column length and accounts explicitly for the change in S with compressive deflection. Let the subscript 0 signify unloaded conditions and

$$\sigma_c = P/A_0 \qquad \text{(E-39a)}$$

$$\phi = h_{ct0}/h_{rt0} \qquad \text{(E-39b)}$$

The assumption of constant volume requires that the average plan dimensions under load be $1/(1 - \epsilon_c)$ times their value under no load. This gives

$$A(\epsilon_c) = A_0/(1 - \epsilon_c) \qquad \text{(E-40a)}$$

$$I(\epsilon_c) = I_0/(1 - \epsilon_c)^2 \qquad \text{(E-40b)}$$

$$S(\epsilon_c) = S_0/(1 - \epsilon_c)^{1.5} \qquad \text{(E-40c)}$$

The tangent compressive stiffness, developed in Appendix B, is

$$\frac{d\sigma_c}{d\epsilon_c} = \frac{EB_c S_0^2}{(1 - \epsilon_c)^5} \qquad \text{(E-41)}$$

so

$$\sigma_c = \frac{EB_cS_0^2}{4}\left\{\frac{1}{(1-\epsilon_c)^4} - 1\right\} \tag{E-42}$$

if A_c in Eq. E-33a is again neglected.

The shearing stiffness K_S is defined as the force required to impose on the column a transverse deflection equal to the column length. Consider a unit with steel of total thickness h_{st} and a total unstrained elastomer thickness of h_{rt0}, giving a combined thickness of h_{ct0} under no load. The shear force V for a deflection Δ_s is given by

$$V = \frac{\Delta_s}{h_{rt}(\epsilon_c)} GA_s(\epsilon_c) \tag{E-43}$$

but

$$h_{rt}(\epsilon_c) = h_{rt0}(1-\epsilon_c)\frac{h_{ct0}}{\phi}(1-\epsilon_c) \tag{E-44a}$$

and

$$A_s(\epsilon_c) = A_{s0}/(1-\epsilon_c) \tag{E-44b}$$

so

$$V = \frac{\phi\,\Delta_s GA_{s0}}{h_{ct0}(1-\epsilon_c)^2} \tag{E-45}$$

but the total thickness under load is

$$\begin{aligned} h_{ct}(\epsilon_c) &= h_{st}(\epsilon_c) + h_{rt}(\epsilon_c) \\ &= h_{ct0}\left(1 - \frac{\epsilon_c}{\phi}\right) \end{aligned} \tag{E-46}$$

So for a shear deflection Δ_s equal to the compressed thickness of the unit, Eqs. E-45 and E-46 combine to give

$$K_s = V = \frac{GA_{s0}(\phi - \epsilon_c)}{(1-\epsilon_c)^2} \tag{E-47}$$

Treating a similar steel and elastomer unit for rotation

$$EI_{eff} = E_rI\frac{(\phi - \epsilon_c)}{(1-\epsilon_c)} \tag{E-48}$$

But

$$E_rI = \frac{E(A_r + B_rS^2(\epsilon_c))\,I_0}{(1-\epsilon_c)} \tag{E-49}$$

so

$$K_r = EI_{eff} = EI_0A_r + \frac{B_rS_0^2}{(1-\epsilon_c)^3}\frac{(\phi - \epsilon_c)}{(1-\epsilon_c)^3} \tag{E-50}$$

The foregoing equations were developed for a single unit consisting of one elastomer layer bonded between two steel plates. The buckling load for a column of units may now be calculated from Eq. E-24, incorporating the stiffnesses and lengths from Eqs. E-46, E-47, and E-50.

$$P_{cr} = \frac{K_s}{2}\left\{\sqrt{1 + \frac{4\pi^2K_r}{K_s(kh_{rt0}(1-\epsilon_c/\phi))^2}} - 1\right\} \tag{E-51}$$

or

$$\sigma_{cr} = \frac{G}{2}\frac{(\phi - \epsilon_c)}{(1-\epsilon_c)^2}\left\{\sqrt{1 + \left(\frac{4\pi^2E/G}{\lambda_0^2(1-\epsilon_c)(1-\epsilon_c/\phi)^2}\right)\left(A_r + \frac{B_rS_0^2}{(1-\epsilon_c)^3}\right)} - 1\right\} \tag{E-52}$$

where $\lambda_0 = \dfrac{kh_{rt0}}{r_0}$ = the unloaded slenderness ratio.

Equation E-52 defines the nominal buckling stress in terms of the nominal strain, which is unknown. However, they are also related by Eq. E-42; therefore, simultaneous solution of these two equations gives the buckling stress. The approximate equation equivalent to Eq. E-22b (assuming the shear flexibility dominates buckling) becomes, for $A_r = 0$,

$$\sigma_{cr} = \sqrt{\frac{G}{E}}B_r\frac{\pi ES_0}{\lambda_0}\frac{\phi}{(1-\epsilon_c)^4} \tag{E-53}$$

This can be solved with Eq. E-42 in closed form to give

$$\sigma_{cr} = \frac{D_1S_0\dfrac{EB_c}{4}}{\lambda_0 - D_1/S_0} \tag{E-54a}$$

where

$$D_1 = \frac{4\pi\phi}{B_c}\sqrt{\frac{GB_r}{E}} \tag{E-54b}$$

Thus the Tangent Stiffness model predicts a limiting slenderness $\lambda_{0,\text{lim}}$ below which buckling will not occur. Its value is close to that predicted by the Poisson model (Eq. E-37a), apart from the terms in ϕ and ν. The models also differ in that the Tangent Stiffness model predicts an infinite buckling load and 100 percent strain when the slenderness reaches its limiting value, but the less refined Poisson model shows a finite buckling stress. This latter is somewhat surprising because it means that at the limiting slenderness buckling occurs at a finite load, but that an infinitesimally stockier column will never buckle. However, such discontinuous behavior is not peculiar to the Poisson model, because Timoshenko (*45*) finds similar response for helical springs using linear stiffness models. For physical reasons it is unlikely in practice and, therefore, represents only a shortcoming of the model.

Both of these models predict buckling loads that converge to those predicted by the Basic Theory (Eq. E-27a) for tall slender columns, but are larger for stocky columns. In both cases a limiting slenderness is predicted below which columns will not

buckle. It is inversely proportional to the shape factor, which means that a high shape factor bearing may theoretically be made to buckle, when one with the same external dimensions but a lower shape factor would never do so.

It should be emphasized that many nonlinear models are possible. The Poisson model was chosen as a simple illustration, and the Tangent Modulus model is an attempt to provide a more precise characterization of the changes in geometry that occur. In both cases the possibility of material failure prior to buckling is ignored.

Transverse Stiffness

The linearized elastic theory of buckling used for conventional columns shows that the transverse stiffness of an axially loaded member reduces as the axial force increases. As the axial load approaches the buckling load the transverse stiffness approaches zero. The same phenomenon underlies the magnification factors used for moments that are applied at the same time as axial load.

Similar behavior is to be expected from elastomeric bearings, although their shear flexibility and finite changes in height under compressive load complicate the relation between axial force and transverse stiffness.

Equation E-16 relates axial force and transverse stiffness for the physical conditions underlying the Basic Theory (i.e., the composite bearing is characterized as a homogeneous material and shortening under compression is ignored). Development of more elaborate theories which take into account some of these complexities, along lines similar to the Tangent Modulus approach, for example, was considered. However, it was not pursued, because correlation of the buckling loads measured in the experiments with any rational modification of the Basic Theory for buckling proved somewhat unsatisfactory. It was felt that even greater difficulties would exist for transverse stiffness.

EXPERIMENTS

General

Tests (*66*) were performed to measure the buckling load and the variation in transverse stiffness with axial load of different columns made from steel-reinforced bearings. Because the theory requires a knowledge of the axial, rotation and shear stiffnesses, experiments were also performed to investigate those.

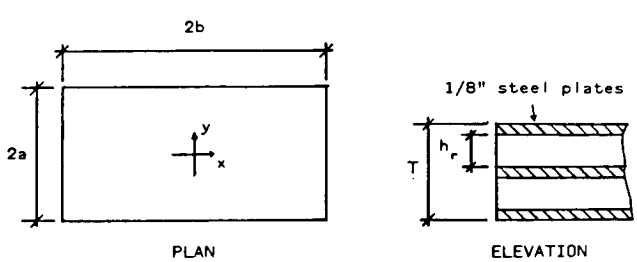

Figure E-5. Typical dimensions of bearing units used in stability tests.

Table E-1. Dimensions of units employed in stability tests.

Unit	A 11	A 12
Length, L (in.)	11.33	8.50
Width, W (in.)	5.66	4.25
Elastomeric layer thickness, h_r (in.)	0.375	0.400
Total unit thickness, h_{rt} (in.)	1.125	1.175
Shape factor, S (-)	5.03	3.54
Cross-sectional area, A_o ($in.^2$)	64.2	36.1
Nominal I_{ox} ($in.^4$)	171.9	54.3
Radius of gyration, r_x (in.)	1.64	1.23

They are reported in Appendixes B and C. Special tests to establish the shear modulus of the buckling test bearings are reported in Appendix G.

Buckling Load Tests

The tests were conducted on columns made from stacks of steel-reinforced bearing units. Two different types of units (designated A 11 and A 12) were used, and their geometric properties are given in Figure E-5 and Table E-1. The elastomer was neoprene of nominal Shore A hardness 55, and the steel was ASTM A570 grade 40 CE with a measured yield stress of 46 ksi. Each unit consisted of two elastomer layers bonded between three $\frac{1}{8}$-in. steel plates. They were cut with a band-saw in the University machine shop from large sheets of material made up by a commercial manufacturer, therefore they had no cover. Consistency of the elastomer hardness and layer thickness was good.

Tests were conducted on the following columns:

A 11: Stacks of 16, 14, 12, 10, 8, 5, 4 and 3 units
A 12: Stacks of 16, 14, 12, 10, 8, 6, 4 and 3 units

The typical test setup for the A 11 tests is shown in Figure E-6. A 300 kip Baldwin Universal test machine was used. Vertical load was recorded electronically by means of a potentiometer connected to the test machine dial. Vertical deflections of the stack and horizontal displacement at the one-quarter points were measured using the LVDTs shown. For the tests on the 5, 4, and 3 unit A 11 stacks and all of the A 12 tests, only the horizontal LVDT located at the column mid-height was employed.

For the setup shown, the end conditions of the stack may be considered as fixed against rotation. The individual bearing units used in any one test were not bonded to each other and therefore depended primarily on the development of friction between the steel plates to transmit shearing forces between units and to prevent any relative slip. In addition, under large lateral displacements, the units could (and did) separate locally because of roll-off at the edges. The effect of roll-off has been studied analytically by Simo and Kelly (*49*).

All columns required shimming to establish a flat initial contact surface due to an unavoidable slight tilt of the topmost bearing relative to the loading surfaces. The tilt varied from column to column in both magnitude and direction, but had no

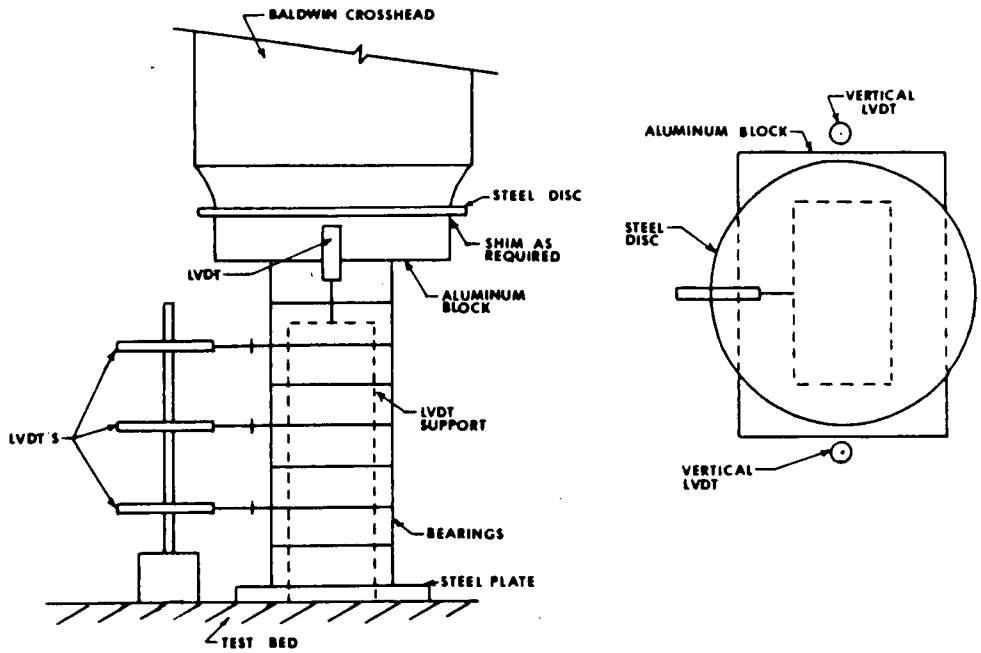

Figure E-6. Typical test setup for stability tests.

significant effect on the test results. This was checked by rotating several of the bearings in a stack by 180 deg about the vertical axis, which changed the tilt of the top bearing and had some effect on the initial lateral deflections, but had an insignificant effect on the buckling load.

To check for the possible effects of creep, several tests were repeated with different time intervals between load increments. While transverse and vertical creep deformations were clearly evident, there again was no significant difference in the measured buckling loads.

After several trial runs to establish the relative effects of the above factors, the following typical test procedure was adopted:

a. Apply load increment (varied with test and with load previously applied).
b. Hold load for 1 min.
c. Record load and LVDT measurements.

This pattern was continued until the lateral deflection became excessive and roll-off began or until the column would no longer accept additional load, i.e., the incipient collapse load had been reached.

The buckling load was determined in each case by the Southwell plot method. The values so determined agreed closely with the maximum applied load in those cases where the incipient collapse load had been reached. In addition, the buckling loads in each test were estimated by two modified versions of the Southwell technique. In the first, the transverse deflection Δ_t is plotted against Δ_t/P^2. This technique, originally credited to Massey, can be shown to be suitable for certain structural systems such as the lateral-torsional buckling of beams. In the other modified method, the transverse deflection is plotted against the product of the load and the deflection. This is an empirical method suggested by Trahair (*50*). A detailed discussion of both of these methods is available in (*50*). For the bearings tested here, the buckling loads as estimated by the modified techniques agree closely with those determined by the traditional Southwell method. The experimental buckling loads reported herein are those obtained by the Southwell method.

The results of all of the tests are summarized in Table E-2.

Table E-2. Summary of the results of the stability tests.

No. of units	P_{cr}* (kips)	$_{cr}$ (psi)	L_r (in.)	$kL_r/2a$ (-)	$kL_r/2aS$ (-)	Comments
A 11 units						
16	37.5	584	12.00	1.060	0.211	Incipient collapse at $P_{max} = 36^K$
14	42.2	657	10.50	0.928	0.184	Incipient collapse at $P_{max} = 42^K$
12	53.0	826	9.00	0.795	0.158	
10	74.8	1165	7.50	0.663	0.132	Incipient collapse at $P_{max} = 72^K$
8	115.3	1796	6.00	0.530	0.105	
5	-	-	3.75	0.331	0.066	$P_{max} = 100^{K**}$
4	-	-	3.00	0.265	0.053	$P_{max} = 100^{K**}$
3	-	-	2.25	0.199	0.040	$P_{max} = 150^{K**}$
A 12 units						
16	9.5	263	12.80	1.506	0.425	
14	11.2	310	11.20	1.318	0.372	
12	12.7	352	9.60	1.129	0.319	
10	16.6	460	8.00	0.941	0.266	
8	20.8	576	6.40	0.753	0.213	
6	30.6	848	4.80	0.565	0.160	
4	68.8	1906	3.20	0.376	0.106	
3	-	-	2.40	0.282	0.080	$P_{max} = 60^{K**}$

* Determined from Southwell plot
** No evidence of instability

Figures E-7 and E-8 are typical examples of the vertical load-transverse deflection curve and the Southwell plot obtained for a given test. Figure E-9 is a plot of the test results for both sections in which the buckling stress σ_{cr} (defined by $\sigma_{cr} = P_{cr}/A_0$) is plotted against a measure of the column slenderness given by kh_{rt0}/L, where h_{rt0} is the total height of the elastomeric blocks in the column, L is the unloaded short plan dimension of the bearing, and the effective length factor k is equal to ½ for fixed-fixed end conditions.

As can be seen in Table E-2 and in Figure E-9, several short columns showed no evidence of approaching instability at any level of applied load. Figures E-10 and E-11 show the load deflection plot and the Southwell plot for five units of the A 11 bearing. Loading was terminated at the indicated point to prevent damage to the bearings.

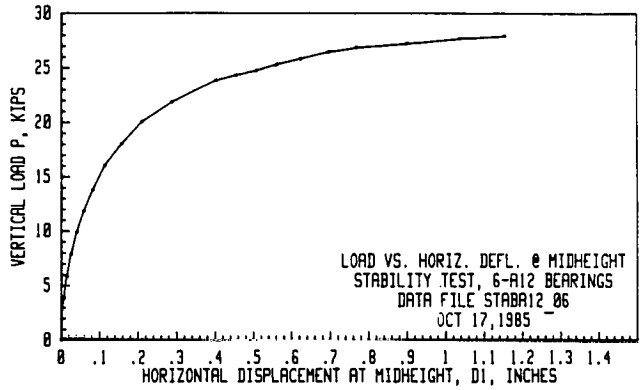

Figure E-7. Vertical load and lateral deflection for six Type A 12 bearing units.

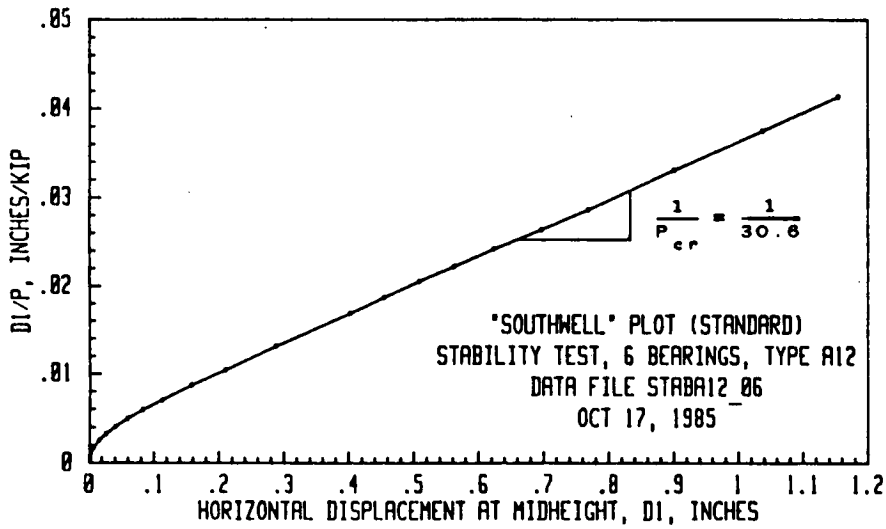

Figure E-8. Southwell plot for six Type A 12 bearing units.

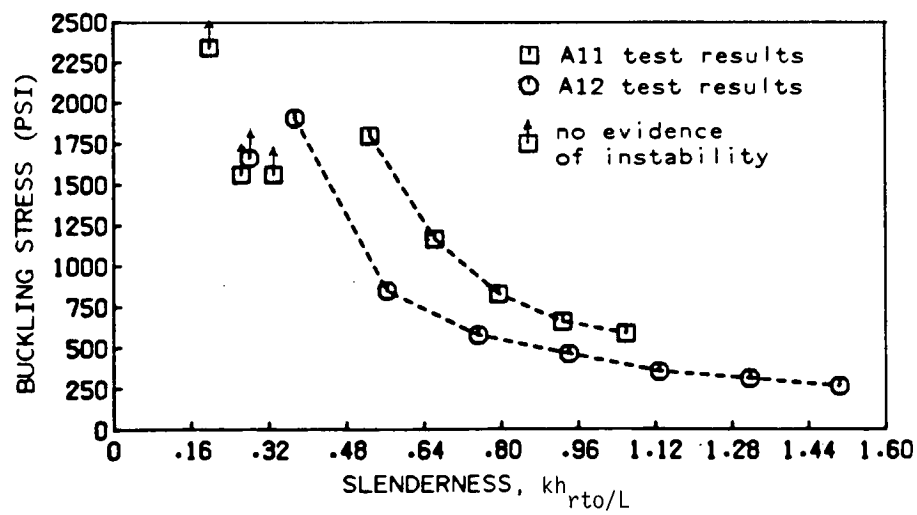

Figure E-9. Measured buckling stress σ_{cr} vs. slenderness ratio $kh_{rt0/L}$ for Type A 11 bearings.

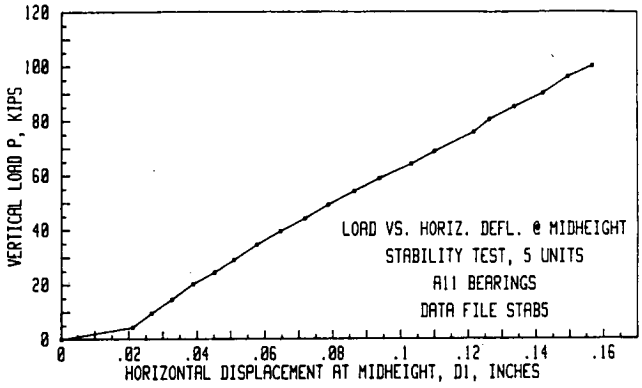

Figure E-10. Measured vertical load and lateral deflection for five Type A 11 bearing units.

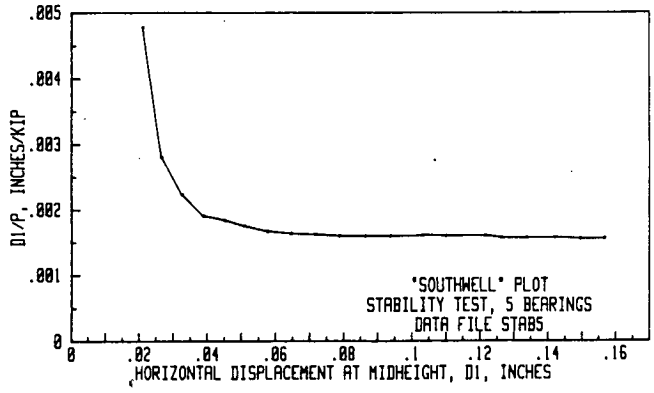

Figure E-11. Southwell plot for five Type A 11 bearing units.

In all of the tests in which instability effects were clearly evident, the lateral deflections were observed to be significant compared to the specimen dimensions even for axial loads considerably less than the buckling load. This is due to the unavoidable initial out-of-true present in a column of this sort, caused by local internal imperfections (e.g., uneven elastomer layers), slight lack of verticality in the column, etc. Rearrangement of the units within the column had no noticeable effect on the buckling load although the deflection pattern under light load changed. In fact, in three tests (A 11-14 units and 10 units, and A 12-12 units), the initial deflections were substantially dominated by second mode (*S*-shape) deformations, and it was not until P reached a fairly high fraction of P_{cr} that the fundamental mode became visibly dominant.

Thus, as expected, the elastic buckling load was independent of geometric imperfections. The close agreement between the four measures of buckling load (three Southwell-based methods and observations of incipient collapse) suggests that the measured results are reliable.

Figure E-9 shows that in both series of tests the buckling load increased at lower slenderness ratios, as expected. However, the consistent separation between the two curves shows that σ_{cr} also depends on some other parameter(s). The major difference not accounted for in Figure E-9 is the shape factor *S*, and in Figure E-12 σ_{cr} is plotted against kh_{rt0}/LS. The results from the two different series then agree closely, and the empirical equation

$$\sigma_{cr} = \frac{C_4}{\dfrac{kh_{rt0}}{LS_0} - C_5} \qquad \text{(E-55)}$$

was found to fit well with $C_4 = 90$ psi, $C_5 = 0.055$. It is shown as a full line in Figure E-12. The fact that C_5 is greater than 0 suggests a lower limit of slenderness below which buckling is impossible ($\sigma_{cr} = \infty$), although using the experimental data to find it is not very reliable because of the extrapolation required. Of the four columns that did not buckle, two (three and four units of A 11) had kh_{rt0}/LS_0 ratios lying below the limiting value of 0.055, so their failure to buckle is in agreement with Eq. E-55. For the other two (three A 12 and five A 11 units), Eq. E-55 predicts buckling stresses of 3,600 psi and 8,200 psi,

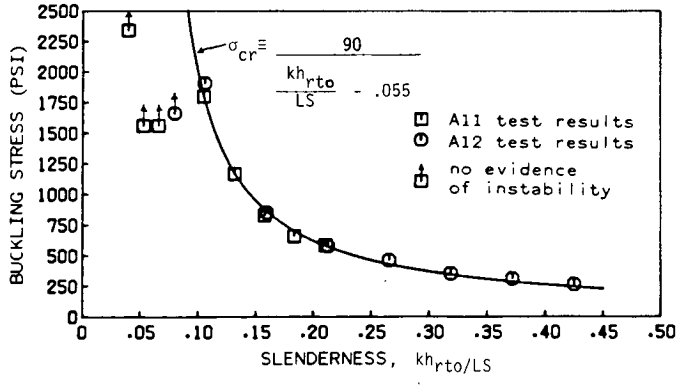

Figure E-12. Buckling stress σ_{cr} vs. slenderness ratio kh_{rto}/LS.

respectively, which far exceed the highest stresses imposed during testing.

Column Shear Stiffness Tests

Tests were conducted on columns consisting of Type A 11 rectangular bearing units to measure the transverse stiffness of the columns under varying amounts of axial load. The test parameters and results are summarized in Table E-3.

The test setup is shown in Figure E-13. The test machine was the 300K Baldwin used in the stability tests. Vertical displacements were monitored using two LVDTs mounted on the center plate of the rig along the long axis of the bearings. Horizontal displacements were measured using two potentiometers mounted on the north column of the test rig. Vertical load was measured and recorded by means of a potentiometer connected to the test machine dial. Horizontal load was applied manually using center-hole hydraulic rams and was measured using 25-kip load cells positioned as shown in the figure.

A vertical load was chosen for each test. Horizontal load was applied in increments in each direction in turn, and after each increment the vertical load was readjusted to its preselected

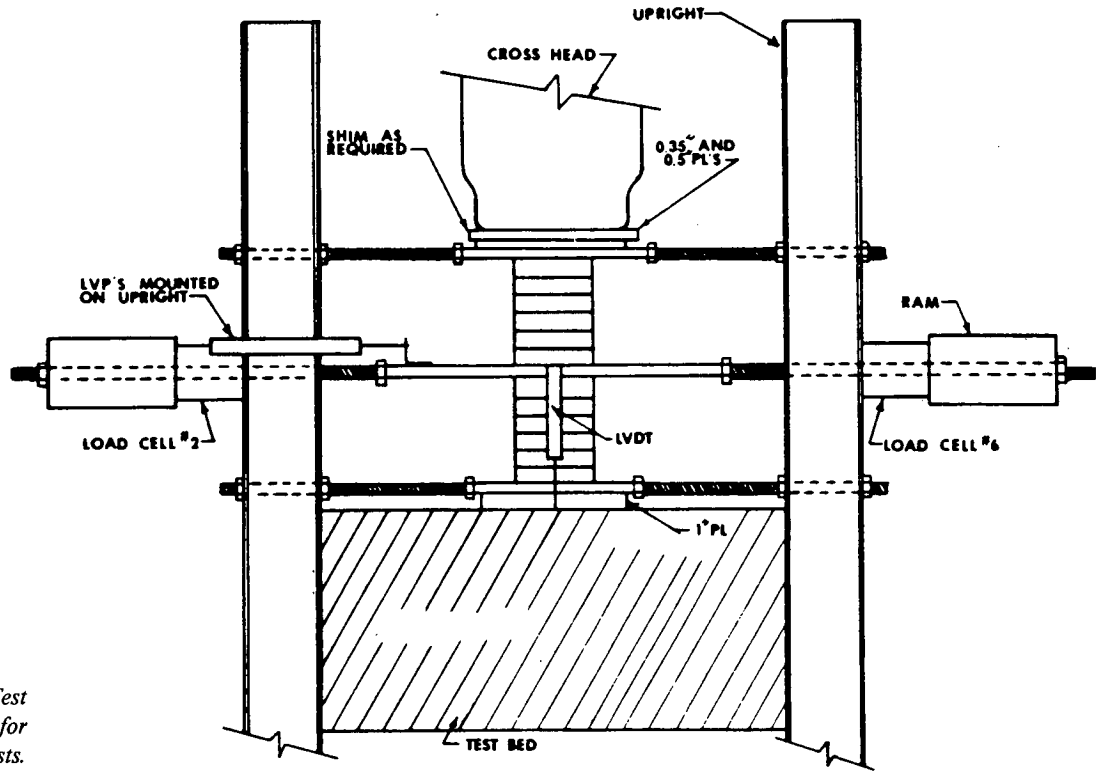

Figure E-13. Test rig and setup for column shear tests.

Table E-3. Summary of the column shear tests.

No. of units	σ_c (psi)	σ^*_{cr} (psi)	h_{rt} (in.)	Max. Δ_t (in.)	K_t (lb./in.)
2 x 3	500	-	4.50	1.85	2045
2 x 3	1000	-	4.50	1.85	1365
2 x 4	500	1796	6.00	2.3	1535
2 x 4	750	1796	6.00	2.3	1064
2 x 4	1000	1796	6.00	2.3	600
2 x 6	375	826	9.00	2.6	750
2 x 6	500	826	9.00	2.6	452
2 x 6	625	826	9.00	2.6	92
2 x 8	100	584	12.00	0.75	1102
2 x 8	250	584	12.00	2.3	619
2 x 8	400	584	12.00	2.3	248

* Experimental results (Table E-2.)

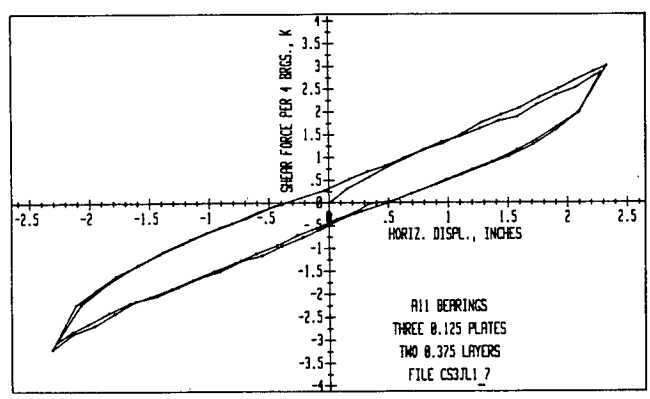

Figure E-14. Shear force vs. transverse displacement for two 4-unit stacks at 750 psi compressive stress.

value. The maximum displacement was limited either by incipient slip between individual units or by lift-off of the most critically loaded unit over one-half to one-third of its width. The latter did not occur suddenly at a clearly defined load, but rather it started at the corners and progressed in towards the center of the edge in question.

For each test, a plot of *H*, defined as one-half of the measured transverse force versus the transverse displacement Δ, was made. A typical plot is shown in Figure E-14. On the basis of all of the tests, the following general observations can be made:

1. The force-displacement curve is relatively linear over a wide range of displacement.
2. Considerable hysteresis is evident in each load cycle. This appears to increase with increasing axial load.
3. The shape of the curve is essentially the same for both cycles of applied load; no degradation is apparent even though the displacements are quite large.
4. For a given column height, the slope of the force-displacement curve decreases with increasing axial load. This is in qualitative agreement with all of the theoretical predictions. The

slope K_t of the force-displacement curve was estimated in each case and is recorded in Table E-3.

CORRELATION OF TEST RESULTS WITH THEORETICAL PREDICTIONS

Buckling Loads

Gent (*41*), Schapery (*48*), and Buckle (*51*) have each shown that the basic shear-flexible theory embodied in Eq. E-24 predicts buckling well for tall columns at relatively low stress when length and area changes are negligible compared to the original specimen dimensions. However, even under these circumstances difficulties exist because the calculation of a rotation stiffness is clouded in some uncertainty. Gent used a measured value for rotation stiffness without specifying how it was measured, and still had to change it by 25 percent to obtain good correlation with measured buckling loads for one bearing size. Buckle adopted a relation from EDS 19 (*52*) in which E is taken to be $4G$, implying a Poisson's ratio of 1.0. If E and G are tangent moduli, this relation implies a material that expands under pressure, violating the 2nd law of Thermodynamics. If one is a secant and one a tangent modulus, then use of both simultaneously is inconsistent.

Shorter columns have higher buckling loads that are unlikely to be reached in practice, but still form an important step in calculating shear stiffness reductions. They could be critical in quality assurance shear tests which might be carried out at relatively high compression stresses. At such high stresses additional difficulties arise concerning the appropriate way of incorporating the changes in height, cross-section dimensions, and material properties. In closed-form the best that can be done is to approximate these changes by modified theories such as the Tangent Modulus, because the true problem is nonlinear in both material and geometry, whereas the analysis is based on classical linear elasticity. More precise solutions require the use of nonlinear finite element programs (*53*).

The Tangent Stiffness model is theoretically the more defensible of the two presented here. Nominal buckling stresses computed using Eqs. E-42 and E-52 together are computed for the Type A 11 and Type A 12 bearings and are plotted against slenderness in Figures E-15 and E-16. The geometric and material parameters used were:

$$E = 420 \text{ psi} \qquad G = 140 \text{ psi}$$

$$A_c = 1.0 \qquad B_c = 1.3$$

$$A_r = 1.0 \qquad B_r = 0.5085$$

Moduli were derived for a 55 hardness elastomer from the relations in Ref. *9*. The geometric properties excepting B_c were obtained from Ref. *15*, using a 2:1 rectangle. B_c was obtained from Ref. *16*, using $B_c = 2k = 1.3$, as recommended for 55 hardness. The curves thus represent the predictions of the most rational theory in which "standard" material and geometric constants are used.

The figures show that the experimental and theoretical results display a common trend of increased buckling stress at lower slenderness, but that the match is certainly not perfect. The buckling stresses predicted by the Tangent Modulus theory (Eqs. E-42 and E-52) and the Basic Theory (Eq. E-24) approach each other at high slendernesses. This is to be expected, because under those circumstances the compressive stress and strain fall, and as the strain approaches zero the two theories become identical.

Changes to the theory to improve the correlation can be addressed in two steps. The first is to improve the fit at high slendernesses (low stress) when the dependence of the various stiffnesses on stress or strain may be expected to be low, because little bulging has taken place. In the second step, different strain dependencies for the stiffnesses may be considered in an attempt to improve the fit for squat bearings. For small compressive strains Eq. E-24 may be expected to suffice. Others (*41, 48*) have already found it adequate, within the limitations cited earlier. Thus, it is reasonable to accept the basic form of the equation, but to adjust the constants to optimize the fit. If the ratio E/G is assumed equal to 3.0 for the materials used in the tests, the two constants available for adjustment are G and f_r where

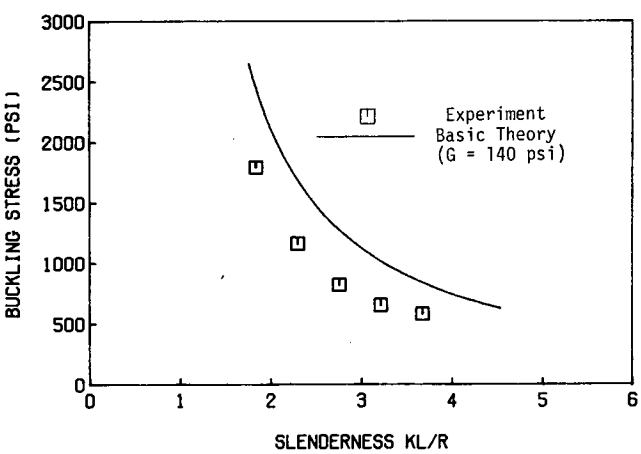

Figure E-15. Buckling of Type A 11 bearings.

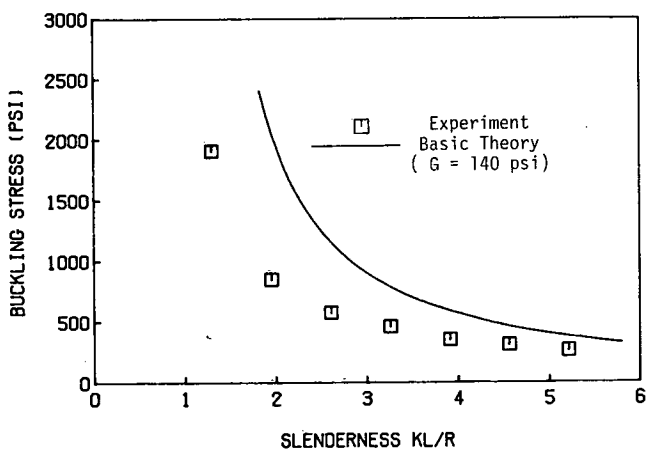

Figure E-16. Buckling of Type A 12 bearings.

$$f_r = \frac{E_r}{E} = A_r + B_r S^2 \qquad \text{(E-57)}$$

Since $A_r = 1.0$ and $S_0^2 \geq 12.5$, the value of B_r is the most important geometric parameter. The theoretical value of B_r for a 2:1 rectangle and incompressible material is 0.5085, as shown in Appendix C. The unmodified predicted buckling loads are about 20 percent too high; therefore, to obtain a good fit either G must be multiplied by about 0.84, or f_r (or essentially B_r) must be multiplied by 0.84^2. There is no independent evidence on which to base the choice. However, G was selected for adjustment here for three reasons: (1) Linear elastic equivalents for material properties of elastomers are difficult to obtain accurately, show scatter, are not highly repeatable and are subject to interpretation (i.e., fitting a "best" straight line to points lying on a slight curve). (2) No substantiated reasons to doubt the theoretical developments in Refs. *36, 16* have been presented, other than the fact that a nonlinear material is treated as linearly elastic. (3) The coefficient f_r lies inside the square root sign in Eq. E-24 and so must be changed by nearly twice as large a percentage as G in order to achieve the same quality of fit.

Equation E-24 can be rewritten

$$\frac{\sigma_{cr}}{G} = \frac{\phi}{2}\left\{\sqrt{1 + \frac{4\pi^2}{\phi^2}\frac{E}{G}\frac{f_r}{\bar{\lambda}_r^2}} - 1\right\} \qquad \text{(E-58)}$$

where $\bar{\lambda}_r = h_{rt0}/r_0$.

For practical $\bar{\lambda}_r$ values, σ_{cr}/G is almost independent of ϕ; therefore, if the equation is valid, a plot of

$$\sigma_{cr}/G \text{ vs. } \frac{\sqrt{f_r}}{\bar{\lambda}_r} \qquad \text{or} \qquad \frac{G}{\sigma_{cr}} \text{ vs. } \frac{\bar{\lambda}_r}{\sqrt{f_r}}$$

should predict critical stresses for all bearings, regardless of height, shape factor, or materials. Furthermore, Eq. E-55, which was found to predict well the critical stresses of both sets of bearings tested in this study, can be rewritten as

$$\frac{G}{\sigma_{cr}} = \frac{kh_{rt0}/LS - C_3}{C_2/G} \qquad \text{(E-59)}$$

which is of the same form, because S is nearly proportional to $\sqrt{f_r}$.

$$\text{Defining } \bar{\lambda} = \frac{\bar{\lambda}_r}{\sqrt{f_r}} = \frac{kh_{rt0}}{r_0\sqrt{f_r}} \simeq \frac{kh_{rt0}\sqrt{12}}{LS} \qquad \text{(E-60a)}$$

Figure E-17 shows the variation of G/σ_{cr} with respect to the modified slenderness, with G taken as 117 psi, and the geometric parameters as before. The data from both sets of experiments now lie on what is very close to a straight line given by

$$\frac{G}{\sigma_{cr}} = 0.268\,(\bar{\lambda} - 0.225) \qquad \text{(E-61a)}$$

or for low $\bar{\lambda}$ values a slightly better fit is obtained from

$$\frac{G}{\sigma_{cr}} = 0.311\,(\bar{\lambda} - 0.290) \qquad \text{(E-61b)}$$

Equation E-61a is essentially an asymptote to Eq. E-24 at high $\bar{\lambda}$. Only one curve for Eq. E-24 is shown. There should strictly be two, based on $\phi = 1.46875$ (A 12 bearings) and $\phi = 1.50$ (A 11 bearings), but they are so close as to be identical for practical purposes.

The Basic Theory for buckling is verified at high $\bar{\lambda}$ by the fact that the experimental results for the two different bearing types lie close to the predicted curve. The main concerns center around the choice (or measurement) of the appropriate G. At high $\bar{\lambda}$ the Tangent Modulus theory also predicts buckling adequately. (The errors are magnified on the plot because the ordinate is G/σ_{cr} rather than σ_{cr}). It gives different curves for the two bearing types. This is almost entirely because they have quite different compressive stiffnesses. In each case, the predicted G/σ_{cr} for all $\bar{\lambda}$ greater than about 0.75 is closely approximated by

$$\left(\frac{G}{\sigma_{cr}}\right)_{TM} = \left(\frac{G}{\sigma_{cr}}\right)_{B} + \text{constant} \qquad \text{(E-62)}$$

where subscripts TM and B stand for the Tangent Modulus and Basic formulas. The constant depends on bearing type.

The predictions are all based on a G of 117 psi because that gave the best fit between the Basic Theory and the experimental data. A different G value could have been chosen to achieve a better fit between the Tangent Modulus Theory and the data at high $\bar{\lambda}$, but the overall match would have been worse.

At lower $\bar{\lambda}$ the Basic Theory underpredicts the experimental buckling stress as expected, but the geometric corrections in the Tangent Modulus Theory appear to be too strong, because it overpredicts the experimental results. Furthermore, the amount

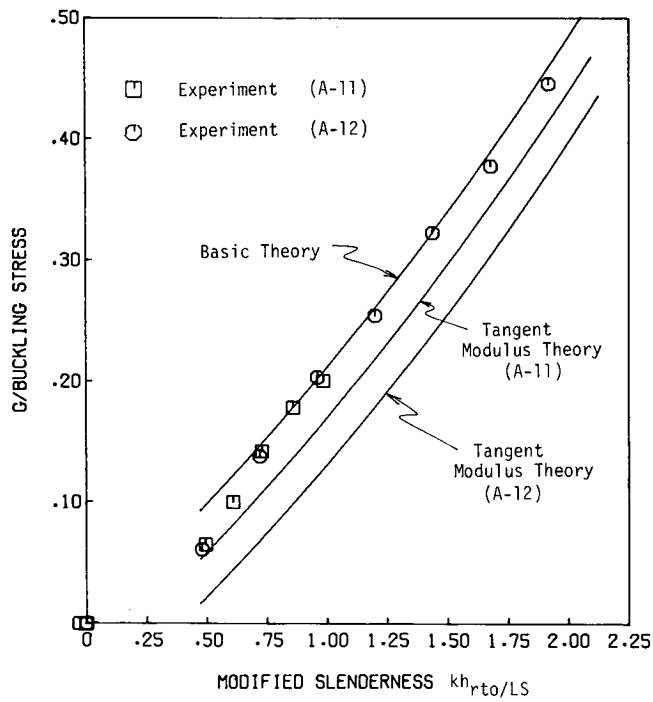

Figure E-17. Inverse buckling plot for all bearings.

by which it does so is very different for the two bearing types, although at the lowest $\bar{\lambda}$ tested, all the experimental results approach the Tangent Modulus Theory predictions for the A 11 bearings.

Perhaps the most serious criticism is that the experimental data for both bearing types lie on one line, but the Tangent Modulus Theory predicts two separate ones. To predict one curve for all bearings requires either that geometric changes should be ignored (as is done in the Basic Theory), or that all the nonlinearities, both material and geometric, should exactly cancel each other for all the test bearings in the range tested, or that the theory used is not valid. The geometric changes clearly happen and were observed in the tests, so presumably the first possibility must be ruled out. The second seems highly improbable because it depends on errors from different sources cancelling out everywhere. It is therefore concluded that the weakness lies in the use of a continuum theory for a structure that is made of sufficiently few discrete components that a continuum approximation is not valid.

The first step in correlating the results has thus been achieved by using $G = 117$ psi. For the second step the Tangent Modulus approach, though apparently rational within the limits of using a continuum theory, proves inadequate in the range in which it really is needed, namely at low $\bar{\lambda}$. Some other adjustments must then be made to Eq. E-24 to raise its predictions for squat bearings. This could be done by introducing empirical expressions that have no rational basis but fit the experimental data for individual stiffnesses. For example, the measured nominal compression stress and strain of the A 11 bearings are well represented by

$$\sigma_c = 0.80 \{ (1 - \epsilon_c)^{-10} - 1 \} \text{ ksi} \qquad \text{(E-63)}$$

An equation such as this could then be combined with Eq. E-52 in a manner similar to the construction of the Tangent Modulus approach. However, without a rational basis for such a scheme it would have little predictive use unless the same formulas were found to fit a wide variety of bearings. Its success also appears dubious because the stiffnesses are strain-dependent, which is the very feature that appears to underlie the inadequacy of the Tangent Modulus theory.

A simpler empirical approach would be to adopt as a buckling curve the tangent at some arbitrary but large slenderness to the Basic curve (Eq. E-24). This procedure is partly rational, because it agrees with the Basic Theory at high $\bar{\lambda}$ and coincides with the test data over the whole range tested. More testing would clearly be needed to establish its validity for other bearing shapes and materials, but at present it offers the best hope for a unified solution.

The use of such a procedure would give rise to the dashed line in Figure E-17, and suggests a limiting slenderness $\bar{\lambda}$ below which buckling is impossible (and which happens to be between the two limiting slendernesses predicted for the A 11 and A 12 bearings by the Tangent Modulus formula). The validity of this procedure in the range $G/\sigma_{cr} < 0.05$ remains speculative because no experimental data exist there. However, that portion of the curve has little application in practice because bridge bearings in the United States are presently neither used nor tested at stresses higher than 2,000 psi.

Column Shear Stiffness

Basic Theory values for the transverse stiffness of a compressed homogeneous shear-flexible column are given by Eq. E-23. It reduces to

$$K_{t0} = \frac{h_{rt0}}{GA_s}\left(1 + \frac{\phi^2 h^2_{rt0}}{12EI_0 f_r}\right) \qquad \text{(E-64)}$$

when the axial load is zero.

In a conventional Euler column the reduction in transverse stiffness caused by axial load can be very closely approximated by

$$\frac{K_t}{K_{t0}} = \left(1 - \frac{P}{P_{cr}}\right) \qquad \text{(E-65)}$$

In a shear-flexible column a rational derivation becomes very complex but the reduction can be approximated by

$$\frac{K_t}{K_{t0}} = \left(1 - \frac{P}{P_{cr}}\right)^m \qquad 1 \le m \le 2 \qquad \text{(E-66)}$$

The exponent m varies with the degree to which shear deformations are important, reaching 2 for very short columns completely dominated by shear. The variable $\bar{\lambda}$ is a measure of the importance of shear, and, over the range of columns tested, the best relationship between the approximate predictions of Eq E-66 and the "exact" predictions of Eq. E-23 was found with

$$m = 2.08 - 0.54\,\bar{\lambda} \qquad \text{(E-67)}$$

but $1.0 \le m \le 2.0$. Equation E-67 was obtained by correlating results at $P = 0.5\,P_{cr}$, and was found to provide a good fit elsewhere.

Experimental and theoretical transverse stiffnesses are compared in dimensionless form in Figure E-18. Four theoretical curves relating to K_t/K_{t0} to P/P_{cr} are presented. Two are obtained using Eq. E-23, for the shortest and highest columns of bearings. Results for intermediate lengths lie in between. The other two curves were obtained from Eq. E-66 with $m = 1$ and 2, respectively, so they bracket the more exact theoretical solutions. G was taken as 117 psi, in keeping with the buckling load correlations, although its influence on the dimensionless results is small.

For each experimental point, the measured P was divided by the P_{cr} obtained from the buckling tests, and the K_t measured in the column shear tests was divided by the value of K_{t0} derived from Eq. E-64 with $G = 117$ psi. This was used in place of an experimental value for K_{t0} which could not be obtained because a compressive load is needed to prevent slip between units.

The correlation between experimental and theoretical results is poor, particularly for the 2×3 unit column (3 units above and 3 below the central shear plate). First, the points are nearly colinear instead of lying on a curve. The points representing the column of 2×8 units even curve slightly in the wrong direction, although they are close to the predictions of Eq. E-65. Second, the experimental values are all significantly smaller than the predicted values. At first sight this appears to be in keeping with the results of the shear modulus tests of Appendix G, in

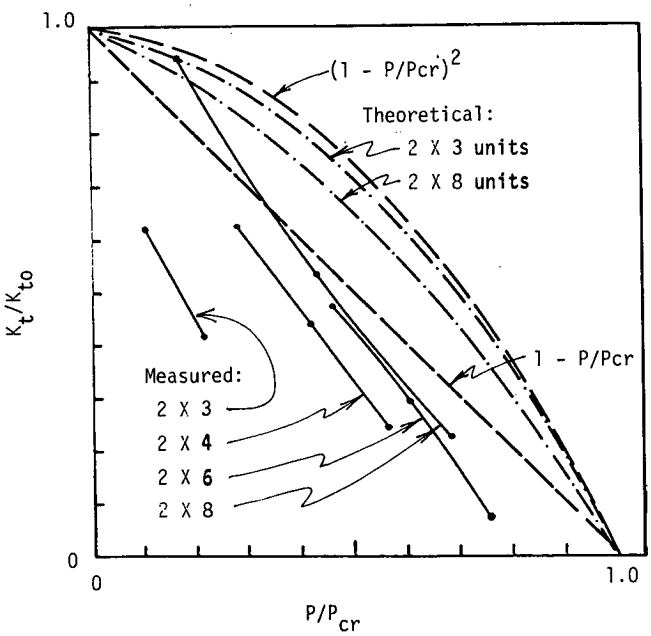

Figure E-18. Influence of P/P_{cr} *on transverse stiffness (using measured* P_{cr} *for measured stiffnesses).*

which evidence was found that the shear modulus itself decreases under simultaneous axial stress, but in Figure E-18 the reduction found in those tests has already been taken into account by using $G = 117$ psi. If the experimental points were based on K_{ro} using $G = 140$ psi (the value found under low compressive stress), the discrepancies in Figure E-18 would increase.

The fact that the experimental transverse stiffnesses were lower than expected appears to be beneficial in practice because it means that the forces transmitted to the substructure will be reduced. However, there may be occasions (such as when resistance to braking forces is needed) when the lower stiffness may prove disadvantageous. It also poses problems for quality assurance shear tests on complete bearings, which of necessity are performed under significant compressive stress.

None of the obvious potential causes for error could plausibly cause such consistent and large differences as were found. The load displacement plots from which measured stiffnesses were obtained (e.g., Fig. E-14) were remarkably linear. The experimental buckling loads for the 2 × 8 unit and the 2 × 6 unit columns were predicted within 5 percent by the Basic Theory, yet the same theory with the same material properties shows much larger errors in predicting the measured transverse stiffness.

The critical stress for the 2 × 3 unit column was obtained by extrapolating the straight line through the other experimental results, because no 6-unit column was tested. This gave a best estimate buckling stress of 4,850 psi. If, instead, critical stresses for both the 2 × 3 unit and 2 × 4 unit columns are taken from Eq. E-24 with $G = 117$ psi, rather than using the measured (or best estimate) values, the correlation improves considerably as can be seen from Figure E-19. However, there is no rational basis for doing so, particularly for the 2 × 4 unit column for which a measured buckling stress is available.

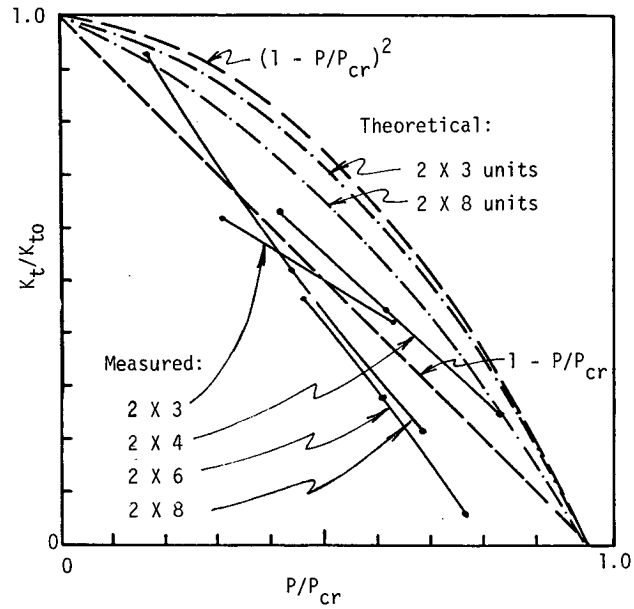

Figure E-19. Influence of P/P_{cr} *on transverse stiffness (using predicted* P_{cr} *for measured stiffness).*

SUMMARY AND CONCLUSIONS

The following conclusions may be drawn:

1. Buckling loads predicted by Eq. E-24 for bearings made of any material and of any geometry can be represented in dimensionless form by a single curve relating G/σ_{cr} to $\bar{\lambda}$.

2. Experimental buckling loads, using two different bearing geometries and a range of column heights for each, showed excellent correlation with predictions of the Basic Theory at slendernesses, $\bar{\lambda}$, greater than 0.8. Shorter column heights resulted in measured buckling loads increasingly higher than those predicted by the Basic Theory. The section properties used (such as f_r) were those derived theoretically by others, but to obtain a good fit the shear modulus had to be reduced 17 percent below the value measured at low compressive stress.

3. Experimental values of transverse stiffness under simultaneous compressive stress were found to be significantly smaller than predicted ones. Theory shows that the transverse stiffness should be a function of P/P_{cr}. Difficulties were encountered in confirming that relationship experimentally with medium to short columns because material failure preceded buckling, thereby making it impossible to obtain a reliable estimate of P_{cr}, even using Southwell techniques. Even for higher columns, the correlation was found to be quite sensitive to the conditions assumed. Positive verification of the Basic Theory predictions was therefore not possible.

APPENDIX F

FATIGUE

INTRODUCTION

Fatigue is regarded (*3*) as an important potential mode of failure in elastomeric bearings, but it has received only sporadic study. The earliest known investigation of fatigue in elastomers (*38*) consisted of experiments on small natural rubber blocks that were attached to the heads of bolts. The blocks were tested in cyclic shear and compression, and it was noted that longer fatigue life resulted for strain crystallizing rubber if complete relaxation was not permitted after each load cycle. The study showed a strong correlation between the magnitude of the strain and the fatigue life, and the temperature of the rubber was also found to influence the results. It was observed that harder rubber generally had shorter fatigue life. The specimens were very small and had very small shape factors, and so the results may or may not be relevant to practical bridge bearings.

Despite these limitations, this study was used as the rationale for the shear limit employed in the BE1/76 design specification (*27*). This specification limited the sum of the shear strain due to compressive loading and shear deformation (see Fig. F-1) to a percentage of the elongation at break. That is,

$$\gamma_c + \gamma_s \leq \eta EB \qquad \text{(F-1)}$$

where γ_c and γ_s are the maximum shear strain caused by compression and shear loading respectively, EB is the elongation at break of the material, and η is a numerical constant. The strains are illustrated in Figure F-1. This approach is somewhat rational because it limits the value of the maximum total strain in the material to a fraction of the material capacity. Furthermore, harder elastomers usually have smaller EB values, therefore their allowable shear strains are lower, in keeping with the test results. However, Eq. F-1 is a significant extrapolation of the findings of the study, which were based on specimens whose sizes and shape factors were significantly different from those found in bridge bearings, and which did not explicitly correlate fatigue strain capacity with the material elongation at break. Equation F-1 also implies that strains can be superimposed even though they are much larger than the infinitesimal values on which the validity of superposition is based.

A later series of tests (*55*), including a few specimens tested under cyclic load, were performed on full size bridge bearings, and the results were used as the basis for UIC 772 Specification (*30*). These test results are not well documented, and many details are missing. However, the results of the fatigue tests led to the recommendation that the shear stress be limited to $5G$. That is,

$$\tau_c + \tau_s + \tau_r \leq 5G \qquad \text{(F-2)}$$

For a linear elastic material, Eq. F-2 may be divided by G, resulting in a limit of 500 percent on the total shear strain. However, UIC 772 (*30*) specifies that the shear stresses in Eq. F-1 should be taken as the static components plus 2.0 times the dynamic components to reflect the more damaging effects of dynamic loads. These provisions are quite different from those in BE1/76. The UIC provisions are more generous for harder elastomers, which generally have a smaller elongation at break. Further, the UIC specification suggests a preference for neoprene, while BE1/76 appears to favor natural rubber, because natural rubber usually has a lower G value and higher elongation at break under similar compound conditions. The UIC approach of limiting the total shear stress to a value independent of the elongation at break is also carried forward to the recent BS 5400 Specification (*8*).

Theoretical studies have also been made of fatigue. Propagation under cyclic compression load of cracks initiated due to ozone cracking or mechanical cracking was studied (*56, 57, 58*), and it was found that fatigue cracks in elastomeric bearings become significant primarily in the elastomer near the steel laminate interface. Most cracking was found to propagate in directions which led to a stable self-limiting crack, and these results (*56, 59, 60*) led to suggested bearing details that would theoretically minimize fatigue crack problems.

Other experimental studies (*61, 62, 63*) have been performed. One (*62*) provided some understanding of the sequence of fatigue cracking under cyclic shear loading, but there were insufficient tests to develop any far reaching conclusions. Other (*61, 63*) focused on unreinforced pads. These pads behave differently from reinforced bearings because bulging in them is restrained only by frictional resistance (*3*). It appears that the test results were influenced by damage initiated by frictional effects, and so the results may not be relevant to reinforced bearings. Some reinforced bearings (*63*) were also tested, but they were of an unusual design so the results are probably not a good indicator of reinforced bearing performance in general. Finally, the material properties, size, and shape factor of many of the bearings tested in these studies would not be relevant to present day practice.

FATIGUE TEST PROGRAM

The existing literature on fatigue does not present a very clear picture of this mode of failure. As a result, an experimental

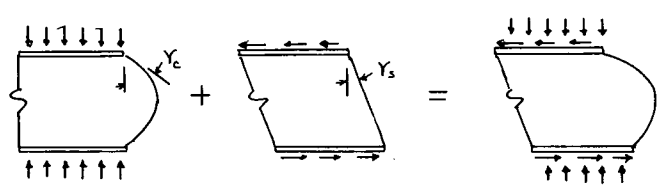

Figure F-1. Shear strain components of elastomeric bearings.

program was performed to understand the phenomenon better. The normal objective of fatigue research is the development of S-N curves such as those shown in Figure F-2. Such curves indicate the number of cycles of a given type of loading which can be safely sustained by a specific structural detail. A substantial number of tests are required to generate a single S-N curve, and the curve is still specific to a given material, detail, and loading. Fatigue of elastomeric bearings is even more complex. Elastomers are viscoelastic materials, and so the rate of loading and temperature of testing are interrelated and important. Further, elastomers may be materially nonlinear, and the very large strains which they can sustain without failure render them geometrically nonlinear, so the usual fatigue concepts of accumulated damage and fatigue failure may not apply.

In view of these problems, it was not practical to attempt to develop design S-N curves, because the time and funds were not available. Instead, the research was directed toward finding the factors that have the greatest impact on fatigue life and toward determining how these factors can be controlled to produce a satisfactory design. Therefore, certain parameters were selected for study, and a test matrix was set up. The matrix was defined to cover the range of practical application of each parameter. If all test points in the matrix were filled, hundreds and perhaps thousands of fatigue tests would be required. Instead, one parameter at a time was varied over the range of practical importance while attempting to hold all other parameters fixed in so far as possible. This approach permitted comparison of the relative importance of the different parameters. The investigation was clearly not exhaustive, but the resulting analysis should lead to better guidelines for design.

The most important variables for consideration in a test program are the following:

1. *Type and magnitude of loading.* Elastomeric bearings usually support large compressive loads while accommodating shear deformations introduced by creep, shrinkage, or thermal effects. In addition, rotation of the bearing caused by deformation or initial camber of the bridge girders must also be permitted. The compressive load will have a constant component due to the dead weight of the bridge, and a cyclic component due to bridge traffic. Shear deformations will have one cyclic component due to the daily temperature cycle, and they may have another, higher frequency one due to bridge traffic if the bearings provide elastic restraint. These different types of loading require separate consideration in the development of reliable fatigue design criteria.

2. *Rate of loading.* This is important for fatigue of elastomeric bearings for three major reasons. First, elastomers are viscoelastic, and so it is reasonable to expect that the rate of loading will affect the fatigue life. Second, the rate of loading in actual bridge bearings will vary widely for different types of loading as outlined in Item 1. Finally, fatigue tests require many cycles of loading, and time becomes critical. A good understanding of rate effects is necessary to gain the maximum benefit from the available testing time.

3. *Mean stress and stress range.* These influence fatigue life significantly, and so they are a primary criterion in design of any experimental program. The question of the relative importance of cyclic strain as opposed to cyclic stress must also be considered.

4. *Material properties of the elastomer.* Present code provisions for fatigue design vary widely. Some specifications appear to favor harder elastomers (*8, 30*) while others (*27*) favor softer elastomers with larger elongation at break. Study is needed to determine which material properties are most important and how they affect the fatigue life.

5. Shape factor, size and geometry may also affect the fatigue life and tests are required to evaluate the importance of these parameters.

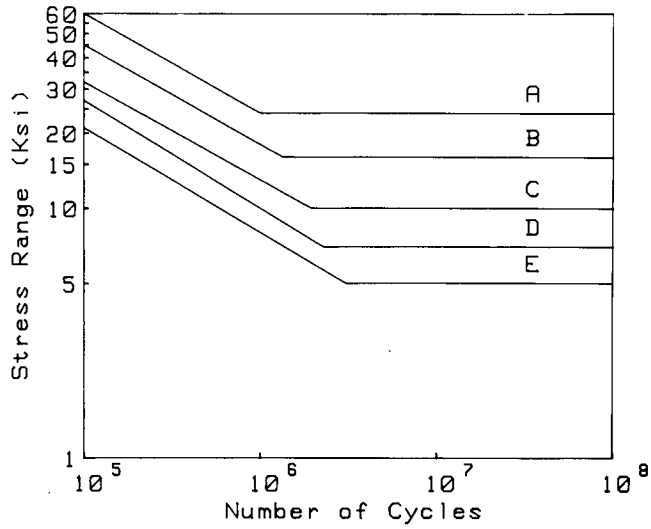

Figure F-2. Typical S-N curves for fatigue design.

CYCLIC SHEAR TESTS

The type of loading is a major parameter in fatigue of elastomeric bearings, and so separate fatigue experiments were performed in cyclic shear and cyclic compression. Fourteen specimens were tested in cyclic shear, and the test conditions and results are summarized in Table F-1. The primary source of cyclic shear deformations imposed on elastomeric bridge bearings is the lengthening and shortening of the entire bridge in response to temperature variations. A typical bearing is thus subjected to one shear cycle per day as the bridge structure responds to day-to-night temperature variations, causing approximately 20,000 such cycles over the course of 55 years. The fatigue tests were conducted at constant amplitude about a zero mean. However, the severity of daily cycles for the actual bridge will be smaller for many days, so the test results should be conservative for these cases. Bridge bearings experiencing shear deformation due to traffic loading may experience many more cycles at a more rapid rate than were imposed in the tests, and so the results may be unconservative for these cases. However, it is likely that the amplitude of loading would be smaller.

Shear testing invariably requires a simultaneous compressive load, which simulates the gravity load on the bearing and prevents slip under shear deformation. A test frame was built to develop an approximately constant compression load and a cyclic shear deformation, and the general design of the rig is shown in Figure F-3. The test frame was arranged so that the bearings (a) were tested in pairs. The compressive load was applied to the bearings by means of high-strength threaded rods (b) which were tensioned by means of a center-hole hydraulic

Table F-1. Shear fatigue tests.

Test No.	Shape Factor	Material Type	Shore A Hardness[1]	Tensile Strength[3] (psi)	Elong. @ Break[3] (%)	Compressive Stress (psi)	Compressive Strain (in/in)	Applied Shear (in/in)	Cycle Rate Hz.	Total No. Cycles	Total Debonding[2] in/100
1	5.3	CR	52 (52)	2777	591	550	.04	0.6	0.2	21000	182
2	5.3	CR	52 (52)	2777	591	1550	.11	0.5	0.2	20100	308
3	5.3	CR	52 (52)	2777	591	1680	.11	0.5	1.0	20000	697
4	5.3	CR	52 (52)	2777	591	1530	.12	0.5	.04	20000	83
5	5.3	CR	52 (52)	2777	591	2300	.14	0.5	0.2	20000	356
6	5.3	CR	52 (52)	2777	591	1450	.12	0.85	0.2	20000	1081
7	5.3	CR	52 (52)	2777	591	1580	.11	0.15	0.2	20000	0
8A	4.4	CR	(54)	--	--	1000	.10	0.5	0.2	20000	--
8B	4.4	CR	(54)	--	--	1010	.10	0.85	0.2	10000	--
9	5.3	CR	74 (65)	2559	351	2470	.11	0.85	0.2	20000	1186
10	5.3	CR	60 (62)	2876	439	2240	.13	0.85	0.2	20000	1350
11	5.3	NR	60 (64)	2801	575	2200	.12	0.85	0.2	20000	961
12	5.3	CR	49 (51)	3123	678	1500	.13	0.85	0.2	20000	1188
13	5.3	NR	53 (58)	2865	602	2220	.13	0.85	0.2	20000	919

Notes

1 Nominal hardness (measured hardness).
2 Sum of debonding measurements at all locations - 2 bearings.
3 Manufacturer's data.

a = test bearings
b = threaded rods
c = center plate
d = hydraulic activator
e = intermediate plates
f = clamping plates
g = cross beams
h = elastomeric springs

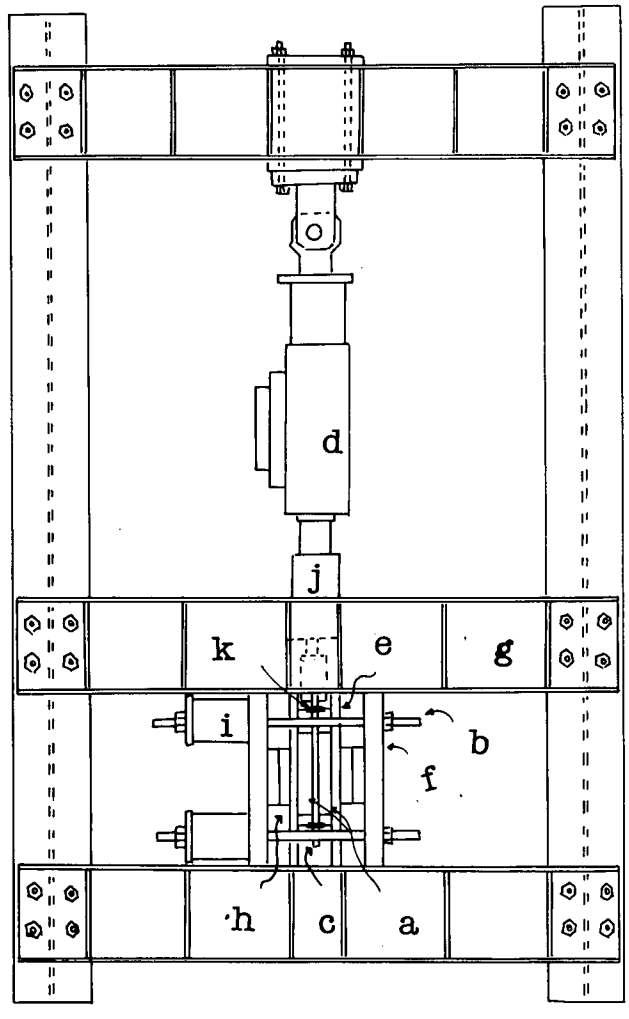

Figure F-3. Load frame for shear fatigue testing.

ram. A plate (c) between the two test bearings was moved cyclically upward and downward by a 55,000-pound capacity hydraulic actuator (d) which is part of a closed-loop MTS hydraulic testing system. The actuator was programmed to impose a precise shear displacement on the test bearings. Two intermediate plates (e) and two clamping plates (f) were held in position vertically by cross beams (g). Preliminary tests revealed that each time the test bearings were deformed in shear their thickness changed slightly, and as a result the compressive load changed. Therefore, in order to supply a more nearly constant compressive load, additional elastomeric bearings (h) were positioned between the clamping plates and the intermediate plates. These bearings acted as springs to smooth out variations in the compressive load applied to the test bearings. The test bearings were held in position in the rig by friction between the steel reinforcing plates of the bearings and the steel plates of the test rig. In all of the tests the ratio of compressive force to maximum shear force was large enough to prevent slip.

Compressive load on the test bearings was measured using four load cells (i) placed over the high strength threaded rods. Shear load applied to the test bearings was measured by means of a load cell placed between the end of the hydraulic actuator piston and the center plate of the test rig (j). Compressive displacement of the test bearings was measured using four LVDTs (k), mounted on the corners of the intermediate plates. An LVDT mounted permanently inside the hydraulic actuator measured shear displacement of the test bearings. Because repeated shear cycling of the bearings resulted in a buildup of heat, it was necessary to monitor the temperature of the bearings. This was accomplished by inserting a thermocouple into a hole drilled into the edge of the center plate (c), and the temperature was monitored with an Analogic AN 2572 Digital Indicator. The location of the thermocouple was near the center of mass of the two test bearings, and the temperature was dependent on the heat conducted from the test bearings clamped on both sides of the center plate. It was found that the thermocouple responded quickly to changes in the rate of shear cycling, indicating that the thermocouple was a sensitive indicator of the variation of temperature in the test bearings. All load cells and LVDTs were monitored by a Hewlett Packard HP9816 computer and HP3497 Data Acquisition Unit, permitting nearly simultaneous measurement of voltage from all instruments and rapid recording of data.

The test specimens (except no. 8) were 8.5-in. square bearings with two 0.4-in. elastomer layers and three 0.125-in. plates (see Fig. F-4a). The nominal shape factor of these bearings was 5.3. All of the specimens except no. 8 were cut with a band saw from sheets of bearing material, and therefore they had no edge cover. This permitted ready observation of crack development. It is believed that cracks develop more quickly without edge cover and, thus, the fatigue results should be conservative. The specimens for shear test no. 8 were of a different size and had top and bottom cover, as well as edge cover on three sides (see Fig. F-4b). They also had double steel plates on the top and bottom as shown in the figure. This allowed the top and bottom cover to be removed easily by slitting the edge cover at the level where the two plates were in contact. The same specimen could then be tested with and without cover. The edge without cover was cut using a band saw to expose the edges of the steel plates. This test specimen was used to illustrate the effect of edge cover on fatigue behavior.

All bearings were measured and inspected for defects before being tested. The test specimens and spring bearings were then placed in the rig, and the compression load was applied. The shear fatigue cycles were then started at a prescribed rate and displacement range. Soon after starting the shear fatigue cycles

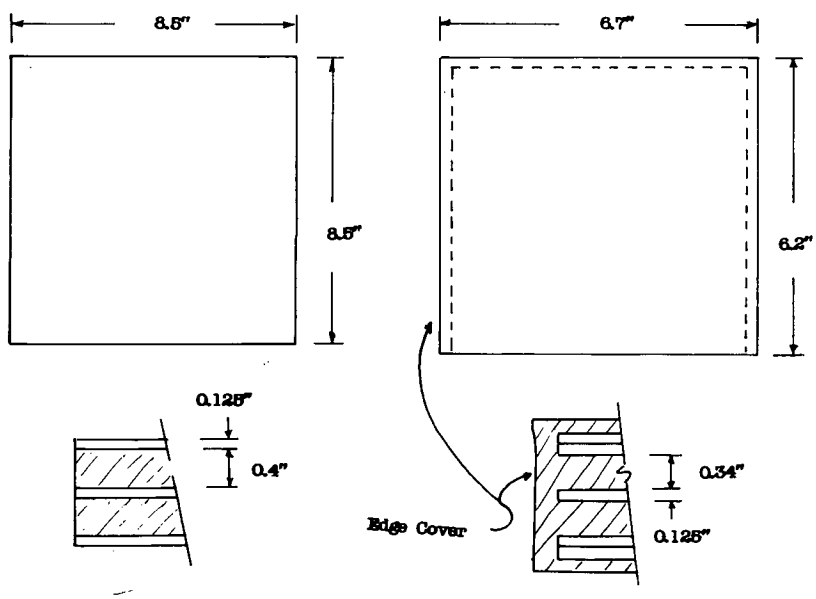

a) Type 1 Shear Specimen

b) Type 2 Shear Specimen

Figure F-4. Dimensions of bearings for shear fatigue tests.

the shear stiffness of the test bearings was measured by applying several shear cycles at a rate of 0.3 Hz, and using the computer to take load and displacement measurements at closely spaced time intervals. Periodically during the test, the shear fatigue cycles were again slowed temporarily to take shear stiffness readings. Throughout the test the temperature of the bearings was monitored in order to avoid overheating the bearings. In most of the tests the temperature did not rise above 52°C (126°F), which was considered acceptable. If the temperature was still rising at a significant rate when it reached about 50°C, the test was stopped to allow the bearing to cool. In later tests a fan was used to keep the temperature down. Occasionally it was necessary to stop the test overnight in order to allow the bearings to cool. These interruptions of the test did not appear to have any effect on the shear fatigue damage suffered by the bearings, and provided the opportunity to study the change in shear stiffness of the bearings resulting from changes in temperature. In some tests abrasion and fretting of the elastomer occurred. The debonded elastomer lips (see Fig. F-5) worked against the edges of the steel plates as the bearings were cycled in shear. The abraded material shed by the bearings was collected and weighed.

After the start of testing, fatigue cracks frequently developed in the elastomer near the interface of the steel laminate. The cracking generally progressed in a sequence and was similar to that reported by Chhauda (62). No cracking was observed for any of the specimens until cyclic loading was started. Generally cracking was first observed at the steel and elastomer interface for outer plates (i.e., locations 1, 2, 3, or 4 shown in Fig. F-6), where the combination of compressive and shear loading causes high shear strains. The cracking then progressed through locations 5, 6, 7 and 8 for most specimens and, in severely damaged bearings, progressed to the less severely strained edges of locations 9 through 16. The fatigue cracks grew quite severe for some specimens, but none of the specimens failed. That is, all bearings continued to support their loads and accommodate movements, although some were in a severely deteriorated condition. A measure of relative damage was needed to compare

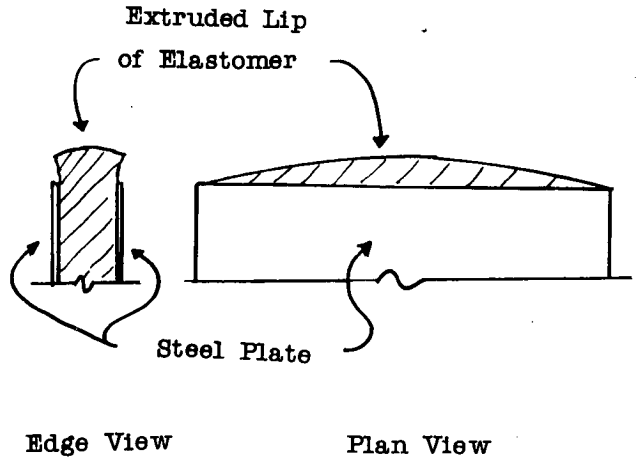

Figure F-5. Protruding lip of elastomer caused by the fatigue cracks in the bearing.

the condition of individual bearings, and to define when the bearings were no longer acceptable. Two major damage measures were employed.

The first was the distance by which the delaminated elastomer projected beyond the steel. It was easily measured and appeared to be a good relative indicator of cumulative fatigue damage. First, the test was stopped at various points in the test, and a sketch was made of the locations where debonding had occurred on each edge of the test bearings. Next, a depth gage was used to measure the height of the debonded lip of elastomer, which projected from between the steel plates, as shown in Figure F-5. This maximum height was measured at the four steel to elastomer interfaces, one on each edge of each bearing. These heights were recorded on the sketch of debonding locations. Details of the appearance of the debonding were also noted at a number of times during the test, and the total crack depth was plotted as a function of the cycle number as shown in

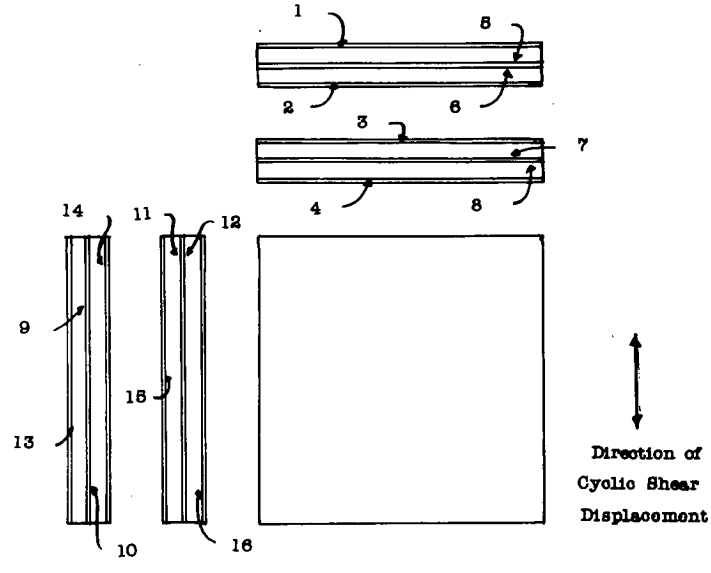

Figure F-6. Locations of fatigue cracking.

Figure F-7. The total debond height was the sum of the height of the maximum protruding elastomer at all cracked interfaces on all four edges. The value given is the total for the pair of bearings in the shear fatigue tests.

This measure is incomplete because it does not include the depth of crack penetration into the bearing. Further, it will have different importance for different shape factor bearings. The rate and the extent of crack growth depended on several factors described in later discussion, but all crack depth curves appeared to exhibit similar charactertistics. That is, the cracks propagated relatively rapidly during the early part of the test, and they then reached a plateau where the cracks grew very slowly. This observation appears to support the suggestion (*56, 59*) that fatigue cracks are a self-limiting phenomenon for elastomeric bearings.

Change in bearing stiffness was used as the second measure of fatigue damage. The reduction in shear stiffness was small, and was often overshadowed by temperature effects. Therefore, the change in compression stiffness, which was larger, appeared to be a more reliable indictor of fatigue damage; however, it was much more difficult to perform compression stiffness tests at intervals during the shear fatigue tests. As a result, much less data for compression stiffness are available. However, measurements of both types of stiffness were compiled and compared as a measure of the fatigue damage. These data are summarized in Table F-2.

Table F-2. Shear fatigue damage.

Test No.	Shear Stiffness Initial (lb/in)	Shear Stiffness Final (lb/in)	Shear Stiffness Change %	Max. Debond in/100	Compressive Stiffness Initial (K/in)	Compressive Stiffness Final (K/in)	Compressive Stiffness Change %
1	8380	7580	-9.5	182	1340	1430	+6.7
2	7540	7760	2.9	308	1340	1360	+1.1
3	7170	7280	1.5	697	1340	1460	+8.5
4	8630	8800	2.0	83	1340	1360	+1.1
5	8810	8150	-7.5	356	--	--	--
6	6200	5400	-12.9	1081	--	--	--
7	13470	12890	-4.3	0	--	--	--
8A	3770	3680	-2.4	--	--	--	--
8B	3220	3190	-0.9	--	--	--	--
9	11160	10900	-2.3	1186	2530	2260	-10.4
10	10560	10480	-0.8	1350	2210	2130	-3.6
11	9160	9170	0.1	961	2390	1810	-24.2
12	7250	6780	-6.5	1188	1430	1530	+6.8
13	7780	7570	-2.7	919	2130	1570	-26.4

RESULTS OF THE SHEAR FATIGUE TESTS

The effect of the rate of loading was the first parameter considered. A daily shear cycle due to temperature effects suggests a load rate of 0.000015 cycles per second. This load rate may be realistic for temperature-dependent loading, but impossible for testing inasmuch as 20,000 cycles require 55 years to complete. As a result, rates of 1, 0.2, and 0.04 cycles per second were investigated. Figure F-6 shows the results of these tests.

The amount of fatigue damage increases with increasing load rate. Further, rapid cyclic load heats up the elastomer more, and it was presumed that fatigue resistance of the material would depend in some way on the temperature. Thus, the standard rate selected for all tests was the slowest practical rate of 0.2 Hz (one cycle every 5 sec). Although this is faster than the probable rate in the field, the results obtained from tests conducted at this rate should be conservative. The results may be unconservative for traffic-induced shear deformation because more cycles may be applied with a more rapid load rate than used in the test program.

Heat buildup also appeared to be an important parameter in the fatigue test program. Elastomers are viscoelastic materials, and heat is developed due to the internal work done during the testing. In the tests, the heat dissipated very slowly, and spec-

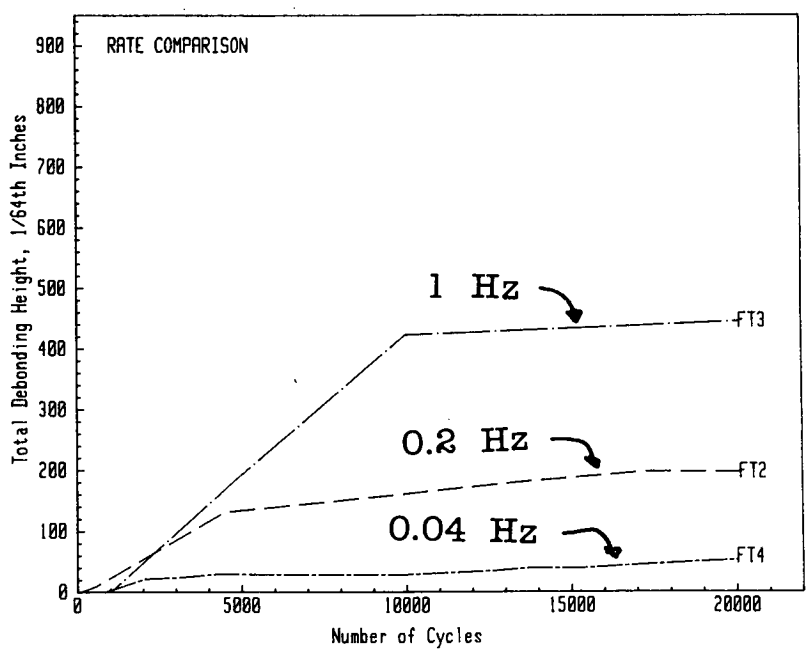

Figure F-7. Shear fatigue tests—variation in measured elastomer protrusion with load rates.

imens which generated higher temperatures usually had a shorter fatigue life. The elevated temperatures apparently led to premature deterioration in the elastomer and the bond. Higher temperatures generally occurred with larger shear strains, larger compressive stress levels, and rapid test rates. Some elastomeric compounds and bearing geometries appeared to be more susceptible to heat buildup than others. The elevated temperatures also reduced the stiffness of the bearing. Stiffness was one of the criteria used to measure fatigue deterioration, and so the temperature effect seriously complicated this analysis. A separate study of the effect of temperature on bearing stiffness was performed to correct the data for this problem.

The magnitudes of the mean stress and the stress range are usually critical parameters in a fatigue test, and so they were monitored during these experiments. However, because of the nonlinear viscous characteristics of elastomers, reversed cyclic loading between constant shear strain limits was used, because strain and displacement control would produce more repeatable experimental results than stress control. Strain control may also be more relevant to bridge bearing field conditions. This cyclic shear strain provided the stress range component. The compressive load was applied at the start of the test and effectively provided the mean stress. However, it should be noted that bearings that were severely damaged by fatigue cracking did not maintain a constant compression load at a constant average compressive strain level. Instead, the compressive load decreased slightly during the test while the average compressive strain increased. This effect was relatively small (20 percent or less), but it suggests that the severely damaged bearings would have sustained somewhat greater damage during the fatigue test if the compressive load had been truly constant.

Figures F-8 and F-9, respectively, show the effect of mean stress and stress range on the fatigue damage. Increasing the compressive stress increased the mean strain and the fatigue damage, but the effect of increasing the shear strain range is much more dramatic. The detrimental effect of cyclic shear strain is particularly dramatic for shear strains in excess of ± 0.5. This increased damage may be caused by the rollover noted in Appendix D for shear strains larger than 0.5, and it provides further evidence to support the 0.5 shear strain limit proposed in that appendix.

The tests described in earlier discussion were all performed on bearings of 52 nominal Shore A hardness neoprene. The compound and material properties were theoretically the same for all specimens. However, it is frequently suggested that some material properties affect the fatigue life, and so a series of tests were performed on a wide range of neoprene and natural rubber compounds. The compounds were chosen to cover a range of practical materials that still satisfy AASHTO (*1*) requirements. The measured fatigue damage for these tests is shown in Figures F-10 and F-11. Figure F-10 shows the progression of cracking for the different materials under comparable loadings. It should be noted that the mean stress and stress range were different for each specimen, but the cyclic shear strain and average compressive strain were nearly the same for all specimens. Figure F-11 indicates that the natural rubber bearings generally had less cracking than neoprene of comparable hardness, but the difference was not dramatic. There was no strong correlation between the degree of shear fatigue damage and the elastomer hardness, the elongation at break or the tensile strength.

The fatigue tests described above were performed without cover. This was done because it permitted ready observations of the fatigue cracks, and it was believed to be conservative. One test was performed to investigate the effect of edge cover on the shear fatigue behavior. Edge cover is used to seal the edges of the steel reinforcing plates against moisture, thereby preventing rust, and top and bottom cover is sometimes employed to encapsulate the steel reinforcing plates within the elastomer. The covered test bearing was Specimen 8a and 8b and was made as shown in Figure F-4b. It had cover on three edges and was cut on the fourth edge to permit observation of crack progression. The bearings were arranged in the test rig

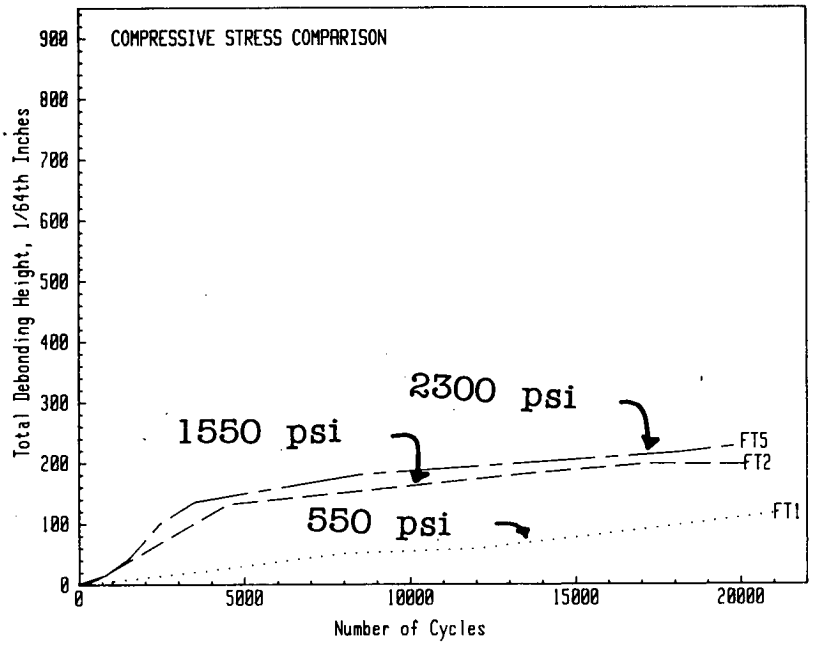

Figure F-8. Shear fatigue tests—variation in measured elastomer protrusion with compressive stress.

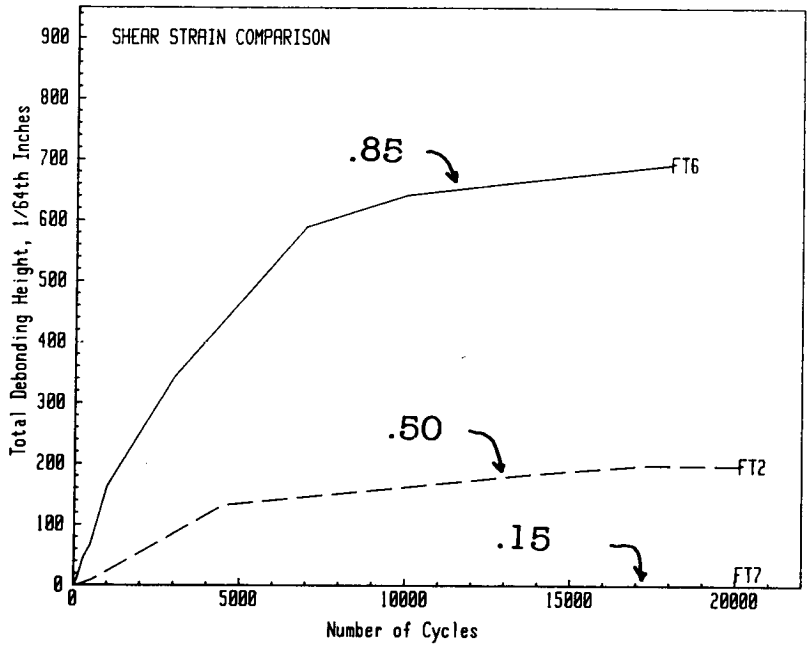

Figure F-9. Shear fatigue tests—variation in measured elastomer protrusion with cyclic shear strain.

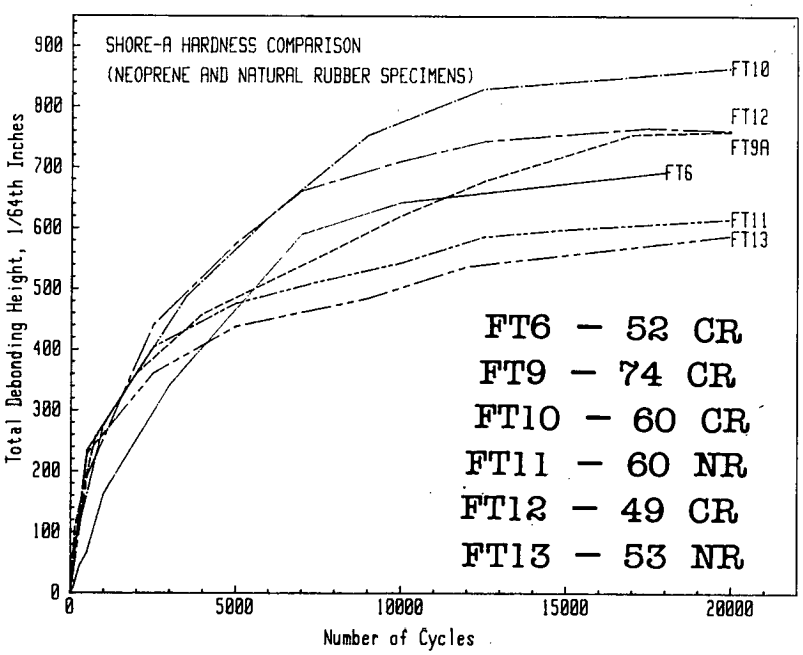

Figure F-10. Shear fatigue tests—variation in measured elastomer protrusion with different elastomeric compounds.

so that the edge without cover of one bearing was vertical in the test rig and the edge without cover of the other bearing was horizontal; in other words, the bearings were rotated 90 deg relative to one another. In this way, the performance of vertical and horizontal edges with and without cover could be compared. They both had the same surface areas and therefore the same nominal shear stiffness. Because the bearings had top and bottom cover they tended to walk or creep in the test rig when cyclic shear loads were applied, and so it was necessary to epoxy the bearings to the steel plates of the test rig. This effectively prevented all movement.

The tests were conducted in two parts: the bearings were first subjected to 20,000 cycles at ± 0.5 shear strain, then an additional 10,000 cycles at ± 0.85 shear strain. Only a moderate amount of damage was observed during the first 20,000 cycles, and the last 10,000 cycles produced more extensive damage. On

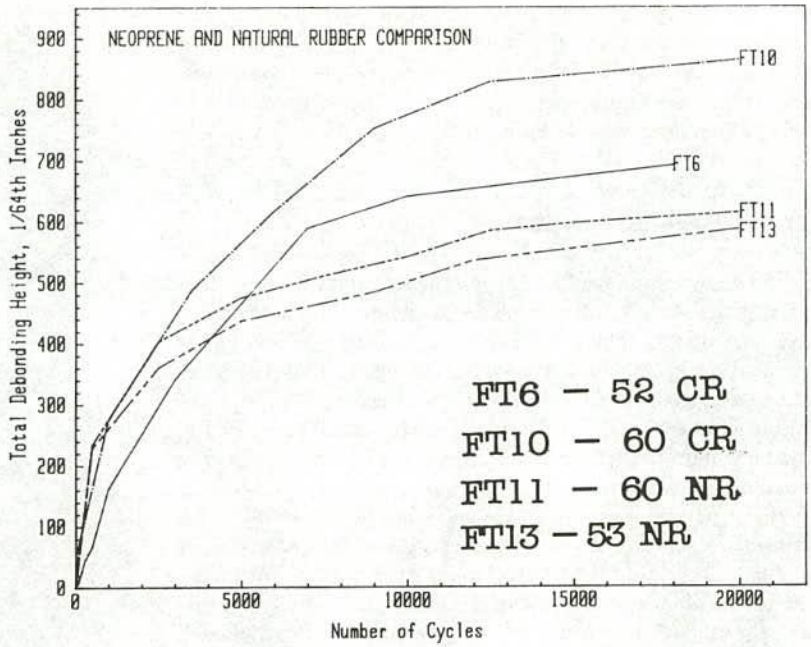

Figure F-11. Shear fatigue tests—variation in measured elastomer protrusion with natural rubber and neoprene compounds.

edges without cover, observations of debonding damage were made in the usual manner. On edges with cover, debonding was observed by noting the changes in the bulge patterns beneath the cover, by examining in cross-section the edges with cover where they were exposed at their ends, and by inserting a wire probe down the length of the cracks in the edges with cover. In addition the bearings were cut into quarters following the tests in order to determine the extent of debonding cracks beneath the cover.

It was found that the nature of the shear fatigue damage with and without cover was different. Without cover, the elastomer debonded from the steel plates at their edges as shown in Figure F-5, whereas with cover the elastomer debonded near the edges of the plates in some locations and cracks propagated through the elastomer in others. These cracks along the covered edges initiated at the edges of the steel plates and propagated at an angle into the elastomer layers away from the edge cover, as shown in Figure F-12. Since the shear fatigue damage is different with and without cover, it is difficult to compare directly the extent of damage occurring on the two types of edges. However, it appears that covered edges sustain slightly less damage than uncovered edges, but that edge cover may conceal considerable debonding. The covered edges appeared undamaged throughout the test but later revealed extensive debonding and cracking beneath the cover when the bearings were cut into quarters for inspection.

The discussion to this point has focused on the extent of cracking. This may be a good relative measure of fatigue damage, but there is no clear cut measure of what level of damage is unacceptable. As a result, the shear and compressive stiffnesses before and after testing were compared and the results are given in Table F-2. The shear stiffness was measured after several cycles of loading, because the stiffness had usually stabilized by this time. The compressive stiffness is more difficult to determine uniquely because of the very nonlinear stress strain behavior of a bearing in compression. Therefore, the stiffness was defined

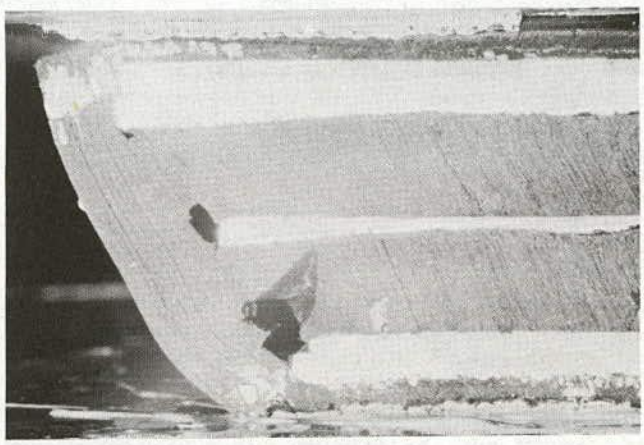

Figure F-12. Photograph of shear fatigue cracking in a bearing with edge cover.

as the secant modulus between the stress and strain at 1,330 psi and the stress and strain at 443 psi. It should be noted that the unloaded stiffness was sometimes measured on different bearings (of nominally the same material) for the shear fatigue tests. This was necessary because no initial shear stiffness reading had been taken at the start of those fatigue tests, and this fact may have contributed to the limited correlation between stiffness change and measured cracking.

The shear stiffness did not appear to be a particularly sensitive indicator of fatigue damage. The maximum change was 12.9 percent, and it did not seem to be well coordinated with the observed and measured damage. The maximum compressive stiffness reduction was 26.4 percent. The correlation was not perfect, but generally the greatest reduction in compressive stiffness occurred on bearings with large measured delamination.

This observation appears to be consistent with theory, since delamination cracking effectively reduces the shape factor of the bearing. A 5 to 10 percent reduction in compression stiffness may be intolerable for some practical situations, and this may help define an acceptable limit for fatigue damage.

CYCLIC COMPRESSION TESTING

The compression loading on elastomeric bridge bearings consists of the static dead load of the structure and the dynamic live load due to vehicle loading. The traffic loading is highly variable in amplitude and frequency, and many millions of cycles must be expected during the life of the structure. However, the vast majority of these load cycles are very small compared to the maximum truck load and the dead load of the bridge. The smallest cycles contribute little or nothing to the fatigue damage to the structure. As a result, the spectrum of real loads on the bridge are represented for design purposes (*1*) by a smaller number of cycles of AASHTO HS-20 truck loading. Although the procedure is not completely rational, it is generally approximately valid (*64*) for a 50-year bridge life, and so this approach was used in the compression fatigue test program.

The testing was directed toward the development of a better understanding of elastomeric bearings. Because of the many variables involved in the study, it was again not possible to generate complete S-N curves. Instead the relative importance of different parameters was assessed, and an approximate design procedure was chosen. The rate of testing was one important consideration, and it was selected based on three major considerations. These included the expected load rate in the actual structure, the time-dependent characteristics of elastomers, and the practical necessity of completing testing in a reasonable period of time. The maximum rate of loading in service is likely to be no greater than 1 Hz—this rate would require a continuous line of trucks 60 ft long spaced 50 ft apart, traveling at 41 mph. Previous investigations of the shear fatigue properties of elastomeric bearings indicated that the fatigue damage to elastomeric bearings increases with increasing frequency of the applied load. Therefore, laboratory tests performed at a rate of 1 Hz, the maximum rate expected in service, should give conservative results. Second, in order to apply a high number of cycles to each test specimen during the time available for the test program, a test rate no less than 1 Hz was required. Finally, pilot tests showed that cycling the bearings at a rate greater than 1 Hz gave rise to excessive heat buildup, and temperatures well above those expected in service. For these reasons all of the compression fatigue tests except No. 1 were conducted at a rate of 1 Hz. Test No. 1 was run at 2 Hz because the relatively small stress range reduced the hysteresis in the elastomer and consequently the temperature rise was small.

The tests also investigated different load levels and cyclic load ranges, different materials, and different bearing sizes and shape factors. The bearings were loaded in compression by using two different load frames (see Fig. F-13), which were identical in operation and had compressive load capacities of 100 and 200 kip. In both frames, compressive load was applied by an MTS hydraulic actuator which was part of a closed-loop hydraulic testing system. The test bearings were positioned between two steel platens, each 2 in. thick (Fig. F-14). The surfaces of the platens were smooth and parallel, and they were rigidly fixed

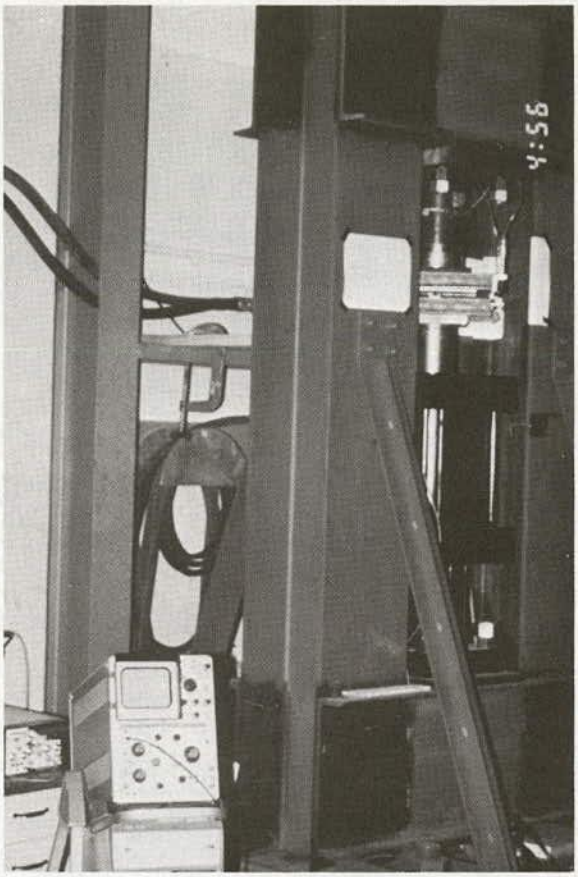

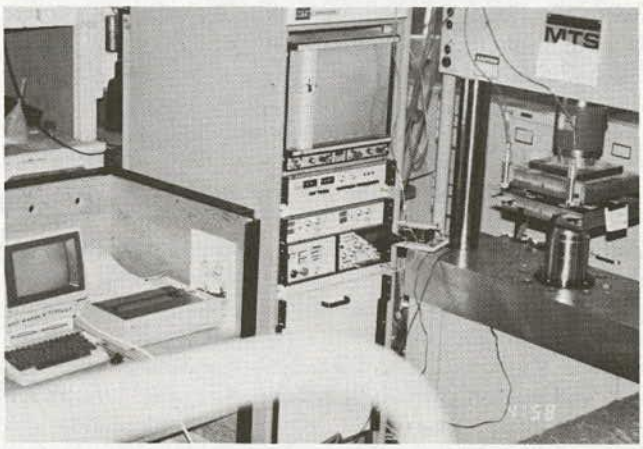

Figure F-13. Photographs of the two load frames used in compression fatigue testing.

to the load frame so that no rotational deformation of the bearing could occur during testing. Retaining stops attached to the face of the lower platen prevented lateral movement of the bearing.

Instrumentation consisted of a load cell to measure compressive load applied to the test bearing, and four LVDT's to measure compressive displacement. The load cell and LVDT voltages were monitored by an HP9816 computer. A miniature thermocouple probe was installed to monitor the internal temperature of the bearing. It was inserted in a $\frac{1}{32}$-in. diameter hole, 1 in. deep, drilled into the edge of the center reinforcing

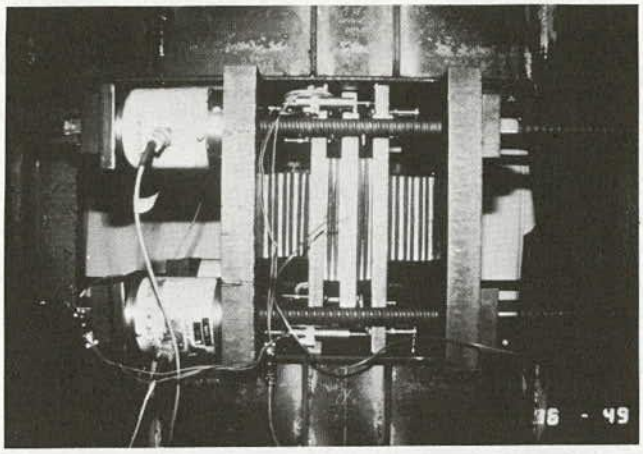

Figure F-14. Photograph of test specimen in shear fatigue test rig.

plate of the test bearing. In this location the thermocouple was able to sense variations in the internal temperature of the bearing.

The specimens tested were all 1.18 in. thick with two elastomeric layers 0.4 in. thick and three steel plates 0.125 in. thick (Fig. F-4). The plan dimensions of the bearings were 8.0 in. except for one 4.8 in. by 4.8 in. and one 10.2 in. by 10.2 in. bearing which were also tested to evaluate the effect of shape factor. The shape factor of the standard size specimens was 5.0; and of the two nonstandard specimens, 3.0 and 6.4. The elastomer for most of the specimens was neoprene with a 52 durometer Shore A hardness. Bearings made of both neoprene and natural rubber with a range of hardnesses were also tested. The properties of all the specimens tested are given in Table F-3. The material properties listed are those provided by the manufacturer of the bearings; the measured hardness is provided in parentheses. Sometimes there were considerable discrepancies between the manufacturer's hardness measurements and those measured by the investigators. The investigators measured the hardness on the edge of the elastomer layer under less than ideal conditions, but it is believed to be a reliable indication of true hardness. All the specimens were cut from sheets of bearing material using a band saw, and so they had no edge cover. The absence of edge cover permitted observation of the development of cracks in the edges of the elastomer layers. Based on the results obtained in previous shear fatigue tests it is believed that cracks develop more quickly without edge cover, and the fatigue results obtained in these tests should be somewhat conservative.

Each test bearing was measured and inspected carefully before testing. The bearing was then centered on the lower platen of the test apparatus, and retaining stops were installed to prevent lateral shifting of the bearing. Next the lower platen was raised so that the bearing was in contact with the top platen, but no compressive load was applied. Zero reference voltage readings were taken from the load cell and LVDT's and the initial temperature of the bearing was noted. The initial compressive stiffness of the bearing was measured by applying a cycle of compressive stress between 0 and 1,500 psi at a rate of 25 psi/sec. After this first cycle of loading, several more cycles were applied and the stiffness of the bearing was measured again, because elastomeric bearings exhibit a somewhat greater stiffness during the first cycle of applied load than during subsequent cycles. It was found that the compressive stiffness of the test

Table F-3. Compression fatigue tests.

Test No.	Shape Factor	Material Type	Shore A Hardness[1]	Tensile Strength[3] (psi)	Elong. @ Break[3] (%)	Mean Compressive Stress (psi)	Mean Compressive Strain (in/in)	Cyclic Loading Stress Range (psi)	Cyclic Loading Strain Range (in/in)	Cyclic Loading No. Cycles x1000	Total Debond[2] in/100
17	5.0	CR	52 (52)	2777	591	1125	.066	750	.041	2121	12
18	5.0	CR	52 (52)	2777	591	800	.053	1400	.075	245	690
19	5.0	CR	52 (52)	2777	591	962	.075	1075	.056	254	539
20	5.0	CR	52 (52)	2777	591	637	.045	1075	.063	338	495
21	5.0	CR	52 (52)	2777	591	1044	.075	912	.046	2003	308
22	3.0	CR	52 (52)	2777	591	582	.092	651	.091	2053	545
23	5.0	NR	53 (58)	2865	602	1360	.078	1520	.053	662	273
24	5.0	CR	49 (51)	3123	678	950	.071	1060	.057	1205	520
25B	5.0	CR	52 (52)	2777	591	1288	.084	1075	.050	554	224
26	6.4	CR	52 (52)	2777	591	1221	.058	1364	.047	499	438
27	5.0	CR	74 (65)	2559	351	1585	.086	1770	.051	484	131
28	5.0	NR	60 (64)	2801	575	1585	.084	1770	.052	490	130
29	5.0	CR	60 (62)	2876	439	1360	.071	1520	.051	663	98

Notes

1 Nominal hardness (measured hardness).
2 Sum of debonding measurements at all locations - 1 bearing.
3 Manufacturer's data.

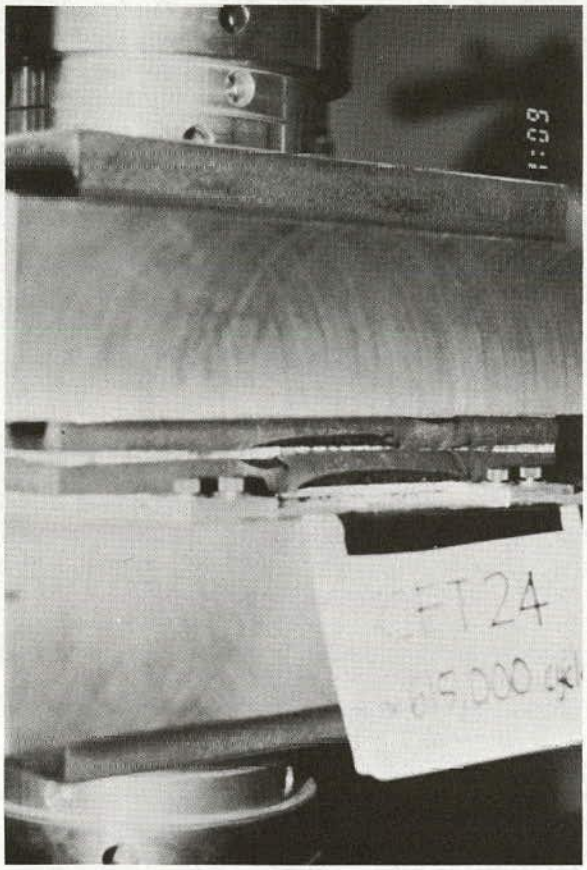

Figure F-15. Photograph of typical fatigue cracking from the compression fatigue tests.

bearings decreased to a nearly constant value after two or three cycles of loading. Next, a static stress equal to the minimum stress of the applied stress range was applied to the bearings, and cyclic loading was started by adding a sinusoidally varying stress. The temperature of the bearing was monitored by means of the thermocouple probe. The maximum temperature permitted was generally 54°C (129°F), although in one test, No. 2, the temperature rose to 59°C. Precise temperature control was not possible because the test rig was not continuously monitored. Compression stiffness readings were taken at intervals throughout each test. The cyclic loading was stopped and the bearing was permitted to cool to room temperature, 21°C to 26°C (70°F to 79°F), before making stiffness readings. In order to obtain data comparable to the initial compressive stiffness readings, several cycles were applied to the cooled bearing before these latter stiffness readings were taken.

During the compression fatigue tests the bearing exhibited two major types of damage. Delamination of the elastomer layers from the steel plates occurred, and consequently there was a reduction in compressive stiffness. This reduction in compressive stiffness was monitored by means of the compressive stiffness readings taken throughout the test. Debonding measurements were made in the same way as during the shear fatigue tests, except that these measurements were from a single bearing. It was not possible to measure the full depth of crack penetration into the elastomer, but only the debonded lip heights projecting from between the steel plates, as shown in Figure F-5. In some tests, abrasion and fretting of the elastomer occurred against the edges of the steel plates. In each test, the abraded material shed by the bearing was collected and weighed.

ANALYSIS OF COMPRESSION FATIGUE RESULTS

The compression fatigue tests were conducted at a rate of 1 Hz for reasons discussed previously, with a target of 2 million cycles. This test rate permitted completion of a test in a reasonable period of time, and it was also consistent with the maximum load rate to be expected during heavy truck traffic. The shear test results indicate that a more rapid test increases the rate and extent of fatigue cracking, and so one compression fatigue test (Specimen 17) was performed at 2 cycles per second to measure the sensitivity to load rate. Specimen 17 did not exhibit exceptional damage, and so it is believed that variations in load frequency may be less important for compression than for shear loading.

Fatigue cracks initiated in the elastomer near the steel laminate interface. The cracks grew with the number of repeated load cycles, and a typical cracked specimen is shown in Figure F-15. The cracks were in many ways similar to those observed in the shear fatigue tests, but there were also definite differences. First, the shear fatigue cracks grew quickly, and then appeared to stabilize after a number of cycles. Compression fatigue cracking did not appear to exhibit this stabilizing effect, as can be seen in Figure F-16. However, the compression cracking is plotted as a semilog curve, while the shear fatigue cracking employs a linear axis. The change in the horizontal axis distorts the curves, and so it is very possible that crack size could increase if many more shear cycles were added. Second, the locations for initiation of cracking were different for compression fatigue cracking. The total debonding height was somewhat smaller for the most heavily damaged compression tests than for the most heavily damaged shear specimens. It should be noted that the heights given in Tables F-1 and F-2 are for a pair of bearings and should be divided by two when they are compared to the compression tests.

Figure F-16 illustrates the effect of stress range on the fatigue crack rate. The degree of cracking and rate of cracking increased dramatically with increasing stress range. Figure F-17 shows the effect of mean stress on the fatigue damage. All three specimens had an identical stress range, but the mean stress increased by 50 percent for specimen 19 over that used for specimen 20 and by 92 percent for specimen 25. However, specimen 25 had the smallest measured cracking, while specimen 19 had the largest. The meaning of these results may be subject to some differences in interpretation. However, it may suggest that an increase in mean stress decreases the fatigue life slightly as suggested in the shear fatigue tests, while a dramatic reduction in fatigue life can be expected if the stress range is large compared to mean stress. This latter observation is consistent with the observations (*38*) made in earlier research, and it may occur because the benefits of strain crystallization are not realized when the mean stress level is relatively small.

Six different materials were tested for compression fatigue, and the results are shown in Figure F-18. The materials were selected to cover a wide range of properties expected with natural rubber or neoprene bridge bearings, and they were identical to those used in the shear fatigue testing. The bearings' load pro-

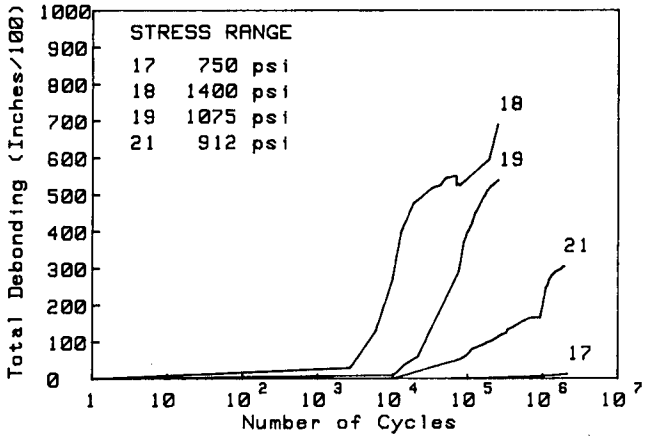

Figure F-16. Compression fatigue tests—variation in measured elastomer protrusion with stress range.

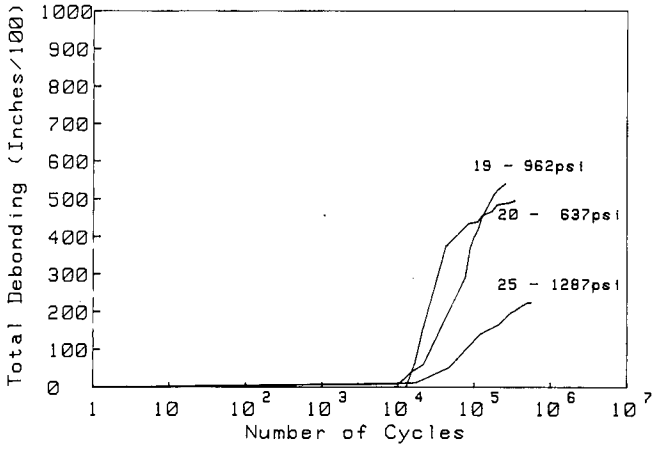

Figure F-17. Compression fatigue tests—variation in measured elastomer protrusion with mean compressive stress.

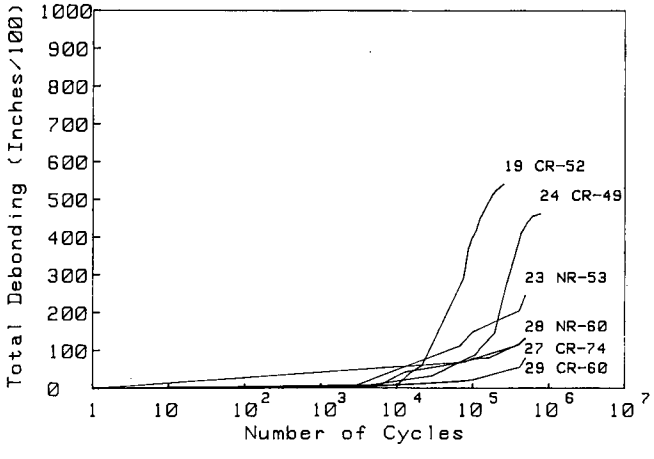

Figure F-18. Compression fatigue tests—variation in measured elastomer protrusion with different elastomeric compounds.

grams were selected to achieve nearly identical cyclic strain ranges and mean strains for all specimens, but the time-dependent characteristics of the elastomer produced some minor differences in the test results. The bearings with smaller elongation at break had smaller fatigue cracks. This is in direct opposition to the rationale employed in the BE1/76 specification. Harder specimens also sustained less cracking, and this appears to be in conflict with the damage observed in the shear tests. There did not appear to be any correlation between the tensile strength of the elastomer and the compression fatigue behavior.

Figure F-19 shows the crack growth rates for three different bearings with different shape factors and identical material and strain levels. The cracking was significant in all three specimens, but the onset of severe cracking occurred at quite different numbers of cycles. It is difficult to evaluate the differences, because the debonding measure is imprecise and the extent of cracking is of different importance with different size and shape factor bearings. As a result, the compressive stiffness of the bearing before and after cracking was examined. The stiffness typically decreased with fatigue damage as illustrated in Figure F-20. While the tangent stiffness decreased, there usually was

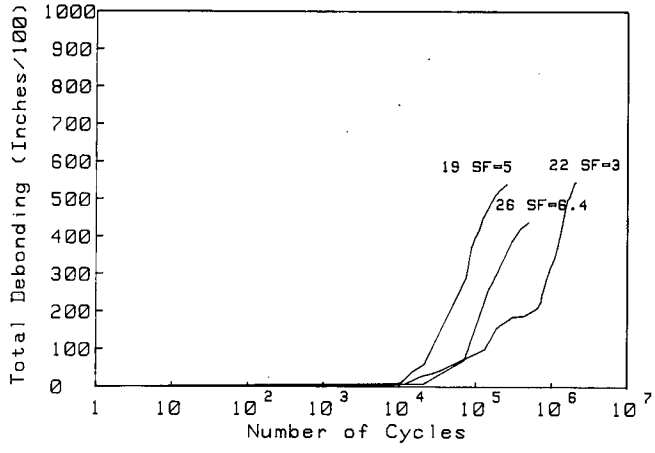

Figure F-19. Compression fatigue tests—variation in measured elastomer protrusion with different shape factors.

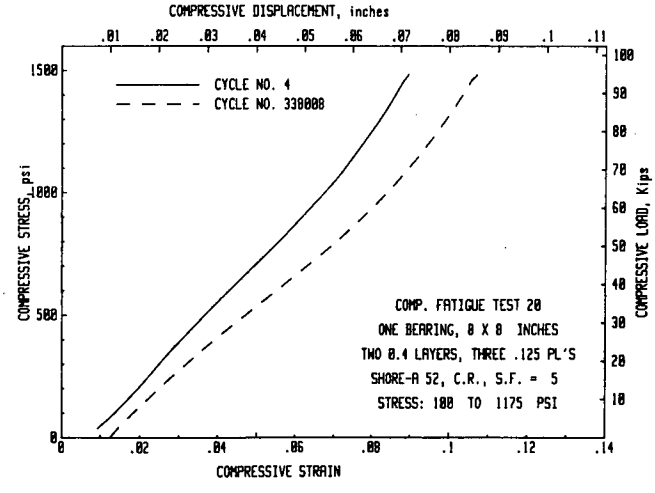

Figure F-20. Typical average compressive stress-strain curves for a bearing subjected to many cycles of compression fatigue loading.

Table F-4. Compression fatigue damage.

Test No.	Maximum Debond in/100	Compressive Stiffness Initial (K/in)	Final (K/in)	Change %
17	12	1099	999	-9.1
18	690	1139	929	-18.5
19	539	1135	977	-13.9
20	495	1103	895	-18.9
21	305	1095	993	-9.3
22	545	208	211	+1.3
23	244	1550	1232	-20.6
24	461	1147	1103	-3.9
25	224	1052	1019	-3.2
26	438	2582	2328	-9.8
27	131	1589	1513	-4.2
28	130	1520	1270	-16.4
29	79	1399	1340	-4.2

also an increase in the permanent deflection as the test progressed. Table F-4 summarizes the stiffness changes observed for all specimens. The greatest reduction was 20.6 percent for specimen 23. In 13 of the 14 specimens the stiffness reduced due to compression fatigue cracking. The correlation between measured crack size and the reduction in stiffness is not perfect. This may be caused by lack of precision and repeatability in the crack measurements and the compression test results, or it may suggest that one or both are not good indicators of fatigue damage.

SUMMARY AND CONCLUSIONS

This appendix has described an experimental study of fatigue of elastomeric bearings. The objectives of the tests were to develop a general understanding of fatigue and to develop rational but approximate design guidelines. Too few tests were conducted to develop S-N curves or precise fatigue limits.

1. The shear tests were designed on the assumption that shear fatigue is controlled by the daily temperature cycle, and a test procedure was developed that is believed to be conservative. The shear tests described in this appendix are not conservative for bearings in which shear deformations are induced by traffic loading. As a result, shear strains should be severely limited for these circumstances.

2. The compression fatigue tests were based on the hypothesis that compression fatigue is controlled by truck loading, and the assumption of 2 million cycles of HS-20 loading was used as the fatigue design service load. This design load is larger than warranted by actual truck loads, but the number of cycles is much smaller than actually expected. However, this procedure has generally resulted in a simple, approximate method for design of bridge members.

3. The test results showed that the strain range is an important parameter in assessing fatigue life. Larger strain range results in increased fatigue cracking and reduced fatigue life. An increase in mean strain reduced the fatigue life of the shear specimens, but had less influence on the cracking than did strain range. Further, dramatic reductions in fatigue life may occur when the mean stress is small compared to the stress range, but the strain crystallization of the elastomer is not utilized.

4. Rapid cycling of loading increases the specimen temperature and the rate of fatigue cracking. Since heat buildup appeared to accompany serious fatigue cracking, the most reliable indicator of potential fatigue problems with elastomers may be the hysteresis observable in the shear and compression test.

5. The elastomeric compound affects the fatigue behavior, but there is no good correlation between the expected fatigue damage and any of the material properties commonly measured in elastomeric compounds. The shear test results suggested that natural rubber has better fatigue performance, while the compression test results suggested that harder compounds of natural rubber or neoprene have less cracking. Fatigue cracking appears to reduce the compressive stiffness significantly, but it has much less effect on the shear stiffness. Fatigue cracks appear to be limited in size under cyclic shear loading, but there is no evidence of this limit in the compression fatigue tests.

6. Edge cover appears to reduce the rate of fatigue cracking. Additional research is clearly needed to evaluate fatigue behavior fully. It would be desirable to develop S-N curves for shear and compression loading, because this will be needed when more refined variable amplitude fatigue design procedures are employed.

APPENDIX G

SHEAR MODULUS TESTS

Tests were conducted to investigate the dependence of shear modulus on axial stress for the material used in the buckling and column shear tests. They were undertaken because buckling loads and transverse stiffnesses measured in the column shear tests did not correlate well with theoretical values obtained using the Basic Theory and nominal values of G. They were performed on pairs of bearings separated by a shear plate so as to avoid the geometric (buckling) effects that would occur with a taller stack of bearings.

Five bearing types were examined, and details are given in

Table G-1. They were tested in the rig that had been specially built for the simultaneous application of compression and shear and had been used for the shear fatigue tests. The axial loading arrangements were such that displacement rather than force was maintained constant. Several previously tested specimens were introduced into the axial load train to act as springs, and by this means the axial load variation during each cycle was limited to about 3 percent. At high stresses the load tended to creep down with time. The values of the apparent shear modulus, G_a, were obtained by fitting the best straight line to the second cycle of the shear force-deflection curve near the origin. G_a was then obtained from

$$G_a = \frac{K_t h_{rt0}}{2A_0} \tag{G-1}$$

where K_t = measured transverse stiffness of two bearings, A_0 = unloaded plan area of one bearing, and h_{rt0} = unloaded total elastomer thickness of one bearing.

The loading curves were very nearly linear, as can be seen from Figure G-1 which shows shear force-displacement curves for 5.66 in. × 11.33 in. bearings under different compressive stresses. Some material hysteresis was present in all cases. During the test at 110-psi compressive stress, the bearing slipped in shear, which accounts for most of the hysteresis in that curve. The shear load was limited either by slip or by keeping the shear strain below 0.83.

The test results are plotted in Figure G-2. The apparent shear modulus G_a was divided by G_{a0}, its value at zero compressive load, to give a dimensionless result. G_{a0} values were obtained from tests at a compressive stress of 100 psi, because some compression is needed to prevent slip. The abscissa in Figure G-2 was chosen to be σ_c/σ_{cr} because the results from the different shaped bearings would be expected to lie on a single line if the reduction in transverse stiffness (or apparent shear modulus) depended only on the stability effects outlined in Appendix E.

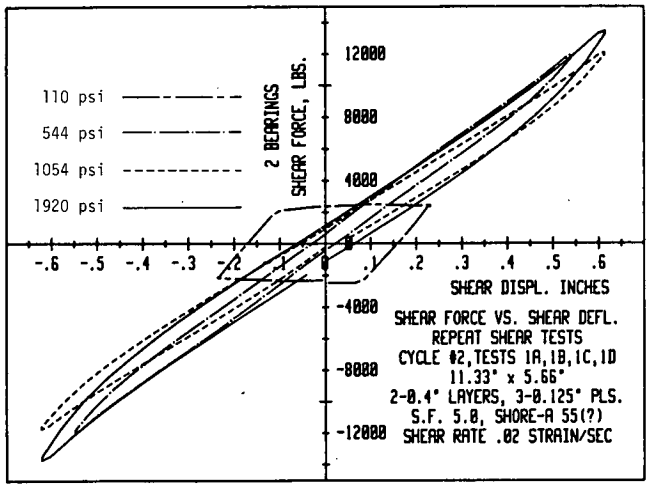

Figure G-1. Shear force vs. displacement at different compressive stress—5.66 in. × 11.33 in. bearings.

Table G-1. Material shear tests.

Specimen Plan Dimensions (in.)		Elastomer Layers	Steel Layers	Shape Factor	Axial Stress Range (psi)	Shear Strain/ sec
4 x 16	Rectangle	2 @ 0.306"	3 @ 1/8"	5.2	106 - 958	.01
5.66 x 11.33	Rectangle	2 @ 9.383"	3 @ 1/8"	4.9	100 -1920	.01-.02
8 x 8	Square	4 @ 0.375"	5 @ 1/16"	5.3	100 - 942	.01
9 dia.	Circle	2 @ 0.4375"	3 @ 1/8"	5.1	106 - 973	.01
8 x 16	Rectangle	2 @ 0.503"	3 @ 1/8"	5.3	103 - 973	.01

Note: All rectangular bearings were sheared parallel to their long dimension.

Two values for observed shear stiffness ratio are shown for each test. The higher one is derived using Eq. G-1, which includes no correction for changes in thickness and area, while the lower one includes a simple correction for each, giving

$$G_a = \frac{K_t h_{rt0}}{2A_0}(1 - \epsilon_c)^2 \tag{G-2}$$

Continuous curves are drawn through each set of points to represent approximately the trend of the experimental results. In all cases the component of deflection due to bending was less than 0.1 percent of the total, and therefore was ignored.

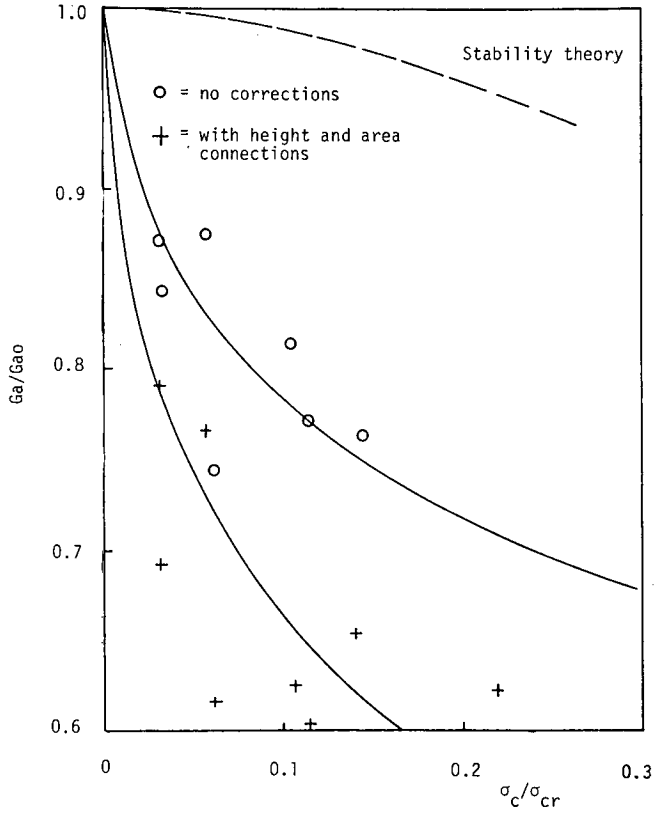

Figure G-2. Variation of apparent shear modulus with σ_c/σ_{cr}.

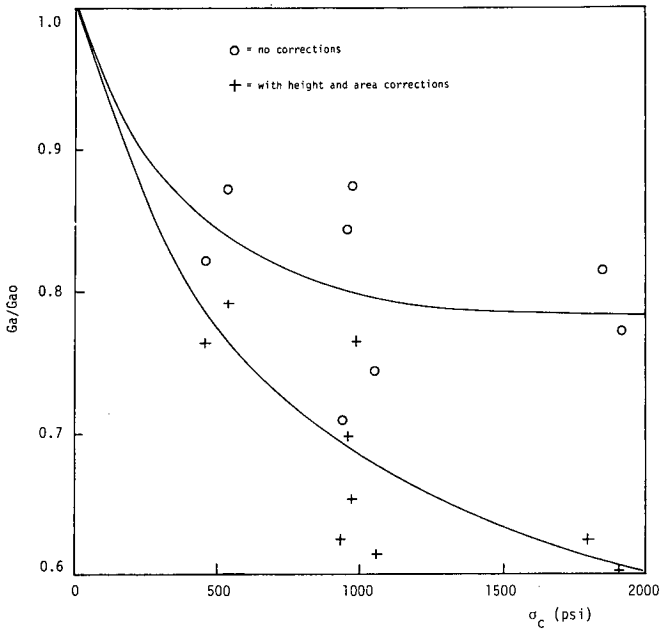

Figure G-3. Variation of apparent shear modulus with σ_c.

In Figure G-2 the apparent shear modulus can be seen to drop significantly with increasing σ_c/σ_{cr}. Stability theory, characterized in this case by Eq. E-23 of Appendix E, predicts some reduction in transverse stiffness with higher compressive stress, but the effect is small because the bearings were squat. It is shown as a dashed line in Figure G-2.

The experimental stiffness ratio falls much faster than the predicted one, and so either Eq. E-23 is wrong or other forms of behavior are more influential than the geometric ones. One plausible explanation is that the shear modulus of the material itself was falling under axial stress. To investigate this, the data are replotted against compressive stress in Figure G-3. If the area and height corrections of Eq. G-2 are ignored the observed shear modulus ratio appears to level out at about 0.80. When the corrections are included, it continues to fall.

Other explanations may also be offered. For example, the use of a continuum theory to predict stiffness reductions is clearly wrong when the bearing is made of only two discrete layers. Although this probably contributed to the error, it seems unlikely to account for all of it, because the discrepancy between the measured loss of stiffness and that predicted by Eq. E-23 is so large.

No cases are known of similar behavior being reported by other researchers. The findings contrast with Wong's (*42*) test results on circular natural rubber bearings in which he found that compressive stresses of up to 3,000 psi made almost no difference to the shear modulus after correction for area and thickness changes under load. However, Stevenson (*65*) reports that the shear moduli of some highly filled elastomers are very dependent on shear strain amplitude. Since compression causes shear strains, applying compressive and shear loads together causes some parts of the bearing to be subjected to higher shear strains than they would be under shear loading alone. If G falls with increasing shear strain, the simultaneous application of compression would reduce the transverse bearing stiffness, as was found here. The main difficulty with this argument is that a nominal 55 hardness elastomer would not normally have a high filler loading.

Gent (*41*) performed tests under simultaneous compressive stress and transverse load, but they were intended to investigate buckling; therefore, the specimens were slender columns and the stresses were low (less than 200 psi). It is not surprising,then, that he did not observe this effect.

It is concluded that the reduction in shear modulus observed in the tests described here was most probably a property of the particular elastomer used. Because that was a typical bridge bearing neoprene compound from a major manufacturer, the same effect may be expected to occur elsewhere. The significance is that any reduction in material modulus must be included in any predictions for transverse stiffness. It may prove important in quality assurance tests in which shear stiffness is measured under simultaneous compressive load.

The reduction was included in a simple way in the correlation between experimental and theoretical transverse stiffness values in Appendix E. By taking a G value of 117 psi in the theoretical predictions rather than the value of 140 psi found at low compressive stress, better correlation was achieved for both buckling loads and transverse stiffness. For a stack of bearings high enough to buckle at a compressive stress of about 100 psi, better correlation between theory might be obtained using a G of 140 psi (i.e., the value measured for low stresses). However, no tests were performed in this range. The use of a single reduced modulus does not reflect the trend of a continually reducing stiffness suggested by Figures G-2 and G-3, but at least its value lies within the range of measured values shown in those figures.

SUMMARY AND CONCLUSIONS

Shear tests on pairs of bearings subjected to simultaneous compressive stress showed a reduction in shear modulus with increasing compressive stress. The reduction was about 20 percent at compressive stresses in the range 500 to 1,000 psi. It appeared to be a material phenomenon rather than one associated with buckling. Such behavior was not observed in earlier tests (*42*) on bearings made from different material.

APPENDIX H

PROPOSED MODIFICATION TO AASHTO SPECIFICATION

SECTION 14—ELASTOMERIC BEARINGS

14.1. General

An elastomeric bridge bearing is a device constructed partially or wholly from elastomer, the purpose of which is to transmit loads and accommodate movements between a bridge and its supporting structure. This section of the Specification covers the design of plain pads (consisting of elastomer only) and reinforced bearings (consisting of layers of elastomer restrained at their interfaces by integrally bonded steel or fabric reinforcement). Tapered elastomer layers are not permitted. In addition to any internal reinforcement, bearings may have external steel load plates bonded to the upper or lower elastomer layers or both. Such load plates shall be at least as large as the elastomer layer to which they are bonded.

The materials, fabrication, and installation of the bearings shall be in accordance with the requirements of Section 25 of Division II of the Specification. Two design procedures are provided in this section. Bearings reinforced with steel may be designed either by the procedure defined in 14.4.A or the one in 14.4.B. Bearings with fiberglass reinforcement or unreinforced pads shall be designed by 14.4.A. Both design procedures are based on service loads.

14.2. Definitions

Longitudinal Axis: The axis of the bearing parallel to the longitudinal axis of the bridge girder(s)

Transverse Axis: The axis of the bearing perpendicular to the longitudinal axis

D = Gross diameter of a circular bearing (in.)

E_c = Effective compressive modulus of the elastomer, taking account of restraint of bulging $= 3G(1 + 2\bar{k}S^2)$ (psi)

H = Shear force on bearing (lb)

F_y = Yield stress of the steel reinforcement (psi)

G = Shear modulus of elastomer (psi) at 73°F

h_{rt} = Total elastomer thickness of the bearing (in.) $= t_{ri}$

h_{ri} = Thickness of elastomer layer number i (in.)

h_s = Thickness of the steel reinforcement (in.)

I = Moment of inertia of the bearing about its transverse axis (in.^{4})

$\bar{k}$ = Constant dependent upon elastomer hardness

L = Gross dimension of rectangular bearing parallel to the longitudinal axis (in.)

M = Moment required to rotate the bearing (lb-in.)

P = Compressive load on the bearing (lb)

S = Shape factor of one layer of a bearing

$$= \frac{\text{Effective Area Free to Bulge}}{\text{Loaded Area}}$$

$$= \frac{2\,h_{ri}\,(L + W)}{LW} \text{ for rectangular bearings}$$

$$= \frac{4\,h_{ri}}{D} \text{ for circular bearings}$$

W = Gross dimension of rectangular bearing parallel to the transverse axis

θ = Relative rotation of top and bottom surfaces of bearing. Subscripts:
- TL = total load
- LL = live load
- x = about transverse axis
- z = about longitudinal axis

β = Modifying factor having a value of 1.0 for internal layers of reinforced bearings, 1.4 for cover layers, and 1.8 for plain pads. Note that $\beta = 1.8$ applies only to 14.4.A.

Δ_c = Instantaneous compressive deflection of bearing (in.)

Δ_s = Shear deformation of the bearing in one direction from the undeformed state (in.)

ϵ_{ci} = Compressive strain in elastomer layer number i (change in thickness divided by the unstressed thickness)

$\sigma_c = P/A$ = Average compressive stress on the bearing caused by the dead and live load, excluding impact

τ_s = Average shear stress induced in the elastomer by shear deformation

14.3. Material Properties

Values for the material properties of the elastomer are needed for design. However, the properties of elastomeric compounds depend on their constituents and on the temperature of the material.

The shear modulus at 73°F shall be used as the basis for design for compression and stability. When the properties of the elastomer from which the bearings are to be made are known, they shall be used. The shear modulus shall be determined using the test specified in Section 25 of Division II of this Specification. When only the hardness is specified, the other properties shall be taken as the least favorable values from the range for that hardness given in Table 14.3.1. Values for intermediate hardnesses shall be obtained by interpolation.

Table 14.3.1.

Hardness (Shore 'A')	50	60	70
Shear Modulus at 73° F (psi) (MPa)	85-110 (0.6-.77)	120-155 (0.85-1.1)	160-260
Creep Deflection at 25 Years / Instantaneous deflection	25%	35%	45%
$\bar{k}$	.75	.60	.55

Material with a nominal hardness greater than 60 shall not be used for reinforced bearings.

For the purposes of bearing design, all bridge sites shall be classified as being in temperature zone I, II, or III. Zone I consists of all regions where the 50-year extreme low temperature does not fall below 0°F (18°C) and the overnight low temperature does not drop below 25°F (−5°C) for more than a 6-hour duration on three nights in succession. Zone II consists of all regions not qualifying for Zone I, but in which the 50-year low temperature is not less than −30°F (−35°C). All other regions fall into Zone III.

Bearings shall be made from grades of elastomer in accordance with Table 14.3.2. A grade of elastomer higher than that required may be used. The special provisions required in Table 14.3.2 are that either a positive slip apparatus be installed or that the components of the bridge be able to resist the forces arising from a bearing force four times the design shear force. The design shear force is defined as the shear force induced in the bearing when it is subjected to a shear deformation, Δ_s, (defined in Section 14.4.A4 or 14.4.B2) at 73°F. If a positive slip apparatus is installed, the components shall be able to withstand forces arising from a bearing force equal to twice the design shear force. All bearings made from Grade 5 elastomer shall be tested in accordance with Section 25.9.1 of Division II of this Specification.

Table 14.3.2. ASTM 4014 elastomer grades to be used in different temperature zones.

Zone	I	II	III
Without Special Provisions	2	3	5
With Special Provisions	1	2	5

14.4. Design Methods

14.4.A. Design Method A

14.4.A.1. Compressive Stress

Unless shear deformation is prevented, the average compressive stress σ_c in any layer shall not exceed the least of:

$$GS/\beta$$

and either 1000 psi, for steel-reinforced bearings
or 800 psi, for plain pads or fiber-reinforced bearings

In bearings containing layers of different thickness, the value of S used shall be that for the thickest layer. Allowable compressive stress may be increased by 10 percent where shear deformation is prevented.

14.4.A.2. Compressive Deflection

Compressive deflection, Δ_c, of the bearing shall be so limited as to ensure the serviceability of the bridge.

Instantaneous deflection shall be calculated as

$$\Delta_c = \sum_i \epsilon_{ci}\, h_{ri}$$

Values for ϵ_{ci} shall be obtained from design aids based on tests such as presented in Figures 14.4.A.2A and 14.4.A.2B, by testing or by rational analysis.

The effects of creep of the elastomer shall be added to the instantaneous deflection when considering long-term deflections. They shall be computed from information relevant to the elastomeric compound used if it is available. If not, the values given in Article 14.3 shall be used as a guide.

14.4.A.3. Rotation

The relative rotation between top and bottom surfaces of the bearing shall be limited by

$$L\theta_{TL,x} + W\theta_{TL,z} \leq 2\Delta_c, \quad \text{for rectangular bearings}$$
$$D\sqrt{\theta^2_{TL,x} + \theta^2_{TL,z}} \leq 2\Delta_c, \quad \text{for circular bearings}$$

14.4.A.4. Shear

The horizontal bridge movement shall be taken as the maximum possible deformation caused by creep, shrinkage, post-tensioning, and thermal effects computed between the instal-

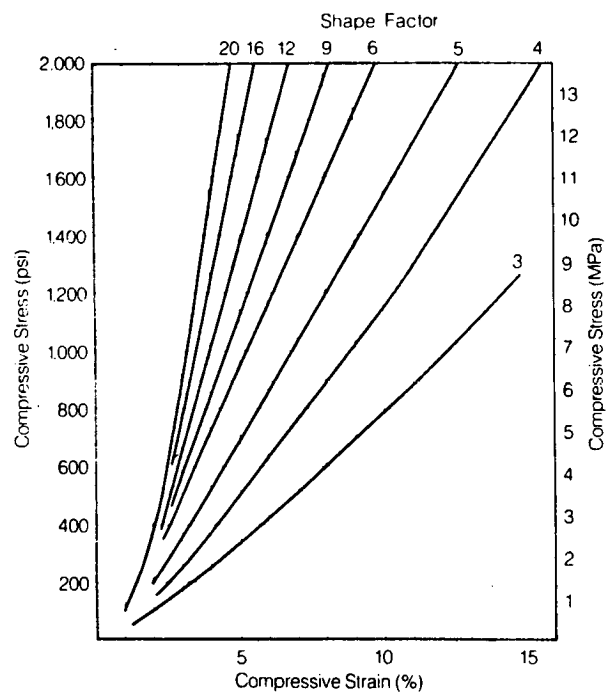

Figure 14.4.A.2A. Compressive stress-strain curves for 50 durometer elastomer.

lation temperature and the least favorable extreme temperature. The maximum shear deformation of the bearing, Δ_s, shall be taken as the horizontal bridge movement, modified to account for the pier flexibility. If a positive slip apparatus is installed, Δ_s need not be taken larger than the deformation corresponding to first slip.

The bearing shall be designed so that

$$h_{rt} \geq 2\ \Delta_s$$

The shear stress induced by shear deformation is given by

$$\tau_s = G \frac{\Delta_s}{h_{rt}}$$

14.4.A.5. Stability

To ensure stability, the total thickness of the bearing shall not exceed the smallest of:

$L/5$, $W/5$, or $D/6$ for plain pads
$L/3$, $W/3$, or $D/4$ for reinforced bearings

14.4.A.6. Reinforcement

The reinforcement shall be fiberglass or steel and its resistance in pounds per linear inch at working stress levels in each direction shall not be less than

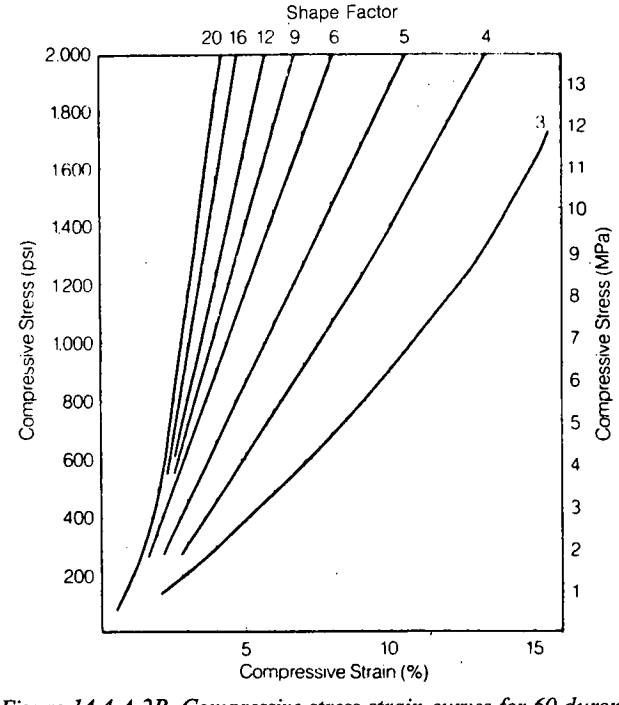

Figure 14.4.A.2B. Compressive stress-strain curves for 60 durometer elastomer.

$1400\ h_{ri}$ for fiberglass
$1700\ h_{ri}$ for steel

For these purposes, h_{ri} shall be taken as the mean thickness of the two layers of the elastomer bonded to the reinforcement if they are of different thicknesses. The resistance per linear inch is given by the product of the material thickness of the reinforcement and the allowable stress. The allowable stress shall be calculated taking into account fatigue loading but ignoring holes in the reinforcement. Holes shall be prohibited in fiber reinforcement. They are not recommended in steel reinforcement, but if they exist, the steel thickness shall be increased by a factor

$$\frac{2 \times \text{gross width}}{\text{net width}}$$

14.4.B. Method B Optional Design Procedure for Steel Reinforced Bearings

14.4.B.1. Pure Compression

In any internal layer of the bearing, the average compressive stress, σ_c, due to the total dead and live load on the bearing, shall not exceed 1600 psi or 1.66 *GS*. The average compressive stress due to live load shall not exceed 0.66 *GS*. For bearings fixed against translation, these limits may be taken as 2.0 *GS* and 1.0 *GS*, respectively. No increase in load for impact need be included.

Instantaneous changes in deflection due to short-term loading shall be calculated by

$$\Delta_c = \sum_i \epsilon_{ci} h_{ri}$$

where

$$\epsilon_{ci} = \frac{P}{AE_c}$$

and

$$E_c = 3G\ (1 + 2\ \bar{k}S^2)$$

In these equations P, Δ_c, and ϵ_{ci} refer to the changes in load, deflection, and strain caused by the instantaneous load. The use of test results and design curves for deflection calculations is also acceptable. The effects of creep of the elastomer shall be added when considering long-term deflections. They shall be computed from information relevant to the elastomeric compound used if it is available. If not, the values given in Article 14.3 shall be used as a guide.

14.4.B.2. Shear

The shear deformation shall be taken as the maximum possible deformation caused by creep, shrinkage, post-tensioning, and thermal effects computed between the installation temperature and the least favorable extreme temperature, unless a positive slip apparatus is installed.

The bearing shall be designed so that

$$h_{rt} \geq 2\ \Delta_s$$

The shear stress induced by shear deformation may be approximated by

$$\tau_s = G\frac{\Delta_s}{h_{rt}}$$

14.4.B.3. Rotation

The rotational deformation shall be taken as the maximum possible rotation between the top and bottom of the bearing caused by initial lack of parallelism and girder end rotation. Rotation about the transverse axis of the bearing shall be limited to:

$$\theta_{TL,\,x} \leq \frac{2\Delta_c}{L}$$

Rotation about the longitudinal axis of the bearing is not recommended. The moment induced by the rotation, M, about the transverse axis of the bearing may be calculated by

$$M = \frac{E_c\, I\theta_x}{h_{rt}}$$

where

$$I = \frac{WL^3}{12}, \text{ for rectangular bearings}$$

If rotation exists about the longitudinal axis, the moment shall be computed by a rational method or be established by test.

14.4.B.4. Combined Compression and Rotation

In bearings subjected to both compression and rotation about the transverse axis of the bearing, the average compressive stress due to total dead and live load on the bearing, without increase for impact, shall be limited to

$$\sigma_c \leq \frac{1.66\ GS}{1 + \dfrac{L\theta_{TL,\,x}}{4\ \Delta_c}}$$

and the total compressive stress due to live load alone shall be limited to

$$\sigma_c \leq 0.66\ GS$$

where $\theta_{TL,\,x}$ is the rotation about the transverse axis of the bearing due to total dead and live loads. For bearings fixed against translation, the constants 1.66 GS and 0.66 GS in the foregoing equations for stress limits may be taken as 2.0 GS and 1.0 GS, respectively.

Rotations about the longitudinal axis of the bearing are not recommended, but if they exist, reduced stress levels for these rotations shall be computed by a rational method.

14.4.B.5. Stability

The bearings shall be proportioned with a geometry that prevents stability failure. The average compressive stress due to total dead and live load on rectangular bearings shall be less than

$$\frac{GL}{1.15\ h_{rt}}\sqrt{1 + \left(\frac{2L}{W}\right)\frac{S^2}{4}}$$

Rectangular elastomeric bearings that are restrained to prevent all relative movement between the top and bottom of the bearing shall have average compressive stress due to total dead and live loads less than

$$\frac{GL}{0.6\ h_{rt}}\sqrt{1 + \left(1 + \frac{2L}{W}\right)\frac{S^2}{4}}$$

The stability of circular bearings may be evaluated by using the equations for a square bearing where

$$L = 0.8\ D$$

If L is greater than W for a rectangular bearing, stability shall be checked by the above formulas with L and W interchanged.

14.4.B.6. Reinforcement

The thickness of the reinforcement, h_s, shall satisfy

$$h_s \geq \frac{1.5\ (h_{ri} + h_{ri})\ \sigma_{c,\,TL}}{F_y}, \quad \text{for total load}$$

$$h_s \geq \frac{1.5\ (h_{ri} + h_{ri})\ \sigma_{c,\,LL}}{F_{sr}}, \quad \text{for live load}$$

where F_{sr} is the allowable stress range based on fatigue loading, but ignoring holes. If holes exist the minimum thickness shall be increased by a factor

$$\frac{2 \times \text{gross width}}{\text{net width}}$$

14.4.B.7. Special Testing and Acceptance Requirements

All elastomeric bearings that are designed by Section 14.4.B shall satisfy the acceptance and testing requirements of Section 25.7.8 of Division II.

14.5. Anchorage

If the maximum shear force due to bearing deformation, H,

exceeds one-fifth of the compressive force P due to dead load alone, the bearing shall be secured against horizontal movement. The bearing shall not be permitted to sustain uplift forces.

14.6. Stiffeners for Steel Beams and Girders

The flanges of steel members seated on elastomeric bearings must be flexurally stiff enough not to risk damage to the bearing. Any necessary stiffening may be accomplished by means of a sole plate or vertical stiffeners. The stiffening requirements of this section do not replace any others in this specification, but should be read in conjunction with them.

Single-webbed beams and girders symmetric about their minor (vertical) axis and placed symmetrically on the bearing need no additional stiffening if

$$\frac{b_f}{2t_f} < \sqrt{\frac{F_{yg}}{3.4\ \sigma_c}}$$

where

b_f = total flange width,
t_f = thickness of flange or combined flange and sole plate, and
F_{yg} = yield stress of the girder steel.

14.7. Installation

Misalignment in bridge girders due to fabrication tolerance, camber, or other source shall be considered in the bearing design.

COMMENTARY—SECTION 14

14.1. Tapered layers are expressly prohibited because they cause larger shear strains and bearings made with them fail prematurely due to delamination or rupture of the reinforcement.

14.2. A refined definition of the shape factor is not warranted because quality control on elastomer thickness has a more dominant influence on bearing behavior. The coefficient $\beta = 1.8$ does not apply to design Method B (i.e., 14.4.B.) because this method is strictly for reinforced bearings with steel reinforcement. The β values greater than 1.0 account approximately for the slip that may occur at friction surfaces.

14.3. The same material properties are used for both design methods, but Method B permits taller bearings and greater allowable stresses. The low temperature requirements are based on an analytical study of the low temperature stiffening of the bearing. Analysis suggests that bearing forces due to low temperature crystallization of 3 to 4 times the design force can be developed if the bearing is made from a low temperature grade of elastomer that is not consistent with the expected temperatures. Instantaneous low temperature stiffening may cause bearing forces that are several orders of magnitude larger than the design force, and so Grade 5 elastomer is required for Zone III. The analyses were based on the best available experimental information, but they are necessarily approximate. More experimental research is needed in this area.

14.4.A. This method is nearly identical to the existing AASHTO (1985) provisions and requires no special comment. Only the organization has been changed to be consistent with the new Method B provisions. The reader is therefore referred to *NCHRP Report 248* for these provisions.

14.4.B.1. The 1600-psi stress limit is intended to control delamination of the elastomer from the reinforcement. There is tremendous scatter in delamination test results, but the 1600-psi stress limit appears to provide satisfactory results if it is combined with a limit on the shear strain. The limits of 1.66 *GS* on total dead and live load and 0.66 *GS* on live load only are intended to control fatigue cracking and delamination. They are based on the observation that fatigue cracking in experiments remained acceptably low if the maximum shear strain due to total dead and live load was kept below 3.0 and the maximum strain range for cyclic loading was kept below 1.5. The level of damage considered acceptable had to be selected arbitrarily, therefore the limits are not clear-cut.

Two limits are given, one for total load and one for live load, and the more restrictive one will control.

Increases in the load to simulate the effects of impact are not required. This is because the impact stresses are likely to be only a small proportion of the total load, and also because the stress limits are based on fatigue damage, the limits of which are not clear cut. Furthermore, the AASHTO impact fraction does not represent the effective load increase on a bearing.

14.4.B.2. Experiments show that corners of a bearing roll over if the shear strain due to shear deformation exceeds 50 percent. Roll-over may cause damage to the reinforcement and the elastomer and should be avoided. This shear deformation limit also helps prevent excessive fatigue cracking of the elastomer. The cyclic fatigue tests from which the provisions are derived were based on a 20,000 cycle life expectancy, so the results will be unconservative if the shear deformation is caused by high cycle loading due to braking forces or vibration. The maximum shear strain due to these high cycle loadings should be restricted to less than 0.10 unless better information is available.

14.4.B.3. The rotational stiffness equation is an approximate relationship which appears to provide reasonable correlation with experimental results. The limitation on maximum rotation is based on the prevention of lift-off. Lift-off bends the plates and may introduce tensile stress in the elastomer and should be avoided. Ordinarily bearings should be oriented so that rotation occurs about their long axes, because rotation about the short axis causes relatively larger strains in the elastomer.

14.4.B.4. The limitations on compressive stress due to live loads alone and to total dead and live loads are based on the shear strain limits for fatigue noted earlier. The equations are simplified by the observation that the maximum shear strain due to rotation is relatively insensitive to the aspect ratio of the bearing if the bearing is rotated about its longer axis. If rotation occurs about the short axis, the equations given in 14.4.B.4 may not be conservative, and the strains must be computed by a rational analysis.

14.4.B.5. The stability checks in this section are based on a conservative application of the buckling theory derived by Gent and a safety factor of 1.7. Experiments have suggested that this theory is fairly realistic for tall bearings or those with low shape factors. The equation is quite conservative for most practical bridge bearings. This provision will permit taller bearings and reduced shear forces compared to those permitted under previous specifications.

14.4.B.6. Special testing and acceptance requirements are needed for bearings designed by Section 14.4.B. Method B permits taller bearings and greater allowable stresses. Therefore, Method B will require that each bearing be proof loaded to 150 percent of its service load and be examined for misplaced reinforcement or poor layer thickness control and for partial delamination. Shear tests are needed on randomly selected bearings to assure that the elastomer has material properties that are compatible with the design assumptions.

REFERENCES

1. *Standard Specifications for Highway Bridges.* AASHTO, 13th Edition, Washington, D.C. (1983).
2. DU PONT, "Design of Neoprene Bearing Pads." (Apr. 1959).
3. STANTON, J. F., and ROEDER, C. W., "Elastomeric Bearings, Design, Construction and Materials." *NCHRP Report 248,* Washington, D.C. (Aug. 1982) 82 pp.
4. *Standard Specifications for Highway Bridges.* 1985 Modifications, AASHTO, Washington, D.C. (1985).
5. MURRAY, R. M., and DETENBER, J. D., "First and Second Order Transitions in Neoprene. *Rubber Chemistry and Technology* (Apr.–Jun., 1961).
6. STEVENSON, A., "Characterization of Rubber Vulcanizates for Bridge Bearings at Low Service Temperatures." *Final Report,* MRPRA (Jul. 1973).
7. *Low Hardness Butyl Dynamics Compounds,* Exxon Corporation ETD-7504 3352.
8. British Standards Institution, BS5400; Steel, Concrete and Composite Bridges, Part 9A and 9B (1983).
9. GENT, A. N., "On the Relation between Indentation Hardness and Young's Modulus." *Transactions of the Institution of the Rubber Industry,* Vol. 34, No. 2 (1958) pp. 46–57.
10. HOLMAN, J. P., *Heat Transfer.* Fifth Edition, McGraw-Hill, N.Y. (1981).
11. CARSLAW, H. S., and JAEGER, J. C., *Conduction of Heat in Solids.* Second Edition, Oxford University Press, Fairlawn, N.J. (1959).
12. WOOD, L. A., "Physical Constants of Different Rubbers." *Rubber Chemistry and Technology,* Vol. 49, No. 2 (1976).
13. *Rubber: Physical and Chemical Properties,* R.A.B.M. (1935).
14. MEINECKE, E. A., "Comparing the Time and Rate Dependent Mechanical Properties of Elastomers." *Rubber Chemistry and Technology,* Vol. 53, No. 5 (1980) pp 1145–1159.
15. GENT, A. N., and LINDLEY P. B., "The Compression of Bonded Rubber Blocks" *Proc. Instn. Mech. Engnrs* (England), Vol. 173, No. 3 (1959) pp. 111–122.
16. CONVERSY, F., "Appareils d'Appui en Caoutchouc Frette" (Bonded Rubber Bearings—in French). *Annales des Ponts et Chaussees,* VI (Nov.–Dec. 1967).
17. TOPALOFF, B. "Gummilager fur Brucken" (Rubber Bearings for Bridges—in German). *Beton und Stahlbetonbau,* Vol. 54, No. 9 (Sept. 1, 1959) pp. 229–230.
18. REJCHA C., "Design of Elastomeric Bearings. " *PCI J.* (Oct. 1964) pp. 62–78.
19. HATTORI, R. and TAKEI, K. *J. Soc. Rubber Industry of Japan.* Vol. 23, (1950) p. 194.
20. HOLOWNIA, B. P., "Compression of Bonded Rubber Blocks." *J. Strain Analysis,* No. 7 (1972).
21. PAYNE, A. R., *Nature,* Vol 177 (1956) p. 1174.
22. HERRMANN, L. R., WELCH K. R., and LIM C. K., "Composite F.E.M. Analysis for Layered Systems." *J. Eng. Mechan.,* ASCE Vol. 110, No. 9 (1984) pp. 1284–1302.
23. GENT, A. N. "Load-Deflection Relations and Surface Strain Distributions for Flat Rubber Pads." *Rubber Chemistry and Technology,* Vol. 31 (1958) pp. 395–414.
24. HOLOWNIA, B. P. "Effect of Different Types of Carbon Black on Elastic Constants in Elastomers." *Plastics and Rubber: Materials and Applications* (Aug. 1980) pp. 129–132.
25. Program AXISOL, for Analysis of Axisymmetric Solids. Originally programmed by E. L. Wilson (University of California at Berkeley), modified at the University of Washington.
26. McDonnell-Douglas Automation Co. "STRUDL Version 5.1." St. Louis, MO.
27. "Design Recommendations for Elastomeric Bridge Bearings." *Technical Memorandum BE1/76,* Highways Directorate, Dept. of Environment, Great Britain (Feb. 1976).
28. Australian Standard 1523-1976, "Elastomeric Bearings for Use in Structures."
29. Consiglio Nazionale Delle Ricerche, "Appogi di Gomma nelle Construzioni Istruzioni per il Calcolo e l'Impiego" ("Elastomeric Bearing Pads—Instructions for Design and Application"). CNR-UNI 10018-72, Milan (1972).

30. "Code for the Use of Rubber Bearings for Rail Bridges." UIC Code 772R, Brussels (1973) 56 pp.
31. "Gumba-Gummi im Bauwesen GMBH," (Approval by Institute of Civil Engineering for Elastomeric Bearings Produced by GUMBA), West Germany (Oct. 1973).
32. TIMOSHENKO, S. P. and GOODIER, J. N., *Theory of Elasticity.* Second edition, McGraw-Hill.
33. GRAFF, G. A., "Closed Form Solutions for Stresses on a Circular Elastomeric Bearing Subjected to a Concentric Axial Load." MSCE Project Report, University of Washington (Jun. 1986).
34. BRANLUND, C. S., "Steel Plate Stresses in Reinforced Bearings with Holes." MSCE Project Report, University of Washington (Dec. 1986).
35. HERRMANN, L. R., SHAFIGH-NOBARI, E., and HAMIDI, R., "On the Verification of a Finite Element Analysis for Elastomeric Bridge Bearings." Vol. I, *Joint Sealing and Bearing Systems for Concrete Structures,* SP94, ACI, Detroit (1986) pp. 1–30.
36. GENT, A. N., and MEINCKE, E. A., "Compression Bending and Shear of Bonded Rubber Blocks." *Polymer Engineering and Science,* Vol. 10, No. 1 (Jan. 1970) pp. 48–53.
37. TAMHANKAR, M. G., and CHHAUDA, J. N., "Assessment of Rotational Stiffness of Elastomeric Bridge Bearings." *Indian Roads Congress J.,* Vol. 40, No. 1 (Oct. 1979) pp. 219–238.
38. CADWELL, S. M., MERRILL, R. A., SLOMAN, C. M., and YOST, F. L., "Dynamic Fatigue Life of Rubber." *Industrial and Engineering Chemistry,* Analytical Edition, Vol. 12, No. 1 (Jan. 1940) pp. 19–23.
39. PRICE, A. R., "Abnormal and Eccentric Forces on Elastomeric Bridge Bearings." TRRL Laboratory Report No. 708 (1978).
40. PORTER, L. S. and MEINECKE, E. A., "Influence of Compression upon the Shear Properties of Bonded Rubber Blocks." *Rubber Chemistry and Technology,* Vol. 53, No. 5 (Dec. 1980).
41. GENT, A. N., "Elastic Stability of Rubber Compression Springs." *J. Mechan. Eng. Sci.,* Vol. 6, No. 4 (1964) pp. 318–326.
42. WONG, B. K., "Compression and Shear Test of Full Size Elastomeric Bearings." A thesis submitted in partial fulfillment of the requirements of the degree of Master of Science in Civil Engineering, University of Washington, Seattle (1984).
43. CURRY, K. N., "Compression and Shear Tests of Reinforced Elastomeric Bearings of Different Shapes and Sizes." A report submitted in partial fulfillment of the degree of Master of Science in Engineering, University of Washington, Seattle (1985).
44. BRIELMAER, A. A., HOBLITZELL, J. R., and BORDEN, G. G., "Neoprene Bridge Pads: Fatigue Behavior Compression and Shear." *Engineering Research Bulletin B-97,* The Pennsylvania State University (Jan. 1968).
45. TIMOSHENKO, S. P., and GERE, J. M., "Theory of Elastic Stability" McGraw-Hill, Second Edition (1961).
46. ENGESSER, F., *Zentr. Bauverwaltung.* Vol. II, p. 483, 1891.
47. HARINGX, J. A., "On Highly Compressive Helical Springs and Rubber Rods, and their Application for Vibration-free Mountings." Parts I, II, III, *Phillips Res. Reports* (1948–1949).
48. SCHAPERY, R. A., and SKALA, D. P., "Elastic Stability of Laminated Elastomeric Columns." *International Journal of Solids and Structures,* Vol. 12, No. 66 (1976) pp. 401–417.
49. SIMO, J. C., and KELLY, J. M. "Finite Element Analysis of the Stability of Multilayer Elastomeric Bearings." *Engineering Structures,* Vol. 6 (Jul. 1984) pp. 162–174.
50. TRAHAIR, N. S., "Deformations of Geometrically Imperfect Beams." *J. Struct. Div. Proc. ASCE,* ST7 (Jul. 1969) pp. 1475–1496.
51. BUCKLE, I. G., and KELLY, J. M., "Properties of Slender Elastomeric Isolation Bearings During Shake Table Studies of a Large-scale Model Bridge Deck." *Joint Sealing and Bearing Systems for Concrete Structures,* ACI SP 94 ACI, Detroit (1986).
52. LINDLEY, P. B., "Properties Given for the Natural Rubber Engineering Vulcanizates in the EDS Series." Natural Rubber Engineering Data Sheet, EDS 2, Malaysian Rubber Producers' Research Association (1979).
53. HERRMANN, L. R., HAMIDI, R., and SHAFIGH-NOBARI, E., "Nonlinear Behavior of Elastomeric Bridge Bearings." Unpublished Progress Report to California DOT, Dept. of Civil Eng., University of California at Davis (Sept. 1985).
54. GENT, A. N., and LINDLEY, P. B., "Internal Rupture of Bonded Rubber Cylinders in Tension," *Proc. Royal Society of London,* A249, (195) (1958).
55. Union Internationale des Chemin de Fer (UIC), Office for Research and Experiments (ORE), Question D60, "Use of Rubber for Bridge Bearings." Interim Reports I and II and Final Report, Utrecht (1962–1963).
56. LINDLEY, P. B. and STEVENSON, A., "Fatigue Resistance of Natural Rubber in Compression." *Malaysian Rubber Producers Research Association,* England (Mar. 1981).
57. LAKE, G. J., and LINDLEY, P. B., "Ozone Attack and Fatigue Life of Rubber." *Use of Rubber in Engineering,* MacLaren and Sons, Ltd., London (1967) pp. 56–71.
58. LAKE, G. J., and LINDLEY, P. B., "Ozone Cracking, Flex Cracking and Fatigue of Rubber." *Rubber J.* (Oct. and Nov. 1964) pp. 1–16.
59. LINDLEY, P. B., and TEO, S. C., "Strain Concentration Factors for Bonded Blocks with Radiused Fillets." *Plastics and Rubber Materials and Applications* (Nov. 1977) pp. 152–155.
60. LINDLEY, P. B., "Engineering Design with Natural Rubber." *Malaysian Rubber Technical Bulletin,* MRPPA (1978).
61. OZELL, A. M., and DINIZ, J. F., "Report on Tests of Neoprene Pads under Repeated Shear Loads." *Highway Research Board Bulletin 242* (1960) pp. 20–27.
62. CHHAUDA, J. N., and TAMHANKAR, M. G., "Experimental Investigation on Restrained Neoprene Bearings." *Indian Roads Congress J.,* Vol. 34, No. 1 (Apr. 1971) pp. 185–205.
63. BRIELMAER, A. A., and HOBLITZELL, J. R., "Neoprene Bearing Pads under Repeated Compression and Shear." *Highway Research Record 253* (1968) pp. 97–104.
64. ALBRECHT, P., "Review of Fatigue Design Methods for Highway Bridges." Dept. of Civil Engineering, University of Maryland (May 1986).
65. STEVENSON, A., "Laminated Rubber Properties for Structural Offshore Applications." *Offshore Technology Conference,* OTC 5232, Houston, Texas (May 1986).

66. SCROGGINS, G. C., "Stability of Elastomeric Bearings." Thesis submitted in partial fulfillment of the requirements for the degree of Master of Science in Civil Engineering, University of Washington, Seattle (1986).
67. *Climates of the States.* Second Edition, Gale Research Co, Detroit, Michigan (1974).
68. *Climatological Data of the States,* U.S. Weather Bureau, Dept. of Commerce (multi-volume set of data for each state of the U.S.).
69. ASTM, "Standard Specification for Plain and Steel-Laminated Elastomeric Bearings for Bridges." ASTM D4014-81 (1981).

THE TRANSPORTATION RESEARCH BOARD is a unit of the National Research Council, which serves the National Academy of Sciences and the National Academy of Engineering. It evolved in 1974 from the Highway Research Board which was established in 1920. The TRB incorporates all former HRB activities and also performs additional functions under a broader scope involving all modes of transportation and the interactions of transportation with society. The Board's purpose is to stimulate research concerning the nature and performance of transportation systems, to disseminate information that the research produces, and to encourage the application of appropriate research findings. The Board's program is carried out by more than 270 committees, task forces, and panels composed of more than 3,300 administrators, engineers, social scientists, attorneys, educators, and others concerned with transportation; they serve without compensation. The program is supported by state transportation and highway departments, the modal administrations of the U.S. Department of Transportation, the Association of American Railroads, the National Highway Traffic Safety Administration, and other organizations and individuals interested in the development of transportation.

The National Academy of Sciences is a private, nonprofit, self-perpetuating society of distinguished scholars engaged in scientific and engineering research, dedicated to the furtherance of science and technology and to their use for the general welfare. Upon the authority of the charter granted to it by the Congress in 1863, the Academy has a mandate that requires it to advise the federal government on scientific and technical matters. Dr. Frank Press is president of the National Academy of Sciences.

The National Academy of Engineering was established in 1964, under the charter of the National Academy of Sciences, as a parallel organization of outstanding engineers. It is autonomous in its administration and in the selection of its members, sharing with the National Academy of Sciences the responsibility for advising the federal government. The National Academy of Engineering also sponsors engineering programs aimed at meeting national needs, encourages education and research, and recognizes the superior achievements of engineers. Dr. Robert M. White is president of the National Academy of Engineering.

The Institute of Medicine was established in 1970 by the National Academy of Sciences to secure the services of eminent members of appropriate professions in the examination of policy matters pertaining to the health of the public. The Institute acts under the responsibility given to the National Academy of Sciences by its congressional charter to be an adviser to the federal government and, upon its own initiative, to identify issues of medical care, research, and education. Dr. Samuel O. Thier is president of the Institute of Medicine.

The National Research Council was organized by the National Academy of Sciences in 1916 to associate the broad community of science and technology with the Academy's purpose of furthering knowledge and advising the federal government. Functioning in accordance with general policies determined by the Academy, the Council has become the principal operating agency of both the National Academy of Sciences and the National Academy of Engineering in providing services to the government, the public, and the scientific and engineering communities. The Council is administered jointly by both Academies and the Institute of Medicine. Dr. Frank Press and Dr. Robert M. White are chairman and vice chairman, respectively, of the National Research Council.

TRANSPORTATION RESEARCH BOARD
National Research Council
2101 Constitution Avenue, N.W.
Washington, D.C. 20418

ADDRESS CORRECTION REQUESTED

NON-PROFIT ORG.
U.S. POSTAGE
PAID
WASHINGTON, D.C.
PERMIT NO. 8970

000015M003
MATERIALS ENGR

IDAHO TRANS DEPT DIV OF HWYS
P O BOX 7129
BOISE ID 83707